DIAMOND-BASED THERMO–TUNNEL DEVICES FOR HOSTILE ENVIRONMENTS

by Amit K. Tiwari

School of Electrical and Electronic Engineering

Newcastle University

A thesis submitted for the degree of

Doctor of Philosophy

February 2013

Dedicated to

My parents and brother

Declaration

I certify that all material in this thesis which is not my own work has been identified, and no materials has not previously been submitted and approved by the award of a degree in this or any other university.

Amit K. Tiwari

February 2013

Acknowledgements

There are many people I wish to thank for their support and encouragement in the sojourn of my PhD research, without whom this thesis would not have been possible. Foremost, special thanks to Dr. Jon Goss for his scientific insight, patience, inspiration and stalwart supervision. Hearing his enthusiastic and supportive cry 'Is everything alright?' after having an encounter with his unquenchable inquisitiveness will probably be remembered for a long time.

Another special thanks to Dr. Alton Horsfall, who offered the opportunity to pursue this PhD with his leading research group. I have immense admiration for his extremely supportive and encouraging supervision, particularly his stress relieving sense of humour.

I am deeply grateful to Prof. Nick Wright, who has not only supervised me but also gave me another excellent opportunity to extend my stay at Newcastle by offering me a position as a Post–Doctoral Research Associate in his fast changing research group.

Despite the anonymity of the individuals, I must thank the EPSRC and BAE systems for arranging the funds through the DHPA scheme for the duration of my PhD at Newcastle University. I would also like to acknowledge the School of Electrical and Electronic Engineering for providing the necessary resources and research environment for me to conduct my PhD work.

Next there are all the friends cum office mates that I've worked with, who made the stay in Newcastle not only enjoyable but also productive one. I am thankful to Ben, Karthik, Lucy, Omid, HK, Simon, Leonie, Dan, Rupert, Graeme, Sandip, Neal, Shahin, Raied, Ferran and Raman. Having a dedicated technical session on the PhD research, school policies and some burning global issues with Ben and Karthik every Friday night was probably the most recurring and enjoyable extra–curricular event during my PhD research.

Many thanks to the AIMPRO father Prof. R Jones for his precious ideas on my research work, and Dr. Patrick Briddon and Dr. Mark Rayson for their excellent development and maintenance of the DFT code. Dr. Jerry Hagon deserves special attention too for developing

the AIMVIEW software, which has been enormously helpful in visualising the wave function iso–surfaces.

On a more personal level, finally my family members, who have been great over the last 3 years and never raised an eyebrow at my profession till this day.

Abstract

Solid state thermal energy conversion techniques are becoming increasingly important for both terrestrial and extraterrestrial applications, such as space power systems and waste heat scavenging from different heat sources. In the current scenario, due to the potential of providing an efficient thermal energy conversion with respect to the thermoelectric and thermo–photovoltaic conversion methods, thermionic energy conversion is of particular interest. Research has shown that the conventional design of thermionic converters is capable of exhibiting a thermal energy conversion efficiency of around 20%, significantly higher than those of solid state thermal energy conversion methods and broadly comparable to those of most dynamic energy conversion techniques.

Unfortunately, the output power density of a conventional thermionic converter is found to be very small (typically a few Watts) and further improvements in the key output characteristics require high temperature operation (emitter temperature $>$ 1200 K), limiting the widespread use of this technique. Additionally, the materials used in the fabrication of electrodes are not only toxic but also prone to radiation damage, and are therefore not suitable for operation in hostile environments, such as those found in deep space probes. A few research reports indicate that the output power density and heat conversion efficiency of a thermionic converter can be enhanced by minimising the work function of electrodes and the interelectrode gap. Such new configurations that possess a nano–scale vacuum gap are known as thermo-tunnel devices due to the thermo–tunnelling of electrons in the vacuum gap.

Although thermo–tunnel devices offer several inherent advantages over most solid state energy conversion techniques, fabrication of such devices has not been possible due to the lack of a promising electrode material, process technology and the fundamental understanding of the device operation. In fact, optimisation of physical parameters, such as the interelectrode separation, work function and temperature, for a nano–scale vacuum spaced thermo–tunnel device is extremely important in order to test the feasibility of this tech-

nique for thermal energy conversion. In this thesis, an attempt has been made to develop a roadmap to show how this technique can be scaled for efficient thermal energy conversion.

Quantum mechanical calculations performed for the function and physical parameter optimisation of the thermo–tunnel device show that the choice of physical parameters dramatically influences the output characteristics and such configurations can be of particular interest for both power generation and refrigeration applications. In power generation mode, the thermo–tunnel device structure with an ultra thin vacuum gap (2–3 nm) is capable of delivering a very high output power density of around 1000 $W.cm^{-2}$, while retaining the advantage of having a feasible thermal energy conversion efficiency of around 12%. These values are obtained for low electrode temperatures, typically in the 300–700 K range. Calculations further suggest that the work function of the electrodes should be as low as possible, ideally smaller than 1.5 eV.

Diamond is undoubtedly the most preferential candidate for this purpose because of the superb chemical inertness, thermal, electrical and radiation resilience properties, particularly relative ease of manipulating the work function via specific surface treatments. Results of density functional theory (DFT) simulations have been presented for different diamond/adsorbate interfaces in order to find a thermally stable and effective surface treatment that is capable of reducing the work function of diamond to a suitable value.

It is observed that the thermodynamic stability of halogen terminated diamond surfaces is relatively higher than those of previously studied surface treatments, including H, alkali halides and alkali oxides. However, halogen surface treatments generally increase the work function by inducing a positive electron affinity. In contrast to halogens, transition metals and particularly their oxides reduce the work function by inducing a negative electron affinity. The oxides of transition metals, particularly Ti and Zn, onto a diamond surface exhibit a negative electron affinity of around 3 eV. This value is much higher than the widely used H–termination ($\sim$ 2 eV) and can reduce the work function of a clean diamond surface from around 4.5 to 1.5 eV. Energetics suggest that the thermal stability of such metal oxide treatments is better than previously investigated H and Cs–O treatments and is therefore promising for the wide operating temperature range of thermo–tunnel devices.

Contents

List of Figures

List of Tables

Publications and Conferences

0.1 List of Publications

1. **A. K. Tiwari**, J. P. Goss, P. R. Briddon, N. G. Wright, A. B. Horsfall, R. Jones and M. J. Rayson, Ultra–thin transition metal oxides films for diamond–based thermionics, submitted to Phys. Rev. Lett., (2013).

2. **A. K. Tiwari**, J. P. Goss, P. R. Briddon, N. G. Wright, A. B. Horsfall, and M. J. Rayson, Ultra thin transition metal oxide coatings on diamond for thermionic applications, MRS Proceedings **1511** (2013).

3. **A. K. Tiwari**, J. P. Goss, P. R. Briddon, N. G. Wright and A. B. Horsfall, Nano–scale vacuum spaced thermo–tunnel devices for energy harvesting applications, MRS Proceedings **1490** (2013).

4. **A. K. Tiwari**, J. P. Goss, P. R. Briddon, N. G. Wright, A. B. Horsfall, and M. J. Rayson, Transition metal oxide–diamond interfaces for electron emission applications, Materials Science Forum **740–742**, 761 (2013).

5. **A. K. Tiwari**, J. P. Goss, P. R. Briddon, N. G. Wright, A. B. Horsfall and M. J. Rayson, Electronic and structural properties of diamond (001) surfaces terminated by selected transition metals, Phys. Rev. B **86**, 155301 (2012).

6. **A. K. Tiwari**, J. P. Goss, P. R. Briddon, N. G. Wright and A. B. Horsfall, Density functional simulations of transition metal terminated (001)–diamond surfaces, Materials Science Forum **717–720**, 1311–1314 (2012).

7. **A. K. Tiwari**, J. P. Goss, P. R. Briddon, N. G. Wright, A. B. Horsfall, and M. J. Rayson, Effect of different surface coverages of transition metals on the electronic and structural properties of diamond, Phys. Status Solidi (a) **209**, 1697–1702 (2012).

8. **A. K. Tiwari**, J. P. Goss, P. R. Briddon, N. G. Wright, A. B. Horsfall, and M. J. Rayson, Bromine functionalization of diamond: An Ab initio study, Phys. Status Solidi (a) **209**, 1703–1708 (2012).

9. H. Pinto, R. Jones, D. W. Palmer, J. P. Goss, **A. K. Tiwari**, P. R. Briddon, N. G. Wright, A. B. Horsfall, M. J. Rayson and S. Öberg, , Phys. Rev. B **86**, 045313 (2012).

10. **A. K. Tiwari**, J. P. Goss, P. R. Briddon, N. G. Wright, A. B. Horsfall, and M. J. Rayson, Thermodynamic stability and electronic properties of F– and Cl–terminated diamond, Phys. Status Solidi (a) **209**, 1709–1714 (2012).

11. **A. K. Tiwari**, J. P. Goss, P. R. Briddon, N. G. Wright, A. B. Horsfall, R. Jones, H. Pinto and M. J. Rayson, Calculated electron affinity and stability of halogen–terminated diamond, Phys. Rev. B **84**, 245305 (2011).

0.2 List of Conferences

1. 62nd De Beers Diamond Conference, 4 – 7 July 2011, University of Warwick, Warwick, UK.

2. NanoTP: Cost Action MP0901: WG4Metting 2011, 13 – 16 July 2011, University of Strathclyde, Glasgow, UK.

3. ICSCRM-2011: International Conference on Silicon Carbide and Related Materials, 11 – 16 September 2011, Cleveland, Ohio, USA.

4. SBDD XVII: Hasselt Diamond Workshop 2012, 14 – 18 March 2012, Hasselt University, Hasselt, Belgium UK.

5. 63rd De Beers Diamond Conference, 9 – 12 July 2012, University of Warwick, Warwick, UK.

6. ECSCRM-2012: European Conference on Silicon Carbide and Related Materials, 2 – 6 September 2012, Saint Petersburg, Russia.

7. MRS Fall 2012, 25 – 30 November 2012, Hynes Convention Center – Boston, Massachusetts, USA.

The following abbreviations and notations have been used within this thesis.

0.3 Abbreviations

Abbreviation	Definition
AIMPRO	*Ab Initio* Modelling PROgram
DFT	Density Functional Theory
LDA	Local Density Approximation
GGA	Generalised Gradient Approximation
HGH	Hartwigsen-Göedecker-Hutter
MP	Monkhorst-Pack
IP	Ionisation Potential
EA	Electron Affinity
HOMO	Highest occupied molecular orbital
LUMO	Lowest unoccupied molecular orbital
XPS	X-ray Photoemission Spectroscopy
UPS	Ultraviolet photo–electron spectroscopy
TF	Thin Film
TEG	Thermoelectric generator
PV	Photovoltaic
TPV	Thermophotovoltaic
EA	Electron affinity
NEA	Negative electron affinity
PEA	Positive electron affinity
KE	Kinetic energy

0.4 Notations

Notation	Definition
E_{g}	Energy Gap
ψ	Wave function
$\hbar$	Reduced Planck constant
k_{B}	Boltzmann constant
σ	Stefan–Boltzmann constant
e	Electron charge
V_{ext}	External Potential
E_{xc}	Exchange Correlation Energy
U_{H}	Hartree Energy
V_{eff}	Effective Potential
χ	Electron affinity
E_{ads}	Adsorption energy per adsorbate
ϕ	Work function
ϕ_{e}	Emitter work function
ϕ_{c}	Collector work function
E_{c}	Conduction band minima
E_{v}	Valence band minima
E_{vac}	Vacuum level
T	Temperature
T_{e}	Emitter temperature
T_{c}	Collector temperature
d	Interelectrode separation
J	Current density
P	Output power density
η	Efficiency
E_{F}	Fermi level
μ	Chemical potential
A	Richardson–Dushman constant

Chapter 1

Introduction

> Almost every way we make electricity today, except for the emerging renewable and nuclear, puts out CO_2. And so, what we're going to have to do at a global scale, is create a new system. And so, we need energy miracles.
>
> William Henry Gates III (October 28, 1955 – present)

1.1 Background

The coming scarcity of fossil fuel reserves and rapidly accelerating energy consumption have provoked severe global social and political unrest. According to the international energy agency 2012 report [26], an approximately 50% escalation in global energy consumption is expected by 2035, suggesting that in the near future, proven reserves, which are sufficient only for a few more decades at current consumption rates, will deplete more rapidly than ever. The role of energy is critical in bolstering the sustainable development and economic growth of any nation, as the way of life that an average human takes for granted every day depends directly and indirectly upon a stable and abundant supply of energy. A small disruption in energy needs can quickly cripple our daily life by influencing the scientific, communication, computing and transportation networks. The necessity of obtaining clean and renewable energy alternatives has become more evident in recent years due to the catastrophic impact of fossil fuels upon the environment.

Several types of clean energy resources (*e.g.* solar, nuclear, wind, hydro, tidal, ambient vibrations) exist around us and extraction of useful energy (electricity) from such ambient

energy sources could provide a potential solution for the global energy crisis via reducing the dependence on fossil fuels [3, 4]. Nevertheless, efficient exploitation of energy resources requires different types of sophisticated energy conversion techniques, systems and devices, whose performance generally rely upon the structure and properties of the constituent materials. Due to the small efficiencies of energy conversion systems, efficient exploitation of energy resources was considered to be a big problem until recently. However, the advent of nanotechnology in material science and engineering, which has already revolutionised various research areas, has paved the way for efficient energy conversion and storage to meet this challenge.

To exploit the ambient energy in order to reduce dependence on fossil fuels and decrease environmental impact, the development of new efficient energy conversion techniques and storage systems has become more important than ever. In fact, the requirement for autonomous quasi–perpetual and compact sources of electrical energy has dramatically evolved from a number of niche applications, including space missions, advances in medical physics, deployment of marine and terrestrial surveillance systems, the exploitation of the earth's resources and scientific data collection in increasingly hostile and inaccessible locations [3, 4, 27–30]. As an example, mechanically excited piezoelectric elements and thermoelectric devices employing radioactive isotopes as a heat source have been used extensively for powering electronic circuitry of wireless sensor networks on the earth and deep space probes, respectively.

This PhD work is centred on developing a road map for a new kind of energy harvesting technology called *thermo–tunnel device* that is efficiently capable of converting thermal energy into electricity in hostile environments. In the forthcoming sections of this chapter, a brief overview of existing direct energy conversion technologies, working principles and recent advances that have been made in this area, particularly in the case of thermo–tunnel energy conversion, are summarised.

1.2 Energy conversion technologies

Solid state energy conversion is one of the most important topics in the area of energy research. Although there is a multitude of options available, the most commonly used

compact electrical power generators transduce solar, vibrational or thermal energy into electricity.

1.2.1 Vibrational energy conversion

The vibrational energy harvesters use one of three methods: electromagnetic (inductive), electrostatic (capacitive) or piezoelectric to produce electric energy from mechanical vibrations.

Electromagnetic (EM) vibration–to–electric energy conversion

In an EM energy converter system, which works on Faraday's law of induction, mechanical vibrations provide necessary kinetic energy to bring a coil (conductor) into motion with respect to a fixed permanent magnet (magnetic field). The relative motion between a conductor and magnetic field results in an induced electro motive force (emf) in the conductor and thus the vibrational energy is converted into electrical energy. Since conducting coils are generally fragile in comparison to a magnet and use of a static coil can increase the lifespan of the energy harvester so in most of recent designs the coil is kept fixed while the magnet is connected to a vibrating element [3, 4, 31–33].

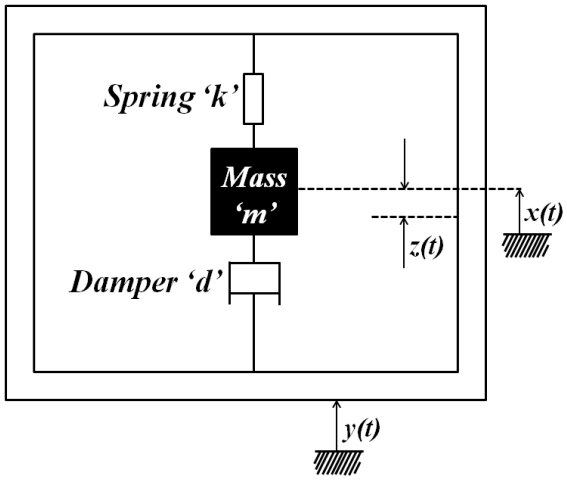

Figure 1.1: Schematic diagram of a linear inertial EM generator (from ref. [1, 2]).

A typical EM energy converter configuration, as shown in Fig. 1.1, consists of a mass mounted on a spring. The mass mounted on a spring moves out of phase with respect to generator housing when subjected to an external source of vibrations. The moving mass is connected to a magnet or a coil in such a way that when the system vibrates, the coil cuts the lines of magnetic field generated by the magnetic core. The combination of moving magnet and the coil is called electromechanical–transducer/damper and represented by '*d*' in Fig. 1.1. The EM energy converter systems are divided in two categories [4]. In the first

type, the permanent magnet moves with respect to the coil in a lateral manner, whereas in the second type, the magnet moves in and out of the coil. Due to better electromagnetic coupling, the the first type is more popular over the second type.

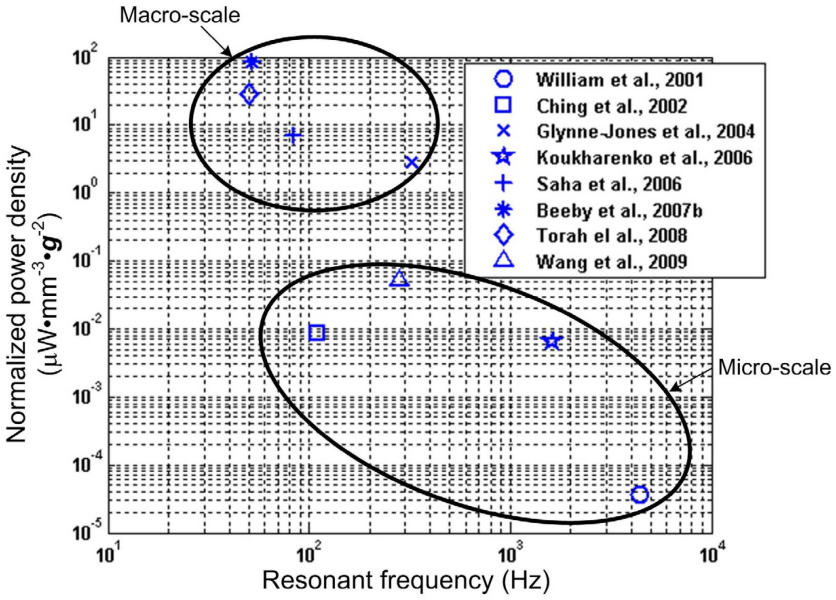

Figure 1.2: Comparisons of normalised power density of some existing EM vibrational energy harvesters. On Y-scale, the unit of '**g**' is equivalent to that of acceleration (from ref. [3, 4]).

Although EM energy converters generate a high output current density (mA.cm^{-3}) in the absence of any input voltage, the output voltage is observed to be small (typically in the millivolt range). The performance of the vibrational energy conversion systems is generally evaluated on the basis of a more precise term called normalised power density (NPD=$P/A^2.V$), a function of stated power output (P), volume of the harvester(V) and acceleration (A). In the case of EM energy converters, the NPD is varied over a wide range and up to $\approx$1000 μW.sec^4.cm^{-2}.m^{-3} has recently been reported [3,4,31–34]. The NPD of an EM vibrational energy harvester varies dramatically with its dimensions and according to recent studies, the NPDs of macroscale EM vibrational energy conversion units are found to be much higher than those of microscale energy conversion units (Fig. 1.2) [1,2,31,32,35–39].

Electrostatic (ES) vibration–to–electric energy conversion

The basic operation of an ES energy converter is rather simple. An ES energy converter exploits vibrations to change the separation between the plates of an embedded variable capacitor. In other words, if the charge on the variable capacitor is fixed, a decrement in the capacitance forces surplus charge to move from the variable capacitor to a storage device or to a load.

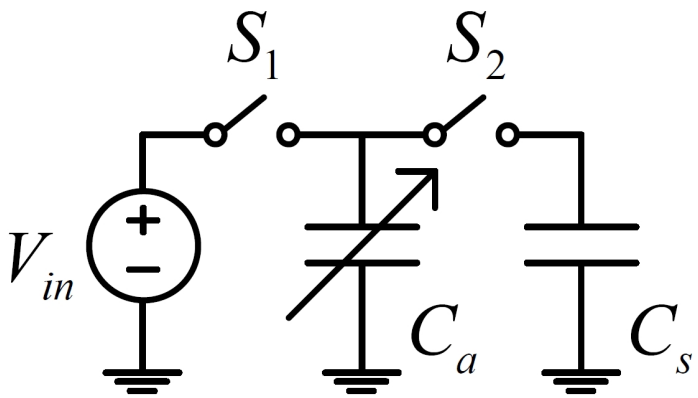

Figure 1.3: An equivalent circuit diagram for an ES energy harvester unit (from ref. [5]).

.

To illustrate the mechanism of energy conversion, an equivalent circuit diagram for a simple ES energy converter unit is shown in Fig. 1.3, comprising two capacitors $C_{\rm a}$ and $C_{\rm s}$ and a startup voltage source $V_{\rm in}$. Here, the variable capacitor $C_{\rm a}$ consists of two sets of plates. The first set of plates is fixed on the housing, while the other set of plates is associated with an inertial mass, vibrating with the source vibrations. Since the capacitance of a capacitor lies between the maximum and minimum values and if the variable capacitor, $C_{\rm a}$, is somehow already charged from a startup voltage source $V_{\rm in}$ through the switch/diode S_1, a reduction in its capacitance caused by the change in inter–plate separation will move charge into the storage device ($C_{\rm s}$) or to a load through the switch/diode S_2. Thus an ES energy harvesting unit converts mechanical energy into electrical energy.

Depending upon the movement of the second set of plates that are connected to an inertial mass, the ES energy converters are divided in three categories:

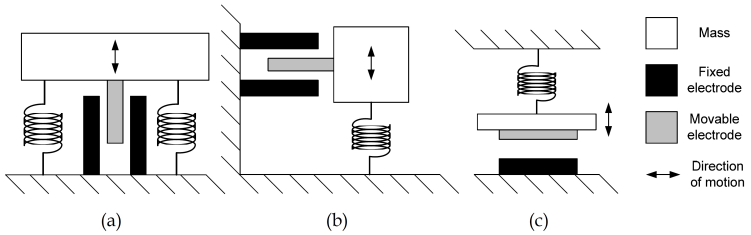

Figure 1.4: Schematics of three types of ES energy harvesters (a) In–Plane Overlap (b) In–Plane Gap Closing (c) Out–of–Plane Gap Closing (from ref. [4]).

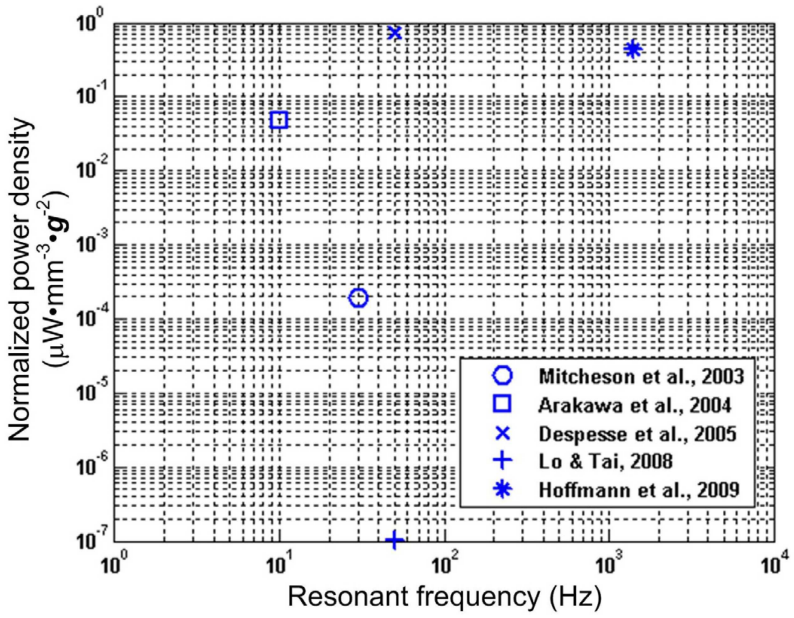

Figure 1.5: Comparisons of normalised power density of some existing ES vibration energy harvesting units (from ref. [3, 4]).

1. In–Plane Overlap where the change in the overlap area between fixed plates depends upon the movement of mobile plate [Fig. 1.4 (a)].

2. In–Plane Gap Closing where the change in the gap between fixed plates depends upon the movement of mobile plate [Fig. 1.4 (b)].

3. Out–of–Plane Gap where the change in the gap between the fixed and mobile plate is associated with the movement of the mobile plate [Fig. 1.4 (c)].

The output voltages of the ES energy converters are normally high, in some cases a few hundred volts (up to 200 V) [40]. However, due to high input impedance, such configurations yield very low output current densities ($\approx 10^{-9}$–10^{-6}A.cm^{-3}). Typical NPDs of the ES energy conversion units lie in the range 10^{-4}–10^{2} μW.sec^{4}.cm^{-2}.m^{-3}, which are generally lower than those of EM and piezoelectric energy converters (Fig. 1.5) [39–44]. The biggest advantage of the ES energy converters over the EM converters is that the dimensions of these configurations are rather small and can easily be incorporated with the chip–level systems.

Piezoelectric (PE) vibration–to–electric energy conversion

The PE energy conversion units utilise the PE effect to convert mechanical vibrations into electricity. The PE effect is closely related to the occurrence of electric dipole moments (and surface charge densities) in those materials, which are normally electrically neutral but do not possess inversion symmetry. These crystals generate a small voltage whenever they are subjected to mechanical stress. The crystals, which are centrosymetric, show no PE effect. The PE effect is a reversible process in this sense that a change in the dimensions can also be induced by the application of a voltage to a PE material.

(a) (b)

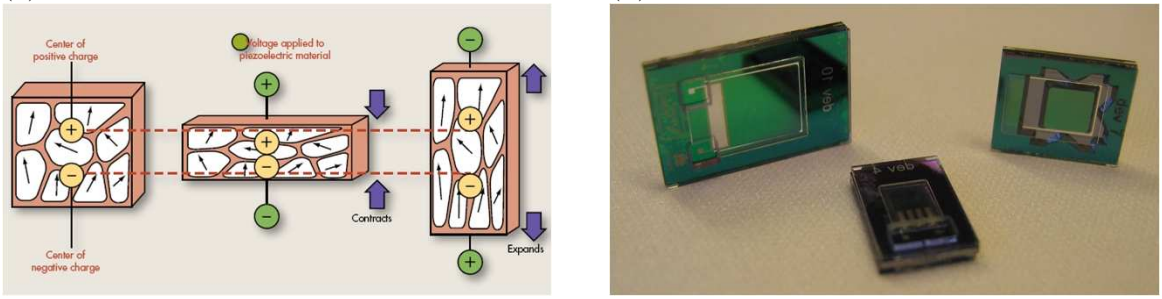

Figure 1.6: (a) Imbalance of charges in a PE crystal caused by applied stress and (b) Photograph of commercial PE energy converter devices with different size and mass (source: Interuniversity Microelectronics Centre)

Fig. 1.6 (a) illustrates the PE effect in the crystal. In the case of zero strain, electrical charges insides the PE crystal are perfectly balanced, which means a positive charge in one place cancels out a negative charge nearby. Implementation of an external force deforms the

crystal structure, pushing some of the atoms closer together or further apart. Deformation of the crystal structure destabilises the balance of positive and negative charge that results in a voltage at the electrodes.

Many materials possess piezoelectricity, which can be divided in two classes: natural and synthetic [4, 6, 45]. Table sugar, bone, quartz, rochelle salt, berlinite, silk, enamel, dentin, DNA and tourmaline–group minerals are some well known example of naturally occurring PE materials. In the synthetic class, in addition to $GaPO_4$ and La_3Ga_5SiO, the materials having perovskite structure often exhibit strong PE properties. $BaTiO_3$, Na_2WO_3, $LiTaO_3$, $PbTiO_3$, $LiNbO_3$ and $LiTaO_3$ are some of the most common examples of perovskite structure. ZnO is also known for exhibiting PE properties. It is notable that some specific polymers, for example, cellular polypropylene and polyvinylidene fluoride, and organic nanostructures are also recognised for their strong PE behaviour.

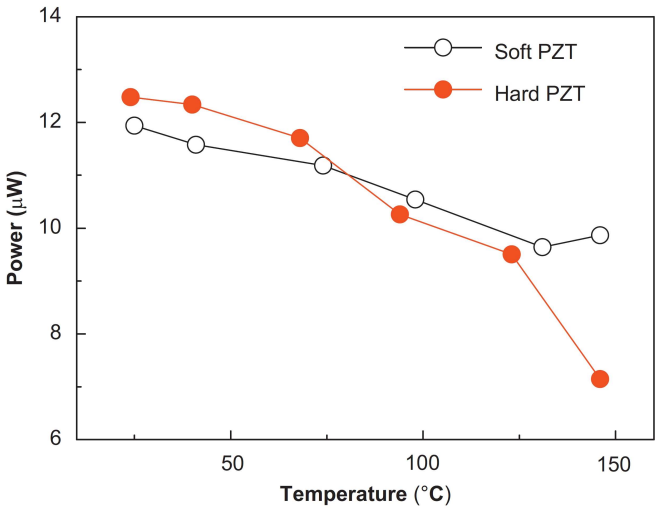

Figure 1.7: Measured output power from the PE energy harvesters based on soft (donor doping) and hard (acceptor doping) PZTs (Lead zirconate titanate), as a function of temperature (from ref. [6]).

Both theoretically and experimentally, the PE vibrational energy converters exhibit the highest NPDs among other vibrational energy conversion techniques (PE and ES) [3]. The typical NPDs for a PE vibrational energy converter ranges from 10^{-1} to 10^4 μW.sec^4.cm^{-2}.m^{-3} (Fig. 1.8) [39, 46–55]. In contrast to the EM energy harvesters, the NPDs of microscale PE energy harvesters are found to be higher than those of macroscale PE energy harvesters (Fig. 1.8). In line with the ES energy harvesting units, the PE energy converter systems generally yield high output voltages (a few volts). However, the output current density of

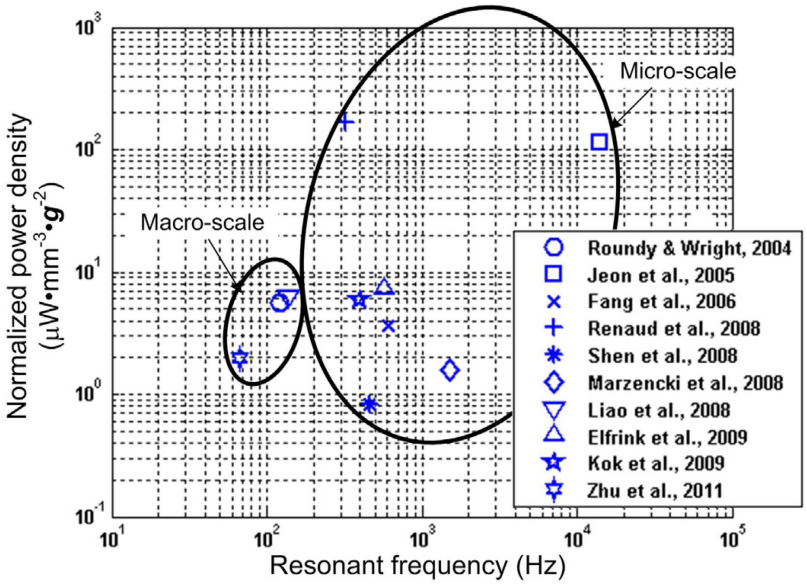

Figure 1.8: Comparisons of normalised power density of some existing PE vibrational energy harvesters (from ref. [3, 4]).

such systems is measured to be small (a few μA.cm^{-3}). Although the output power density shown in Fig. 1.8 may seem small for high power electronics applications, modules that consist thousands of interconnected PE elements have been widely used to power electronic circuitry of wireless sensor networks [4, 56].

For an efficient vibrational energy to electrical energy conversion, it is critical that the resonance frequency of the PE energy harvester matches with the frequency of the source vibration. This is in–fact an important area of research, as a change in ambient conditions, such as temperature (Fig. 1.7), can affect the resonance frequency and hence the output power of an energy harvester by modifying the material properties [6].

1.2.2 Solar photovoltaics

Solar photovoltaic systems convert sunlight into electricity using a p–n junction based device called a solar cell. Unlike a conventional p–n junction diodes, solar cells are based on the photovoltaic effect, in which two n– and p–type semiconductor materials in close contact produce an electrical voltage when struck by light. Incident light on a solar cell generates free electron–hole pairs on both sides of the junction and an inbuilt electric field at the

junction separates the charge carriers with opposite charge and thus generates an electric current by extraction of these charge carrier across the p–n junction.

Solar cells have been widely used for both micro and macro scale power generation [27–29]. Under normal operating cell temperature (NOCT) conditions [27–29], a single crystal Si solar cell generates around $20\,\mathrm{mW.cm^{-2}}$, with 0.6 V output voltage, which can be extended easily upto several hundreds MW by creating solar cell arrays, making it promising for low power as well as high power applications. The typical output power density and the efficiency of a solar cell depend upon multiple factors, such as material quality, light intensity and environmental temperature and humidity. For example, a single crystal Si solar cell is more efficient and generates more power density than an amorphous Si solar cell. In addition, the open circuit voltage (V_{oc}) reduces with increasing ambient temperature.

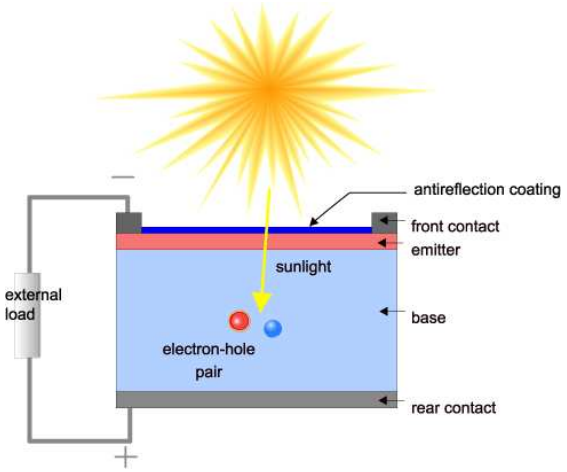

Figure 1.9: Schematic of a solar cell.

Although a wide range of configurations, including the thin film, dye–sensitized, organic and multijunction solar cell, has already been explored [28, 57, 58], fresh efforts are still being made to reduce the cost, and to increase the output power density and efficiency of photovoltaic systems [27–29]. Research has also focused on the use of direct bandgap materials, such as GaAs and InGaP, in solar cell fabrication. Due to high material cost direct bandgap solar cells are not cost effective, however, these exhibit better efficiency (≈35%) in comparison to those of indirect bandgap material–based solar cells (≈28%). A compilation of the best research solar cell efficiencies is shown in Fig. 1.10. Although solar cells offer several promising features, due to lack of sunlight, these options are not of significant interest for many applications such as in deep space and under–water environments.

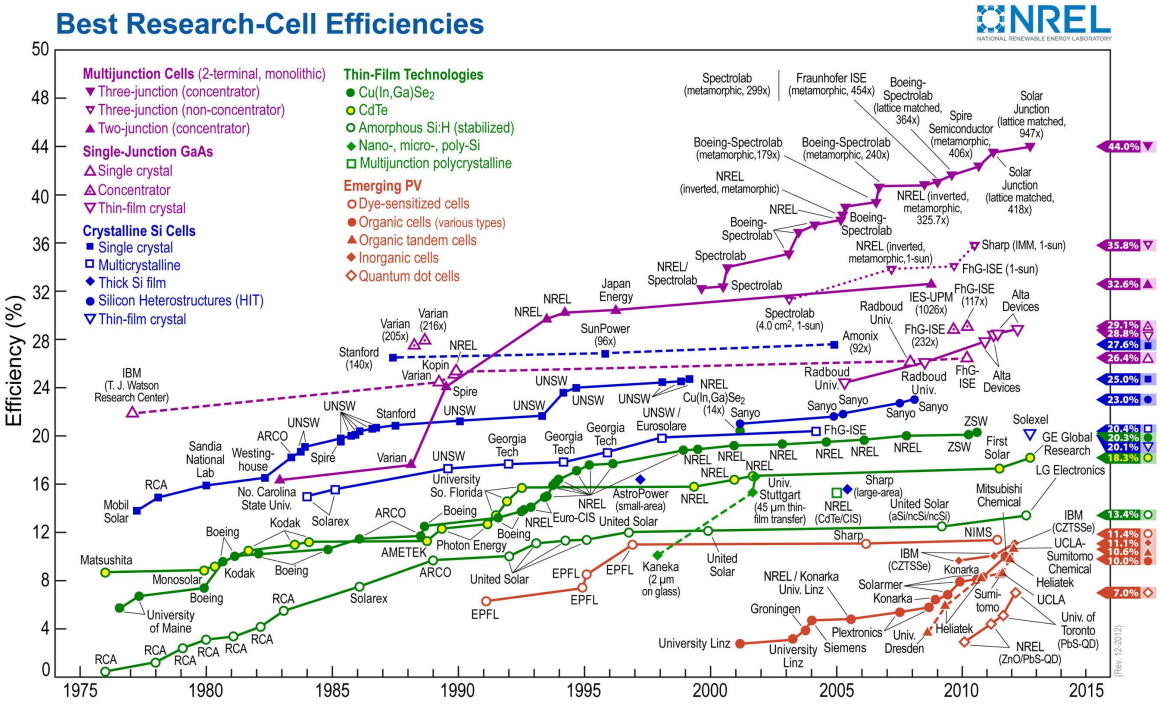

Figure 1.10: A compilation of the best research solar cell efficiencies from 1976 to 2012 (source: National Renewable Energy Laboratory).

1.2.3 Thermal energy conversion

Due to an abundance of waste heat in our atmosphere, thermal energy conversion is a key area of energy research and considered as a potential source of green energy. Moreover, there are some niche applications, such as deep space exploration and under water surveillance systems, where there is no sunlight and vibrations, thermal energy conversion is proven to be the only realistic option. There are multiple techniques to convert thermal energy into electricity. These techniques are generally divided in two main categories: dynamic and static. This thesis is mainly focused on the suitability of static energy conversion methods and therefore rotating (i.e. Brayton and Rankine cycles) and reciprocating (i.e. Stirling engine) machines, which fall under dynamic energy conversion techniques, are not considered in this section.

In static thermal energy conversion, thermoelectric, thermophotovoltaic and thermionic

are three prominent thermal energy conversion techniques. These techniques offer several inherent advantages over dynamic thermal energy conversion. The absence of moving components results in an increase of reliability and system life, and a reduction of maintenance, vibrations and noise. Importantly, the devices based on these techniques require a very small amount of space.

Thermoelectric energy conversion

Thermoelectric energy conversion systems have been used successfully in a wide range of applications, including waste heat recovery applications and deep space missions, such as SNAP, Transit–RTG and GPHS–RTG [4, 30]. In addition, attempts are underway to replace the alternator in vehicles with the thermoelectric modules mounted on the hot components, such as exhaust pipe, thereby reducing the fuel consumption. The most fascinating feature of the thermoelectric devices is the ability to utilise combustion, nuclear, solar or any kind of heat energy sources.

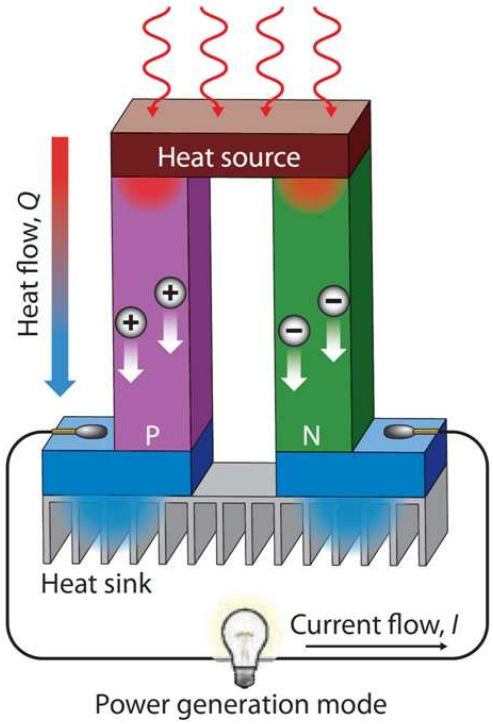

Figure 1.11: Schematic of p– and n–type thermoelectric legs of a thermoelectric generator(from ref. [7]).

A thermoelectric energy generator (TEG), which is based on the Seebeck effect [30], can be treated as a heat engine, where the charge carriers (electrons and holes) serve as the working fluid between the source and sink. Fig. 1.11 shows the schematic of a thermo–electric generator that consists of two semiconductor legs bonded to two heat transfers surfaces, called the hot (source) and cold (sink) junctions. Since the output voltage and the generated power from a single TEG are small, high power devices are made by connecting several TEGs in series to increase the output voltage capability and in parallel to increase the output current capacity. As an example,

an array of TEGs (module) is shown in Fig. 1.12.

The performance of a TEG principally depends upon the thermoelectric properties of a material. The thermoelectric material is characterised by the figure of merit, Z,

$$Z = \frac{\alpha^2}{\rho k}, \tag{1.1}$$

where k the thermal conductivity, ρ the electrical resistivity and α (the ratio of the resulting voltage and the temperature difference, $\Delta V/\Delta T$) is the Seebeck coefficient. Eq. 1.1 indicates that for a large value of the figure of merit, the thermal conductivity should be as low as possible, while having the large values for α and the electrical conductivity ($1/\rho$).

(a) (b)

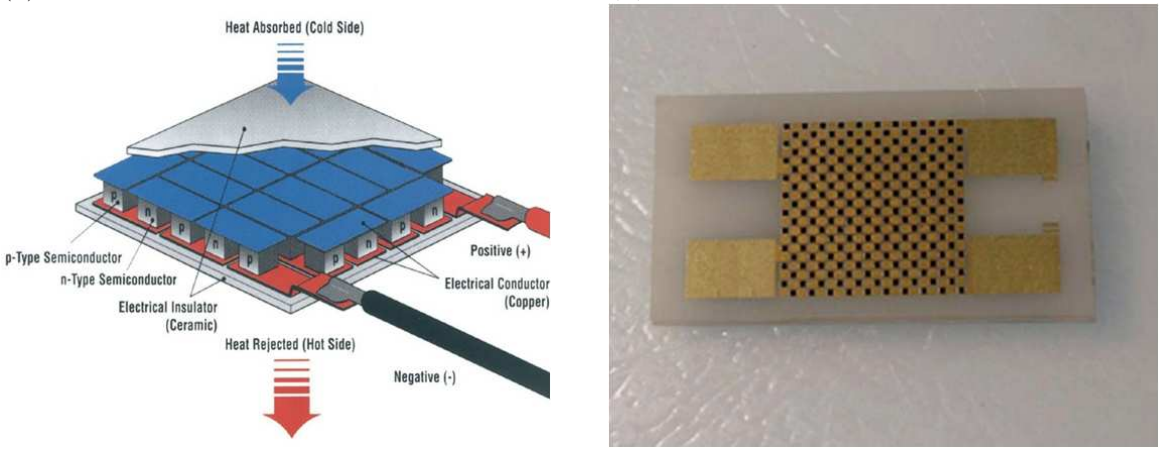

Figure 1.12: (a) Integration of several thermoelectric generators in a module and (b) a 200 element ErAs:InGaAs/InGaAlAs thin film generator module (from ref. [8])

.

Research in this field has traditionally focused on the use of p–type and n–type bismuth telluride (Bi_2Te_3) and lead telluride (PbTe) materials for thermoelectric device fabrication, which generally exhibit a small dimensionless figure of merit ($ZT_{\max} < 1$) [4, 30]. Nevertheless, a wide range of new complex thermoelectric materials, including skutterudites and the Zintl phase compounds, has started to be explored [7, 9, 59–61]. Much of the research in these new thermoelectric materials has focused on increasing α and reducing k by manipulating the nanostructure of the materials. Most of these new materials exhibit extremely low lattice thermal conductivity (less than 0.6 $W.m^{-1}.K^{-1}$ at 1000 K) and tunable electronic properties, which enhance the thermoelectric figure of merit, making them promising ther-

moelectric materials for high temperature TEG operation [7, 9, 59–61]. The dimensionless thermoelectric figure of merit, ZT, for some of these materials is shown in Fig. 1.13.

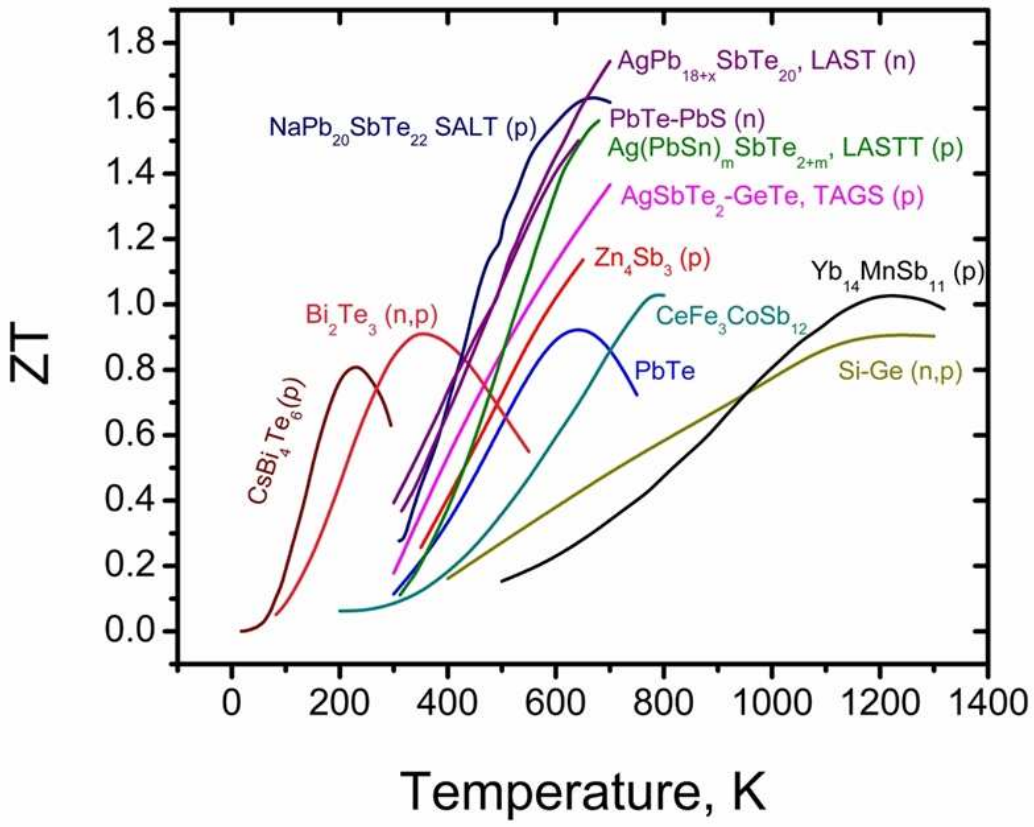

Figure 1.13: The dimension less figure of merit (ZT) of recent high–performance bulk thermoelectric materials as a function of applied temperature (from ref. [9]).

A large ZT is an indication of a large thermodynamic efficiency. To compete with existing mechanical devices in terms of thermodynamics efficiency, the value for ZT should lie in the range between 3.5 and 4.5. However, the maximum reported value for ZT is smaller than 3.5 at 600 K [59–61]. Although low conversion efficiency (between 5–10%) limits the widespread use of TEGs for power stations, the possibility of miniaturisation and a low cost make them attractive for some low power energy harvesting applications.

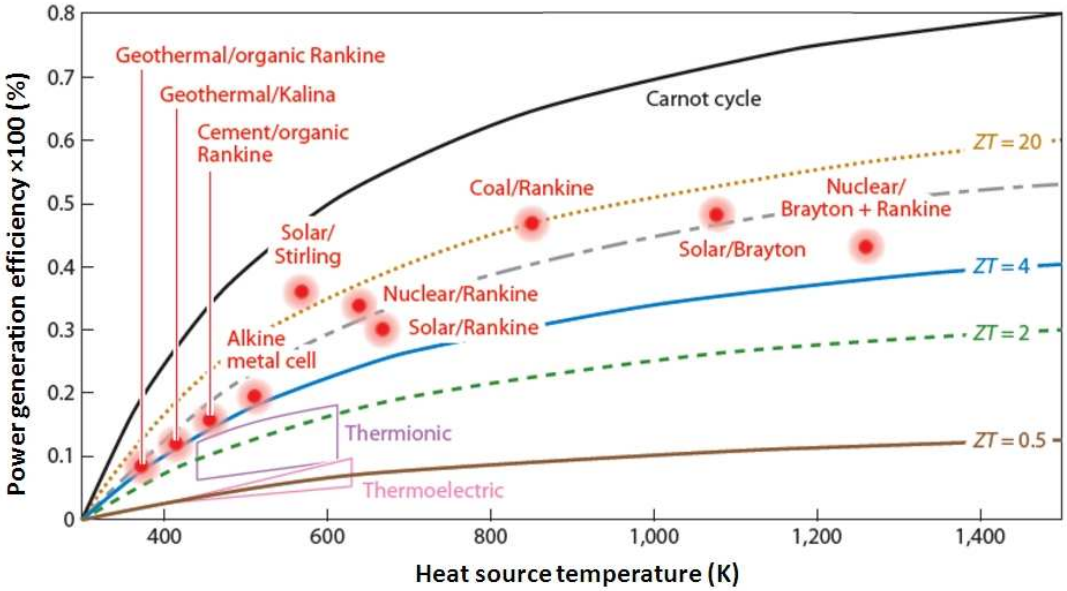

Figure 1.14: Efficiency of some best practice mechanical heat engines compared with an optimistic thermoelectric estimate and a existing thermionic converter (from ref. [10]).

Thermophotovoltaic energy conversion

In thermophotovoltaic (TPV) energy conversion, a solar cell converts generally infrared radiation (0.8–100 μm region of the electromagnetic spectrum) emitted from a hot surface into electricity. The working principle of a TPV solar cell is identical to that of any other PV solar cell, where infrared photon irradiation causes electro–hole pairs to be created in a material and hence produce electricity. TPV energy conversion systems are similar to TEGs in this sense that these can also exploit combustion, nuclear or solar heat sources.

The efficiency of a TPV system is highly sensitive to the spectral range and the operating temperature. The incident photons with energy less than the band gap contribute to waste heat and high temperature operation generally results in the reduced efficiency. Strategies for spectral control are an active focus of research worldwide [62–64]. One solution for spectral control is to use selective emitters, i.e. emitters that emit strongly in those wavelength regions, which are compatible with the specific TPV cell. Recent research shows that rare earth materials Nd, Sm, Ho, Er, Tm and Yb emit selectively radiation with wave length 2.5,

1.8–5.0, 2.0–2.1, 1.5, 1.8 and 1.0 μm, respectively. The wave lengths of oxide-based emitters, such as Yb_2O_3 (0.95 μm) and Er_2O_3 (1.55 μm) also lie in the infrared region [63, 64]. The thermal stability of such oxide–based emitters is very high, generally stable upto around 2500 K. Other oxide based ceramics, such as MgO, SiO_2, BeO, HfO_2, ThO_2 and Y_2O_3, have also been used; however, these exhibit very low emissivity [63, 64].

Another tool for spectral control is to use infrared filters. These infrared filters allow only infrared radiation to pass through them and reflect remaining radiations back to the emitter. The electric efficiency of TPV systems is generally found to be very small ($\approx$ 2%), depending upon the performance of multiple components, such as the emitter, PV cell and filters. In TPV cell fabrication, to capture the entire range of infrared radiation emitted by a 1000–2000 K black body, some selective materials and alloys, such as Ge, GaSb, InGaAs/GaSb, InGaSb/InP and the quaternary InGaAsSb/GaSb and InGaAsP/InP, have also been used, whose performance is better but not cost effective in comparison to those of Si and Ge [63, 64].

Thermionic energy conversion

In recent years, thermionic energy conversion has attracted much attention for thermal energy conversion, as its thermal energy conversion efficiency can be as high as 20%, which is much greater than TEGs (5 – 7%) and broadly comparable to that of a commonly used Si-based PV solar cell (15–25%)(Fig. 1.10) [30]. Thermionic energy conversion devices are not used frequently for space power systems. However, some configurations that contain both nuclear fuel assembly and thermionic generators, such as the TOPAZ light weight thermionic reactor assembly, have been proposed as alternatives to TEGs for space power applications [30].

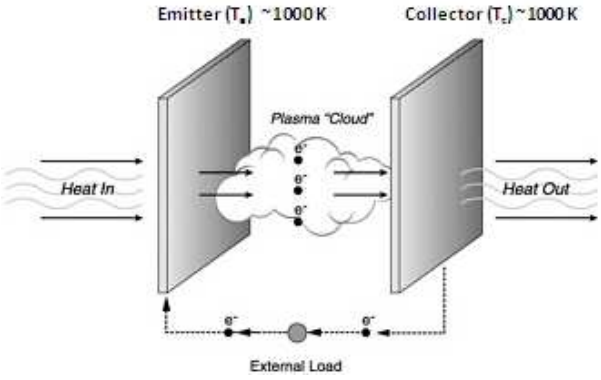

Figure 1.15: Schematic of a thermionic converter [11]. Here, the symbol e^- represents an electron.

A thermionic converter, shown schematically in Fig. 1.15, consists of two electrodes: the emitter, which thermionically emits hot electrons and the collector that collects the emitted electrons. Similar to any other energy conversion technique, thermionic energy converters have their own drawbacks [30]. In addition to thermal losses, thermionic energy converters suffer from a severe space charge problem, which degrades the performance significantly. Space charge accumulated between the electrodes impedes the flow of hot electrons from the emitter to collector and thus reduces the output power.

Based upon the available solutions to this problem, thermionic converters are characterised in two groups: close spaced converters and gas–filled converters. In close spaced converter, the space charge effect is partially eliminated by making the interelectrode gap very small ($\approx \mu$m), while in gas–filled converters, this problem is overcome by filling the interelectrode gap with a rarefied gas, such as a Cs vapour. The positive ions produced by the ionisation of the Cs vapour suppress the space charge in the interelectrode gap. In some designs, an external electric field across the electrodes has been used to eliminate the space charge effects.

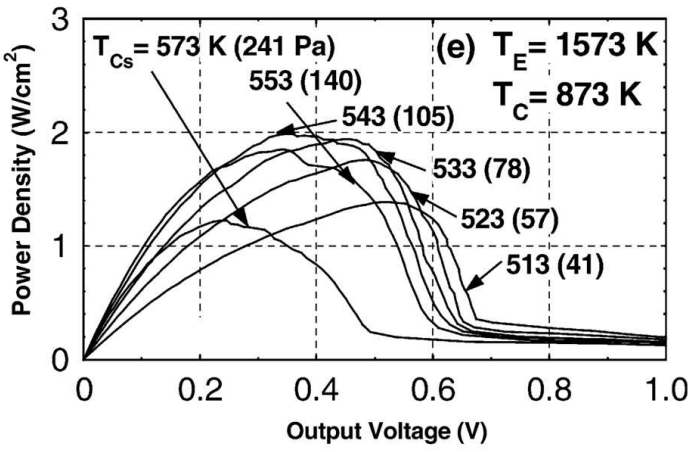

Figure 1.16: Output power density of a Cs vapour filled thermionic converter as a function of output voltage for different collector temperatures when the emitter temperature is fixed at 1573 K (from ref. [12]).

According to previous studies, fabrication of the emitter requires a low work function material [30, 65]. Unfortunately, there are very few materials available that are suitable for electrode fabrication (Table 1.1), and the most commonly used cathode material is the CsO coated tungsten, exhibiting a work function in the 1.3–1.5 eV range [65]. Although thermionic converters yield the highest thermal efficiencies among other static energy conversion techniques

(Fig. 1.14), the typical output power density is still low, lying in the range between 1 and 5 $W.cm^{-2}$ (Fig. 1.16), when the emitter and collector temperatures are at 1500 and 300 K, respectively [12, 30]. Recently, photon enhanced thermionic emission (PETE), which combines both photovoltaic and thermionic effects, has been reported for direct utilisation of solar radiation [66]. However, the reported efficiency is found to be very low at 0.4% [66].

Table 1.1: Work function, ϕ (eV), of some commonly used materials for thermionic emitter applications [16].

Material	ϕ	Material	ϕ	Material	ϕ
LaB_6	2.50	W	4.54	Cs coated W	1.36
CeB_6	2.50	Cs	1.81	Mo_2C	3.70
Mo	4.15	Mo	4.15	Cs_xWO_3	2.12
WC	3.60	Re	4.70	Re + C	4.10
Ir	5.34	Pt	5.52	Thoriated W	2.63

1.2.4 Thermo–tunnel energy conversion:

Thermo–tunnel energy conversion is a more advanced stage of thermionics, where a thermo–tunnel phenomenon brings an abrupt change in the output power density. The thermo–tunnel effect is described in great detail in Chap. 4. In brief, when the interelectrode separation (a few μm) of a conventional vacuum–spaced thermionic converter is reduced down into the nano–regime (a few nanometers), the height and particularly the width of the interelectrode potential barrier decreases rapidly, which allows tunnelling of electrons between the electrodes. Combined thermionic emission and tunnelling of hot electrons results in an enhanced output current density and thus high output power. This is a relatively new class of solid state thermal energy conversion techniques, which is still being explored.

The thermo–tunnel effect, also known as the tunnelling thermoelectric effect, was first observed by Smith *et al.* in 1980 [67]. In both current and voltage measurements, the thermo–tunnelling effect was observed across the ultra thin oxide barriers (10–40 Å) that were sandwiched between metal electrodes. The metal–oxide–metal thermo–tunnel junc-

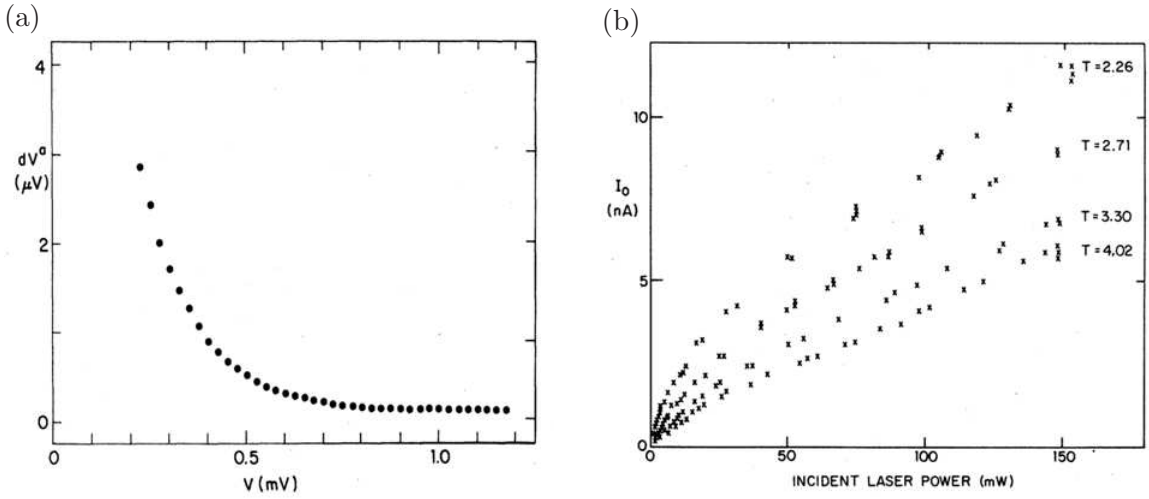

Figure 1.17: (a)Measured dV vs V for an Al–PbBi tunnel junction illuminated on the PbBi side when the temperature was 1.588 K. and (b) I_o, as a function of laser power for four different fixed temperatures (from ref. [8]).

tions were formed using Al, Al_xO_y and $Pb_{0.95}Bi_{0.05}$ (described in their previous work [68]), and one electrode (PbBi side) was heated using laser irradiation. The tunnel junctions were biased at constant current for several voltages and temperatures. The laser induced voltage change dV and current I_o were measured as a function of voltage and laser power, respectively (Fig. 1.17). These results are the first experimental evidence of the thermo–tunnel current between metal electrodes. Since then several efforts, both theoretical [69–77] and experimental [13, 78], have been made to exploit the thermo-tunnel effect for cooling applications. However, for power generation application, this phenomenon has received little attention.

A semi–quantum mechanical thermionic converter model for cooling applications, proposed by Mahan *et al.*, has predicted that for room temperature (300 K) operation, the work functions of the electrodes (emitter: ϕ_e and collector: ϕ_c) should be in the 0.7–0.8 eV range, unattainable in the current context [72]. The maximum efficiency of thermionic refrigerator was calculated to be only 2%, with ϕ_e=ϕ_c=0.7 eV, T_c=500 K and T_e=700K. In later studies by the same authors [73, 74], multilayer thermionic refrigeration (three–layer sandwich consisting of metal–semiconductor–metal) has been proposed to enhance the refrigeration efficiency to around 2.5%. It is important to point out that the interelectrode separation used in these proposed designs lie in the millimeter range and the output characteristics show no dependence on the interelectrode gap. Inclusion of interelectrode gap is indeed very im-

portant for the accurate modelling of the thermo–tunnel devices, as it directly impacts the interelectrode potential barrier by reducing the effective work function of electrodes.

In a later quantum mechanical study, Hishinuma *et al.* showed that the available materials with work functions about 1 eV are mostly suitable for cooling applications. By maintaining a nanometer sized gap between the electrodes and applying only a few volts, the effective work function of the electrodes can be reduced down to 0.4 eV. For gaps of 5–15 nm, which are well within the present state of the art, only a small external voltage of between 1 and 3 V is required to create high current densities ($\approx 10^2$ A.cm^{-2}), useful Peltier coefficient (A criterion for performance evaluation of a cooler/heat pump) of around 0.3, and a cooling power of 100 W.cm^{-2} [75, 76].

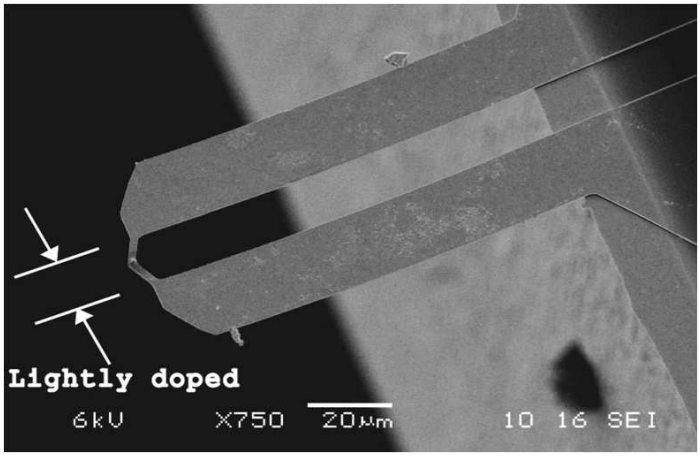

Figure 1.18: SEM photograph of a gold coated cantilever. A tip is located at the lightly doped constriction part (from ref. [13]).

In the experimental investigation conducted by the same author [13], a microfabricated cantilever (work function around 1 eV) with a cesiated metal (gold) coating on the tip (Fig. 1.18) has been realised to measure the thermo–tunnel current successfully across the a nanometer gap (10–20 Å). Using a lock–in technique, temperature changes of 0.1–1.0 mK were observed, corresponding to the cooling power of 1–10 nW. Consistent with their previous theoretical findings [75, 76], the electron emission was enhanced by reducing the vacuum gap, and an emission current of 1–10 nA was measured. The small magnitude of the emission current was due to the small electron emission area of the tip.

In another experimental approach [78], gold electrodes (without Cs coating) were used to establish a tunnel current. Due to the relatively high work function of the pure Au electrodes, the resulting separation was in the 4.5–6.5 Å range, which is much smaller than

the typical 20 Å (or more) used with low work function electrodes, such as Cs coated Au. These experimental results clearly indicate that to realise a large tunnel current between the electrodes, the work function of electrodes and interelectrode separation should be as low as possible. These findings are later supported by recent theoretical and experimental studies [79–83], which utilise different theoretical modelling approaches.

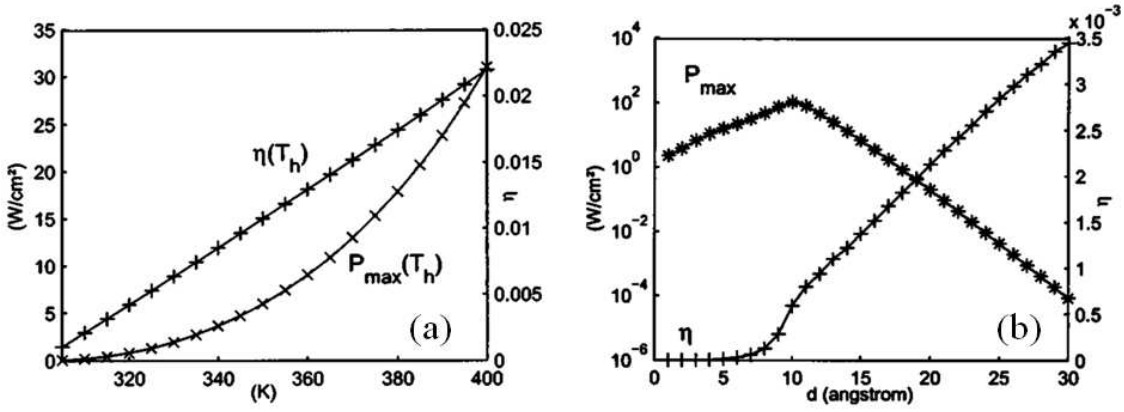

Figure 1.19: Variations of maximum output power density (P_{max}) and conversion efficiency η_{max} depending on: (a) T_h for equal electrode work functions (ϕ_h=ϕ_c=1 eV), T_c=300 K and interelectrode gap width d=20 Å, and (b) the barrier width with ϕ_h=ϕ_c=1 eV, T_h=310 K, and T_c=300 K (from ref. [14]). The symbols ϕ and T correspond to the work function and temperature, respectively, while the subscripts $_h$ and $_c$ represent the emitter and collector.

Quantum–mechanical calculations, performed by Despesse and Jager [14], demonstrate that the thermo–tunnel effect can be exploited for thermal energy harvesting applications. Although this is not an extensive study, it provides an important insight into the factors that affect the output power density and energy–conversion efficiency when a thermo–tunnel device is working in a power generation mode. Results show that the output characteristics of a power generating thermo–tunnel device depend critically upon multiple variables, including the electrode work function, temperature and interelectrode separation, as shown in Fig. 1.19. On increasing the interelectrode separation of a thermo–tunnel device, the maximum output power density reduces, while the maximum efficiency increases. Furthermore, raising the emitter temperature increases both the maximum output power density and heat–

conversion efficiency. Although the work function dependency of the output characteristics has not been investigated, in all calculations, the values for electrode work functions are kept very low (ϕ_h=ϕ_c=1 eV). In addition, high collector temperatures and thermal losses, via conduction and radiation, are not included.

1.3 Importance of electrode material: diamond as a promising electron emitter

The selection of a suitable electrode material is critical in terms of performance improvements of both thermionic and thermo-tunnel devices. A wide range of low work function electrode materials, including metals as well as their carbide and oxides, has been tested in the past for electron emission applications. The work function values for the most of investigated materials, excluding Cs coated W, lie in 2–6 eV range (Table 1.1), which generally require very high operating temperatures ($>$ 1000 K) and are therefore not suitable for the thermo–tunnel device applications. For example, extraction of a thermionic current density (J) of 1 A.cm^{-2} with pure tungsten, which has a work function of approximately 4.6 eV, requires an operating temperature of 2600 K. In contrast, a Cs coated W electrode that has a work function of around 1.36 eV gives a similar current density at much lower temperature ($\approx$1000 K). The values of J for other cathode materials can be calculated using Richardson–Dushman equation

$$J = AT^2 exp\left(\frac{-\phi}{k_{\mathrm{B}}T}\right), \tag{1.2}$$

where A the Richardson–Dushman constant, ϕ the work function, k_{B} the Boltzmann constant and T is the temperature.

For many reasons, diamond is considered as an ideal candidate for fabrication of electrodes in thermionic devices. The advantages of diamond as a promising electrode materials are given below

– An efficient source of electrons [65, 84, 85].

– High thermal conductivity (2200–3000 W.m^{-1}.K^{-1}): ideal for quick heat dissipation in the cold cathode [86, 87].

– Relative ease in the modification of work function (can vary between 1 and 7 eV) [21, 22,

88–95].

– Radiation resilience, promising for both mundane and radiation rich environments [86,87].

– Thermally stable, enabling moderately high temperature (upto 1200 K) operation [65, 86, 87].

–Possibility of growing nearly atomically-flat surface [86, 87].

The work function of the diamond has been modified using both doping and chemical modification of its surface. Although a detailed study on the modification of the work function of diamond is included in Chap. 6 and 7 of this thesis, some of the work function values that have already been achieved experimentally using different surface termination and doping techniques are listed in Table 1.2.

Table 1.2 shows that the work function of diamond is largely independent of choice of substrate material. However, it strongly depends upon the surface preparation and chemical nature of dopants. For example, the average work function of the nitrogen doped diamond is around 1.60 eV. In contrast, sulphur doped diamond has a work function of 2.54 eV.

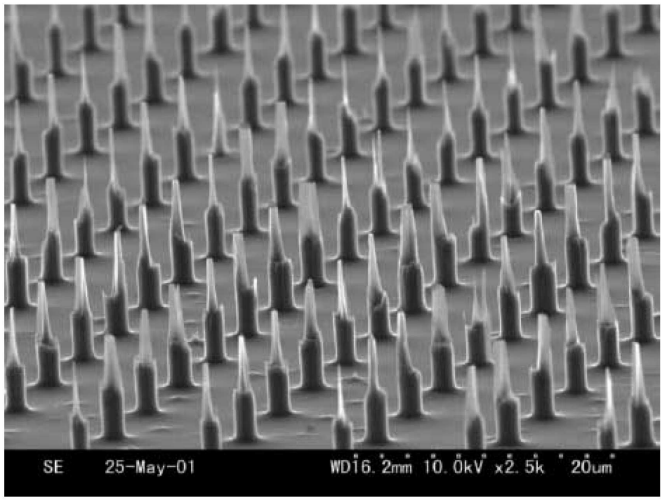

Figure 1.20: Conventional diamond emitters fabricated using Al as etching mask (from ref. [15]).

For the work function modification of diamond, surface termination techniques are generally preferred over doping methods, as surface termination processes are easier and more controllable than doping processes. Different surface treatments yield different values for the work function. Reports demonstrate that the H–treatment significantly reduces the work function of diamond, while oxygen termination increases the work function. It is noted that the presence of C–H surface dipoles induces a negative electron affinity (NEA), whereas C–O dipoles lead to a positive electron

Table 1.2: Obtained work function (ϕ) values for diamond using different doping and surface termination techniques (chronological order).

ϕ (eV)	Comments and References
3.85	Caesiated natural diamond (100) surface, work function experiments performed using X–Ray Photoelectron Spectroscopy (XPS) and ultra-violet photo–electron spectroscopy techniques [96].
2.4	Lithium fluoride (LiF) deposited on to a hydrogenated–terminated B–doped diamond [94].
3.52	Hydrogen terminated type–IIb (low levels of nitrogen but significant concentration of boron impurities) single crystal diamond (111) surface, work function experiments performed using XPS technique [22, 97].
2.54	Sulfur–doped nanocrystalline diamond on a molybdenum substrate, Richardson's constant (A)=40.71 A.cm^{-2}.K^{-2} [98].
1.50–1.90	Nitrogen–doped diamond on a molybdenum substrate, A=0.1–10 A.cm^{-2}.K^{-2} [84].
1.99	Nitrogen–doped nanocrystalline diamond on an n–type Si substrate, A=70 A.cm^{-2}.K^{-2} [99].
1.30	Nitrogen–incorporated ultra nanocrystalline diamond, A=0.84 A.cm^{-2}.K^{-2} [85].
2.22	Nitrogen–incorporated diamond thin films on molybdenum substrates, A=5.96 A.cm^{-2}.K^{-2} [100].
0.90	Phosphorus–doped diamond on a molybdenum substrate, hydrogen plasma exposure, A=10 μA.cm^{-2}.K^{-2} [101].
3.30–4.40	Nanocrystalline diamond thin films on polished molybdenum substrates, work function varied with temperature [102].
1.42, 1.39, 1.40 and 1.34	Nitrogen-doped ultra nanocrystalline diamond films on Mo, W, Re and MO/Re alloy substrates, A=0.69, 1.19, 53.10 and 3.67 A.cm^{-2}.K^{-2} for Mo, W, Re and MO/Re alloy substrates, respectively [65].

affinity (PEA). The origin of surface dipoles and their impact upon the electron affinity (χ) and the work function are discussed in Chapt. 5, 6 and 7.

In several field emission studies [15, 103–105], because of the NEA behaviour, diamond has already been proven as a promising electron emitter. In addition, it also shows good stability and reproducibility, crucial for practical applications. Although to enhance the electron emission, the fabrication of uniformly sharp tips over a large area seems to be a difficult and expensive process, recent reports show that it is possible to fabricate reliable, reproducible and cost effective diamond–based electron emitters (Fig. 1.20) suitable for applications where sufficiently high (>100 mA.cm^{-2}) stable emission currents and low driving voltages are required [15, 103–105].

1.4 Thesis outline

The broad aim of this thesis is to design a diamond–based thermo–tunnel device that is capable of operation in both mundane and harsh environments, such as those found in the nuclear reactor compartments and deep space probes. Akin to a typical semiconductor device fabrication process, the list of requirements for the fabrication of a diamond–based tunnelling device has first to be formulated.

1. Optimisation of physical parameters, such as electrode work function, electrode temperature and interelectrode separation, for a thermo–tunnelling device according to the required output power density and available heat input.
2. Development of low work function diamond electrodes to enhance the thermionic emission at low temperatures.
3. Achievement of thermally robust nanometer vacuum gaps and device packaging.

According to these requirements, to develop a roadmap for the realisation of thermo-tunnel devices, this thesis is divided into three parts: theoretical background, applications and summary and future work. Each part is subdivided into chapters and a summary of the content of each chapter is outlined below.

1.4.1 Part I – Theory and method

Chapter 2 – Theory

A brief overview of quantum mechanics and the many body problem for solving the Hamiltonian of the Schrödinger equation for complex systems are presented at the beginning of this chapter. The discussion then proceeds to the brief introduction of Born–Oppenheimer approximation, followed by *ab initio* density functional theory method that has been universally adopted for the noticeable advances in computational accuracy and speed. This chapter also consolidates the information regarding the exchange–correlation terms, which have been used to obtain the total energies, forces and experimentally observable quantities.

Chapter 3 –`AIMPRO`

In this chapter, an extended discussion regarding the implementation of quantum mechanical density functional theory using the *ab initio* modelling program (`AIMPRO`) is presented. This discussion has widened by introducing the concept of the pseudopotential approximation to replace the effects of the motion of the core electrons of an atom and its nucleus with the effective potential. Details regarding the supercell approach, Brillouin zone sampling, basis sets, self consistency, wavefunction visualisation, Mulliken population analysis, electron affinity calculation, adsorption energy calculation and treatment of evanescent states using 'GHOST' atoms have also been included, which are particularly useful for results presented in Chaps. 5, 6 and 7.

1.4.2 Part II – Application

Chapter 4 – Thermo–tunnel device: operation and physical parameters optimisation

This chapter details the function and physical parameter optimisation of the thermo–tunnel device. Calculations for a simple thermo–tunnel device structure have been performed using a MATLAB code developed for this project. Effects of physical parameters, such as interelectrode separation, electrode work function and temperature, on the output power density and heat–conversion efficiency have been investigated. Results will show that under optimal conditions, a high output power–density of around 10^3W.cm^{-2}, with efficiency in

the range 8–12%, can be achieved with a single thermo-tunnel device. Impact of thermal losses on the output characteristics and a discussion regarding other modes of operation (heating and cooling) are also included.

Chapter 5 – Bulk diamond and its low index surfaces

The structural and electronic properties of bulk and low index (100), (110) and (111) diamond surface are analysed using *ab initio* simulations, as implemented in the AIMPRO code. First, the surface electron affinities of clean, oxygenated and hydrogenated diamond (100), (110) and (111) surfaces are validated against the literature values, thereafter the electronic band structure are analysed for both terminated and unterminated low index diamond surfaces. A brief discussion on the bulk doping of diamond has also been included, along with references that might be helpful to the reader.

Chapter 6 – Halogen functionalisation of diamond surfaces

In this chapter, the results of *ab initio* calculations have been presented regarding the energetics and electron affinity of pure halogen (F/Cl/Br) and mixed halogen–hydrogen terminated diamond surfaces. To investigate the coverage dependence of the electron affinity and adsorption energy, halogen coverages onto clean (C–terminated) and H–terminated (partially terminated) hydrogenated diamond surfaces are systematically varied from relatively low (25% or 0.25 ML) to high (100% or 1 ML) halogen concentrations. This chapter will demonstrate that the adsorption energy per adsorbate atom for small size adsorbates, such as F and H, is largely independent of the surface coverage of adsorbates. However, in the case of large size adsorbates, such as Cl and Br, the adsorption energy depends strongly upon surface coverage. It will also be demonstrated that by careful selection of adsorbates and their surface coverage, the electron affinity of the diamond can be varied over a very wide range from -2.5 to $2.5\,\mathrm{eV}$.

Chapter 7 – Ultra thin films of transition metals and their oxides on diamond

This chapter consolidates the results of *ab initio* simulations of diamond surfaces covered with transition metals (Cu, Ni, Ti, V and Zn) and their metal oxides. Calculations are performed for different surface coverage of TMs and different TM:O stoichiometries. Cal-

culations will show that in addition to the chemical nature of TMs/TMOs, surface coverage/stoichiometry has a significant impact upon the electron affinity and adsorption energy. The reactions of TMs/TMOs with diamond surface are proven to be highly exothermic in nature. Ultra–thin coatings of selected TMs/TMOs may result in an NEA of around $-3.10\,\mathrm{eV}$, reducing the work function significantly and thus enabling one to use diamond for electron emission applications.

Chapter 8 – Overview: Diamond as the electron emitter for thermo–tunnel devices

Key conclusions derived from the thesis have been summarised in this chapter. In addition, this chapter also sheds light on the outlook for further developments, including the experimental analysis on the work function measurement using kelvin probe force microscopy and thermionic emission techniques.

Part I

Theory and method

Chapter 2

Theory

> Every word or concept, clear as it may seem to be, has only a limited range of applicability.
>
> Werner Karl Heisenberg (1901–1976)

2.1 Introduction

A brief discussion of the underpinning theory used in the density functional theory calculations of different diamond/adsorbate systems is presented in this chapter. Quantum many body problem and the methods, including the Born–Oppenheimer approximation, for solving the many body Hamiltonian of the Schrödinger equation are discussed. In addition, the exchange–correlation functional has also been scrutinised.

2.2 Quantum many body problem

In quantum physics, assessment of various properties, such as the energies and structures, for a system of interacting electrons and nuclei requires the solution of the simplified Dirac equation, commonly known as the Schrödinger equation. The time dependent Schrödinger equation for three spatial dimensions can be expressed as

$$-\frac{\hbar^2}{2m}\nabla^2\psi(r,t) + V(r)\psi(r,t) = i\hbar\frac{\partial}{\partial t}\psi(r,t), \tag{2.1}$$

where $\hbar$ is the reduced Planck constant, m the particle's mass, $\psi(r,t)$ the wave function and $V(r,t)$ is the potential energy. The notations 'r' and 't' are used to represent the spatial and temporal coordinates, respectively.

For a free particle, where $V(r)$=0, Eq. 2.1 can be written as

$$-\frac{\hbar^2}{2m}\nabla^2\psi(r,t) = i\hbar\frac{\partial}{\partial t}\psi(r,t), \tag{2.2}$$

Eq. 2.1 can also be described in terms of Hamiltonian ($\hat{H}$) and energy (E) operators

$$\hat{H}\psi(r,t) = E\psi(r,t), \tag{2.3}$$

$$\text{where} \qquad -\frac{\hbar^2}{2m}\nabla^2 + V(r) = \hat{H} \qquad \text{and} \qquad i\hbar\frac{\partial}{\partial t} = E. \tag{2.4}$$

Solving the Schrödinger equation for some simple cases, such as the free particle, harmonic oscillator and hydrogen atom, is relatively easy. However, solving it for a system wherein a number of electrons and nuclei are interacting with each other is not possible due to the lack of an analytic solution and therefore many approximations have to be made.

For a many body system (N electrons and M nuclei), the many body wave function (ψ), which is a function of electron spatial and spin coordinates, and nuclear positions, can be written as

$$\psi = \psi(r_1, r_2, ..., r_{\mathrm{N}}; s_1, s_2, ..., s_{\mathrm{N}}; R_1, R_2, ..., R_{\mathrm{M}}), \tag{2.5}$$

where $r_1, r_2, ..., r_{\mathrm{N}}$ the electron positions, $s_1, s_2, ..., s_{\mathrm{N}}$ the electron spins and $R_1, R_2, ..., R_{\mathrm{M}}$ are the coordinates of the nuclei with masses ($M_1, M_2, ..., M_{\mathrm{M}}$), respectively.

The many body Hamiltonian ($\hat{H}$) usually contains kinetic and potential energy terms and can be written as

$$\begin{aligned} H \;=\; & -\sum_{i=1}^{N}\frac{\hbar^2}{2m_{\mathrm{e}}}\nabla_{\mathrm{i}}^2 - \sum_{A=1}^{M}\frac{\hbar^2}{2M_{\mathrm{A}}}\nabla_{\mathrm{A}}^2 - \sum_{i=1}^{N}\sum_{A=1}^{M}\frac{Z_A e^2}{4\pi\varepsilon_0 r_{\mathrm{iA}}} \\ & + \sum_{i=1}^{N}\sum_{j>i}^{N}\frac{e^2}{4\pi\varepsilon_0 r_{\mathrm{ij}}} + \sum_{A=1}^{M}\sum_{B>A}^{M}\frac{Z_A Z_B e^2}{4\pi\varepsilon_0 R_{\mathrm{AB}}}, \end{aligned} \tag{2.6}$$

$$\text{in which} \qquad r_{\mathrm{ij}} = |r_{\mathrm{i}} - r_{\mathrm{j}}|,\ r_{\mathrm{iA}} = |r_{\mathrm{i}} - R_{\mathrm{A}}|,\ R_{\mathrm{AB}} = |R_{\mathrm{A}} - R_{\mathrm{B}}|. \tag{2.7}$$

If the system of *atomic units* is used, e, m_{e}, $\hbar$ and $4\pi\varepsilon_0$ can be taken to be unity. The 1 a.u.is equal to 0.53Å and 27.21 eV in terms of length and energy, respectively. After considering the atomic unit system, the terms of Eq. 2.6 simplify to

$$\sum_{i=1}^{N}\frac{1}{2}\nabla_{\mathrm{i}}^2 \rightarrow \hat{\tau}_{\mathrm{e}} : \text{kinetic energy (KE) of electrons}, \tag{2.8}$$

$$\sum_{A=1}^{M} \frac{1}{2M_{\mathrm{A}}} \nabla_{\mathrm{A}}^2 \rightarrow \hat{\tau}_{\mathrm{n}} : \text{KE of nuclei}, \tag{2.9}$$

$$\sum_{i=1}^{N} \sum_{A=1}^{M} \frac{Z_{\mathrm{A}}}{r_{\mathrm{iA}}} \rightarrow \hat{\nu}_{\mathrm{e-n}} : \text{Coulombic attraction between the electrons and nuclei}, \tag{2.10}$$

$$\sum_{i=1}^{N} \sum_{j>i}^{N} \frac{1}{r_{\mathrm{ij}}} \rightarrow \hat{\nu}_{\mathrm{e-e}} : \text{Coulombic repulsion between electrons and} \tag{2.11}$$

$$\sum_{A=1}^{N} \sum_{B>A}^{M} \frac{Z_{\mathrm{A}} Z_{\mathrm{B}}}{R_{\mathrm{AB}}} \rightarrow \hat{\nu}_{\mathrm{n-n}} : \text{Coulombic repulsion between nuclei} \tag{2.12}$$

In general there is no analytical solution to this problem, a number of approximations have therefore been introduced.

2.3 The Born–Oppenheimer approximation

According to the *Born–Oppenheimer* or *adiabatic approximation* [106], the wave function (ψ_{total}) of a many body system can be separated into the nuclear contribution (ψ_{nuclei}) and electron contribution ($\psi_{\mathrm{electronic}}$), as an electron is atleast 1836 times lighter that the nucleons (proton and neutron) and therefore is expected to respond without any delay to the motion of the nuclei and achieve the electronic ground state.

$$\psi_{\mathrm{total}} = \psi_{\mathrm{electronic}} \psi_{\mathrm{nuclei}} \tag{2.13}$$

The electronic and nuclear problems can now be solved individually with independent wave functions as follows

$$[\hat{\tau}_{\mathrm{e}} + \hat{\nu}_{\mathrm{e-e}} + \hat{\nu}_{\mathrm{e-n}}]\psi_{\mathrm{electronic}} = E_e \psi_{\mathrm{electronic}}, \tag{2.14}$$

$$[\hat{\tau}_{\mathrm{n}} + \hat{\nu}_{\mathrm{n-n}}]\psi_{\mathrm{nuclei}} = E_n \psi_{\mathrm{nuclei}}, \tag{2.15}$$

Although the Born–Oppenheimer approximation allows the electron problem to be solved separately, in reality, solving the Schrödinger equation for systems larger than single atoms is still difficult. Hence some further approximations have to be made. In addition, in some cases, for example molecular systems which possess Jahn–Teller effect (a type of electronic effect that causes the geometrical distortion in a non–linear molecules under certain situations), the Born–Oppenheimer approximation (Eq. 2.13) is no longer valid. Such cases fall into the category of what is known as the non–adiabatic quantum dynamics and therefore require different and careful treatments.

2.4 Density Functional Theory (Electron Density Approach)

The density functional theory (DFT) [107, 108] method is a highly successful approach to investigate the ground state properties of the many–body systems, including atoms, molecules and various condensed phases. Instead of using the all–electron wave function, the DFT approach makes use of the functions of the electronic charge density, known as functionals, to calculate the total energy of a system. This is also a far less computationally demanding method than the Hartree–Fock method [109], where the total energy of the system is described as a functional the all–electron wave function.

2.4.1 Hohenberg–Kohn theorems

The Hohenberg–Kohn (H–K) theorems [110] are the basic building blocks of density functional theory, which demonstrate that the electronic charge density is a basic variable and in principle capable of finding the exact ground–state energy.

The first Hohenberg–Kohn theorem

The external potential is determined, to within a trivial additive constant, by the electron density, $n(\mathbf{r})$.

This states that the external static potential (V_{ext}) uniquely determines the electronic charge density or *vice versa*, and hence the total energy (E) of a many–electrons system (in the presence of V_{ext}) can be expressed as a functional of the ground state electron charge density ($n(r)$) that is a scalar function of the position.

$$E[n] = F[n] + \int V_{\text{ext}}(\mathbf{r})n(\mathbf{r})d(\mathbf{r}) + \frac{1}{2}\int\int \frac{n(r_1)n(r_2)}{r_{12}}dr_1dr_2, \tag{2.16}$$

where the functional $F[n]$ is an universal functional, as it is independent of system and encompasses only the electron kinetic energy, electron correlation and exchange correlation. The V_{ext} accounts for the effects of the electron–nucleus interactions and the interaction of electrons with other external fields. The third term is the Hartree energy (U_{H}).

The second Hohenberg–Kohn theorem

For a trial density $\tilde{n}(\mathbf{r})$*, such that* $\tilde{n}(\mathbf{r}) > 0$ *and* $\int \tilde{n}(\mathbf{r})d\mathbf{r}=M$.

$$E[\tilde{n}] \geq E_0, \tag{2.17}$$

where E_0 is the true ground state energy.

This suggests that if the electronic density is equal to the ground state electronic density $n(r)$=$n_0(r)$, it will give the lowest energy (ground state energy) of the system. In other words, the energy functional ($E[\tilde{n}]$) for any valid state will always remain larger than the one for the ground state (E_0).

2.4.2 The Kohn–Sham approach

In Hohenberg–Kohn theorems, the functional and exact ground state density remain unexplored, as it is not always possible to write down an explicit and accurate form for $F[n]$, particularly for those systems in which the electronic charge density varies rapidly. This problem was overcome by Kohn–Sham equations [111], where the actual system is replaced with an auxiliary system of non–interacting particles (*i.e.* the Kohn–Sham systems) which has the electronic charge density exactly the same as that of the actual interacting system. Here, $F[n]$ is described as the sum of the kinetic energy ($T_{\rm s}[n]$) and the exchange–correlation term ($E_{\rm xc}[n]$).

According to Kohn–Sham, the electronic charge density can be expressed as the sum of the squares of a set of orthonormal wave functions

$$n(r) = \sum_{\rm i} |\psi_{\rm i}|^2, \tag{2.18}$$

where $\psi_{\rm i}$ are the Kohn–Sham wave functions. In the case of the system of non–interacting electrons, calculation of the kinetic energy is rather simpler than that of the interacting system. Using Eq. 2.18, the expression for the kinetic energy can be written as

$$T_{\rm s}[n] = -\frac{1}{2}\sum_{i} \langle\psi_{\rm i}|\nabla^2|\psi_{\rm i}\rangle. \tag{2.19}$$

In the Kohn–Sham system, the non–interactive particles move in a local effective external potential ($V_{\rm eff}$) and therefore, the Schrödinger equation for N non–interactive particles with the new effective potential is defined as

$$-\frac{\hbar^2}{2m}\nabla^2\psi_{\rm i}(r) + V_{\rm eff}(r)\psi_{\rm i}(r) = \varepsilon_{\rm i}\psi_{\rm i}, \tag{2.20}$$

where the effective potential for charge densities $n(r_1)$ and $n(r_2)$ at spatial coordinates r_1 and r_2 is

$$V_{\rm eff}(r) = V_{\rm ext}(r) + \frac{1}{2}\int\int \frac{n(r_1)n(r_2)}{r_{12}} dr_1 dr_2 + E_{\rm xc}[n]. \tag{2.21}$$

Eqs. 2.19, 2.20 and 2.21 are known as the Kohn–Sham equations in their canonical form and the total energy is rewritten as the functional of the electronic charge density

$$E[n] = T_{\rm s}[n] + \int V_{\rm ext} n(r) dr + \frac{1}{2} \int \int \frac{n(r_1) n(r_2)}{r_{12}} dr_1 dr_2 + E_{\rm xc}[n], \qquad (2.22)$$

2.5 Local density and generalised gradient approximations

In Eq. 2.22, $E_{\rm xc}[n]$ is the only term, which remains unknown. In order to resolve this issue, a number of approximations have been suggested. Currently, popular approximations are the local density approximation (LDA) and generalised gradient approximation (GGA) [112–118]. In local density approximation, the functional depends only on the electronic density at the coordinates where the functional is evaluated. Since the exchange correlation energy is assumed to be local, it can be divided separately into the exchange and correlation parts. In the case of the generalised gradient approximation, which is local too, the gradient of the electronic density is also taken into account.

The exchange–correlation energy terms for LDA and GGA can be expressed as

$$E_{\rm xc,LDA}[n] = \int n(r) \varepsilon_{\rm xc}(n(r)) d^3 r \qquad \text{and} \qquad E_{\rm xc,GGA}[n] = \int n(r) \varepsilon_{\rm xc}(n, \nabla n) dr \qquad (2.23)$$

where $\varepsilon_{\rm xc}(n)$ is the exchange–correlation energy per electron which is universal and independent of system.

The accuracy of LDA and GGA calculations depends upon the chemical nature of the system. In the case of diamond, for most observables, LDA and GGA calculations give generally similar results. As an example, some key parameters for bulk diamond lattice, which are calculated using LDA and GGA approximations, are summarised in Table 2.1. For the DFT results presented in this thesis, local density approximation, which is a standard choice of the `AIMPRO`, has been used.

Table 2.1: Comparison between LDA and GGA calculations.

Method	Energy band gap (eV)	Lattice constant (a.u.)
LDA	4.22	6.68
GGA	4.15	6.75

2.6 Summary

In this chapter, the DFT theory, which utilises the charge density as a basic variable instead of solving the many body Schrödinger equation for all electrons, has been presented as a promising approach to determine the ground state properties of a system of atoms. The DFT method is able to calculate a number of experimentally observable quantities with a high accuracy; however, the representation of the excited states is often incorrect, leading to an underestimation of the energy band gap. In recent years, empirical quantities have been introduced in the DFT method to overcome this problem, which are particularly useful for accurate estimation of the electron affinity (χ). In the next chapter, different analyses and implementation of the DFT theory via the `AIMPRO` code is presented.

Chapter 3

The modelling package AIMPRO

I don't like it, and I'm sorry I ever had anything to do with it.

Erwin Rudolf Josef Alexander Schrödinger (1887-1961)

3.1 Introduction

Density functional theory simulations performed throughout this project utilise the AIMPRO code, developed by Briddon and Jones [119–127]. The acronym 'AIMPRO' stands for *Ab Initio* Modelling PROgram. Details regarding the important elements of the AIMPRO package and different analyses used in this work are described in this chapter.

3.2 Supercell approach

All DFT simulations presented in the thesis are performed under periodic boundary conditions using the supercell approach. The supercell method defines a unit cell, and then repeats it throughout space in an appropriate lattice using the periodic (The Bloch's theorem) boundary conditions. It is an extremely successful approach for investigating the properties of materials which contain impurities, vacancies, dislocations, stacking faults and surface defects.

The (001) diamond surfaces are modelled using the supercells with in-plane lattice vectors $[110]a_0/2$ and $[1\bar{1}0]a_0/2$, (111) surfaces are constructed with in-plane lattice vectors $[10\bar{1}]a_0/2$ and $[1\bar{1}0]a_0/2$, and (110) surfaces with in-plane lattice vectors $[001]a_0$ and

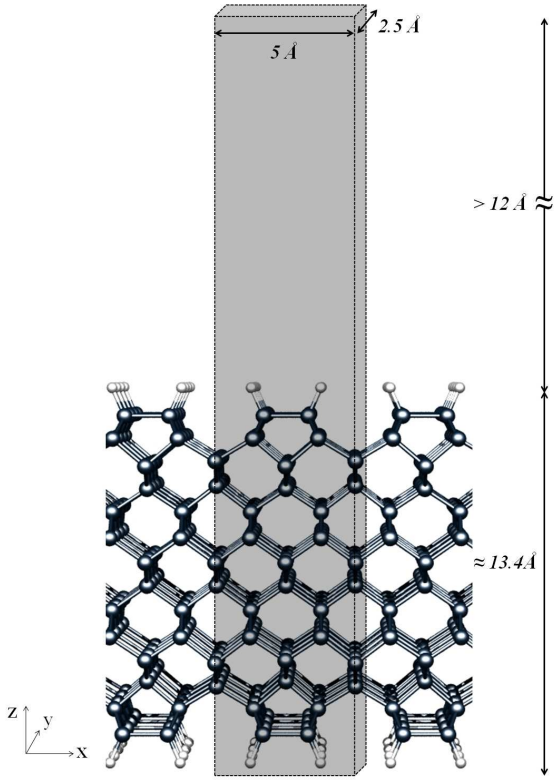

Figure 3.1: Supercell (grey region) for the modelling of a hydrogen–terminated (001)–2 × 1 diamond surface. The supercell of diamond slab consists of 14 layers of 24 C atoms and 4 hydrogen atoms terminating surface dangling bonds. The thickness of the vacuum is at–least 12Å.

$[1\bar{1}0]a_0/2$. Each supercell corresponding to diamond (001), (111) and (110) surfaces contains 14 layers of C atoms. The number of C atoms per layer may vary. For example, for 1×1 geometry of (100) surface, each layer has only 1 C atom, while for 2×1 geometry, each layer consists of 2 C atoms. As an example, a supercell for the modelling of a hydrogenated 2×1-(001) diamond surface is shown in Fig. 3.1. In all calculations, the top and bottom sides of each slab are chosen to be identical to give the system either inversion or reflection symmetry.

The vacuum between two slabs should be large enough in order to reduce the slab–slab interaction. Although depending upon the chemical nature of the system the vacuum thickness may vary considerably, a vacuum thickness of atleast 12Å is found to be sufficient

for the investigated systems. In the case of (001), (111) orientation, the z–direction is normal to the slab surface, while for (110) orientation, the surface normal is in the y–direction.

3.3 Pseudopotentials

The chemical properties of an atom are principally governed by its valence electrons, as the core electrons are highly localised to the nucleus and do not participate significantly in the chemical reactions. Consideration of the effects of the motion of a large number of core electrons of an atom and its nucleus is not only computationally demanding, but also challenging in terms of achieving a good accuracy for two reasons. First, representation of all electronic states requires prohibitively large number of basis functions. Second, the core states in the vicinity of the nucleus are highly localised and in order to maintain the orthogonality with the core electrons, the valence states must oscillate rapidly.

In computational physics, the effect of core electrons is eliminated by using a rather simple but highly effective potential, known as the pseudopotential. A pseudopotential is an effective Coulombic potential that is felt by valence electrons, and describes the interaction with the core electrons and nucleus (Fig. 3.2). The `AIMPRO` package comprises different types of pseudopotentials, such as BHS (Bachelet, Hamann and Schlüter) [128], TM (Troullier and Martins) [129] and HGH (Hartwigsen, Goedecker and Hutter) pseudopotentials [130]. For the DFT results presented in this thesis, the standard `AIMPRO` choice, the HGH pseudopotentials, has been used.

3.4 Self-Consistency cycle

The self consistency cycle is an iterative procedure to solve the Kohn–Sham equations accurately described in Chap. 2 by creating the effective potential. In the self–consistency process, the charge is redistributed around the system until a minimum in the total energy is achieved, thereby leading to an accurate simulation of the charge distribution in a real system. The first guess of the charge density $n(\mathrm{r})$ is taken either from the density of the neutral atoms or the output of a previously optimised structure to generate a potential V. The potential V generated from the initial charge density $n(\mathrm{r})$ is used to solve Kohn–Sham equations, which give rise to a new output charge density $\tilde{n}(\mathrm{r})$. This process continues till

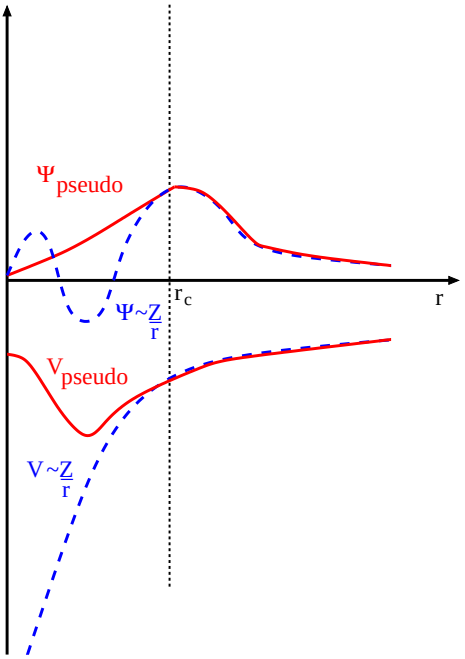

Figure 3.2: Comparison of a wave function in the Coulombic potential of the nucleus (blue) with one in the pseudopotential (red). The real and pseudo wave function and potentials match above a certain cutoff radius r_c (Source: Wikipedia).

the difference between the input and the output of Hartree energies is less than 10^{-5} a.u.. At this point, the self-consistency of charge density is believed to reach convergence point.

3.5 Structural optimisation

In order to determine the minimum energy structure, the forces on each atom must be calculated. The forces can be calculated with the help of the self–consistent charge density, which is described in the previous section. Once the forces are calculated, the atoms move along the direction of the net force until a minimum in the total energy of the system is achieved. This process is called structural optimisation or relaxation. In the `AIMPRO` code, structural optimisation is performed using a conjugate gradients scheme, with the optimised structures having forces on atoms $< 10^{-3}$ atomic units, and the final structural optimisation step is required to result in a reduction in the total energy of less than 10^{-5} Hartree. It is important to note here that the total energy obtained for an equilibrium structure may

not be the global minimum. Depending upon the starting structure, it may be a local minimum. Therefore, one must perform several tests using different initial configurations to get the right structure corresponding to global energy minimum.

3.6 Brillouin zone sampling

The first Brillouin zone is defined as the Wigner–Seitz primitive cell in the reciprocal lattice. The calculation of physical quantities, such as total energy, charge density and density of states requires an integration or averaging over the Brillouin zone. For this purpose, the AIMPRO–DFT calculations use a Monkhorst-Pack (MP) sampling mesh [131], of special k–points defined by three integers I, J and K. The integers I, J and K define a grid of $I \times J \times K$ points in a reciprocal space:

$$\mathbf{k}(i,j,k) = \frac{2i-I-1}{2I}g_1 + \frac{2j-J-1}{2J}g_2 + \frac{2k-K-1}{2K}g_3, \tag{3.1}$$

where

$$\begin{aligned} i &= 1, ..., I \\ j &= 1, ..., J \\ k &= 1, ..., K, \end{aligned} \tag{3.2}$$

and g_1, g_2 and g_3 are the unit–vectors of reciprocal space and I, J and $K \geq 1$. When I=J=K the sampling scheme is referred to as MP-I^3.

The density of k–point sampling grid is critical in terms of the impact upon the accuracy and computation time. As shown in Fig. 3.3, use of highly dense sampling increases not only the accuracy of calculations but also the computation time. In all diamond surface slab calculations presented in this thesis, the Brillouin zone is two dimensional, and the sampling used is 8×8 for a 1×1 surface cross-section of the z-oriented (001) and (111) surfaces, while 8×6 is used for the (110)-1×1 surface. For simulations where the primitive surface cells are repeated, such as for fractional surface coverage of adsorbates, the sampling is reduced to maintain the sampling density. The sampling used is sufficiently dense, resulting in convergence of the total energy with respect to the expansion of the charge density to within around 10 meV.

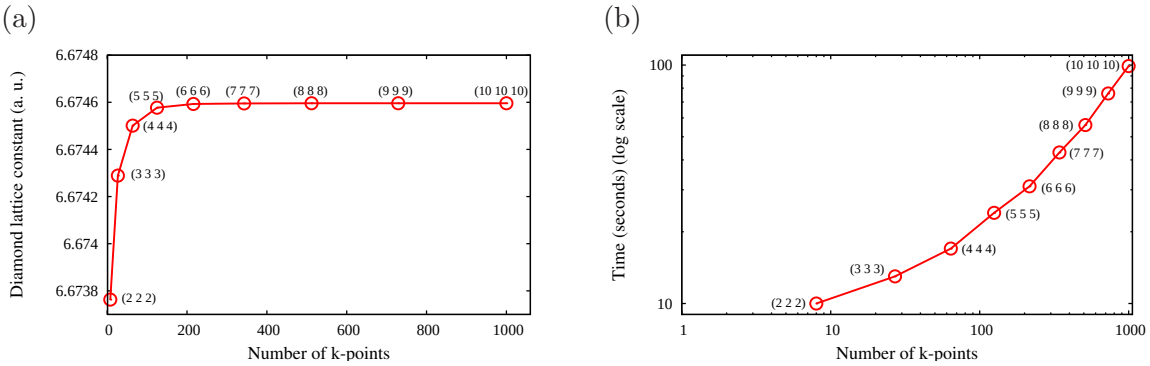

Figure 3.3: Effect of the Brillouin zone sampling on (a) the accuracy of lattice constant of diamond and (b) the calculation time. These calculations are performed using a primitive cell of the diamond lattice, which contains only two C atoms. The integer I, J and K corresponds to each data point are given in parentheses.

3.7 Basis sets

In DFT, molecular orbitals can be expanded using either plane wave basis [132] or Gaussian–type orbitals as a basis. `AIMPRO` utilises Bloch basis functions which are themselves built from a set of Cartesian Gaussian functions centred at the atomic sites. As an illustration, the form of the Gaussian basis functions $\phi_{\rm i}$, localised at the site of the atom, $\mathrm{R_i}$, is

$$\phi_{\rm i}(r-\mathrm{R}_i) = (x-R_{\rm ix})^{n_1}(y-R_{\rm iy})^{n_2}(z-R_{\rm iz})^{n_3}e^{-\alpha_i(r-R_i)^2}, \tag{3.3}$$

where $n_{\rm i}$ (≥ 0) is an integer.

The symmetry of the orbital can be identified using $n_{\rm i}$. For the case $\sum_i n_{\rm i}$=0, the orbital has a spherical symmetry, *i.e.* an s–type orbital. Similarly, $\sum_i n_{\rm i}$=1 represents p–type orbital and $\sum_i n_{\rm i}$=2 gives 5 d–orbital and 1 s–like orbital.

In terms of reducing the computation time of DFT calculations, Gaussian basis sets are generally more effective than the plane wave basis sets. In addition, their integrals have analytic forms and therefore can be solved easily. Although, a number of basis sets options are available in the `AIMPRO` package for the simulation of the diamond lattice, several test calculations were carried out to select the most promising candidate. The basis set, *diamond–dddd*, which consists of 40 functions per C atom, is used for the simulation of the diamond lattice throughout this work. Calculated lattice constants and times taken corresponding to some of the common basis sets are shown in Fig 3.4.

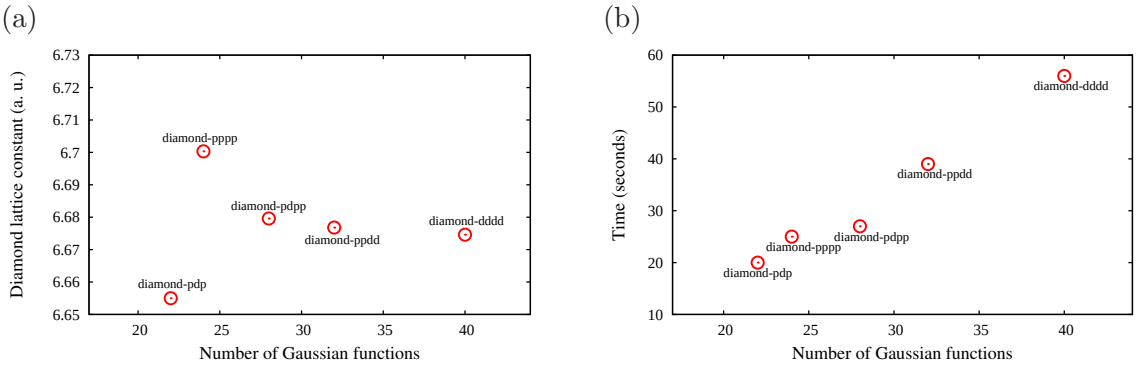

Figure 3.4: Estimation of (a) the lattice constant and (b) the computation time using different basis sets for a primitive diamond cell.

3.8 GHOST atoms: treatment of the vacuum region in surface slab calculations

DFT calculations performed in this work utilise Gaussian–type orbitals as a basis. Unlike plane–wave basis functions, Gaussian basis functions decay rapidly away from the atoms on which they are centred. Due to the highly localised nature of basis functions, it can therefore be argued that the vacuum region just above the slab surface is not treated properly, because there are no basis functions available to model the evanescence of the surface states.

In all simulations, to augment the treatment of the evanescent states at the surface, sets of sixteen *s*-Gaussian basis functions are placed at points in the vacuum region using *ghost atoms*. The treatment of the vacuum using a ghost atom grid is shown schematically in Fig. 3.5. It is important to mention here that the atomic density of the ghost atom grid used in simulations is equal to that of the diamond slab. Moreover, the exponents of the ghost–atom functions are also equal to those of host C atoms. Although ghost atoms have zero nuclear charge and zero pseudopotentials, in order to avoid any possible mutual interaction, the distance between the surface atoms and first layer of 'GHOST' atoms grid is kept sufficiently large. For example, as shown in Fig. 3.5 (b), the distance between H atoms and first atomic layer of the grid is bigger than the C–H bond length; however, smaller enough for an effective treatment of the evanescent surface states. In test calculations, it is found that the ghost atom grid impacts the electron affinity of the reconstructed clean diamond (100) surface more strongly than that of the H–terminated (100) surface.

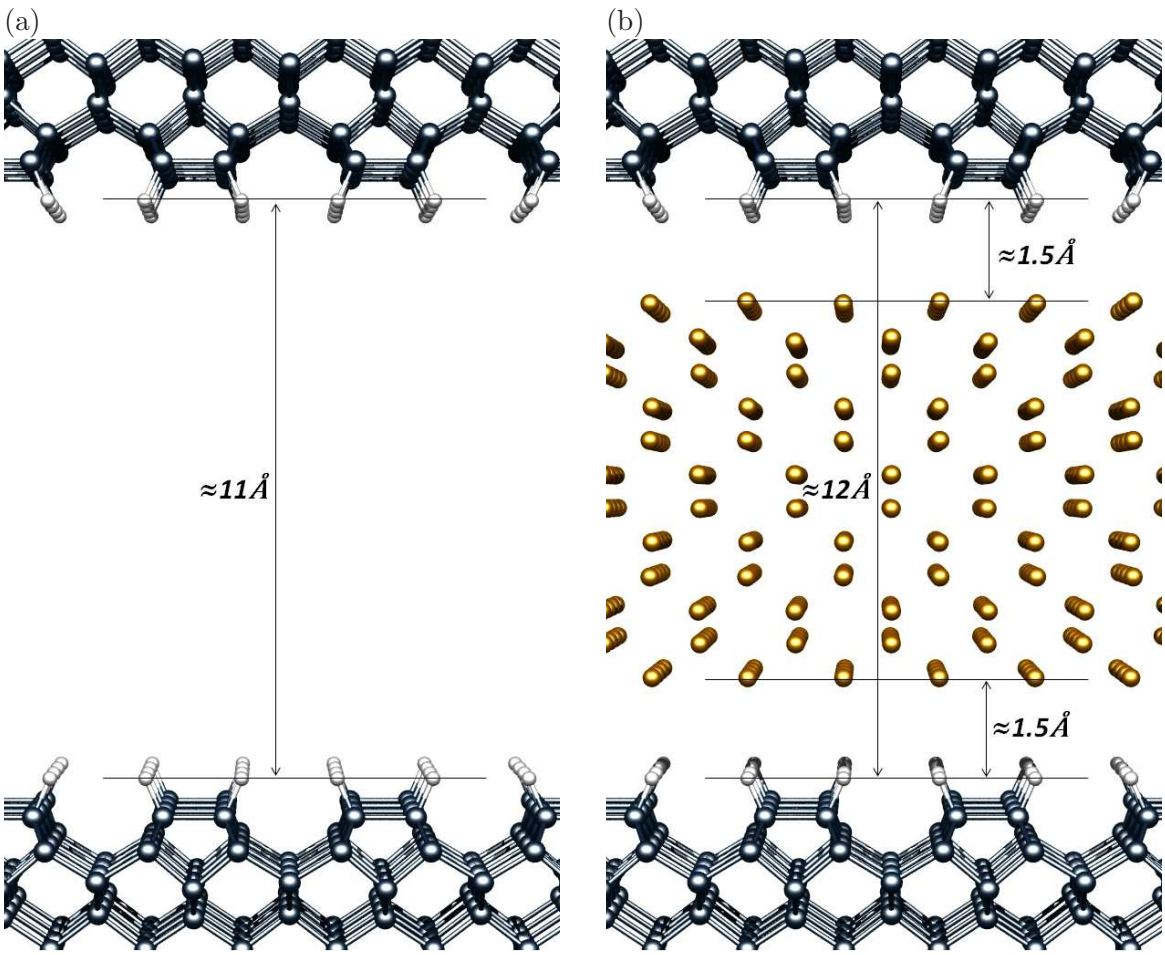

Figure 3.5: A repeated H–terminated diamond slab in (001) direction (a) without a GHOST atom grid and (b) with a GHOST atom grid.

3.9 Calculation of Electron affinity

In band structure (energy–wavevector relationship) terms, the electron affinity, χ, of a semiconductor is defined as the difference in energy between the conduction–band minimum (E_{c}) in the bulk material and the vacuum energy level (E_{vac}) [23, 92, 93].

$$\chi = E_{\mathrm{vac}} - E_{\mathrm{c}}, \tag{3.4}$$

In semiconductors for which χ is negative, E_{c} lies above E_{vac}. In contrast, for PEA semiconductors, E_c lies below E_{vac} (Fig. 3.6). An NEA of semiconductor is of particular interest for a number of applications, including photocathode and advanced electron emitters [23, 24, 92, 93, 133]. This is because an NEA can reduce the energetic barrier to electron

emission, so that conduction–band electrons can be released into the vacuum even at low temperatures.

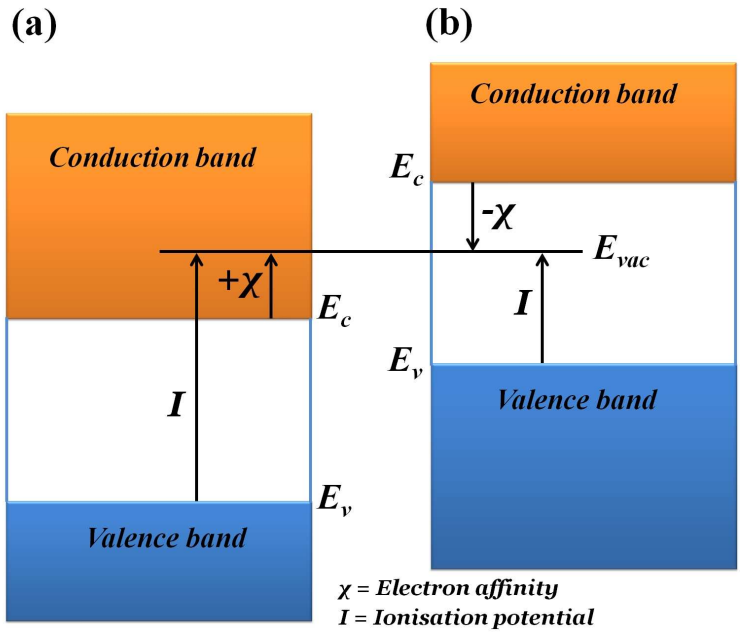

Figure 3.6: Energy level diagrams for semiconductors with (a) PEA and (b) NEA

In order to estimate the electron affinity of different diamond–adsorbate systems, a standard approach [17, 19, 20, 134, 135] has been adopted in this work. The current approach includes the calculation of the electrostatic potential as a function of position through the slab into the vacuum, and thereafter alignment of this to the corresponding potential variation in bulk diamond. For the best agreement with experiment, it is a normal practice to determine the offset between the bulk valence band top and the vacuum-level, and locate the conduction band using the experimental value of the band-gap (5.47 eV for the diamond) added to the valence band maximum (E_v), similar to the scheme which has been used previously [17,19,20,134,135]. Then the difference between the conduction band minimum and vacuum level gives the electron affinity. An example of calculation of electron affinities for terminated (oxygenated and hydrogenated) diamond surfaces is shown in Fig. 3.7.

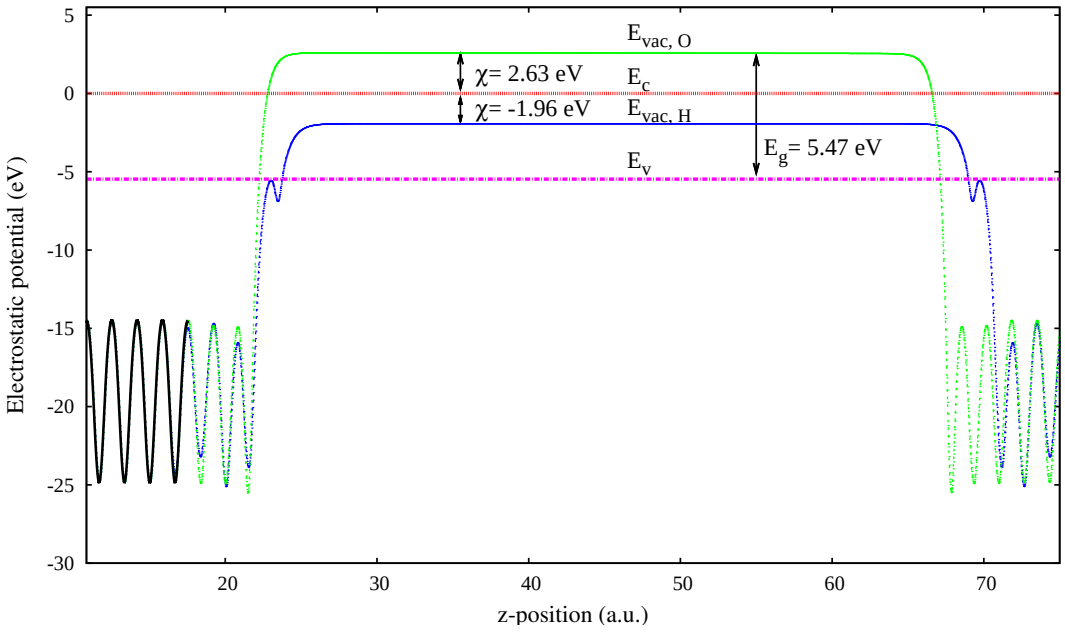

Figure 3.7: Electrostatic potentials and vacuum reference energy levels for the diamond (001) surfaces with adsorbed O ($E_{\mathrm{vac,O}}$: green) and H ($E_{\mathrm{vac,H}}$: blue) atoms. The average bulk potential (black) have been aligned with the electrostatic potentials of the terminated surfaces to place the conduction–band minimum (E_{c}: red) at zero. E_{c} is set 5.47 eV above E_{v}.

3.10 Mulliken population analysis

Mulliken population analysis is a widely used method to estimate partial atomic charges (Mulliken charges) [136]. It has been used frequently to identify which of the atoms in a system are associated with a particular electronic state [137]. In this thesis, Mulliken population analysis is carried out to calculate the partial atomic charges at diamond/adsorbate interfaces, particularly for transition metal oxide coated diamond surfaces (Chap. 7). Although this analysis exhibits some severe discrepancies, for example the overestimation of the covalent character of a bond and ultra–high sensitivity to the choice of basis sets, consideration of relative values of Mulliken charges is found to be extremely helpful in identifying the polar/non–polar nature of diamond/adsorbate interfaces. Currently, the `AIMPRO` package offers a number of optional arguments to Mulliken analysis and computational details regarding this method can be find on the `AIMPRO` group website [138].

3.11 Adsorption energy calculation

In this work, adsorption energy calculations are used to investigate the thermodynamics of the reactions of adsorbates with diamond surfaces, *i.e.* whether these reactions are exothermic or endothermic. Although the procedure of adsorption energy calculations is described thoroughly in the methodology sections of Chaps. 6 and 7, a general idea in conjunction with a schematic (Fig. 3.8) for a simple system is illustrated here.

The average adsorption energy per adsorbate atom (E_{ads}) for a terminated surface can be written mathematically as

$$E_{\text{ads}} = \frac{1}{n}\left(E_{\text{tot}} - E_{\text{clean}} - n\mu_{\text{X}}\right), \tag{3.5}$$

where E_{clean} is the energy of a clean surface, E_{tot} is the energy of the same surface but with adsorbed atoms, μ_{X} is the chemical potential of the adsorbate and n is the number of adsorbate atoms.

A negative average adsorption energy is indicative of an exothermic reaction, *i.e.* the adsorption is thermodynamically stable. In contrast, a positive adsorption energy suggests an endothermic reaction. Since the chemical potential of an adsorbate depends upon its reference state, a careful examination is warranted in identifying the nature of the surface reactions. The reactions that are exothermic corresponding to a particular reference state of an adsorbate may be endothermic for a different reference state. Furthermore, the quoted values of the adsorption energies throughout this work are zero temperature free energies, and therefore neglect the impact of the temperature dependence of the internal energy and the contribution of entropy.

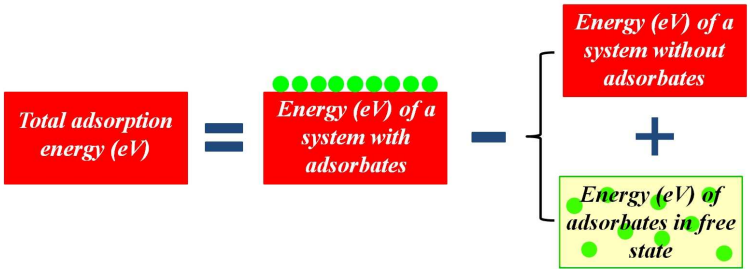

Figure 3.8: A schematic diagram depicting the adsorption energy calculation.

3.12 Chapter summary

In addition to describing the technical terms, such as the Monkhorst-Pack grid, pseudopotentials and basis sets, details regarding the calculations of the electron affinities, Mulliken charges and adsorption energies are discussed in this chapter. Treatment of the vacuum region in surface slab calculations using ghost atoms is particularly useful, as it enables accurate estimation of a key parameter, the surface electron affinity, from the short range Gaussian–type basis functions. Furthermore, adsorption energy calculations help enormously in the investigation of the energetics of different diamond/adsorbate systems.

Part II

Applications

Chapter 4

Thermo-tunnel device: operation and physical parameters optimisation

> Glory is like a circle in the water, which never ceases to enlarge itself, Till by broad spreading it disperses to nought.
>
> –William Shakespeare (1564–1616)

4.1 Introduction

Conventional designs of the thermionic converter exhibit a number of severe issues, such as complete elimination of the space charge effects and low power output, which limit their widespread use for thermal energy conversion. Nevertheless, because of the profound importance of limited solid–state thermal energy conversion technologies in both terrestrial and extra–terrestrial applications, and high energy conversion efficiency (≈20%), interest in thermionics has been recently rekindled [30]. As a result of the dedicated efforts, the combined thermionic emission and tunnelling of hot electrons called the thermo–tunnelling has surfaced as a potential new technology that is capable of providing exceptionally high output power densities with a nano–scale thermo–tunnel device [13, 14, 70, 72, 73, 75, 78, 81, 139].

The thermo–tunnel device is a distinguished class of thermionic converter (Fig. 4.1), where the interelectrode separation is within the nano–regime (a few nanometres), thereby allowing the tunnelling of electrons between the electrodes [72, 75]. The inclusion of tunnelling (Fig. 4.2) in a thermionic converter increases its output power density significantly,

while preserving the high thermal energy conversion efficiency.

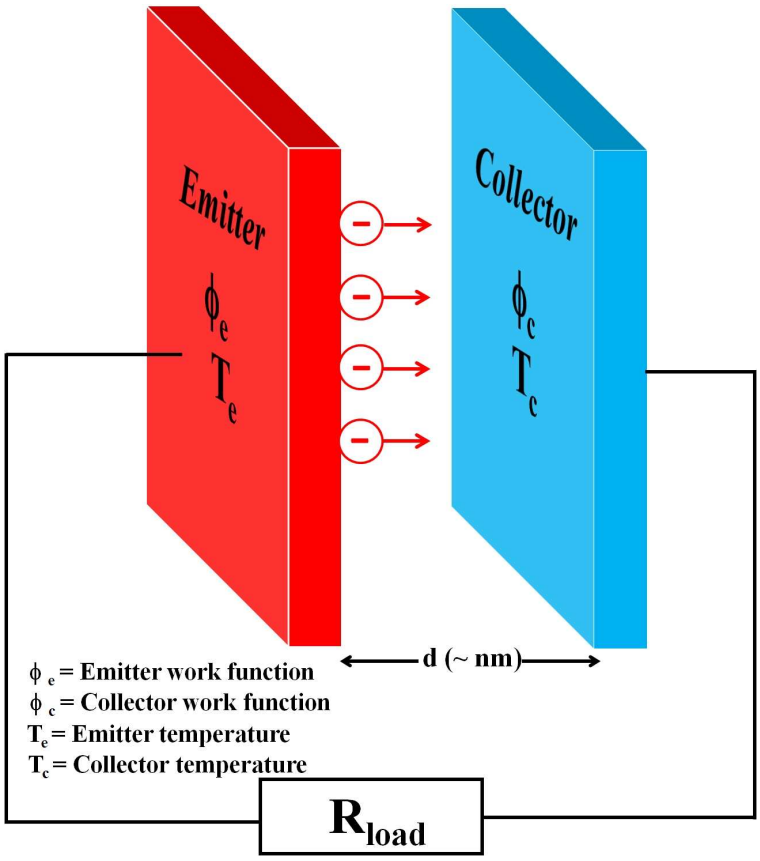

Figure 4.1: Schematic of a thermo–tunnel device. The left electrode (red shaded) is the emitter, while the right electrode (blue shaded) is the collector.

Tunnelling is a thought–provoking quantum mechanical phenomenon, where even a low energy electron can pass through a high but narrow potential barrier that it classically could not surmount (Fig. 4.2). In equilibrium, the thermo-tunnel device does not yield any output current since equal number of electrons cross the potential barrier in each directions and the net transfer of charge or energy is zero. Implementation of an electric field or thermal gradient destabilises the equilibrium by changing the tunnelling and thermionic emission probabilities, and thus a net flux of electron appears across the gap. It is worth mentioning here that the internal electric field caused by the difference in the work functions of electrodes also helps in establishing a net flux of electrons across the vacuum gap.

It has been suggested previously that both the height and width of an interelectrode

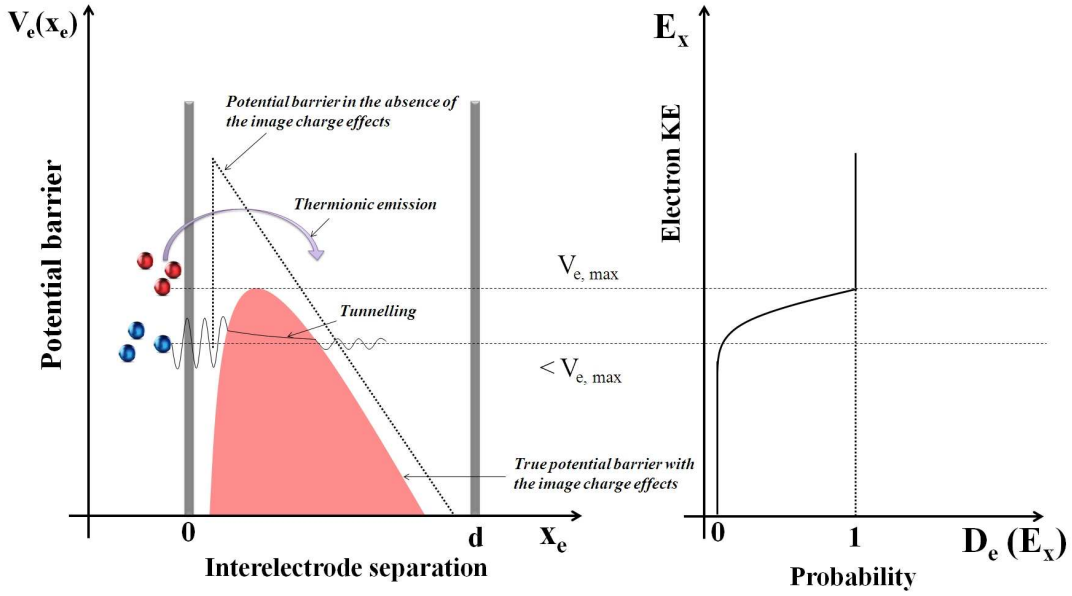

Figure 4.2: Diagram depicting the basic physics of thermo–tunnelling between the electrodes of a thermo-tunnel device. The decay of the electron wave function inside the barrier is not exponential since the potential barrier is not rectangular in shape. However, similar to the case of a rectangular barrier, the tunnelling probability will be small for a thick and high barrier. The interelectrode separation strongly impacts the height (V_e) and width (x_e) of the potential energy barrier, which are of critical importance for both tunnelling and thermionic emission of electrons. Reduction in the interelectrode separation significantly increases the tunnelling and thermionic emission probabilities. Electrons (blue spheres) with a given energy E_x lower than $V_{e,max}$ cross the potential barrier with a tunnelling probability $D_e(E_x)$ lower than 1. For electrons whose KEs are higher than E_x, there is no more tunnelling and the electrons (red sphere) are emitted with a probability equal to 1. In non-equilibrium, the magnitude of thermo-tunnel current of one electrode will be higher than that of the other electrode, which will give rise to a net flux of thermo–tunnel current between the electrodes of a thermo-tunnel device.

potential barrier of a thermo–tunnel device, which an electron must overcome to be emitted into the vacuum, can be controlled by physical parameters, particularly the interelectrode separation (Fig. 4.2) and work functions of electrodes (emitter and collector) [14, 72, 73, 75,

81]. Research has also shown that for small sufficiently values of the interelectrode separation and electrode work function, electrons can easily tunnel through the vacuum gap [14, 72, 73, 75, 81]. Hence, in principle, by applying a thermal gradient across the ultra-thin (few Å) vacuum gap of a tunnel device, a large unidirectional flux of combined thermionic and thermo–tunnel currents between the emitter and collector, and a thermal potential difference can be achieved.

Thermotunnel devices offer a number of advantages over both conventional thermionic and thermoelectric devices. Since the interelectrode separation in a thermo–tunnel device is very small, negative–space–charge effects [30], which impede the flow of electrons from emitter to collector in a conventional thermionic converter, are negligible (Chap. 1). Furthermore, for thermoelectric devices, in addition to a high Seebeck coefficient, high electrical and low thermal conductivity are necessary to achieve a high figure of merit. In contrast, thermo–tunnel devices have no such requirements, although in practice the encapsulating material must have a low thermal conductivity to prevent a thermal short between the electrodes.

For an optimal interelectrode spacing and temperature gradient, the performance of a thermo–tunnel device principally depends upon the work function of electrodes, which can be modified in some materials, such as by terminating the surface of diamond using specific treatments [73,88,92]. A detailed study on the modification of the work function of diamond surfaces using different surface treatments is presented in Chaps. 6 and 7.

As summarised in the introduction (Chap. 1), a number of mathematical models, mostly for cooling applications of the thermo–tunnel phenomenon, have been presented in the literature. These demonstrate that for a small interelectrode separation, a significant output power density in the 10^2–10^3 W.cm^{-2} range is achievable [13, 73, 81]. However, for energy harvesting applications, the thermo-tunnel effect has received a little attention so far [14, 140].

Although the heat removal efficiency of the cooling configurations could approach Carnot efficiency, the efficiency for energy scavenging configurations is calculated to be very small, less than 10% of the Carnot efficiency [14, 140]. It is observed that the choice of physical parameters of a thermo–tunnel device, such as the work function, the interelectrode separation and electrode temperatures, will be critical in terms of impact upon both power output

and efficiency. Hence, for the fabrication of an efficient and power generating thermo–tunnel device, optimisation of geometrical and physical parameters is understood to be a prerequisite, which has yet not been examined to a significant degree. To test the feasibility of the thermo–tunnel device for heat to electricity conversion, this chapter details the function and parameter optimisation of the device configuration shown in Fig. 4.1. Presented mathematical simulations are performed using a code that has been developed with MATLAB.

The basic configuration of the thermo–tunnel device consists of a conducting emitter electrode, a conducting collector electrode, a very small evacuated interelectrode gap, d, and two electrical leads. The distance between the two electrodes can be maintained by use of electrically and thermally insulating pillars. The temperature of the emitter is T_{e}, while the collector is at cold temperature T_{c} ($T_{\mathrm{e}} > T_{\mathrm{c}}$). The work functions of emitter and collector electrodes are ϕ_{e} and ϕ_{c}, respectively.

4.2 Calculation of net thermo–tunnel current

Since the work functions and the temperatures of the electrodes are different, the energy repartition of emitting electrons for each electrode will also be different. Additionally, if the mean free path of electrons crossing from hot to cold or vice versa is greater than the interelectrode spacing, in both directions, the flow of electrons in the interelectrode gap will be nearly unidirectional and the output–current characteristics can be presented in terms of output–current densities. The resultant current density, J_{tot}, for a thermo–tunnel device can be expressed as the difference between the current densities of the emitter and the collector [14, 140],

$$J_{\mathrm{tot}} = J_{\mathrm{e}} - J_{\mathrm{c}}, \tag{4.1}$$

where J_{e} is the electron current emitted from the emitter, while J_{c} is the electron current emitted from the collector.

Calculations of these current densities, and the heat carried by electrons emitted from both electrodes are discussed in following sections.

4.2.1 Emitter contribution

To calculate the total thermo–tunnel (combined thermionic and tunnelling) current between the emitter and the collector, it is necessary to understand the interelectrode potential profile between the two electrodes. For an electron moving from the emitter to the collector, the potential energy, as used previously [14, 75, 78, 79], can be written as

$$V_{\mathrm{e}}(x_{\mathrm{e}}) = \phi_{\mathrm{e}} - \frac{x_{\mathrm{e}}}{d}\left(eV_{\mathrm{bias}} + \phi_{\mathrm{e}} - \phi_{\mathrm{c}}\right) - \frac{e^2}{4\pi\varepsilon_0}\left[\frac{1}{4x_{\mathrm{e}}} + \frac{1}{2}\sum_{n=1}^{\infty}\left(\frac{nd}{n^2d^2 - x_{\mathrm{e}}^2} - \frac{1}{nd}\right)\right], \qquad (4.2)$$

where x_{e} is the distance of an electron from the emitter and e is the electronic charge. The first two terms describe the impact of the bias voltage (V_{bias}) and the work functions of the electrodes, whereas the third term describes the image charge effects [14, 75, 78, 79, 141]. The image charge term is highly sensitive to the choice of the interelectrode separation and its magnitude increases with decreasing d. V_{bias} is calculated as the difference between the electron chemical potential of the emitter (E_{Fe}) and the collector (E_{Fc}). It is worth mentioning here that both E_{Fe} and E_{Fc} are the temperature dependent terms.

The interelectrode separation has a significant impact upon both the magnitude and the shape of the potential energy barrier ($V_{\mathrm{e}}(x_{\mathrm{e}})$) profile. The plot of $V_{\mathrm{e}}(x_{\mathrm{e}})$ vs interelectrode spacing shown in Fig. 4.3 demonstrates that, on reducing d, the height of the potential energy barrier decreases rapidly and the potential energy barrier becomes more strongly peaked. This result is unsurprising, as image charge effects are calculated to be significant at small (< 25Å) interelectrode separations (Eq. 4.2). Low height and narrow width for the potential energy barrier are always desirable in order to enhance the tunnelling of electrons, as these facilitate low energy electrons to tunnel through the resulting potential energy barrier which is classically not possible. Since electrons, whose energies are higher than $V_{\mathrm{e,max}}$, are emitted thermionically, reduction in the height of V_{e} is also helpful in terms of increasing the low temperature thermionic emission.

Fig. 4.4 shows the effect of the work function of the emitter on the potential energy barrier. On increasing the work function of the emitter, the shape of the potential energy barrier becomes asymmetric and the barrier height increases continuously. Equal work function values of the electrodes, regardless of their magnitude, give a symmetric potential energy barrier.

The tunnelling probability that a particle will tunnel through the potential energy barrier

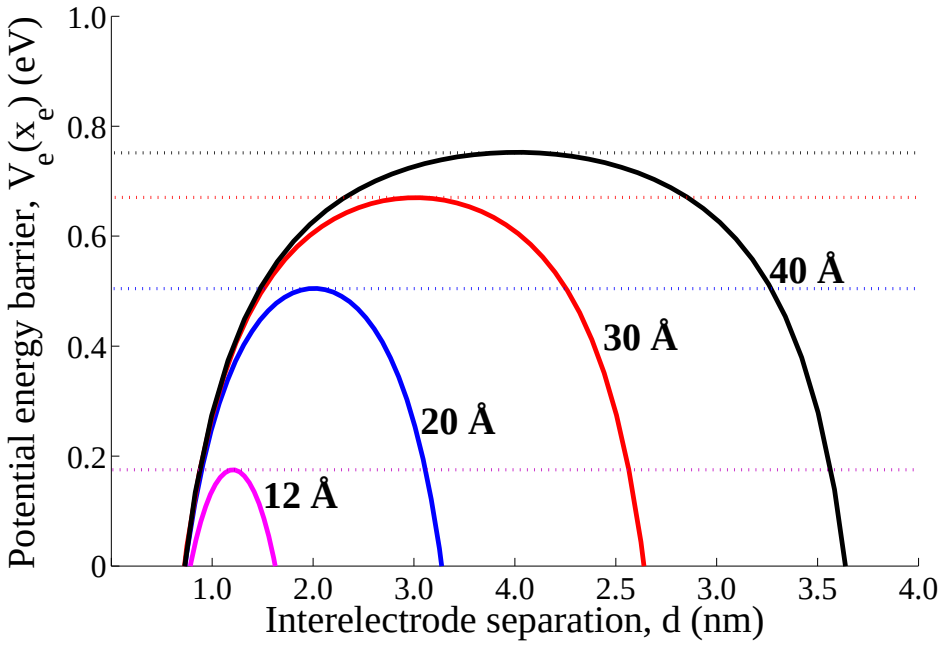

Figure 4.3: Potential energy barriers for an electron moving from the emitter to the collector for different values of interelectrode spacing (d) with ϕ_e=ϕ_c=1 eV and V_{bias}=0 eV. $V_{e,max}$ levels corresponding to each energy barrier are shown in respective coloured horizontal dotted lines.

depends upon the thermal KE, interelectrode potential barrier and its maximum. Using the WKB approximation, the tunnelling probability for the emitter as a function of KE E_x, $V_e(x_e)$ and $V_{e,max}$ can be expressed as

$$\begin{aligned} D_e(E_x) &= \exp\left[-\frac{2}{\hbar}\int_{x_{e1}}^{x_{e2}}\sqrt{2m\left[V_e(x_e)-E_x\right]}\,dx_e\right] \quad \text{if} \quad E_x < V_{e,max} \\ &= 1 \quad \text{otherwise,} \end{aligned} \tag{4.3}$$

where m is the mass of an electron, and x_{e1} and x_{e2} are the roots of the following equation

$$V_{e,max} - E_x = 0. \tag{4.4}$$

Figs. 4.5 and 4.6 show the variation of the tunnelling probability with KE of an electron crossing from the emitter to the collector. The electrons whose KE is greater than $V_{e,max}$ are emitted with the probabilities equal to 1 (*i.e.* 100% transmission). These electrons

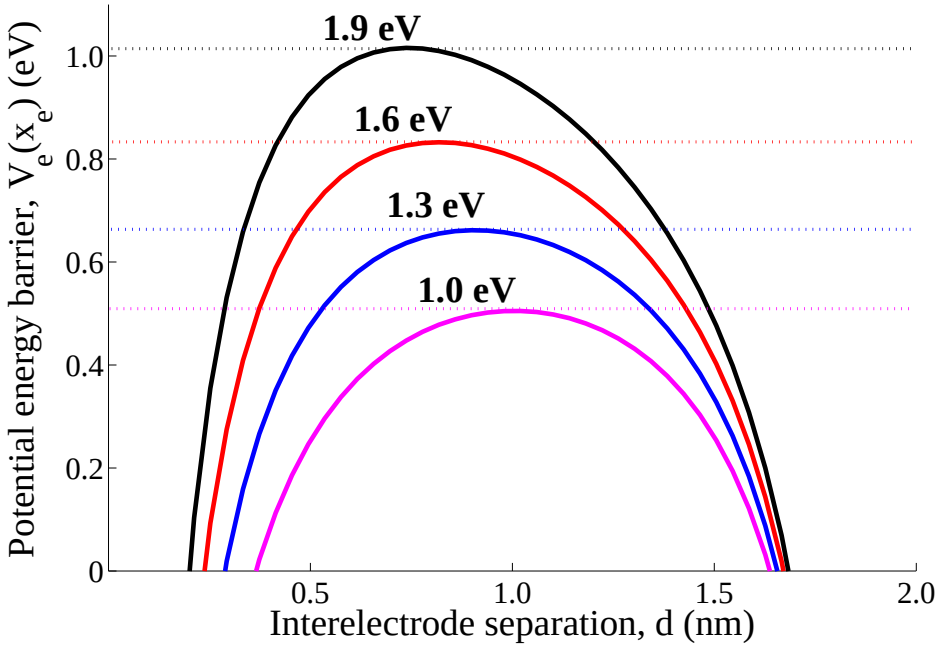

Figure 4.4: Potential energy barriers for an electron moving from the emitter to the collector for different values of the emitter work function (ϕ_e) with V_{bias}=0 eV, and fixed d=20Å and ϕ_c=1 eV. $V_{e,max}$ levels corresponding to each energy barrier are shown in respective coloured horizontal dotted lines.

will contribute to the thermionic current. It is clearly evident from these figures that the reduction in the width and height of a potential energy barrier decreases the threshold KE that is necessary for an electron to be emitted with the tunnelling probability equal to 1. In some cases, for example for 12Å, a nonzero probability is calculated. It can therefore be suggested that to achieve the high tunnelling probability, the interelectrode separation and the electrode work function should be as low as possible.

The total current density, which is a combination of thermionic and tunnelling current can be written analytically as follows

$$J_{etot} = e \int_{-\infty}^{\infty} N_e(E_x) D_e(E_x) dE_x. \tag{4.5}$$

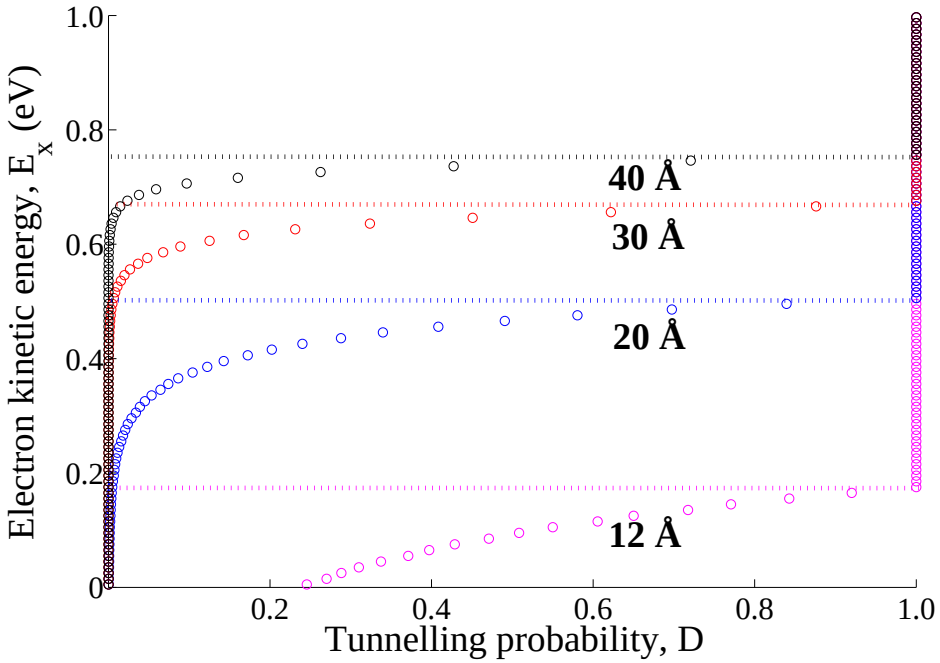

Figure 4.5: Electron tunnelling probability as a function of KE for different inter-electrode separations with $\phi_e = \phi_c = 1\,\text{eV}$ and $V_{bias} = 0\,\text{eV}$. Depiction of coloured lines are similar to those used in Fig. 4.3. Although the tunnelling probability is the dependent variable, to correlate with Figs. 4.3 and 4.4, the tunnelling probability is taken on x–axis.

Hence tunnelling and thermionic contributions can be determined as

$$J_{etun} = e \int_{-\infty}^{V_{emax}} N_e(E_x) D_e(E_x) dE_x, \tag{4.6}$$

$$J_{ether} = e \int_{V_{emax}}^{\infty} N_e(E_x) D_e(E_x) dE_x, \tag{4.7}$$

where $N_e(E_x)$ is the number of electrons per unit area in unit time that can escape from the emitter (hot) and reach the collector (cold) with their K.E. in x–direction in the range from E_x to $E_x + dE_x$.

The $N_e(E_x)$ is calculated using following equation [75]

$$N_e(E_x) = \frac{4\pi m k_B T_e}{h^3} \ln\left[1 + \exp\left(\frac{-E_x}{k_B T_e}\right)\right], \tag{4.8}$$

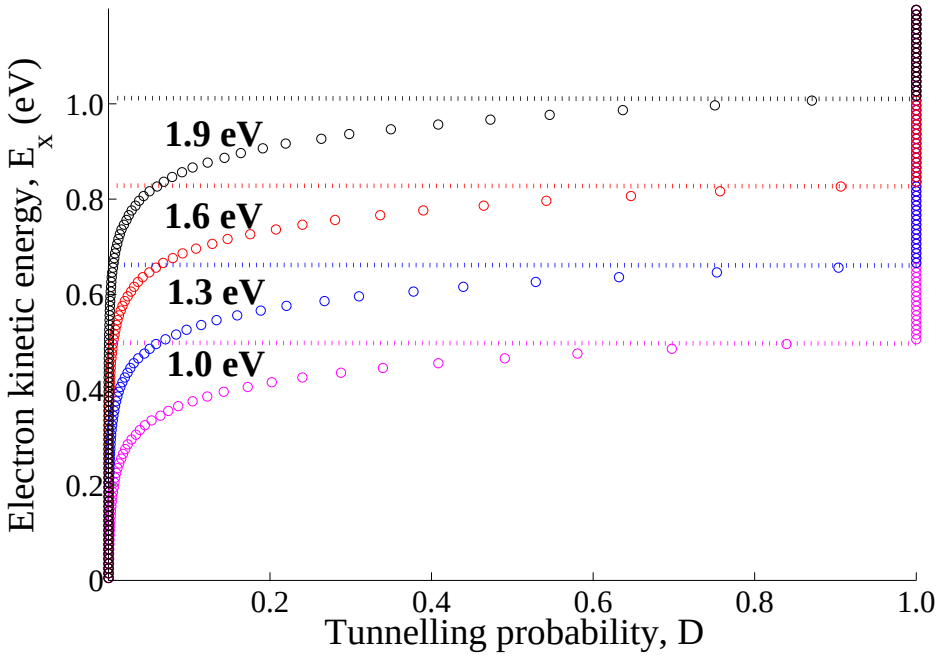

Figure 4.6: Electron tunnelling probability as a function of KE for different values of the emitter work function with d=20Å, ϕ_c=1 eV and V_{bias}=0 eV. Depiction of coloured lines are similar to those used in Fig. 4.4.

where $k_B T_e$ is the average kinetic energy of electrons crossing the gap from the emitter to the collector.

The emitted electrons carry energy from the emitter to the collector, in a process known as emitter–electron cooling. The thermal power density of emitted electrons or emitter electron cooling can be calculated from the following expression

$$Q_e = \int_{-\infty}^{\infty} (k_B T_e + E_x) N_e(E_x) D_e(E_x) dE_x. \tag{4.9}$$

4.2.2 Collector contribution

For most of calculations presented in this chapter, the collector electrode is fixed at 300 K, which is always smaller than that of the emitter. However, due to the tunnelling effect, back emission from the collector could be significant even at such small temperatures, reducing the net output current density and thereby output power density. Following the principle

of Eq. 4.2, the potential energy for the electrons moving from the collector to the emitter can be expressed as

$$V_{\rm c}(x_{\rm c}) = \phi_{\rm c} + \frac{x_{\rm c}}{d}\left(eV_{\rm bias} + \phi_{\rm e} - \phi_{\rm c}\right) - \frac{e^2}{4\pi\varepsilon_0}\left[\frac{1}{4x_{\rm c}} + \frac{1}{2}\sum_{n=1}^{\infty}\left(\frac{nd}{n^2d^2 - x_{\rm c}^2} - \frac{1}{nd}\right)\right], \quad (4.10)$$

where $x_{\rm c}$ is the distance of an electron from the collector.

The tunnelling probability $D_{\rm c}(E_{\rm x})$ for a collector electron, which crosses the interelectrode gap and reaches the emitter, is given by

$$\begin{aligned} D_{\rm c}(E_{\rm x}) &= \exp\left[-\frac{2}{\hbar}\int_{x_{\rm c1}}^{x_{\rm c2}}\sqrt{2m\left[V_{\rm c}(x_{\rm c}) - E_{\rm x}\right]}\,dx_{\rm c}\right] \qquad \text{if} \quad E_{\rm x} < V_{\rm c,max} \\ &= 1 \qquad \text{otherwise.} \end{aligned} \quad (4.11)$$

In eq. 4.11, $x_{\rm c1}$ and $x_{\rm c2}$ are the roots of the equation

$$V_{\rm c,max} - E_{\rm x} = 0. \quad (4.12)$$

The total current density associated with the electrons emitted from the collector is given by

$$J_{\rm ctot} = e\int_{-\infty}^{\infty} N_{\rm c}(E_{\rm x})D_{\rm c}(E_{\rm x})dE_{\rm x}. \quad (4.13)$$

Tunnelling and thermionic contributions can therefore be expressed as

$$J_{\rm ctun} = e\int_{-\infty}^{V_{\rm cmax}} N_{\rm c}(E_{\rm x})D_{\rm c}(E_{\rm x})dE_{\rm x}, \quad (4.14)$$

$$J_{\rm cther} = e\int_{V_{\rm cmax}}^{\infty} N_{\rm c}(E_{\rm x})D_{\rm c}(E_{\rm x})dE_{\rm x}, \quad (4.15)$$

where $N_{\rm c}(E_{\rm x})$ is the number of electrons per unit area in unit time that are emitted from the cold electrode and reach the hot one with their K.E. in x–direction in the range from $E_{\rm x}$ to $E_{\rm x}$+$dE_{\rm x}$.

The calculation of $N_{\rm c}(E_{\rm x})$ is performed by using

$$N_{\rm c}(E_{\rm x}) = \frac{4\pi m k_{\rm B}T_{\rm c}}{h^3}\ln\left[1 + \exp\left(\frac{-E_{\rm x}}{k_{\rm B}T_{\rm c}}\right)\right], \quad (4.16)$$

where $k_{\rm B}T_{\rm c}$ is the average kinetic energy of electrons crossing the gap from cold to the hot side.

The thermal power density or collector electron cooling is then given by

$$Q_{\mathrm{c}} = \int_{-\infty}^{\infty} (k_{\mathrm{B}}T_{\mathrm{c}} + E_{\mathrm{x}})N_{\mathrm{c}}(E_{\mathrm{x}})D_{\mathrm{c}}(E_{\mathrm{x}})dE_{\mathrm{x}}. \tag{4.17}$$

Hence, the net thermal power density Q_{tot} for a thermo–tunnel device can be expressed as the difference between the electron coolings of both electrodes.

$$Q_{\mathrm{net}} = Q_{\mathrm{e}} - Q_{\mathrm{c}}. \tag{4.18}$$

Similar to the conventional design of a thermionic converter, thermal losses may have a significant impact upon the performance of the thermo-tunnel device. It is therefore necessary to include the thermal losses, particularly the conduction and radiation, for accurate modelling of the thermo-tunnel device.

4.3 Calculation of thermal power losses

The interelectrode separations used in this study in the range of 10–50Å is considered to be regulated using thermally and electrically insulating pillars. At very low interelectrode separation, conduction losses will be very high that may influence the output characteristics significantly. In order to maintain the separation and temperature gradient, thin pillars made from very low thermal conductivity material are required. In these calculations, these are assumed to be made of commonly used dielectrics, such as SiO_2 (thermal conductivity = $1.4\,\mathrm{W.m^{-1}.K^{-1}}$), which cover less than 1% (0.01) of the total surface area of the electrodes. The conductive power losses through the pillars can therefore be calculated using the Fourier equation,

$$Q_{\mathrm{cond}} = \frac{0.01k_{\mathrm{p}}(T_{\mathrm{e}} - T_{\mathrm{c}})}{d}, \tag{4.19}$$

where k_{p} is the thermal conductivity of the pillar material ($k_{\mathrm{p}} = 1.4\,\mathrm{W.m^{-1}.K^{-1}}$) [142].

Radiation losses (Q_{rad}) between the emitter and the collector are calculated using the Stefan–Boltzmann equation,

$$Q_{\mathrm{rad}} = \frac{\sigma(T_{\mathrm{e}}^4 - T_{\mathrm{c}}^4)}{(\frac{1-e_1}{e_1}) + (\frac{1}{F_{\mathrm{ec}}}) + (\frac{1-e_2}{e_2})}, \tag{4.20}$$

where σ is the Stefan–Boltzmann constant, e_1 and e_2 the emissivities of the emitter and collector, and F the radiation shape factor, which relates the lateral extent of the emitter

and collector and their separation. In these calculations, for convenience, the emissivities of electrode's surfaces are assumed to be constant, being e_1=e_2=1. The value of F is taken to be 1, which means that the collector surface will receive the maximum amount (100%) of the radiation that has emitted by the emitter surface.

The resultant thermal power–density $Q_{\rm tot}$ transferred from the emitter to the collector can be expressed as.

$$Q_{\rm tot} = Q_{\rm h} - Q_{\rm c} - Q_{\rm loss}, \tag{4.21}$$

where the additional term $Q_{\rm loss}$ is the sum of the radiation and conduction thermal losses for the emitter.

4.4 Thermo–tunnel device operation

Typical behaviour of a thermo–tunnel device is shown in Fig. 4.7. Depending upon the bias voltage, thermo–tunnel devices can be operated in three modes: heating, generating and cooling. When the product of $J_{\rm tot}$ and $V_{\rm bias}$ is negative, this represents the generating behaviour of the thermo–tunnel device desired for energy scavenging.

Although all three modes of operation hold significant potential for a number of applications, in this chapter, only generating behaviour of the thermo–tunnel device is being emphasised. Similar to other solid–state energy–conversion devices, such as solar cells and thermoelectric generators, the maximum power point (MPP) has been calculated (Fig. 4.7). The maximum voltage ($V_{\rm max}$) and the current density ($J_{\rm max}$) can then be estimated, corresponding to the MPP.

The maximum output power density ($P_{\rm max}$) and the efficiency, η, for the thermo–tunnel device can be expressed as

$$P_{\rm max} = J_{\rm max} \times V_{\rm max} \tag{4.22}$$

and

$$\eta_{\rm max} = \frac{P_{\rm max}}{Q_{\rm tot}}. \tag{4.23}$$

The generator behaviour of the thermo–tunnel device has been investigated for different values of the interelectrode separation, work function and electrode temperatures. The dramatic impact of the interelectrode separation and work functions of the electrodes upon the generating regime of the device is depicted in Figs. 4.8 and 4.9, respectively.

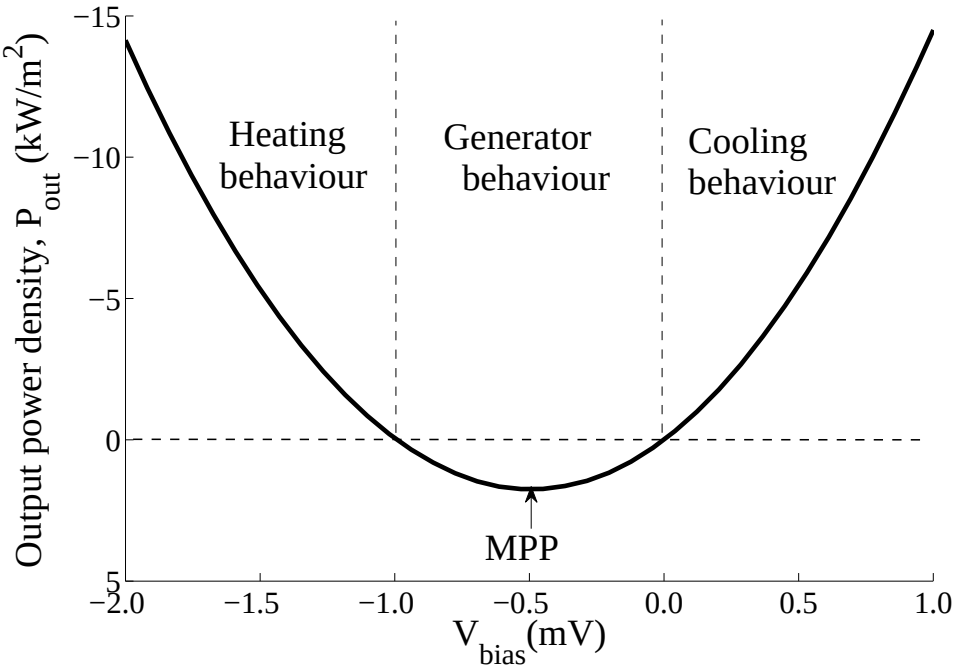

Figure 4.7: Power density as a function of voltage with ϕ_e=ϕ_c=1.0 eV, T_e=310 K, T_c=300 K and d=20Å.

It is interesting to note that although the maximum output power density decreases dramatically with increasing interelectrode separation, the range of voltages within the generating regime has not increased significantly. For example, typical voltage values corresponding to the generating region of 10Å lie in the range between −4.5 and 0 mV, whereas for 15Å, these values range between −7.0 and 0 mV. Calculations suggest that reduction in the image charge effects is responsible for this behaviour. Overall, results indicate that for a large MPP output voltage range, the interelectrode separation should be maximised. In the case of the work function, the voltage range remains nearly constant; however, the maximum power density reduces rapidly.

The generating region of the thermo–tunnel device is found to be highly sensitive to the temperature of the emitter. As shown in Fig. 4.10, increasing the emitter temperature influences both the maximum output power density and the voltage range of the generating regime. At 400 K, a very large MPP output power density of around 10^5 W.m^{-2}, in the voltage range from 0 to 12 V, has been calculated. This power output density is much

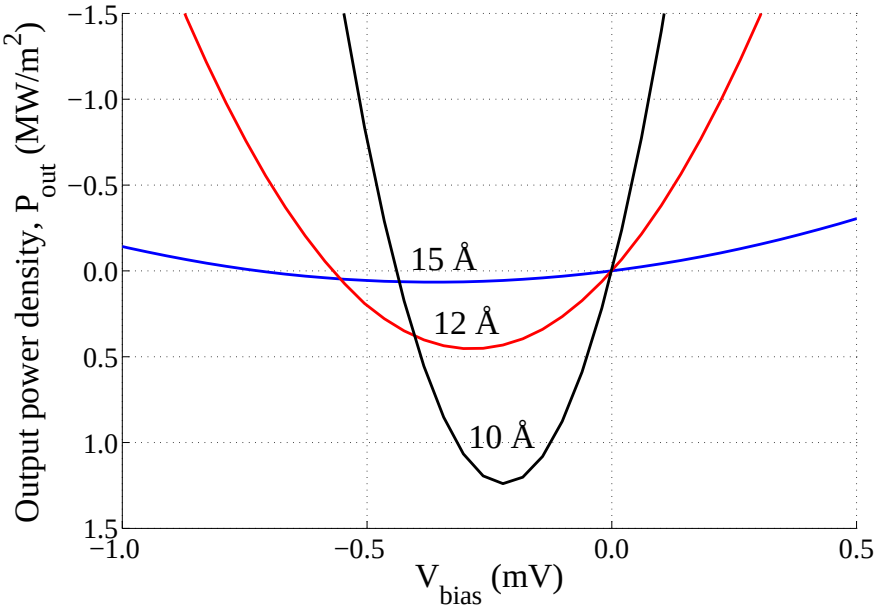

Figure 4.8: Power density as a function of voltage for different values of the inter-electrode separation with ϕ_e=ϕ_c=1.0 eV, T_e=310 K and T_c=300 K.

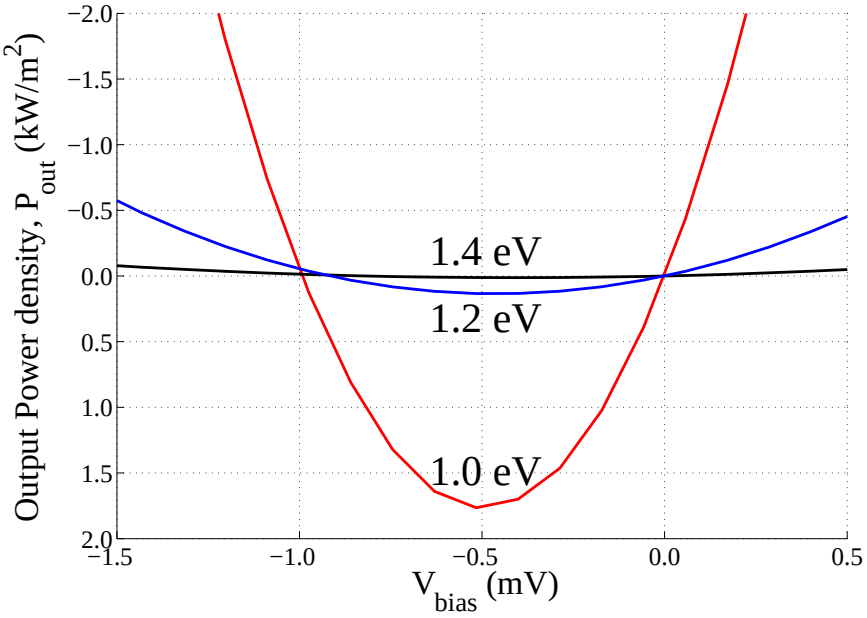

Figure 4.9: Power density as a function of voltage for different values of the work function of electrodes (ϕ_e=ϕ_c=ϕ) with T_e=310 K, T_c=300 K and d=20Å. The values for ϕ are depicted with P_{out} plots.

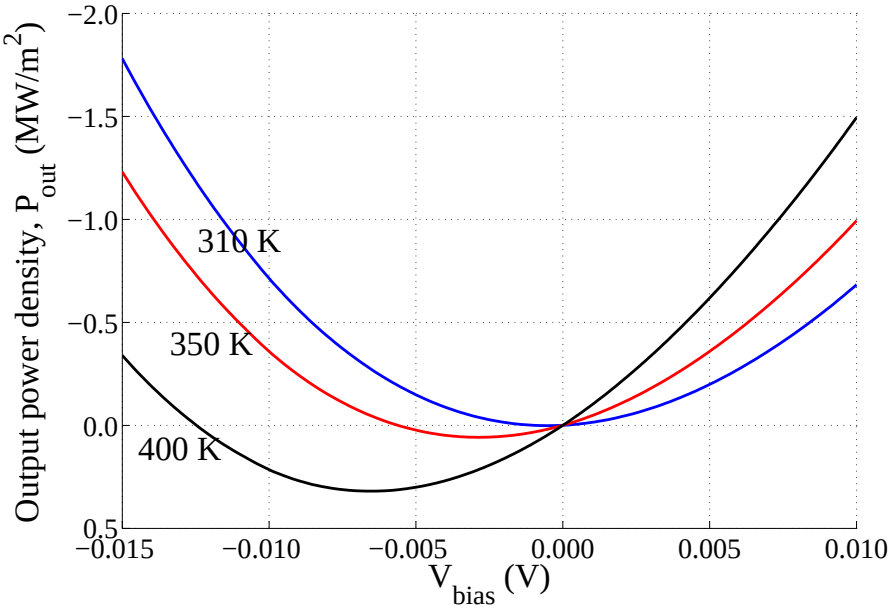

Figure 4.10: Power density as a function of voltage for different values of the emitter temperature with ϕ_e=ϕ_c=1.0 eV, T_c=300 K and d=20Å.

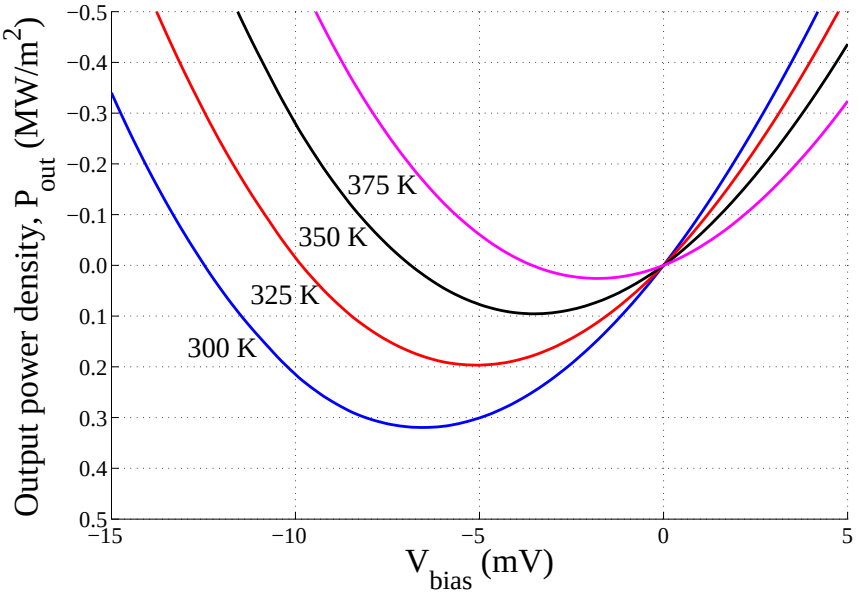

Figure 4.11: Power density as a function of voltage for different values of the collector temperature with ϕ_e=ϕ_c=1.0 eV, T_e=400 K and d=20Å.

higher than 1700 W.m^{-2}, calculated when T_e was fixed at 310 K. The variation in the MPP

power output density and voltage with the emitter temperature is explicable from the fact that the emitter temperature directly influences the thermo–tunnel current and bias voltage.

The MPP output power density and the typical voltage range of generating regime have reduced with increasing collector temperature. However, change in the collector temperature does not affect the order of magnitude of $P_{\max}$. Fig. 4.11 shows that the maximum output power density reduces from -0.31 to $-0.01\,\mathrm{MW.m^{-2}}$, as the collector temperature increases from 300 to 375 K. At moderately high collector temperatures, for example at 350 and 375 K, back emissions are calculated to be significant, reducing the net output current density.

4.5 Effect of physical parameters on the output characteristics

The efficiency of the thermo–tunnel device as a function of emitter temperature, interelectrode separation and electrode work functions is shown in Figs. 4.12, 4.13 and 4.14. For a small value of interelectrode separation, for example 10Å, the efficiency of the thermo–tunnel device has increased continuously from 0 to ≈1.3% in the emitter temperature range from 301 to 700 K, compared to 57% Carnot efficiency. In contrast, for large value of the interelectrode separation, for example 23Å, the efficiency has increased from 0 to ≈12% in similar temperature range.

It is notable that in low temperature ranges of the emitting electrode, for example from 301 to 400 K, the efficiency increases very slowly with increasing interelectrode separation. However, in high temperature range (400–700 K), a drastic change in the efficiency is observed when the interelectrode separation is varied from 10 to 23Å. For example, at 700 K, the difference in the heat conversion efficiencies for 10 and 23Å is around 10.5%, while in low temperature range (300–400 K), this difference is smaller than 2%. Significant thermionic electron emission in high temperature range is found to be accountable for such behaviour.

Overall, the heat conversion efficiencies corresponding to small vacuum gaps and temperature gradients are found to be very small. To compete with the typical efficiency range (5–8%) of TEGs, a thermo–tunnel device with the vacuum gap in the 15–25Å range must operate in the 600–700 K temperature range. It is important to mention here that in a previous study [14], the maximum efficiency of a thermo–tunnel device for a temperature

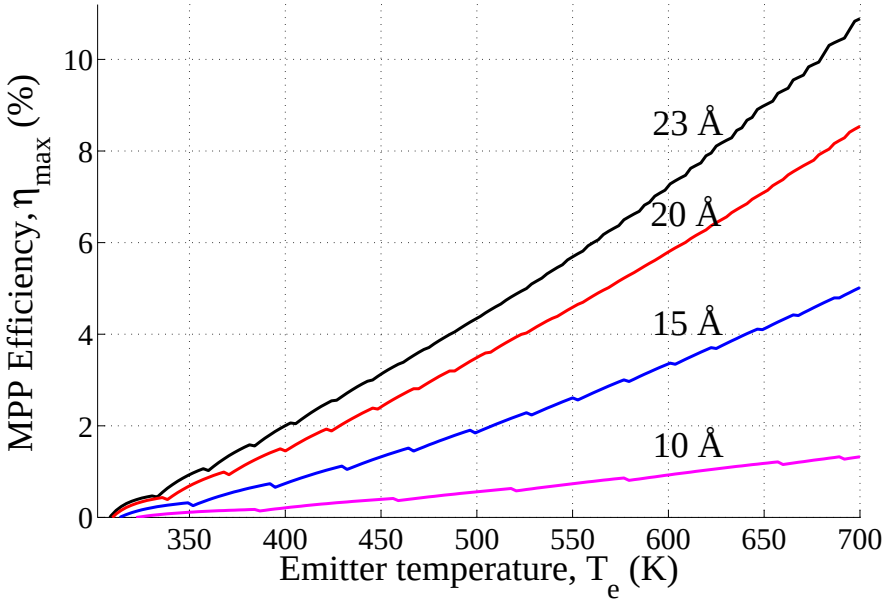

Figure 4.12: Dependence of the MPP efficiency on the interelectrode separation when ϕ_e=ϕ_c=1 eV and T_c=300 K.

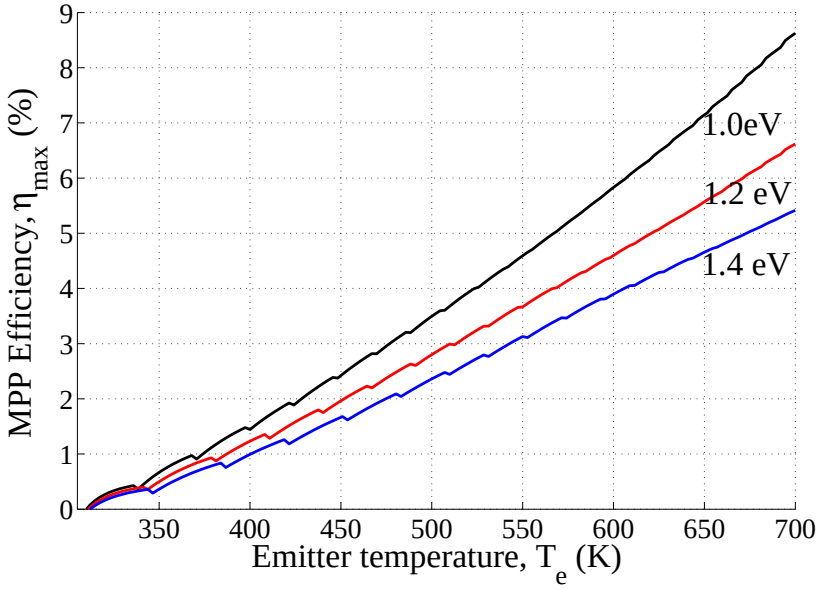

Figure 4.13: Dependence of the MPP efficiency on the electrode work functions (ϕ_e=ϕ_c=ϕ) when T_c=300 K and d=20Å. The values for ϕ are shown with η_{max} plots.

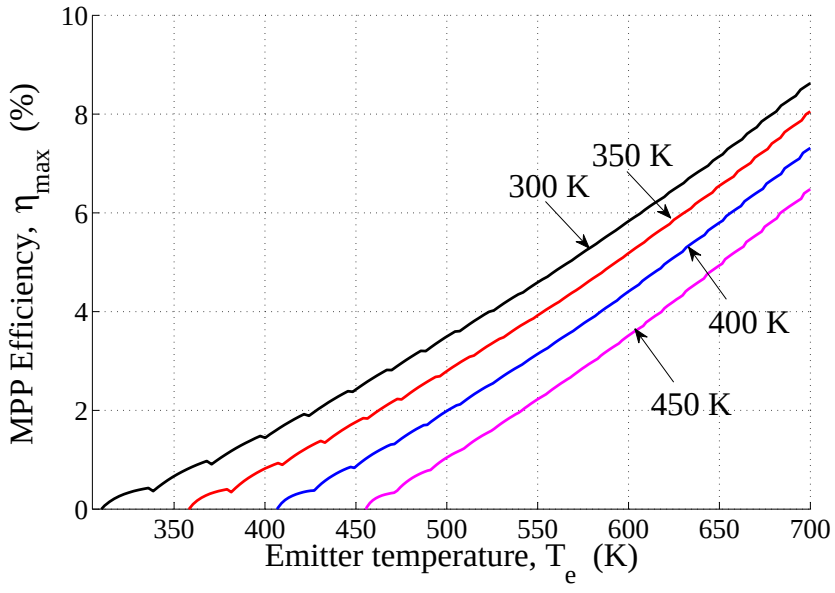

Figure 4.14: Dependence of the efficiency on the collector temperature when ϕ_e=ϕ_c=1 eV and d=20Å.

difference of 10 K was 0.34% for d=25Å. This value has been reproduced in these calculations and for a temperature difference of 300 K, improved efficiency of around 8.5% has been calculated, emphasising the importance of the temperature difference on the operation of thermo–tunnel devices.

Fig. 4.13 shows that the efficiency of the thermo–tunnel device decrease continuously with increasing electrode work function. Although increasing the work function of the electrodes has a small impact upon the optimum operating voltage, the output power density has reduced significantly. It has been suggested in a previous study [73] that for an efficient thermal energy conversion, the work function of the electrodes should be as small as possible. This is indeed supported by the current simulation findings (Fig. 4.13), where the maximum efficiency reduces with the electrode work function.

In the above mentioned efficiency calculations, the temperature of the collector is fixed at 300 K. However, change in the collector temperature is likely to affect the output power density of the thermo–tunnel device by increasing the collector current and reducing the thermal losses (Fig. 4.11). Calculations show that increasing the collector temperature

results in significant back emission, which further reduces the heat conversion efficiency. The MPP efficiency as a function of the collector temperature, is shown in Fig. 4.14.

As shown in Fig. 4.15, because of the high thermo–tunnel current density at small d, the MPP output power–density is predicted to be rather large which further increases with increasing the emitter temperature. Similar to the trend of the MPP efficiency (Fig. 4.12), in the 301–375 K temperature range for the emitter, the differences in the output power densities corresponding to different interelectrode separations are rather small than those calculated for high emitter temperature ranges. These results are consistent with the data in Fig. 4.8, where the output power density is small at large interelectrode separation. Furthermore, as discussed earlier (as shown in Fig. 4.9), due to the impact of electrode work function upon the MPP current density, and rather smaller impact upon the MMP voltage, the MMP output power density reduces with increasing the work function.

In line with the efficiency as shown in Fig. 4.14, an increment in the collector temperature increases the collector current and thus reduces the output current and MPP power density.

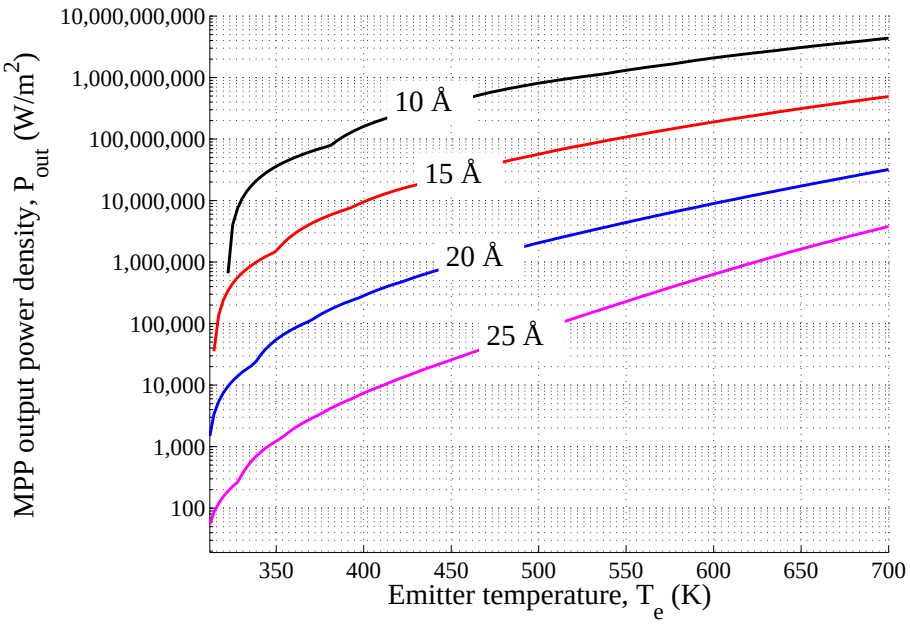

Figure 4.15: The MPP output power density as a function of the emitter temperature for different values of interelectrode separation with ϕ_e=ϕ_c=1 eV and T_c=300 K.

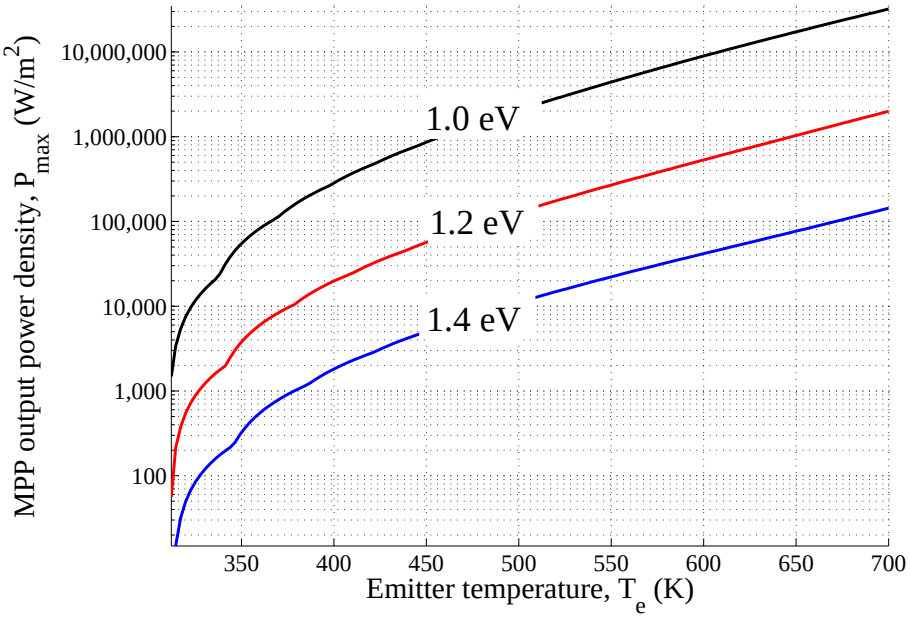

Figure 4.16: The MPP output power density as a function of the emitter temperature for different values of the work function of electrodes (ϕ_e=ϕ_c=ϕ) with T_c=310 K and d=20Å. The values for ϕ are given with P_{max} plots

.

Impact of T_c upon MPP output power density is illustrated in Fig. 4.17.

4.6 Chapter summary

In summary, mathematical simulations have been performed to investigate the impact of physical parameters upon the generating behaviour of the thermo–tunnel device. It is found that upon increasing the interelectrode separation and the emitter temperature, the efficiency of the thermo–tunnel device increases. In contrast, the output power–density rapidly decreases with increasing electrode separation. An increase in the work–function of the electrodes has an adverse impact upon both the output power–density and efficiency. Results suggest that under optimised conditions, a large output power–density in the 10^4–10^6 W.m^{-2} range, with efficiency in the range $\sim$ 8–12%, can be achieved via a thermo–tunnel device. The values for the interelectrode separation in the 1.5–2.5 nm range and the work function between 1.0–1.3 eV are found to be suitable for a high power efficient thermal energy con-

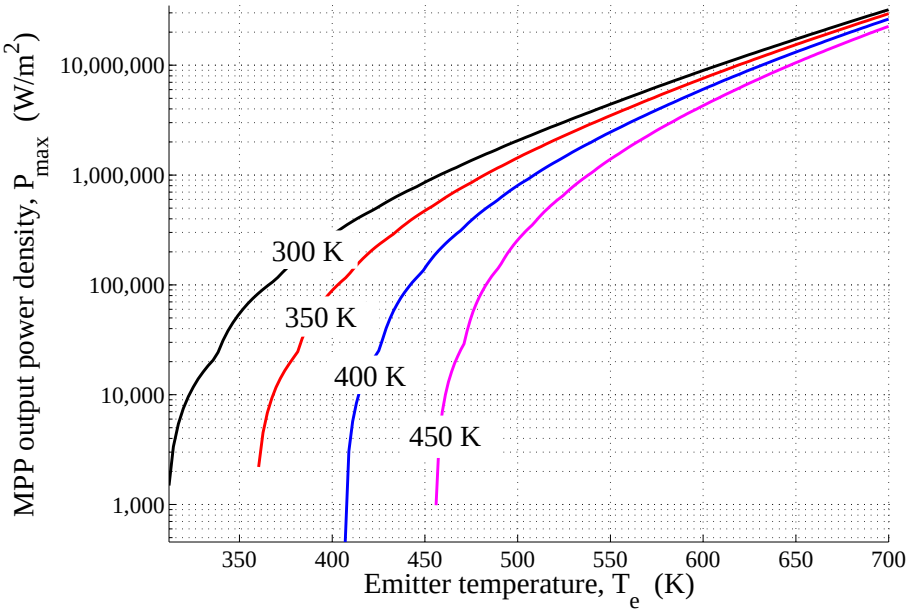

Figure 4.17: The MPP output power density as a function of the emitter temperature for different values of the collector temperature with ϕ_e=ϕ_c=1 eV and d=20Å.

version via a thermo–tunnel device. Although high collector temperature increases the back emission significantly, the order of magnitude of the MPP output power density remains unchanged.

The typical voltage range of the generating regime is found to be highly sensitive to the choice of physical parameters. However, the MPP voltage of a single thermo–tunnel device is still small; in most cases it lies in the millivolt range. Since thermo–tunnel devices yield a exceptionally high output power density, similar to TEGs and PV cells, a cascade configurations of thermo–tunnel devices that are capable of producing a moderately high voltage (a few volts) could be of significant interest for various applications, including wireless sensor networks and macro–scale power generation. Designing and integration of nano–gap thermo–tunnel devices in to a module are major technological obstacles that will require time and further engineering advancements.

In this model, the temperature dependence of the physical parameters, particularly, the work function, has not been considered. In the case of diamond, the work function of diamond decreases with increasing temperature ($\approx 8\times10^{-4}$ eV/K in the temperature range

from 370 to 650 K) [143]. Although the thermal expansion (volumetric) coefficient for the diamond is very small ($\approx 3\times10^{-6}/\,^{\circ}\mathrm{C}$) [142], it may also have an impact upon the inter-electrode spacing. Given the data scarcity in literature and uncertainty in experimental determination of the work function, inclusion of temperature induced effects has little physical meaning in the modelling of a thermo–tunnel device. Nevertheless, it is expected that for a regulated interelectroode vacuum gap, reduction in the work function will improve the performance of the thermo–tunnel device by increasing $P_{\max}$ and $\eta_{\max}$.

The results presented in this chapter, which are obtained for an ideal thermo–tunnel device structure, may show a quantitative deviation with the output characteristics of a real device. However, this investigation has been reasonably successful in highlighting the importance of those physical parameters, which will have a critical impact upon the output characteristics of a real thermo–tunnel device.

Another critical parameter in the realisation of an efficient and high power thermo–tunnel device is the requirement of low work function (ideally 1 eV) electrodes. The most commonly used CsO coated W electrodes in the conventional designs of thermionic converters yield low emission currents due to high work function values and therefore less preferable in the context of the thermo–tunnel device. Importantly, radiation resilience and toxicity are some vital issues associated with CsO coated W electrodes, which limit their use for devices operating in hostile and closed environments. Diamond is an obvious candidate to overcome all these shortcomings and its work function can be reduced significantly using specific dopants and surface treatments. In Chaps. 6 and 7, the results of *ab initio* simulations are presented for different diamond/adsorbate structures, in order to explore a surface termination, which is thermally stable and able to reduce the work function diamond to a suitable value.

Chapter 5

Bulk diamond and its low index surfaces

You cannot teach a man anything; you can only help him discover it in himself.

Galileo Galilei (1564–1642)

5.1 General properties of diamond

Diamond, an allotrope of carbon, is a wide band gap representative of the elemental semiconductors. The experimental band gap of the bulk diamond at room temperature (300 K) is measured to be 5.48 eV, comparable to room temperature band gaps of wide band gap III–V compounds (*e.g.* boron nitride: 5.5–6.5 eV and aluminium nitride: 6.28) and much higher than those of more common group IV semiconductors, Si (1.1 eV) and Ge (0.67 eV) [87,142]. Although, in comparison to conventional narrow and wide bandgap materials, such as Si, Ge and SiC, synthetic diamond is extremely difficult to grow, recent advances in CVD process and surface engineering have allowed diamond to become commercially viable for a wide range of technological applications, including optical windows, piezoresistive sensors, heat sinks, radiation detectors and electrochemical sensors [86, 87, 144–147].

Diamond possesses a remarkable range of optical, thermal and electrical properties [86, 87, 144]. It is transparent over a wide wavelength range from the near–ultraviolet, through the visible, to the far–infrared (up to 100 μm) and exhibits a superlative thermal conductivity (20 $\mathrm{W.cm^{-1}.K^{-1}}$) at room temperature [87]. The refractive index of diamond is measured to be 2.4, which is significantly higher than that of the glass ($\approx$ 1.4–1.95) [87,142]. In addition to the high static dielectric constant (5.70) and high intrinsic breakdown field (10 $\mathrm{MV.cm^{-1}}$),

diamond has very high carrier mobilities (μ_n=2200 $cm^2.V^{-1}.s^{-1}$, μ_p=1600 $cm^2.V^{-1}.s^{-1}$) at room temperature [87]. Due to strong C–C bonds and atomic arrangements, diamond is the hardest among all the naturally occurring terrestrial materials (Knoop scale: 8000 and Mohs scale: 10 Mohs), making it an attractive abrasive material for industrial applications [148].

5.2 Bulk diamond structure

The crystal structure of the bulk diamond is a face–centred cubic (FCC) Bravais lattice with a basis of two carbon atoms at positions: (0, 0, 0) and $(a_0/4)(\hat{x} + \hat{y} + \hat{z})$, where a_0 is the lattice constant of diamond. The diamond lattice can be considered equivalent to two interpenetrating FCC lattices, separated from one another along the body diagonal of cubic cell by one quarter the length of the diagonal. A non–primitive cubic unit cell and the (001) oriented lattice of the bulk diamond are shown in Fig. 5.1 and Fig. 5.2, respectively.

Using local density approximation and the basis sets that consist of independent sets of *s*–, *p*– and *d*– Cartesian Gaussian functions of four widths amounting to 40 functions per atom, the side length a_0 of a conventional cubic unit cell of diamond is calculated to be 3.53Å. The calculated lattice constant is around 1% smaller than the experimental value of 3.56Å; however, this is in very good agreement with previous LDA calculations (less than 0.5% difference) [18–21, 135]. Since the conventional unit cell of diamond consists of the equivalent of 8 carbon atoms, the atomic number density is therefore $8/a_0^3 \approx 1.76 \times 10^{23} cm^{-3}$. The calculated C–C bond length and ∠C–C–C for bulk diamond structure are found to be 1.54Å and 109.5°, respectively, which agree well with the reported values (only 0.3% variation) [18, 144, 149]. The calculated

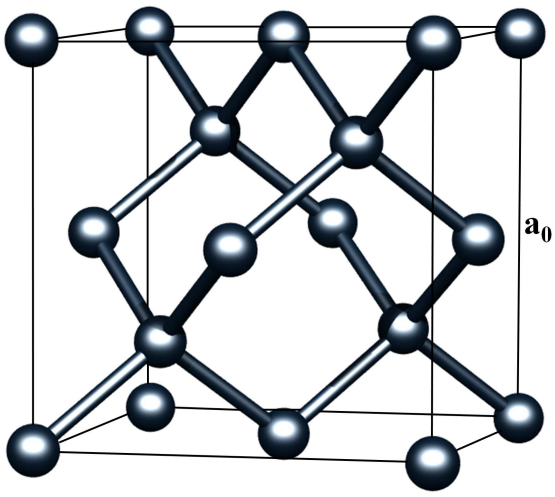

Figure 5.1: Ball and stick model of a conventional unit cell of diamond, where a_0=3.57Å is the experimental cubic lattice parameter at 300 K.

mass density of diamond, a product of atomic number density and average atomic mass of the C atom, is 3516 kg.m^{-3}, which is in good agreement with the experimental value of 3515.25 kg.m^{-3} [150].

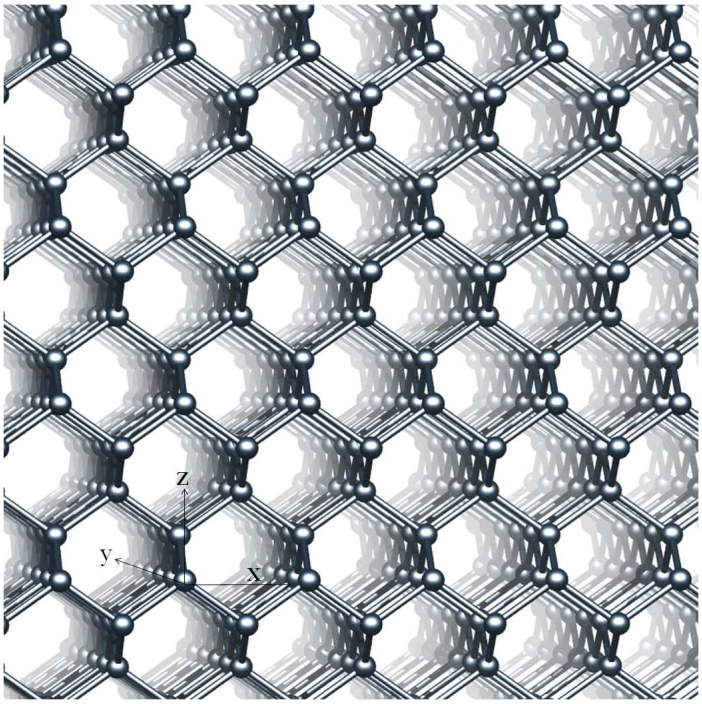

Figure 5.2: Perspective view of a (001) bulk diamond lattice.

The electronic band structure and electrostatic potential variation for the bulk diamond lattice are shown in Fig. 5.3. Experimentally, at room temperature, the indirect band gap of diamond varies in the 5.45–5.55 eV range [87, 151]. However, the calculated indirect band gap in this work is found to be 4.22 eV, $\approx$ 24% smaller than the experimental value. Underestimation of the positions of excited states in DFT calculations has been documented previously for different materials, including diamond, and the difference between two values is found to be consistent with previous LDA–DFT calculations [19, 20, 134, 135].

5.3 Diamond doping

A pure diamond is an excellent insulator of the electricity (10^{16}–10^{18} Ω.m) at room temperature [142] and therefore in order to be used in electronic applications, it requires doping so

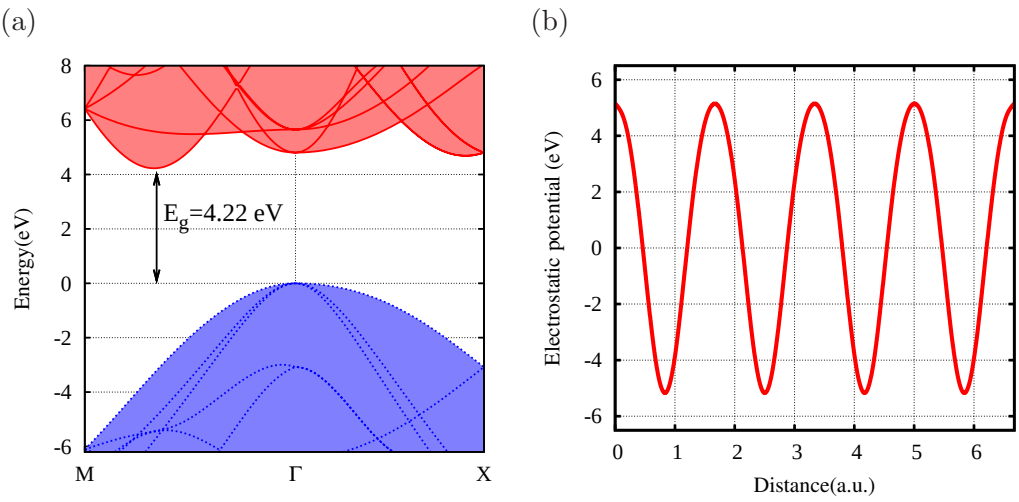

Figure 5.3: (a) Calculated electronic band structure and (b) the electrostatic potential of bulk diamond, using 8 atom unit cell and a lattice parameter 6.68 a.u..Occupied and empty electronic states corresponds to the valence and conduction bands are shown in blue and red lines, respectively.

that electrons can move freely. Doping of the diamond lattice to achieve an efficient *p*–type material is rather easy [152–154]. However, unlike other semiconductors, such as Si and Ge, to create an efficient *n*–type diamond is extremely difficult [155–157].

Unlike Boron, which is a widely used shallow acceptor (activation energy: 0.37 eV), most *n*–type dopants are either deep donors or have very low solubility [157]. For example, substitutional nitrogen, which is the most common impurity in diamond, is a deep donor (donor activation energy of 1.6–1.70 eV) [155–158].

Substitutional phosphorus has been successfully used to produce donor levels with an activation energy of 0.60 eV at 400 K [154, 157, 159]. However, due to the large enthalpy of formation, which implies limited solubility, phosphorus is of lower technological importance [154]. The enthalpy of formation for phosphorus in diamond is calculated to be around 6–11 eV, much higher than 1.13 eV of B [154,157], resulting from the large difference between the covalent bond radius of P (1.06Å) and C (0.77Å).

In recent years, several promising suggestions have been proposed including substitutional pnictogen (As and Sb), chalcogen (S, Se and Te), their complexes, Co and other defects such as N_2–H and N–Si_4 [155, 157, 160, 161]. Research has also been centred on

ion implanted alkali metals, such as Li and Na [162–164]; however, the use of diamond for commercial p–n junction–based devices has not been possible to date.

5.4 Low index diamond surfaces: electronic and structural properties

Because of the possibilities of efficient electron emission at low temperature and the transfer doping phenomenon, diamond surfaces have recently attracted significant attention for a wide range of electronic applications [23, 97, 165–169]. Importantly, modification of the electronic properties of the diamond using different surface treatments is a rather easier process than the doping. As a consequence of the way in which diamond crystal grow during the CVD process, the most technologically relevant low index surfaces are those with (001), (111) and (110) orientations [87, 149]. All three surface orientations are described consecutively in following sections.

5.4.1 (100) surface

Due to its low defect density, the (001) grown surface is important in diamond technology. Importantly, it can be selectively grown under controlled growth conditions [87, 149]. An ideal unrelaxed diamond (001)–1×1 surface, as shown in Fig. 5.4, comprises two dangling bonds per surface carbon atom. This is highly unstable and undergoes a reconstruction into a 2×1 geometry by forming a π–bonded dimer with neighbouring atoms [170, 171]. Present calculations show that a reconstructed 2×1 geometry [Fig. 5.5 (a)] is more stable than the 1×1 geometry by around 1.52 eV per surface carbon atom.

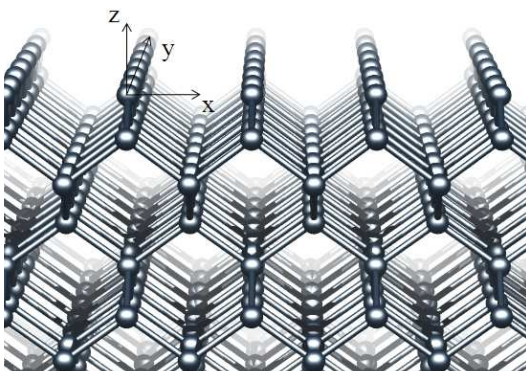

Figure 5.4: Perspective view of a clean 1×1–(001) diamond surface.

As a repercussion of underlying strain effect, a reconstructed 2×2 geometry (combination of alternate dimers) is also less stable and does not represent the ground state. The reconstructed 2×1 surface is also preferred upon hydrogenation, with each surface carbon

forming three C–C single bonds and one C–H bond, as shown in Fig. 5.5 (b) [17, 172].

(a)2 × 1–(100) clean (b) 2 × 1–(100) H–terminated

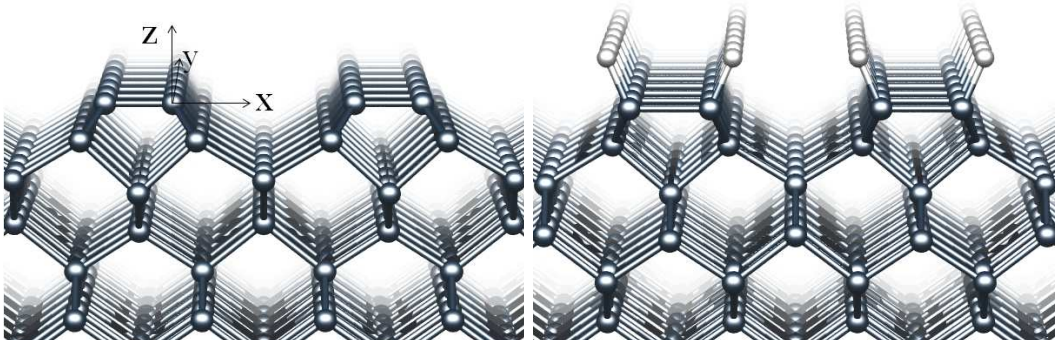

Figure 5.5: Perspective views of the (a)reconstructed 2 × 1 clean and (b)hydrogenated diamond (100) surfaces.

Structural properties, such as bond lengths and layer separations (with arrows), for the clean and hydrogenated 2 × 1 diamond (100) surfaces are shown in Fig. 5.6. The typical surface dimer C–C bond length for the clean (100) diamond is ≈1.37Å, which is somewhat bigger (≈2%) than 1.34Å of C=C double bonds. The slab used in the simulations of terminated diamond surfaces is adequately thick and closely represents the bulk diamond in the middle, as for both clean and hydrogenated diamond surfaces, the C–C bond lengths (1.53Å) in the middle of the slab are equal to those found in the bulk diamond. The clean 2 × 1 surface, where the surface dimers are separated from each other by $a_0 0/\sqrt{2} \approx 2.52$Å is found to be non–metallic in nature.

Fig. 5.7 shows the band structures of the clean and hydrogenated 2 × 1 diamond (100) surfaces. These band structures are plotted for $M(0.5,\ 0.5,\ 0)$–$\Gamma(0,\ 0,\ 0)$–$X(0.5,\ 0,\ 0)$ direction. For a reconstructed clean 2 × 1–(100) surface, the dimer states [Fig. 5.7(a)], which originate from π and π^*–like wave functions [Fig. 5.8 (a)] of surface C atoms, lie in the band–gap just above the valence band maxima and about the midgap, respectively. In the case of H–termination, there are no bands in the band gap and due to the effect of C–H surface dipoles, the entire band structure [Fig. 5.7(b)] is being shifted upwards with respect to the clean surface by about 2.5 eV. The catenary–shaped unoccupied states at 0 eV around the zone centre (Γ) [Fig. 5.7 (b)], are free–electron–like states, although some of them are found to be associated with the surface states [144].

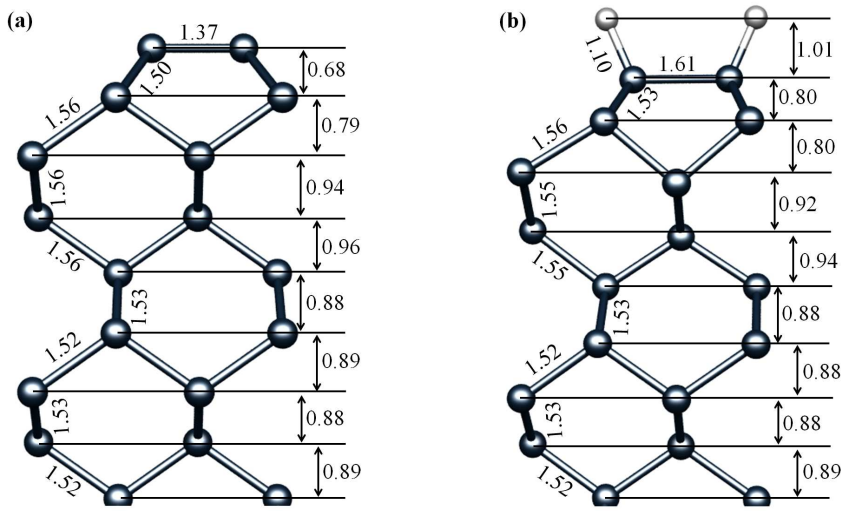

Figure 5.6: Reconstructed (a) C– and (b) H–terminated (001)–(2 × 1) diamond surfaces. Labelled lengths are in Å.

The χ_s for the clean and the hydrogenated 2 × 1–(001) diamond are calculated to be 0.61 and 1.96 eV, respectively, which are consistent with previous theoretical studies [18, 19, 21, 135]. For a clean 2 × 1 surface, the agreement between the current calculations for χ and the experimental values is very good, being within 5%. However, the difference in the theoretical and experimental values of χ for a H–terminated surface is significant, ≈46%. The difference between two values is explicable from the fact that a 100% H–terminated diamond surface is extremely difficult to obtain in practice and the presence of surface impurities (–O, –OH), even in small proportions, can significantly increase χ [144]. The calculated χ_s and adsorption energies for low index stable clean and H–terminated surfaces are listed in Table. 5.1.

Passivation of an unreconstructed surface by two hydrogen atoms per surface site is less energetically favourable [17, 18]. For the hydrogenation of unreconstructed 1 × 1 surface, there are two most plausible configurations: symmetric and canted, as shown in Fig. 5.9 (a) and (b). Calculations show that due to small repulsion between hydrogen atoms, the canted arrangement is more energetically favourable than the symmetric one, by around 0.22 eV per surface H atom.

Oxygen terminated diamond (100) surfaces were also examined briefly in this work. For

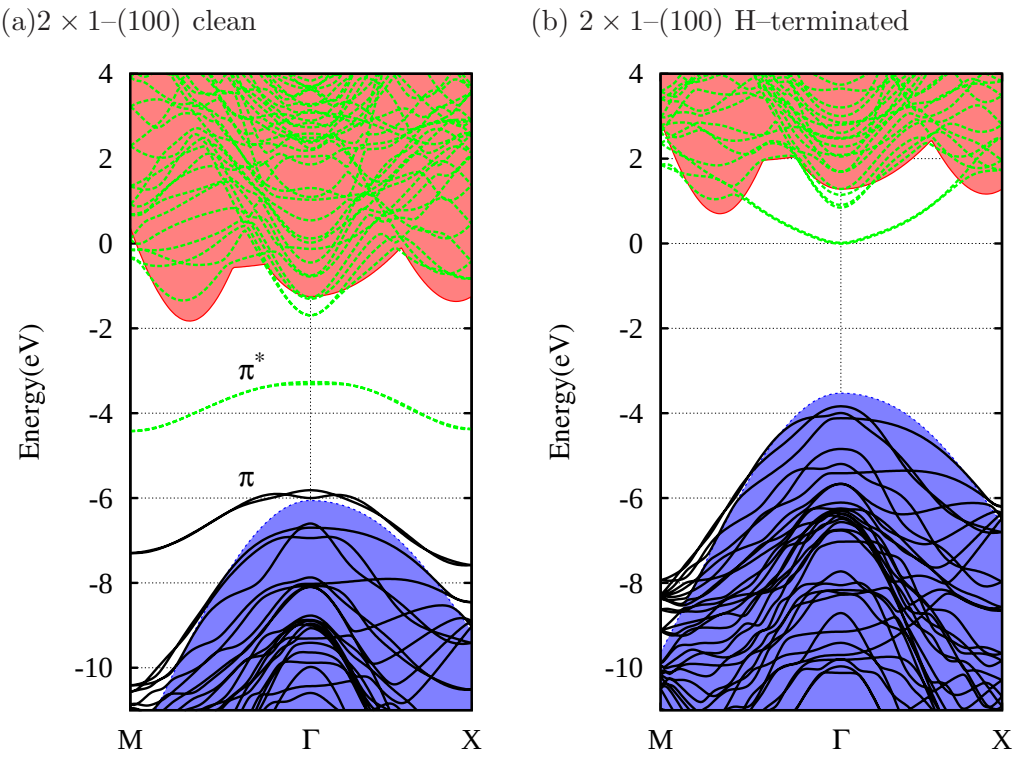

Figure 5.7: Electronic band structures of (a) clean and (b) hydrogenated (001)–(2 × 1) diamond surface. Occupied (black) and empty (green) states of clean and terminated diamond are superimposed upon the bulk, shown as the shaded (blue and red) regions. The zero of the energy scale is the vacuum potential for each system.

an oxygen atom adsorption onto a diamond (100) surface, there are two known surface arrangements: keto and ether (bridge). In the keto configuration, an oxygen atom is linked to a surface carbon atom by a double bond, while for the ether configuration, every oxygen atom forms two single bonds with two surface C atoms. Calculations show that the ether configuration is more stable than the keto configurations, by 0.60 eV per oxygen atom. Reaction of oxygen with the diamond surface is observed to be highly exothermic, indicating that the O–termination will be more thermodynamically stable than H–termination, although the difference in thermal stability of two surfaces is not significant [21, 135].

For both configurations, the C–O bond lengths (ether:1.48Å, keto:1.19Å) and C–O–C bond angle (ether:115.2°) agree with the literature values [17,135]. Moreover, consistent with

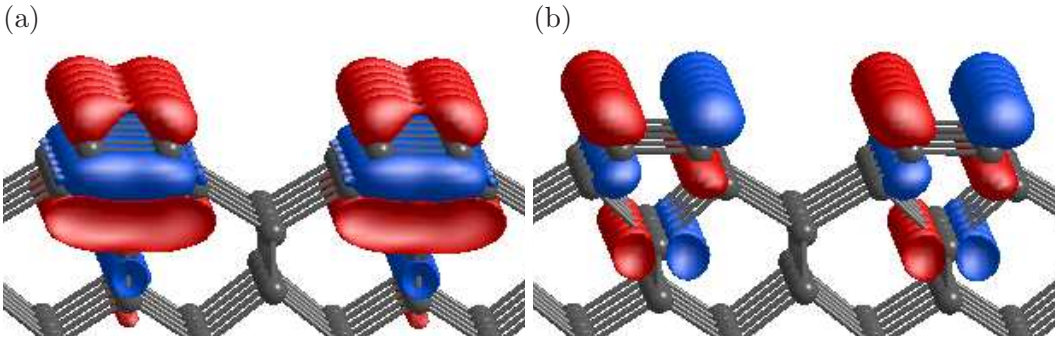

Figure 5.8: Plot of the wave function iso–surfaces corresponding to the (a) occupied π and (b) unoccupied π^* states [Fig. 5.7 (a)] of a reconstructed clean 2×1 surface. Opposite signs of the wave function iso–surfaces are depicted using red (+) and blue (−) colour volumes.

Table 5.1: Calculated electron affinities (eV) of low index clean, oxygenated and hydrogenated diamond surfaces. Typical literature values for calculated [17–21] (column marked with †) and experimentally obtained [22–25] electron affinities are given for comparison.

Orientation	Termination	E_{ads}	Theory	Theory†	Expt
(001)-(2 × 1)	clean	–	+0.61	+0.64	+0.50
(001)-(2 × 1)	H	2.17	−1.96	−1.90	−1.30
(001)-(1 × 1)	O(ether)	5.37	+2.63	+2.73	+1.70
(001)-(1 × 1)	O(keto)	4.76	+3.91	+3.64	–
(111)-(1 × 1)	clean	–	+1.37	–	–
(111)-(1 × 1)	H	2.78	−2.01	−1.97	−1.65
(111)-(2 × 1)	clean	–	+0.32	+0.35	+0.38
(111)-(2 × 1)	H	1.03	−2.19	–	–
(110)-(1 × 1)	clean	–	+0.91	+0.90	+0.70
(110)-(1 × 1)	H	1.96	−2.41	−2.40	−1.10

(a)1 × 1–(100): H (canted) (b) 1 × 1–(100): H (symmetric)

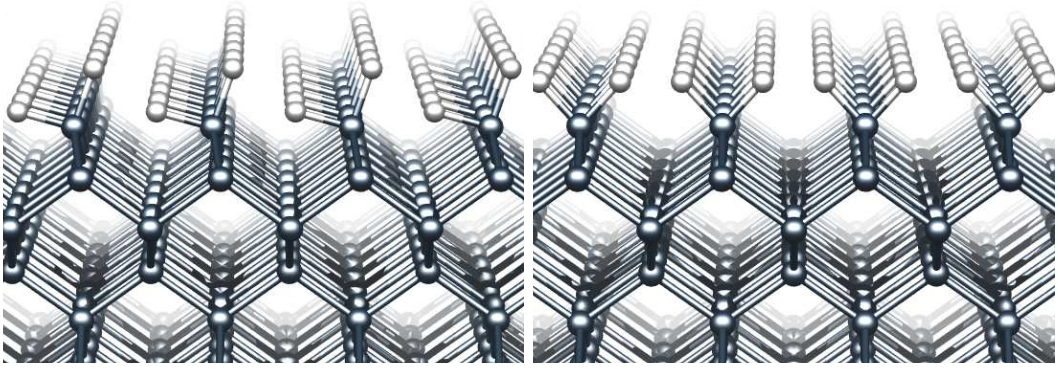

Figure 5.9: Perspective views of (a) canted and (b) symmetric configurations for 2H termination of 1×1 diamond (100) surface. Depiction of axes is similar to those shown in Fig.5.6

the difference in atomic geometry, χ of the keto configuration is more positive in comparison to that of the ether one. It is reported previously [144] that for the equal amount of charge transfer from C to O atoms, keto configuration exhibits a greater z–component of the surface dipole electric field with respect to the bridge configuration and therefore yields a larger χ .

5.4.2 (111) surface

The (111) orientation, a natural cleavage plane, is an important growth plane for CVD diamond [87, 149]. The diamond (111) surface can be constructed with either one or three dangling bonds per surface atom, where the the tri–radical surface is found to be much higher in energy [173].

The clean (111) diamond surface can be reconstructed into several surface geometries [173], and the so called Pandey–chain π–bonding reconstruction [174] with a 2×1 periodicity [Fig. 5.10 (a)] is widely accepted as being the most stable. Other geometries, such as the Seiwatz single–chain, Chadi π–bonded molecule and the hollow (H) site trimer models are found to be less energetically stable [173]. Due to unsaturated surface carbon bonds, the 1×1 geometry [Fig. 5.11 (a)] is found to be less stable than the reconstructed 2×1 (Pandey π–bonded chain) geometry.

The calculated C–C bond length corresponding to zigzag chain is 1.43Å, equal to the

(a)2 × 1–(111) clean (b) 2 × 1–(111) H–terminated

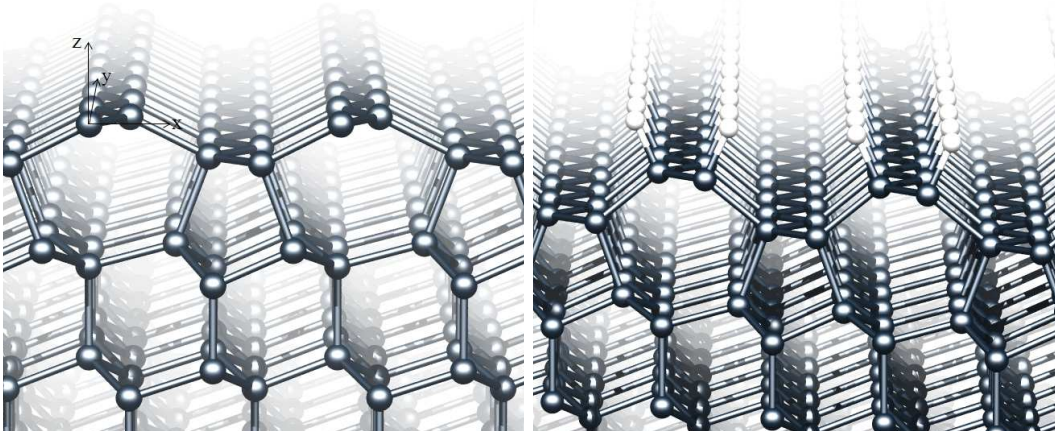

Figure 5.10: Perspective views of the reconstructed 2 × 1 (a) clean and (b)H–terminated diamond (111) surfaces.

(a)1 × 1–(111) clean (b) 1 × 1–(111) H–terminated

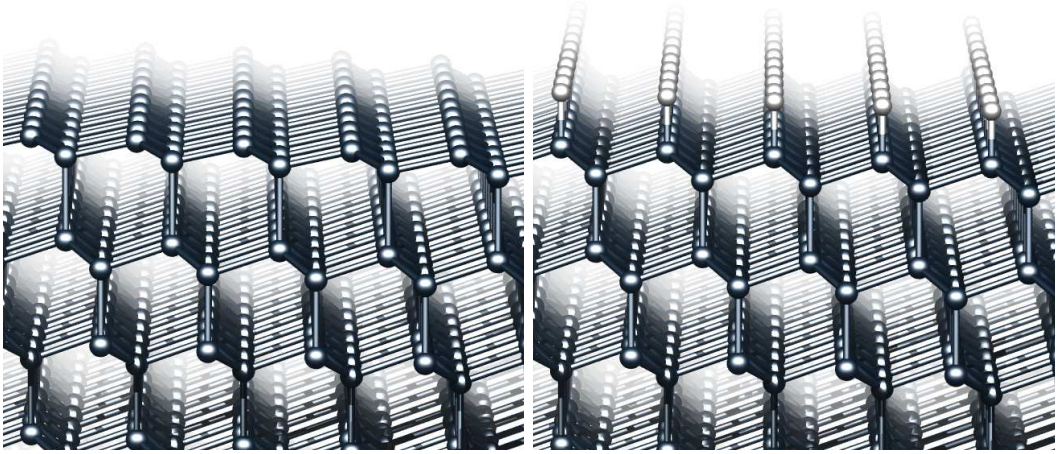

Figure 5.11: Perspective views of the unreconstructed 1 × 1 (a) clean and (b)H–terminated diamond (111) surfaces. Representation of axes is similar to those shown in Fig.5.10

mean value of the C–C single bond (1.54Å) and the C=C double bond (1.32Å). For high surface coverages of adsorbates, the 2×1 surface is known to be energetically unfavourable [175, 176]. However, for low surface coverages, the relative stability of reconstructed and unreconstructed surfaces depends upon the chemical and physical nature of adsorbate. For example, in the case of oxygen termination, for 0.5 ML of oxygen coverage, the stability of both 2×1

and 1×1 surfaces is nearly similar [176], while in the case of –OH termination [175], even a small concentration of functional group can destabilise the reconstructed surface by disrupting the π–bonding.

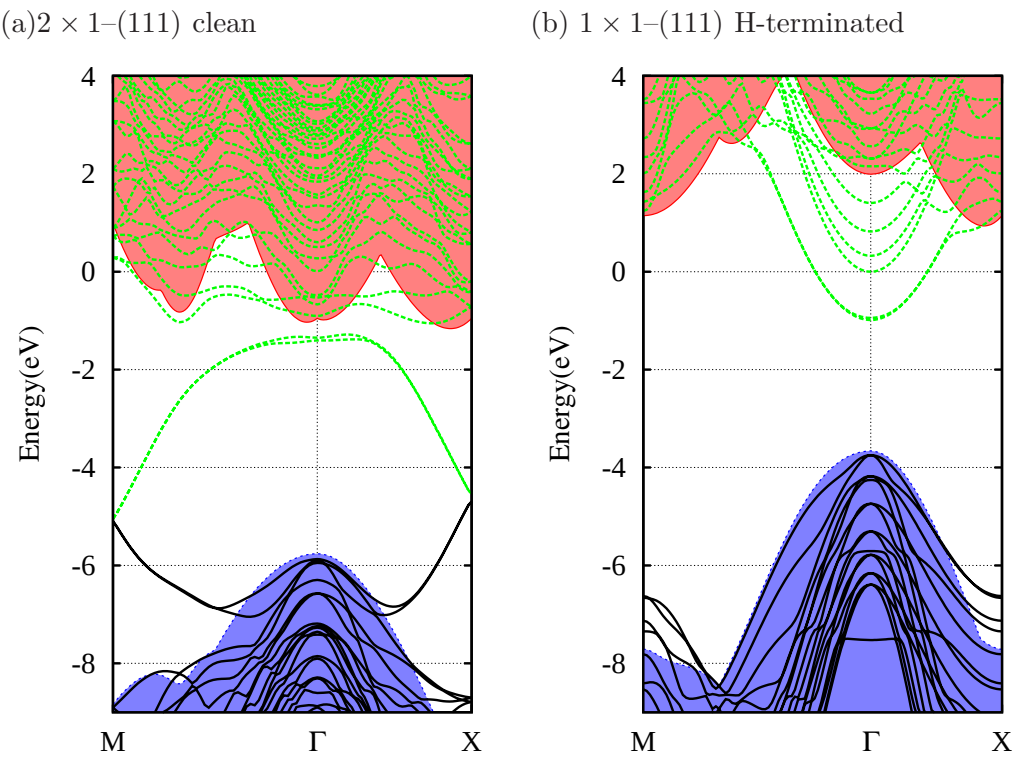

Figure 5.12: Electronic band structures of the (a) reconstructed 2×1 clean and (b) 1×1 H–terminated diamond (111) surface. Depiction of the electronic states is similar to those presented in Fig. 5.7

Calculations performed for H–termination shows that for 100% surface coverage of H, an unreconstructed surface is more stable than a reconstructed surface, by 1.65 eV per H atom. The H–terminated 1×1 and 2×1 geometries are shown in Fig. 5.11 (b) and 5.10 (b), respectively. Although partial H–termination of (111) surfaces has not been examined in this study, adsorption of H on a diamond surface is found to be similar to that of F–termination. A detailed study regarding the thermodynamic stability of partial halogen terminated 1×1 and 2×1–(111) surfaces is included in the next chapter, which will be useful to understand the partial H–termination.

The electronic band structure [Fig. 5.12 (b)] of the H–terminated 1×1–(111) surface is

similar to that of a H–terminated 2×1–(100) diamond surface in this sense that hydrogen saturation of single dangling bonds on 1×1–(111) surface removes the presence of the electronic states in the middle of the band gap. Wave function analysis indicates the highest occupied and unoccupied states are associated with the p orbitals of the surface C atoms. Furthermore, akin to the electronic band structure of the H–terminated 2×1–100 surface, the H–terminated 1×1–(111) surface shown in Fig. 5.11 (b) exhibit free–electron–like states. These states lie in the energy range from 2 to -1 eV at Γ point. The electronic band structure of a clean 2×1–(111) surface does not show any resemblance to that of 2×1–(100) surface and due to the formation of a delocalised π network, it is found to be semimetallic in nature [Fig. 5.12 (a)]. Calculated χ_s for both terminated and unterminated are summarised in Table. 5.1. In addition to adsorption energies, these values are also in good agreement with the previous reports.

5.4.3 (110) surface

The diamond (110) surface exhibits 1×1 low energy diffraction pattern and unlike (100) and (111) surfaces, this surface does not present any reconstruction even when annealed at very high temperatures (1300 K) [177]. There have been some studies on the possibility of dimers on the (110) surface; nevertheless, no evidence for dimerisation has been found to date [135, 177].

Similar to the diamond (111)–2×1 surface, the diamond (110) surface also comprises the delocalised π network running along the zig–zag chains on its surface. However, in contrast to the (111)–2×1 surface, the staggered stacking of these zigzag chains continues throughout the slab, as shown in Fig. 5.13 (a). Consistent with the observations on the 2×1–(111) surface, 1×1–(110) also shows semimetallic behaviour, where the chain bond length is calculated to be 1.42Å, close to the surface C–C chain bond length of 2×1–(111) surface.

Test calculations suggest that an unterminated 1×1–(110) surface is less stable than the clean 2×1–(100) and 2×1–(111) surfaces in terms of energy per unit surface area. However, based upon surface energy calculations, the H–terminated 1×1–(110) surface is found to be the most stable, followed by the 2×1–(100) and 1×1–(111) surfaces, respectively. These findings agree well with those of a previous study [178].

(a)1 × 1–(110) clean (b) 1 × 1–(110) H–terminated

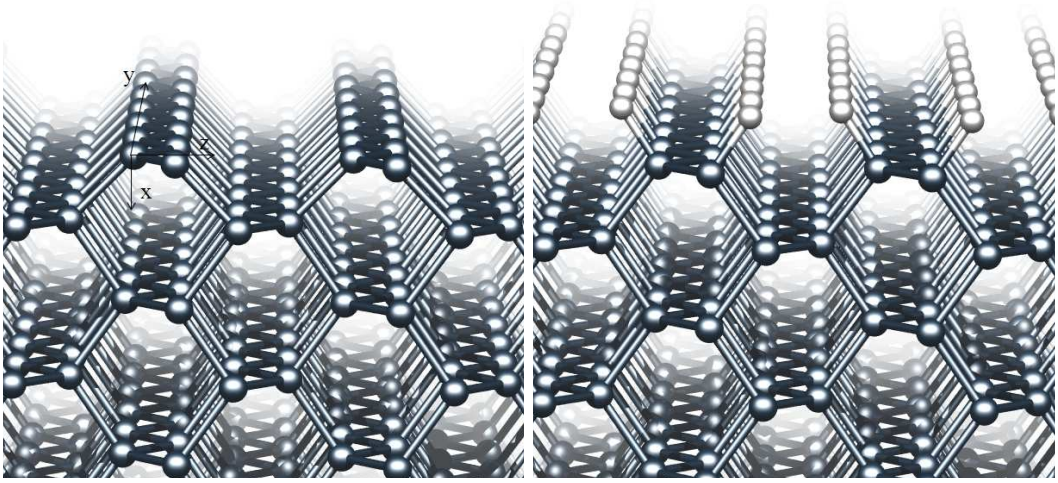

Figure 5.13: Perspective views of the 1×1 (a) clean and (b)H–terminated diamond (110) surfaces.

The C–C chain bond length for the hydrogenated surface is calculated to be 1.51Å, somewhat smaller ($\approx 2\%$) than 1.54Å of a typical single C–C bond and significantly smaller ($\approx 6\%$) than the C–C single bond of the 2×1 hydrogenated (100) surface [Fig. 5.6 (a)]. The electronic band structures of the clean and H–terminated 1×1–(110) diamond surfaces are found to be similar to those of the clean 2×1–(111), and H–terminated 1×1–(111) and 2×1–(100) surfaces, respectively. The χ of the H–terminated $1\times$–110 surface is calculated to be the highest among the studied low index surfaces and as suggested previously [144], this is due to the high surface dipole density per unit surface area.

5.5 Chapter summary

In summary, DFT calculations were performed to investigate the electronic and structural properties of the bulk and low index clean and H–terminated diamond surfaces. It is noted that both the surface geometry and orientation significantly influence the electronic and structural properties of diamond. For example, a clean 2×1–(100) surface is non–metallic in nature, whereas 2×1–(111) and 1×1–(110) surfaces show semimetallic behaviour, which are due to adjacent surface dimers and neighbouring zig–zag chains interactions, respectively. The C–C bond length for surface C atoms of the investigated surface geometries may vary

in the wide range from 1.3 to 1.5Å. However, the C–C bond length ($\approx$ 1.54Å) in the middle of the slab is independent of surface orientation and termination.

Overall, the electronic band structures of H–terminated diamond surfaces are very similar to each other in the manner that there are no electronic states in the middle of the band gap and the electronic states are shifted in the upward direction due to the effect of C–H surface dipoles. The H–termination is of particular relevance for inducing an NEA, making diamond useful for surface conductive devices and some extent to thermionic applications. The validation of the electron affinities and adsorption energies of the clean and H–terminated diamond surface is enormously useful in the investigation of little known surface terminations, for example, halogens and metal terminations, which are discussed in the next chapters.

Chapter 6

Halogen functionalisation of diamond surfaces

> The important thing in science is not so much to obtain new facts as to discover new ways of thinking about them.
>
> Sir William Bragg, British physicist (1862–1942)

6.1 Introduction

Electronic applications of diamond have been severely limited by the scarcity of soluble shallow dopants for its extremely hard FCC lattice of tetrahedrally coordinated, (sp^3)–bonded carbon atoms. Nevertheless, because of its unique surface properties (Chap. 5), particularly the surface conductivity and NEA, diamond surfaces hold great potential for surface conductive and electron emission devices.

Previous studies on diamond have shown that surface termination has important consequences for the electrical properties and different surface functionalities lead to distinct properties of diamond [22, 23, 135]. For example, hydrogen termination induces an NEA, so the conduction band lies above the vacuum level [23]. On the other hand, oxygen termination yields a PEA [22, 135].

Since the electron affinity impacts the work function strongly, the possibility of inducing both NEA and PEA on diamond is indeed very important for the thermo–tunnel device fabrication, which requires two electrodes with dissimilar work functions (Chap. 4). The dependence of work function (ϕ) on χ can be expressed by following equation [23]

$$\phi = E_{\mathrm{g}} - (E_{\mathrm{F}} - E_{\mathrm{v}}) + \chi, \tag{6.1}$$

where E_g is the bandgap of diamond, E_F Fermi level and E_v is the valence band maxima.

The variation in electron affinity (EA) of diamond can be understood in term of surface electric dipoles arising from differences in the electronegativities of the terminating species [135]. Depending upon the partial charge (δ) on each atom, one can imagine two classes of surface dipole: $C^{+\delta}$–$X^{-\delta}$ and $C^{-\delta}$–$X^{+\delta}$, where δ is the partial charge on the atom [17], and X the adsorbate. $C^{-\delta}$–$X^{+\delta}$ dipoles bend the bands upwards with respect to the vacuum level, while $C^{+\delta}$–$X^{-\delta}$ dipoles cause a downward band-bending. Experimentally [22], $C^{-\delta}$–$H^{+\delta}$ dipoles yield a NEA of 1.30 eV, while $C^{+\delta}$–$O^{-\delta}$ dipoles result in a PEA of 1.70 eV.

Although the direction of band–bending arises from the orientation of the dipoles, a quantitative picture of the EA is further complicated by lateral interactions between adsorbates. For example, theoretically, ether–terminated (001)–1×1 has a PEA of 2.70 eV, but addition of hydroxyl components is predicted to rapidly reduces this value [135]. Such effects are likely to be a significant source of difference between the PEA of an ideal O–terminated surface in comparison to the experimental value of 1.70 eV [22].

In recent years, the interaction of halogens with diamond surfaces has been the subject of both experimental [179] and computational studies [172, 180]. Halogenated carbon precursors, such as CF_4 and CCl_4, have been used to grow diamond at relatively low temperatures [179, 181–184]. Substrate temperatures in such growth regimes can be as low as 250 °C [184], offering the wider choice of substrate materials in comparison to conventional diamond CVD growth where growth temperatures are normally greater than 800 °C [182]. Since the substrate temperature is low in halogen–assisted CVD system and the reactions of halogens with diamond surface are highly exothermic, diamond may exhibit the presence of halogen–carbon bonds on its surface [182]. The presence of halogen–carbon bonds on the diamond surface, obtained from halogen assisted CVD systems, has been confirmed using x–ray photoemission spectroscopy, energy dispersive x–ray system and secondary ion mass spectroscopy [182, 185], supporting a view that halogens may play an important role in layer–by–layer growth of CVD diamond.

F and Cl termination of diamond surfaces are found to be reasonably thermally stable (F–830 °C and Cl–700 °C) [186], and to improve the other surface properties, such as lubricity and stability, post–growth processing has deliberately produced fluorine and chlorine

terminated diamond surfaces [22, 184, 185, 187–191]. In addition, fluorinated nanodiamonds exhibit improved luminescence properties in comparison to oxygenated and hydrogenated counterparts [192].

More recently, because of the chemical inertness, radiation hardness and a high degree of biocompatibility, interest in functionalised diamond has been evoked dramatically for application in drug delivery and sensing things, such as radiation and pH in different harsh and biological environments [193–196]. Since a functionalised diamond surface is chemically more suitable for the biomolecule immobilisation in comparison to a pristine diamond surface, a variety of different functionalities (linkers), particularly halogens, have been tested [194, 197–201].

As an example, grafting of thiol–modified DNA or other thiol–bearing biomolecules includes amination of either hydrogenated or chlorinated diamond surface, whereas dodecyl– and polyethylene glycol (PEG)–groups, prefer both Cl and Br–terminated diamond [194, 198, 199]. Fluorination and hydroxylation are also reported as the substitutes for the functionalisation of diamond surfaces, wherein the role of electron affinity (EA) is crucial to understand the band bending [194, 197, 200, 201].

Given the qualitative impact that varying the chemical termination has upon the EA and thermodynamic stability of diamond [17,19], the existence of C–halogen dipoles on diamond surfaces, even where in addition to C–H termination, can be expected to be important due to the relatively high electronegativities of halogens. Completely halogenated surfaces would be expected to exhibit large PEAs in comparison to unterminated or oxygen–terminated diamond. However, noting the extremely compact lattice of diamond, it is not obvious that 100% termination by Cl, Br or even F is possible due to steric interactions between halogen adsorbates [172,180], and either a partial halogen termination or a mixed halogen–hydrogen or halogen–oxygen termination may be expected in practice.

In order to address the likely structures and properties of halogenated diamond, this chapter presents the results of a first principle density functional study into the energetics and surface electron affinity of halogen terminated diamond surface. Although in comparison to F and Cl–termination, high coverages of Br are far less energetically favourable, a brief study regarding the partial adsorption of Br on to a clean and H–terminated (100) diamond surface is also included in the end of this chapter.

6.2 Computational Method

In these simulations, the basis sets consist of independent sets of s and p–type Cartesian Gaussian functions of four widths for all species other than H, for which there were three. In the cases of C, O, and F, an additional four sets of d–type polarisation functions were also included, and two sets for both Cl and Br. Additionally, as discussed in Chap. 3, sets of sixteen s–Gaussian basis functions are placed at points in the vacuum region with an equal density to the atomic density of the diamond host to augment the treatment of the evanescent states at the surface [144].

Matrix elements of the Hamiltonian are determined using a plane wave expansion of the density and Kohn-Sham potential with a cutoff of 175 Hartree energy.

The (001), (110) and (111) oriented diamond surfaces are modelled using a periodic boundary condition with an inversion symmetry, 14 layers of carbon atoms and more than 19Å of vacuum. Details regarding the modelling of these surface have been provided in Chap. 3. For surfaces with sub–monolayer coverages, a wide variety of symmetrically non–equivalent structures were explored to establish the most probable candidate for the lowest energy arrangement. For example, with the 25% halogen coverage, simple surface periodic cells with (2×2) and (4×1) arrangement, along with the various internal arrangements for (4×2), (4×4) and (8×1) periodicities were included. In addition, calculations were performed on the more extended (8×2) systems, which showed no significant differences from the smaller surface cells, justifying at this level the restriction to the indicated surface periodicities. Based upon the general view that the lowest energy structure could be extracted from relatively small surface cells, arrangements for the (110) and (111) surfaces were slightly reduced in extent, but in each case a sufficient variety of surface arrangements are tested to allow the lowest energy configuration to be obtained with a high degree of confidence.

The adsorption energy per terminating atom corresponding to each equilibrium structure is calculated [202] as

$$E_{\text{ads}} = \frac{1}{n}\left(nE_{\text{C}} + n\mu_{\text{X}} + E^{\text{tot}}\right), \tag{6.2}$$

where E^{tot} is the minimum in the total energy of the slab geometry terminated by n adsorbed atoms, E_{C} the total energy per surface site of an unterminated diamond surface slab, and

μ_{X} the chemical potential for the terminating species, X. For all species, μ_{X} is taken as half the energy of a diatomic molecule, X_2. E_{C} is obtained by relaxing the C–terminated surface with the same slab thickness as for the halogen termination, and then dividing the total energy by the number of surface sites.

To examine the energetics of the reaction of the halogen where combined with H–termination, the calculated adsorption energy for the halogen is obtained using following equation

$$E_{\mathrm{ads}} = \frac{1}{n}\left(nE_{\mathrm{C}} + mE_{\mathrm{H}} + n\mu_X - E^{\mathrm{tot}}_{n,m}\right), \tag{6.3}$$

where $E^{\mathrm{tot}}_{n,m}$ is the minimum in the total energy for n halogen and m hydrogen terminating species, E_{H} is the total energy per surface site of a H–terminated surface. E_{H} is obtained by relaxing the H–terminated surface with the same slab thickness as for the halogen termination, and then dividing the total energy by the number of H–terminated sites. The form of Eq. 6.3 is selected to eliminate as much as possible the impact of the hydrogen adsorption energy, and can be regarded as calculating the total adsorption energy for all species and then subtracting the adsorption energy for hydrogen in the limit of 100% H termination.

The impact of the zero–point motion upon the adsorption energy calculations is also considered. As a test, for the (001) surface the vibrational frequencies are calculated for the adsorbates in their diatomic molecular form, those of the C–terminated surface, and those of the H, F, and Cl terminated surface. The frequencies are obtained by first constructing the dynamical matrices using the second–derivatives of the total energy with respect to the displacement of the atoms obtained using the same first–principles method as above. Diagonalising the dynamical matrices yields the frequencies. The zero–point energies can then be obtained for the system before and after adsorption. For H, F, and Cl, the contributions to the adsorption energy per atom are found to be 186, 70, and 41 meV/adsorbate–atom. Therefore, it can be concluded that, especially in the case of the halogen species, that the contribution to the adsorption energies from zero–point motion can be neglected.

6.3 Results

6.3.1 Methodology validation

As described in Chap. 5, DFT calculations are performed for the known clean, oxygen, and hydrogen terminated diamond surfaces. The calculated hydrogen adsorption energies lie in the range 1.0–2.8 eV/atom, which is in good agreement with similar literature values [20, 21, 203]. This may be viewed as a reference energy for comparison with the adsorption energies of the halogens. The fractional differences between the current estimates of the adsorption energy and the literature values are acceptable given that the reference states of the adsorbates include atomic species. The agreement between the current calculations for the EA, and the literature values is very good, with values all within about 10%, and can be explained by variations in functionals and basis sets.

In addition to the adsorption energies and electron affinities, as discussed in Chap. 5, the electronic band structures and structural properties of clean and hydrogenated diamond surfaces are also examined, which are consistent with previous studies. Based upon these results, it can therefore be concluded that the computational approach is suitable for the simulation of halogen terminated diamond surfaces.

6.3.2 Halogens on the (001) diamond surface

To assess the properties of halogen terminated (001)–2×1, model systems have been relaxed with 25, 50, and 100% termination of the surface with the remaining sites being either unterminated or saturated by hydrogen. The most stable surface cells corresponding to 25 and 50% coverages are illustrated in Fig. 6.1. It is important to mention here that both canted and symmetric configurations for 1×1 geometry are less stable and hence are not included in this work.

6.3.3 C–terminated (001)–(2×1) surface

For 100% coverage (Fig. 6.2), the calculated C–F and C–Cl bond lengths are 1.36Å and 1.71Å, respectively, 2–4% shorter than previously calculated 1.39Å and 1.79Å of C–F and C–Cl single bonds, respectively [172]. Furthermore, the calculated C–halogen distances agree with experiments to within 3%. The experimental C–F and C–Cl bond lengths in CF_4 and

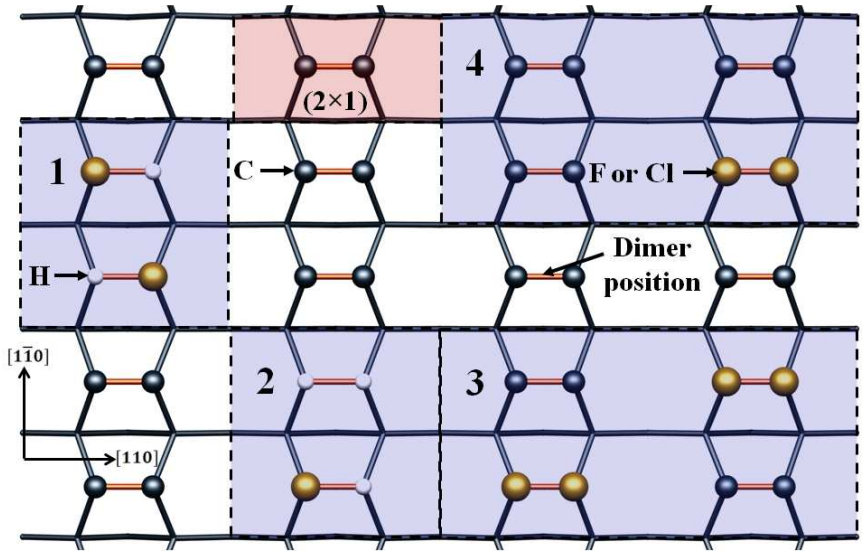

Figure 6.1: Schematic of unit cells for partial coverages of F or Cl on C–terminated and H–terminated (001)–2×1 surfaces. Large, medium and small atoms are halogen, carbon and hydrogen terminated sites, respectively. (1) shows 50% halogen with 50% H, (2) shows 25% halogen with 75% H, (3) shows 50% halogen and (4) 25% halogen, respectively. The (red) shaded region representing the unit surface cell is indicated by '(2×1)', from which the repeated surface cell arrangements for sub–monolayer coverages of F and Cl may be determined.

CCl_4 molecules are calculated to be 1.32 and 1.76Å, respectively [142]. The surface in–plane C–C bond–length are in good agreement with the previous results for H terminated surfaces [17, 172] and the values found in this study for H–terminated surfaces.

The structure of the Cl–termination requires further explanation. The shortest inter–chlorine distance, as shown in Fig. 6.2(b), is just 25% greater than the bond–length in the Cl_2 diatomic molecule. The $4p$ lone–pairs are then overlapping to a significant degree. The calculated surface C–C–Cl bond–angle is 103.9°. This is somewhat smaller than the tetrahedral angle, and significantly smaller than the calculated C–C–Cl bond angles in previous cluster calculations where the steric interactions from neighbouring surface sites were not included [172]. Given this highly strained environment, it is therefore not surprising that the adsorption energy for 100% Cl–termination is only 1.20 eV/atom, much smaller in comparison to those of fluorine (3.94 eV/atom) or for partial Cl coverages (Table 6.1). This

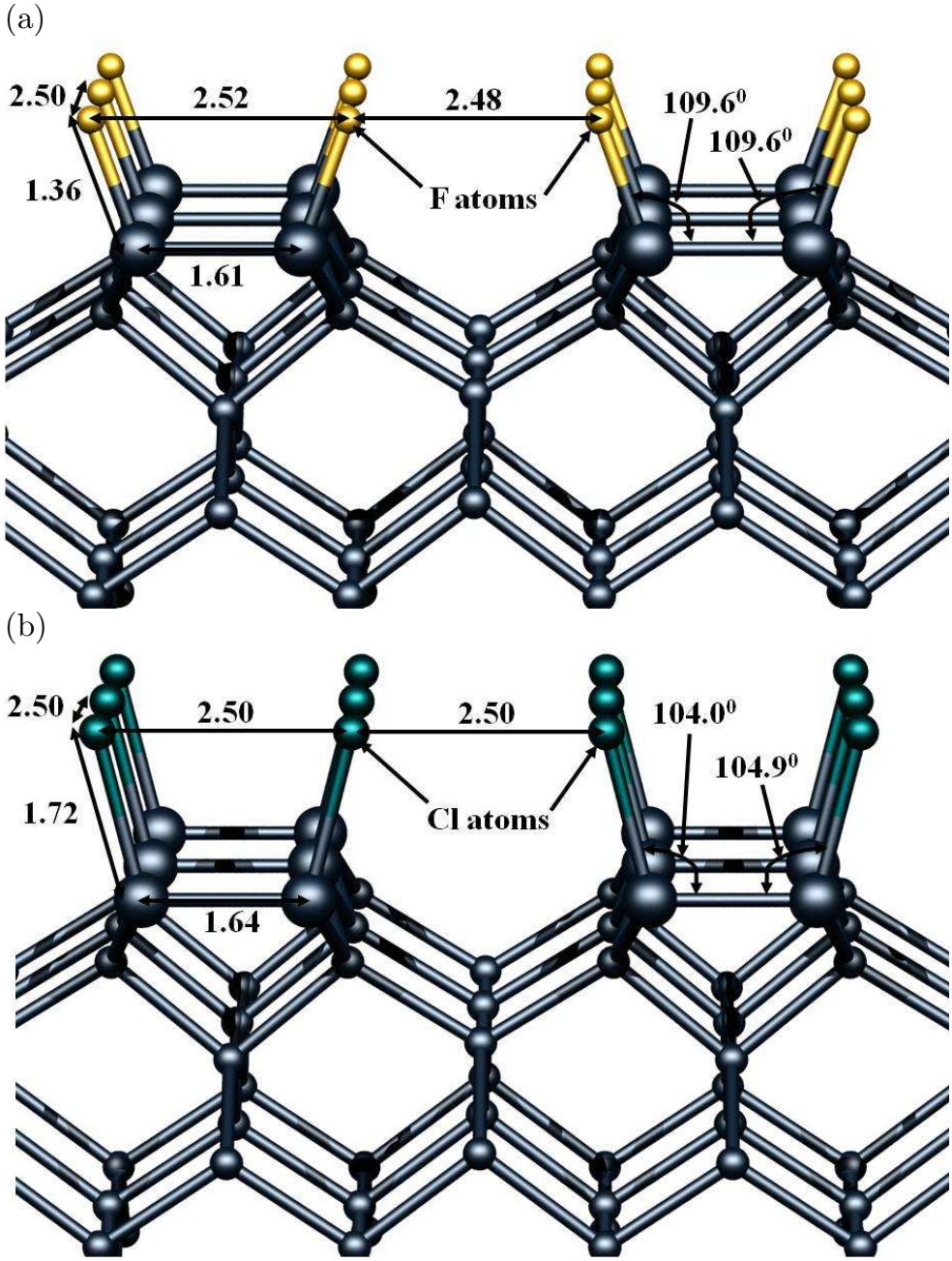

Figure 6.2: Schematic of 100% F or Cl terminated (001)–2×1 surfaces. Distances are indicated in Å, and angles in degrees.

suggests that 100% Cl termination may not be easy to achieve in practice.

Where the coverage of the surface is less than 100%, there are of course an infinite number of ways in which the surface may be constructed. In order to determine the equilibrium

Table 6.1: Calculated adsorption energy per atom (E_{ads}), and electron affinity (EA) for different coverages of the (001)–(2 × 1)C and (001)–(2 × 1)H surfaces of diamond by F or Cl (eV). For H–terminated surfaces, the coverage refers to the fraction of H–sites substituted by a halogen atom. As reference values, the EAs for C– and H–termination are calculated to be 0.61 eV and −1.96 eV, respectively.

	Fluorine				Chlorine			
Coverage	E_{ads}	EA	$d_{11(\text{C–C})}$	$d_{(\text{C–F})}$	E_{ads}	EA	$d_{11(\text{C–C})}$	$d_{(\text{C–F})}$
C–termination								
1.00	3.94	+2.13	1.60	1.36	1.20	−0.03	1.64	1.72
0.50	4.13	+1.60	1.37–1.61	1.37	2.43	+0.84	1.37–1.62	1.77
0.25	4.24	+1.11	1.37–1.60	1.37	2.53	+0.69	1.37–1.63	1.78
H–termination								
0.50	4.21	−0.38	1.60	1.39	2.46	+0.26	1.59	1.80
0.25	4.26	−0.78	1.59	1.40	2.57	−0.52	1.59	1.82

structure for a given sub–monolayer coverage, a range of possible structures have been relaxed.

All equilibrium structures involve halogens saturating carbon atoms sharing a reconstructed bond, with the lowest energy configurations being those presented in Fig. 6.1. The remaining sites on the otherwise unterminated surfaces are not significantly perturbed from the ideal (001)–2 × 1:C surface, indicating that the interaction between the saturated and unsaturated surface dimers is small.

For partial Cl termination, the strain determined for 100% coverages is relaxed considerably, with the distance between Cl atoms on a dimer increasing from the 2.50Å indicated in Fig. 6.2 to 3.16Å for 25% coverage. This is accompanied by an increase in the C–C–Cl bond angle to 116°, close to the value reported previously from cluster calculations [172] where steric interactions were absent.

The effect of steric interaction on adsorption energy is clearly evident in Table 6.1. For fluorine, the adsorption energy (Table 6.1) is weakly dependent upon coverage, consistent

with a low F–F steric interaction, whereas for chlorine, coverages of 50% or less significantly reduces the steric effects noted for 100% coverage, with adsorption energies in the region of 2.5 eV/atom for low coverage.

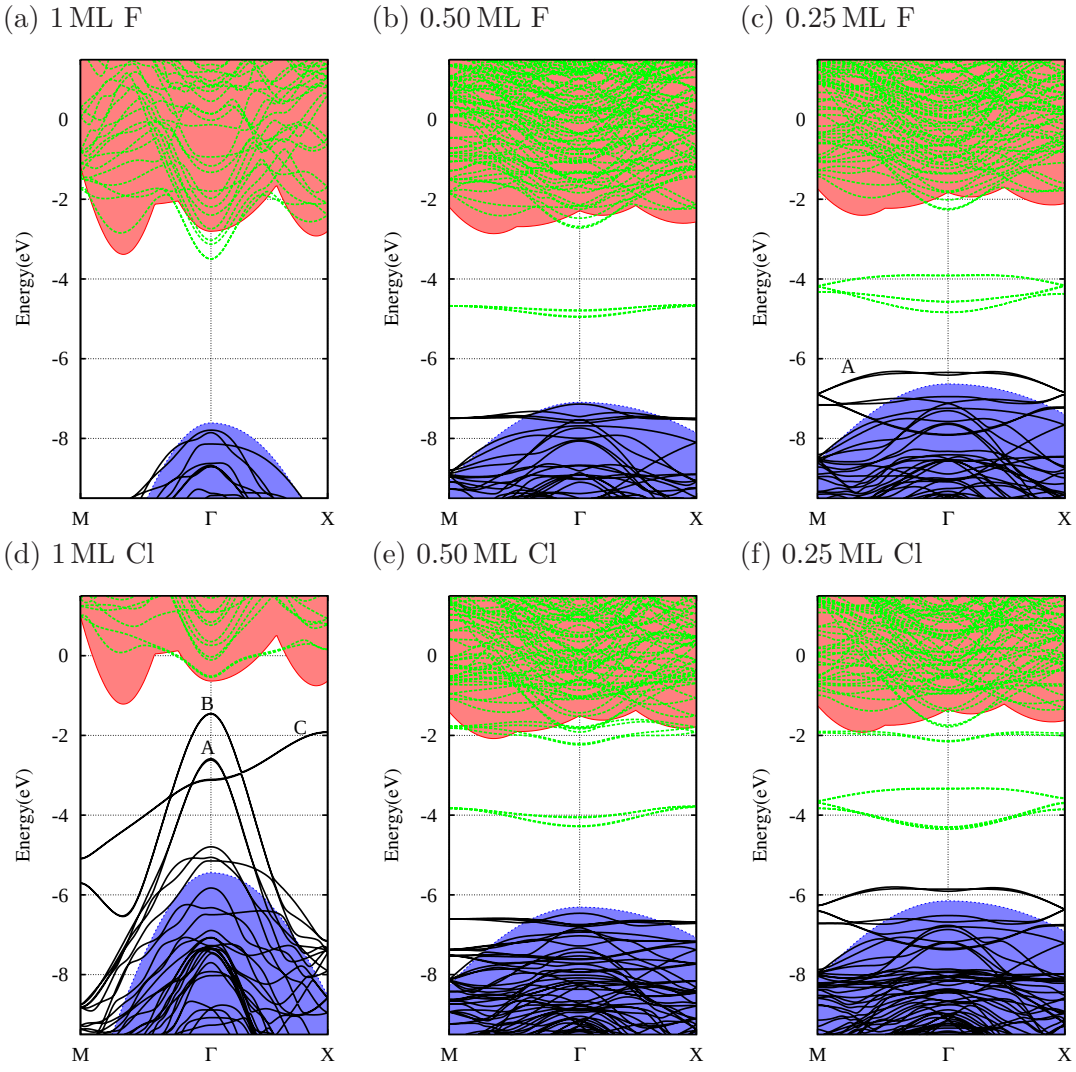

Figure 6.3: Electronic band structures corresponding to different surface coverages of F and Cl adsorbed on a clean reconstructed (001)–(2 × 1) diamond surface. Occupied (black) and unoccupied (green) states of terminated surfaces are superimposed upon the electronic band structure of bulk (shaded regions). The zero of the energy scale is the vacuum potential for each system.

The calculated electron affinities for the equilibrium structures are each coverage are

listed in Table 6.1. The small value for 100% Cl termination is a consequence of the strong interactions between the surface Cl atoms, and is unlikely to be realisable experimentally. Fluorine covered surfaces are predicted to give rise to a large PEA of around 2.13 eV, with value decreasing monotonically with decreasing coverage. For partial Cl coverage, there is also a PEA, but smaller than the comparable coverage of F. Importantly, although Cl is less electronegative than F, because the C–Cl bond–length is greater than C–F, the electric dipoles of C–Cl bond is either equal or greater than of C–F bond. For example chloro–methane (1.8963D±0.0002D) has a large dipole moment in comparison to fluoro–methane (1.858D±0.002D) [142].

Fig. 6.3 shows the band structures corresponding to different surface coverages of halogens on a clean diamond (100) surface. It is found that for the 100% coverage of F [Fig. 6.3(a)] there is no evidence of any surface states, which is found similar to that of a hydrogen saturated diamond. In contrast for 100% of Cl [Fig. 6.3(e)], the electronic states marked A, B and C, are associated with p–like orbitals on both surface C and Cl atoms.

The highest delocalised occupied states corresponding to 0.50 ML of F (Fig. 6.3(b), (c)) are mainly due to the π–states, centred on unsaturated C atoms [Fig. 6.4 (a)], and the unoccupied states in the band gap near -5.00 and -4.30 eV have π^*–like character [Fig. 6.4 (b)]. A similar picture of occupied π– and unoccupied π^*–surface states is followed for 25% coverage by F, and for 25 and 50% Cl termination.

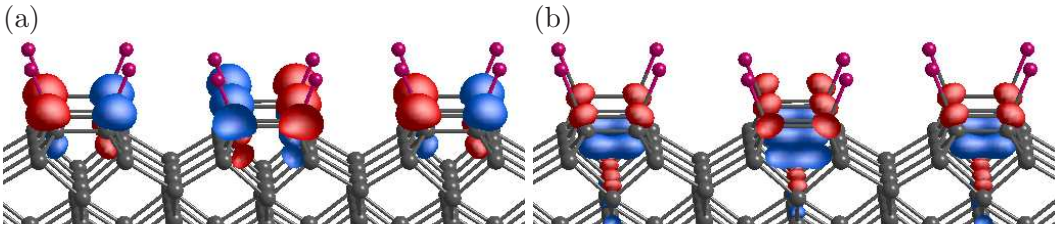

Figure 6.4: Plot of the wave function iso–surfaces for the highest occupied and unoccupied states in the middle of the band gap of partial surface coverages of F and Cl on C–terminated 2×1 diamond (100) surface. HOMOs and LUMOs are represented using red and blue contours, respectively.

6.3.4 H–terminated (001)–(2×1) surface

Many chemical treatments involving halogens also involve a source of hydrogen, such as fluorination of diamond using hydrogen–fluoride, which has the potential to result in a mixed termination [192]. The addition of hydrogen on unterminated sites for partial halogen termination is expected to have two effects. First, the presence of the hydrogen may lead to additional steric interactions, modifying the adsorption energy of the halogen [203]. Secondly, hydrogen is more electropositive than carbon, so the surface dipoles arsing from the hydrogen termination will tend to reduce or negate the PEA due to the halogens.

Unit cells corresponding to the most stable geometries of 50 and 25% coverage on H–terminated surface are also shown schematically in Fig. 6.1. For both F and Cl, halogens occupy sites maximising the distance to the nearest neighbour halogen. The calculated C–C–F bond angles for hydrogen terminated surface having 0.50 ML and 0.25 ML of F are 112.5° and 112.3°, while surfaces with 0.5 ML and 0.25 ML of adsorbed Cl gives the C–C–Cl bond angles of 109.0° and 109.6°, respectively. C–C–H bond angles for lesser surface coverages of halogens on hydrogenated surfaces are close to those of a fully hydrogenated surface. C–H bond–lengths for surfaces having 0.50 and 0.25 ML of adsorbed F are within 1% of the C–H bond–lengths on a hydrogen–terminated surface. The reduction of the C–C–Cl angle relative to the 116° for the C–terminated surface with 25% Cl suggest that there is an interaction between the Cl and H species, which is also reflected in a very small reduction in the C–H bond lengths.

The adsorption energies (Table 6.1) calculated for the halogens on partially H–terminated surface are close reported for the corresponding H–free cases (Sec. 6.3.3), supporting the view provided by the geometry that the steric interactions at sub–monolayer coverages are modest.

As one would expect from the bond–polarity, the presence of C–H surface termination reduces the EA relative to the partial termination by carbon dimers (Table 6.1). 50% surface coverage of F on an otherwise hydrogenated surface exhibits a PEA of just 0.38 eV and at 25% coverage, a NEA of 0.78 eV. The corresponding values for Cl are systematically more positive, being a PEA of 0.28 eV and a NEA of 0.52 eV for 50 and 25%, respectively. The systematically more positive values for Cl termination are consistent with the notion noted previously that C–Cl bonds provide a larger dipole than C–F bonds.

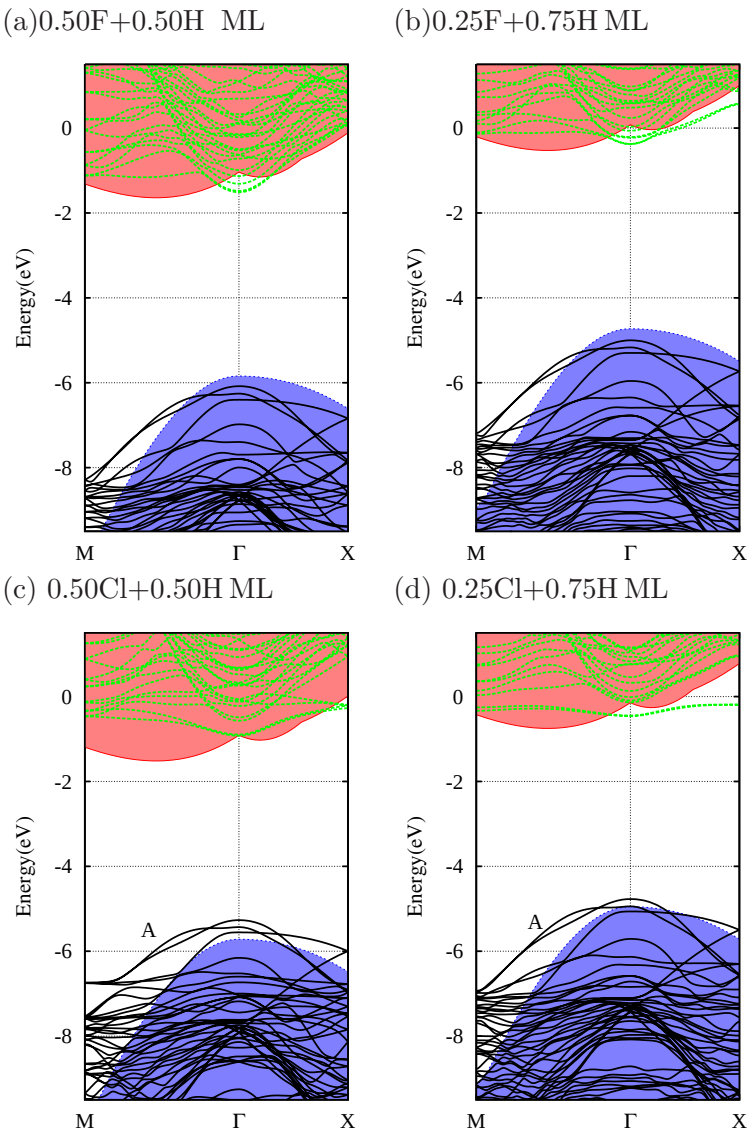

Figure 6.5: Electronic band structures corresponding to partial surface coverages of F and Cl on a H–terminated (2×1) diamond surface. Occupied (solid, black) and unoccupied (dotted, green) states of terminated surfaces are superimposed upon the electronic band structure of bulk (shaded regions). The zero of the energy scale is the vacuum level.

The band structures (Fig. 6.5) corresponding to 0.25 and 0.50 ML of both F and Cl on an otherwise H–terminated diamond surface show that there are no states in the band–gap. This is understandable, as in addition to a small steric interaction, all the surface dimer

sites are terminated, and all carbon atoms in the lattice are now sp^3 coordinated.

A further investigation of filled states for mixed Cl–termination indicates that the first two highest occupied states, marked A in Figs. 6.5 (c) and (d), exhibit a weak π–like character, i.e., made from a combination of Cl p orbitals with host reconstruction states. Since the steric interaction is very low in the case of mixed termination, due to negligible splitting, these states lie in the vicinity of bulk valence band maxima. In contrast to halogen–only termination (Fig. 6.3), the band structures are shifted upward with respect to the vacuum level, due to the presence of the C–H surface dipoles.

6.3.5 Halogens on the (111) diamond surface

A fully terminated 2×1 Pandey–chain geometry, as described in Chap. 5, is less stable than a fully terminated 1×1–(111) geometry. However, given the effect of unsaturated surface C atoms on 1×1 geometry, for partial coverages of halogens, the reconstructed 2×1 geometry remains of significant interest. Similar to the (100) orientation, different repeated model systems corresponding to both 1×1 and 2×1 configurations have been relaxed with pure and mixed 25, 50, and 100% surface coverages of halogens.

C–terminated (111)–1×1 and 2×1 surfaces

Figs. 6.6 and 6.7 show schematic views of the unit cells corresponding to different coverages of F and Cl on the (111)–1×1 and (111)–2×1 surfaces. The calculated C–F bond–lengths are 1.38Å and 1.37Å for 1×1 and 2×1 surface cells, respectively, very close to the C–F bond–lengths on the (001)–2×1 surface. In line with the results for the (001) surface, 1 ML of Cl is unstable on (111)–2×1, and only marginally stable on (111)–1×1 surface.

The adsorption energies (Table 6.2) of F onto (111)–1×1 diamond surfaces are much higher than onto the (111)–2×1 because in the former case each F atom is passivating a carbon radical, whereas in the latter where all atoms are fully bonded, each F is making a C–F bond at the expense of disrupting the π–bonding along the Pandey chains. The destabilising of the reconstruction by fluorination is consistent with the same effect being determined for –OH termination [175].

At sub–monolayer coverage, it is observed that the reconstructed surface remains stable. For example, for 50% F termination, the energy per surface site is 0.18 eV lower in energy

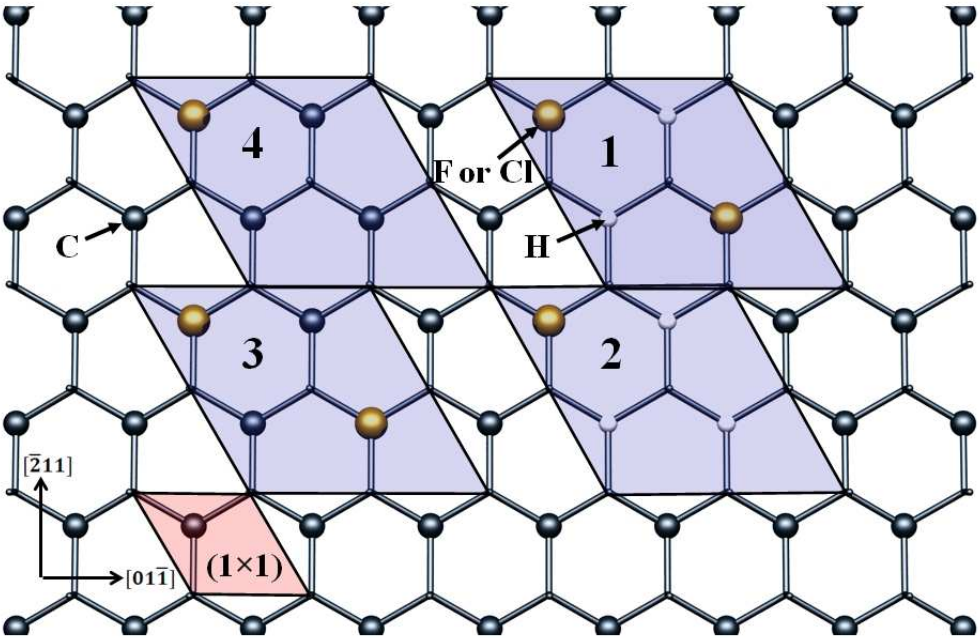

Figure 6.6: Schematic of unit cells for partial coverages of F or Cl on C–terminated and H–terminated (111)–1×1 surfaces. Large, medium and small atoms are halogen, carbon and hydrogen terminated sites, respectively. In all cases the surface cells are (2×2) repeated unit surface cells. (1) shows 50% halogen with 50% H, (2) 25% halogen with 75% H, (3) 50% halogen and (4) 25% halogen, respectively. The (red) shaded region representing the unit surface cell is indicated by '(1×1)'.

for the reconstructed surface than for the most stable arrangement of the unreconstructed surface.

Structurally, the most stable (2×2) unit cells corresponding to 25 and 50% of Cl coverage on C–terminated diamond (111)–1×1 surfaces are similar to the corresponding F coverage, as shown in Fig. 6.6. However, the most stable unit cells(4×2) corresponding to 25 and 50% Cl coverage on the C–terminated (111)–2×1 surface are distinct from the most stable unit cells (2×1 and 4×1) of 25 and 50% of F coverages on C–terminated (111)–2×1 surface. The differences are illustrated in Fig. 6.7.

An analysis of the electron wave functions suggests three important factors: (i) partial coverage leaves complete chains of C–atoms with p_π bonding, (ii) there is no significant wave function overlap between adsorbed F atoms, and (iii) there is a significant wave function

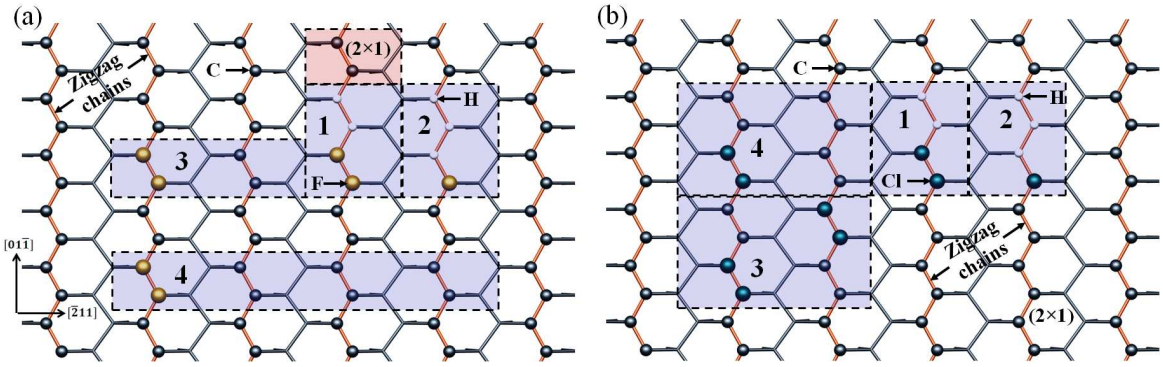

Figure 6.7: Schematics of surface unit cells for partial coverages of (a) F, and (b) Cl on the (111)–2 × 1 surface. In both cases, areas 1 and 3 represent 50% halogen coverage, and areas 2 and 4 show 25% halogen coverage. For areas 1 and 2 the remaining sites are hydrogen terminated. In both (a) and (b), areas 1 and 2 correspond to two unit surface cells. In (a), areas 3 and 4 are correspond to two and four unit surface cells, respectively. In (b), both areas 3 and 4 correspond to two unit surface cells. The (red) shaded region representing the unit surface cell is indicated by '(2 × 1)'. Large medium and small atom sites show halogen, carbon and hydrogen termination, respectively.

overlap between adsorbed Cl atoms. To reduce the repulsive interaction between Cl atoms on the surface, instead of completely saturating Pandey–chains, they only *half* saturate the chains, leaving pairs of carbon atoms between the Cl–termination which may then be fully π–bonded.

The 4 × 2 geometry, which is found be to the most stable in the case of 50% coverage of Cl on the C–terminated (111)–2 × 1 surface (Fig. 6.7(b)), is metastable in the case of 50% coverage of F on the C–terminated (111)–2 × 1 surface. Indeed, the energy differences between the surface arrangements are quite large. In the case of 50% coverage of F on the C–terminated (111)–2 × 1 surface, the most stable 4 × 1 (Fig. 6.7(a)) arrangement is 0.25 eV/atom more stable than the metastable 4 × 2 geometry found to be more stable for Cl–termination. Similarly, for 25% F–coverage, the difference between the most stable 8 × 1 structure and the metastable 4 × 2 geometry found to be most stable in Cl–termination is 0.25 eV/atom.

Table 6.2: Calculated adsorption energy per atom (E_{ads}), and electron affinity (EA) for different coverages of the (111)–(2×1) and (111)–(2×1)H surfaces of diamond by F or Cl (eV). For H–halogen mixed termination surfaces, the coverage refers to the fraction of sites occupied by halogens. E_{rel} reports the energy difference per surface site between the 2×1 and 1×1 structures, positive values representing the Pandey–chain structure being more stable.

	Fluorine				Chlorine			
Coverage	E_{ads}	E_{rel}	EA	$d_{(\mathrm{C-F})}$	E_{ads}	E_{rel}	EA	$d_{(\mathrm{C-Cl})}$
(111)–2×1, C–termination								
1.00	2.75	−0.56	+2.49	1.38	–	–	–	–
0.50	2.82	+0.18	+1.56	1.39	0.64	+0.32	+0.91	1.82
0.25	2.84	+0.54	+0.91	1.39	0.90	+0.45	+0.79	1.83
(111)–2×1, H–termination								
0.50	3.05	−1.15	+0.52	1.41	0.90	−0.91	+0.20	1.86
0.25	3.24	−1.17	−0.70	1.44	1.51	−1.18	−0.39	1.89
(111)–1×1, C–termination								
1.00	4.44	–	+2.63	1.37	0.09	–	+0.93	1.79
0.50	4.72	–	+2.31	1.36	2.22	–	+0.21	1.83
0.25	5.47	–	+2.20	1.38	3.87	–	+1.67	1.79
(111)–1×1, H–termination								
0.50	4.73	–	+0.49	1.40	1.94	–	+0.03	1.80
0.25	4.90	–	−0.73	1.42	3.17	–	−0.41	1.83

For the most stable form for each halogen at each level of coverage, the surface gives rise to a strongly positive EA. For fluorine termination the calculations suggest a range from 1.2 eV at 25% coverage to 2.6 eV at 100% coverage. These values are considerably more positive than the corresponding values for Cl–termination, which lie in the 0.7–0.9 eV range for the energetically stable surface coverages.

The band structures of highly stable terminated (111)–(1×1) diamond surface are shown

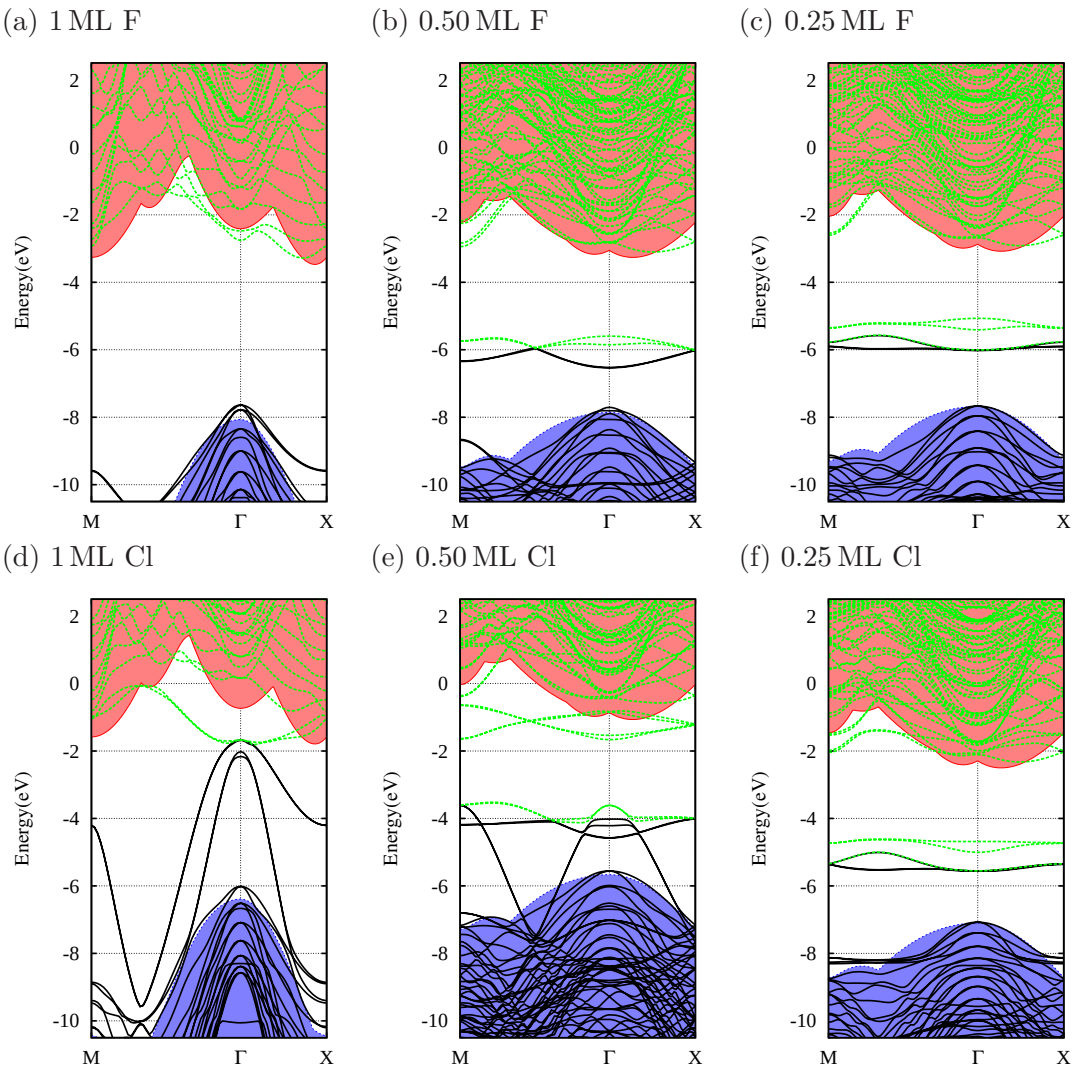

Figure 6.8: Electronic band structures corresponding to different surface coverages of F and Cl adsorbed on a clean (111)–(1×1) diamond surface. Occupied (black) and unoccupied (green) states of terminated surfaces are superimposed upon the electronic band structure of bulk (shaded regions). The zero of the energy scale is the vacuum potential for each system.

in Fig. 6.8. For 100% F–termination, there are no states in the band gap and both filled and empty electronic states are found to be similar to those of bulk diamond. The effect of steric interaction on the band structure of 100% Cl is clearly evident in Fig. 6.8 (a), where some filled and empty states are observed in the band gap.

(a) 0.50 ML F (b) 0.5ML Cl

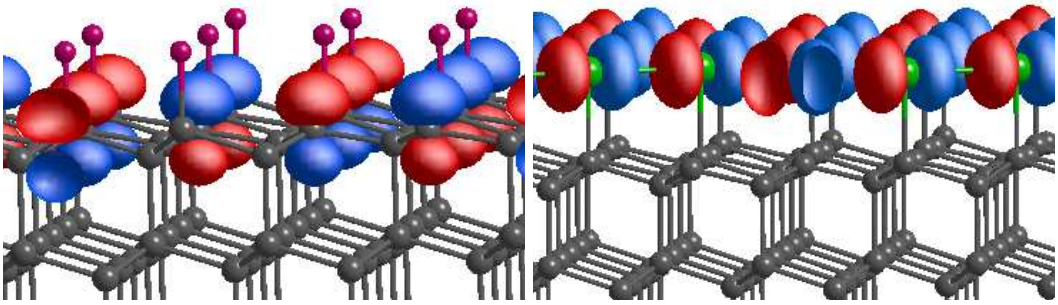

Figure 6.9: Plot of the wave function iso–surfaces for 50% coverage of halogens on C–terminated 1×1 diamond (111) surface. (a) and (b) correspond to the zone–centre states around -6.00 and -4.00 eV in Fig. 6.8(b) and (e), respectively.

A strong interaction between Cl *pi* orbital is also observed in the case of 50% coverage [Fig. 6.9 (b)]. However, for 25% of Cl, and 25 and 50% coverages of F, the filled and empty states in the band gap [Fig. 6.8 (b) and (c)] are due to mainly p orbitals of unterminated surface carbon atoms[Fig. 6.9 (a)].

H–terminated (111)–1×1 **and** 2×1 **surfaces**

For mixed termination, where all surface sites have been saturated by a monovalent species, the (111)–1×1 structure is always more stable than the corresponding coverage for the (111)–2×1 structure. Although there are some differences, the adsorption energies for the mixed termination are broadly in line with the corresponding energies for only the halogen terminated surfaces.

The calculated EAs decrease with decreasing fluorine coverages, consistent with the NEA generated by H–termination. The corresponding values for Cl/H mixed termination are more positive, in line with the values obtained for the (001) surface, and consistent with the larger dipoles arising from C–Cl bonds relative to C–F.

The band structures corresponding to the mixed halogen coverages on a (111)–1×1 diamond surface are shown in Fig. 6.10. Since the steric effect is minimal between F atoms, and surface carbon sites are saturated by either F or by H atoms, no electronic states are found in the bandgap. However, for mixed Cl–termination, due to the strong steric interaction between Cl atoms, the electronic states are observed in the bandgap, which

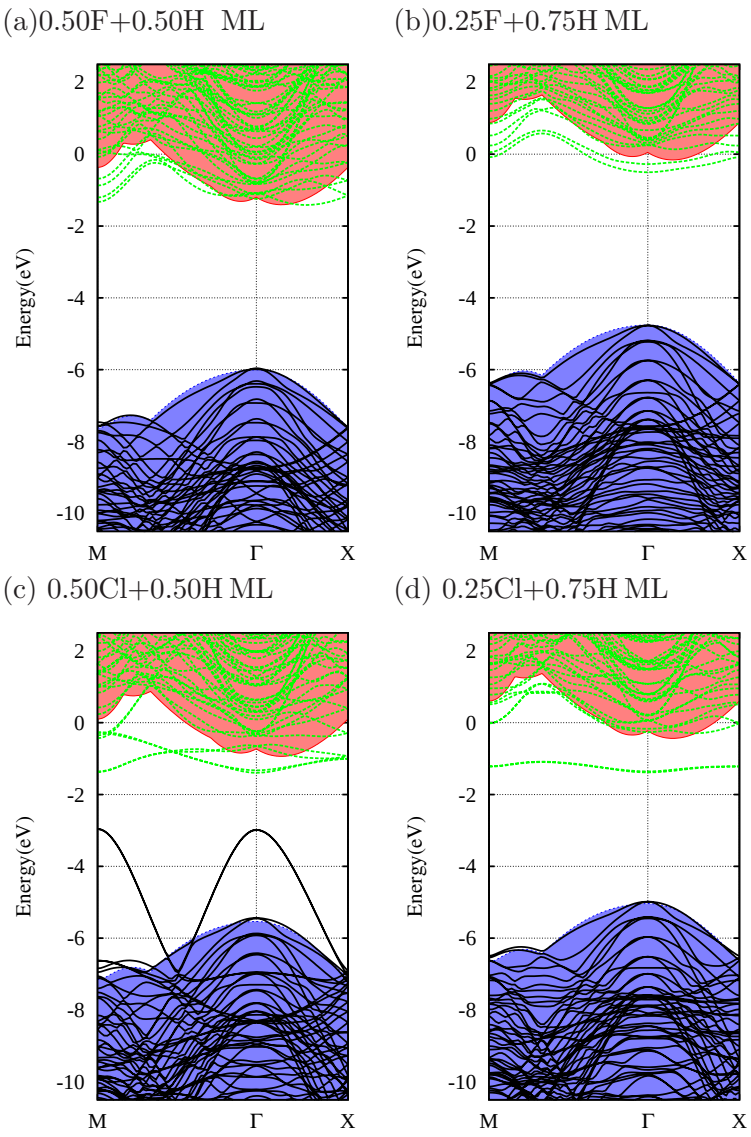

Figure 6.10: Electronic band structures corresponding to partial surface coverages of F and Cl on a H–terminated (111)–(1 × 1) diamond surface. Occupied (solid, black) and unoccupied (dotted, green) states of terminated surfaces are superimposed upon the electronic band structure of bulk (shaded regions). The zero of the energy scale is the vacuum level.

are formed from a combination of p–orbitals of both Cl and surface C atoms. The steric interaction is significantly reduced at 25% surface coverage and very few electronic states are visible in the band gap along the M–Γ–X branch [Fig. 6.10 (d)].

6.3.6 Halogens on the (110) diamond surface

The (110)–surface is perhaps the least studied surface among the low index faces of diamond, as it is less important in terms of technological applications and also difficult to grow selectively using CVD process [195]. However, steps on (001) and (111) surfaces possess this orientation, and therefore understanding of interaction of halogens with (110) surface is critical for both the etching process and CVD growth [20].

C–terminated (110)–1×1 surfaces

As with (001) and (111) surface orientations, it is calculated that 100% termination by F is energetically possible, but that the space is insufficient for complete Cl termination.

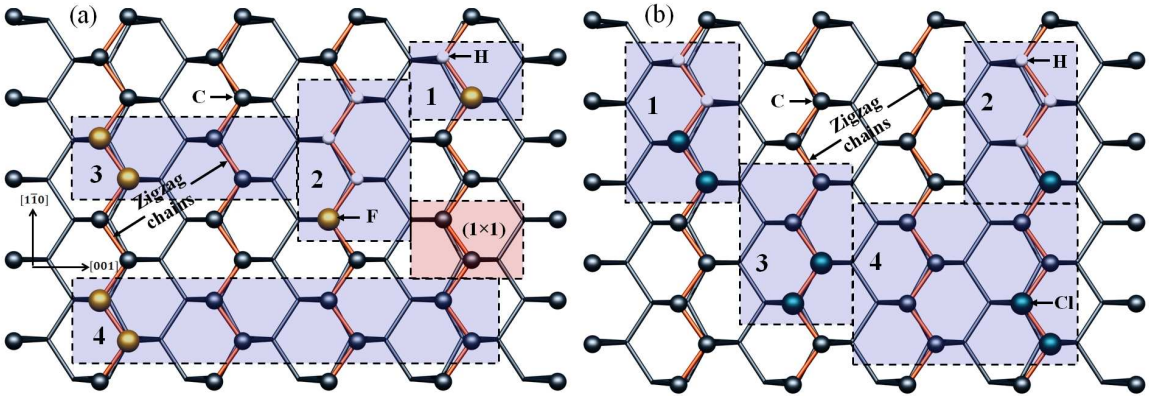

Figure 6.11: Schematics of surface unit cells for partial coverages of (a) F, and (b) Cl on the (110)–1×1 surface. In both cases, areas 1 and 3 represent 50% halogen coverage, and areas 2 and 4 25% halogen coverage. For areas 1 and 2 the remaining sites are hydrogen terminated. Depiction of surface geometries is similar to the Fig. 6.7. The (red) shaded region representing the unit surface cell is indicated by '(1×1)', from which the repeated surface cell arrangements for sub monolayer coverages of F and Cl may be determined. Large, medium and small atom sites show halogen, carbon and hydrogen termination, respectively.

Fig. 6.11 shows the most stable arrangements for 25 and 50% halogen termination of the (110)–1×1 surface. The unterminated (110) surface consists of $[1\bar{1}0]$ chains of carbon atoms, resulting in p_π states akin to the Pandey–chains on the reconstructed (111) surface.

It is perhaps therefore not surprising that the differences found for the arrangements of F and Cl obtained for the (111) surface are reproduced on the (110) surface. Again, partial F–termination results in the addition of halogens in a complete chain, whereas Cl–termination forms Cl–pairs separated by carbon pairs.

Similar to the behaviour of the (111)–2×1 surface, in the case of 50% F–coverage, the equilibrium arrangement for Cl (Fig. 6.11(b)) is 0.43 eV higher in energy per halogen atom than the equilibrium arrangement for 50% F–termination (Fig. 6.11(a)). The differences in adsorption energy are smaller at 25% coverage, where the different periodicities only differ in energy by 0.10 eV per halogen atom. The equilibrium adsorption energies (Table 6.3) for the (110) surface orientation are broadly in line, but slightly greater than the values obtained for the (111)–2×1 surface.

Calculations show that the (110)–(1×1) surface saturated with fluorine exhibits a large PEA of 2.38 eV. Calculated electron affinities for varying surface coverages of F and Cl on (110)–1×1 surface are shown in Table 6.3. The EAs of F–terminated surfaces increase gradually with increasing surface coverage, whereas the PEA for both 25 and 50% termination are approximately the same.

Consistent with pure/mixed F–termination of the (100) surface [Figs. 6.3 and 6.5], there are no electronic states in the band gap. Nevertheless, for 25 and 50% F coverages, both filled and empty surface states are present in the band gap. These surface states originate mainly from the p like orbitals of surface C atoms on unterminated zig–zag chains [Fig. 6.13 (a)], similar to those observed by Kern and Hafner for an unterminated 1×1–(110) surface [20]. In case of partial surface coverages of Cl, the electronic states in the band gap arise from a combination of p–orbitals of both Cl and host surface C atoms [Fig. 6.13 (b)]. Overall, this indicates that the electronic band structures for low surface coverages of halogens, particularly F, are semimetallic in nature.

H–terminated (110)–1×1 surfaces

For mixed halogen and hydrogen termination, there is also a difference in structure between F and Cl. In the case of F, the lowest energy structures are found where F is isolated, i.e. each F–terminated surface site only has H–terminated sites neighbouring them on the same $[1\bar{1}0]$ chain. In contrast, for 50% Cl–termination, the Cl–terminated sites appear in pairs,

Table 6.3: Calculated adsorption energy per atom (E_{ads}), and electron affinity (EA) for different coverages of the (110):C and (110):H surfaces of diamond by F or Cl (eV). For H–terminated surfaces, the coverage refers to the fraction of H–sites substituted by a halogen atom. The EA for 110% H–termination and 110% C–termination are calculated to be -2.41 eV and $+0.91$ eV, respectively.

	Fluorine			Chlorine		
Coverage	E_{ads}	EA	$d_{(\text{C}-\text{F})}$	E_{ads}	EA	$d_{(\text{C}-\text{Cl})}$
(110), C–termination						
1.00	3.06	+2.38	1.35	i–	–	–
0.50	3.85	+1.56	1.38	1.08	+0.95	1.82
0.25	3.88	+1.17	1.37	1.93	+0.91	1.81
(110), H–termination						
0.50	3.79	+0.52	1.41	0.98	+0.25	1.88
0.25	3.98	−0.71	1.45	0.96	−0.29	1.89

which is a more stable geometry than the most stable geometry found for F–termination by 0.3 eV per Cl atom.

Similar to (001) and (111) surfaces, addition of hydrogen decreases the EA and for 25% halogen–coverages a NEA is observed. Moreover, similar to the diamond (111)–2×1 surface, a significant interaction is present between Cl atoms. As a consequence, at low surface coverage, for example at 50%, relaxed geometries of partially F–terminated surface differ considerably with relaxed geometries of partially Cl terminated surface 6.11. Additionally, similar to the 2×1–(111) surface, 1ML of Cl is not stable on the (110)–1×1 surface.

The electronic band structures corresponding to mixed halogen terminations are shown in Fig. 6.14. In Fig. 6.14 (a), all filled and empty states are analogous to bulk electronic states, while for 25% F [Fig. 6.14 (b)], some empty bands below the conduction band minima are associated with the p–orbitals of both F and host C atoms. For mixed Cl termination [Fig. 6.14 (c) and (d)], a combination of p–orbitals of both Cl and surface C atoms is found to be responsible for the empty states, which lie below the conduction band minima at

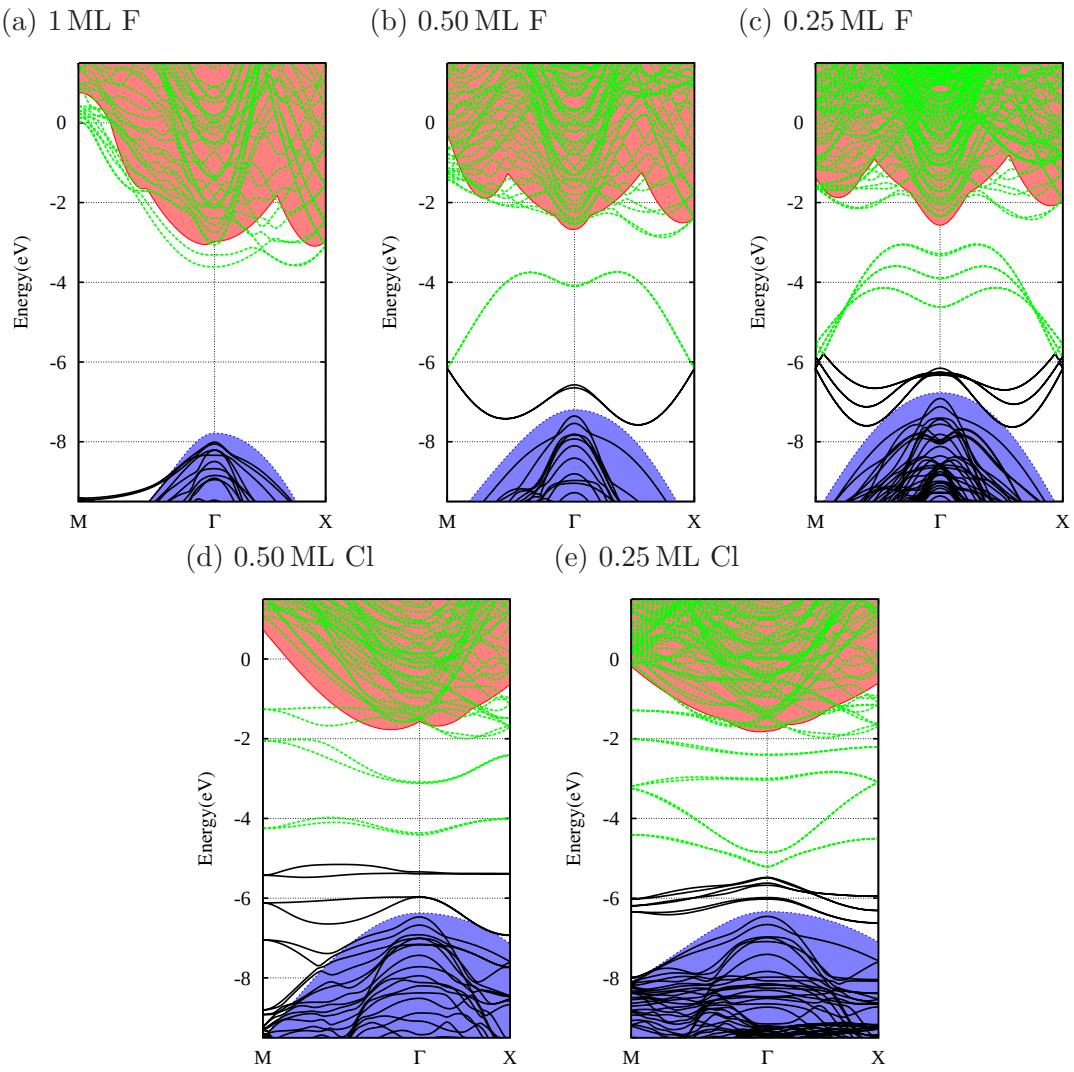

Figure 6.12: Electronic band structures corresponding to different surface coverages of F and Cl adsorbed on a clean (110)–(1×1) diamond surface. Occupied (black) and unoccupied (green) states of terminated surfaces are superimposed upon the electronic band structure of bulk (shaded regions). The zero of the energy scale is the vacuum potential for each system.

around -2 and -3 eV.

(a) 0.50 ML F (b) 0.5ML Cl

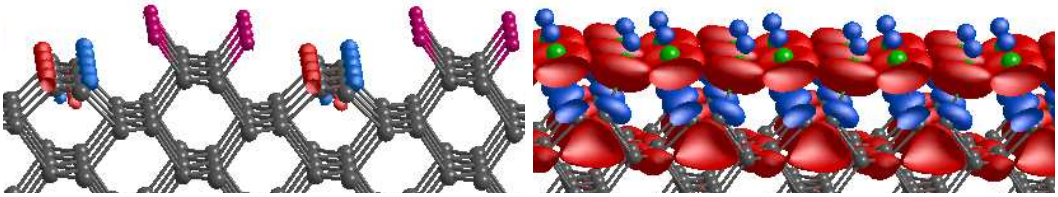

Figure 6.13: Plot of the wave function iso–surfaces for 50% coverage of halogens on C–terminated 1×1 diamond (110) surface. (a) and (b) correspond to the zone–centre states around -6.00 and -4.00 eV in Fig. 6.12(b) and (e), respectively.

6.4 Br–termination

Br–termination, as described in the introduction section of this chapter (sec 6.1), is of particular interest for biomedical applications. Bromination of Si and Ge surfaces has been studied extensively in the past [204–206], which indicates that 100% Br coverage on these semiconductor surfaces is theoretically realisable [204]. Although the (001) diamond surface reconstructs in a similar fashion to those of (001) surfaces of Si and Ge, considering the difference between the C–C and Si–Si/Ge–Ge dimer bond lengths, and the relative electronegativity of C in comparison to Si and Ge, the presence of C–Br dipoles on a diamond surface would be expected to impact the electronic and structural properties differently. Furthermore, due to the significant steric interaction between Br atoms on the length scale associated with diamond surfaces, high surface coverage (100%) may not be stable and partial surface coverages may result in practice. This is indeed supported by very limited experimental evidence [207].

Some quantum–chemical simulations have been performed on the bromination of diamond, which provides some useful insight with regard to the presence of sterical interactions due to the relatively large size of Br atoms in comparison to other halogens, such as Cl [180]. However, the relatively small clusters employed in this study, and the limited relaxation of their structure mean that further study is warranted.

To investigate the interaction of Br with diamond, particularly to predict the likely equilibrium surface coverage and its effect on thermodynamic stability and electronic properties, the DFT results of Br terminated diamond (100) surfaces are summarised in this section.

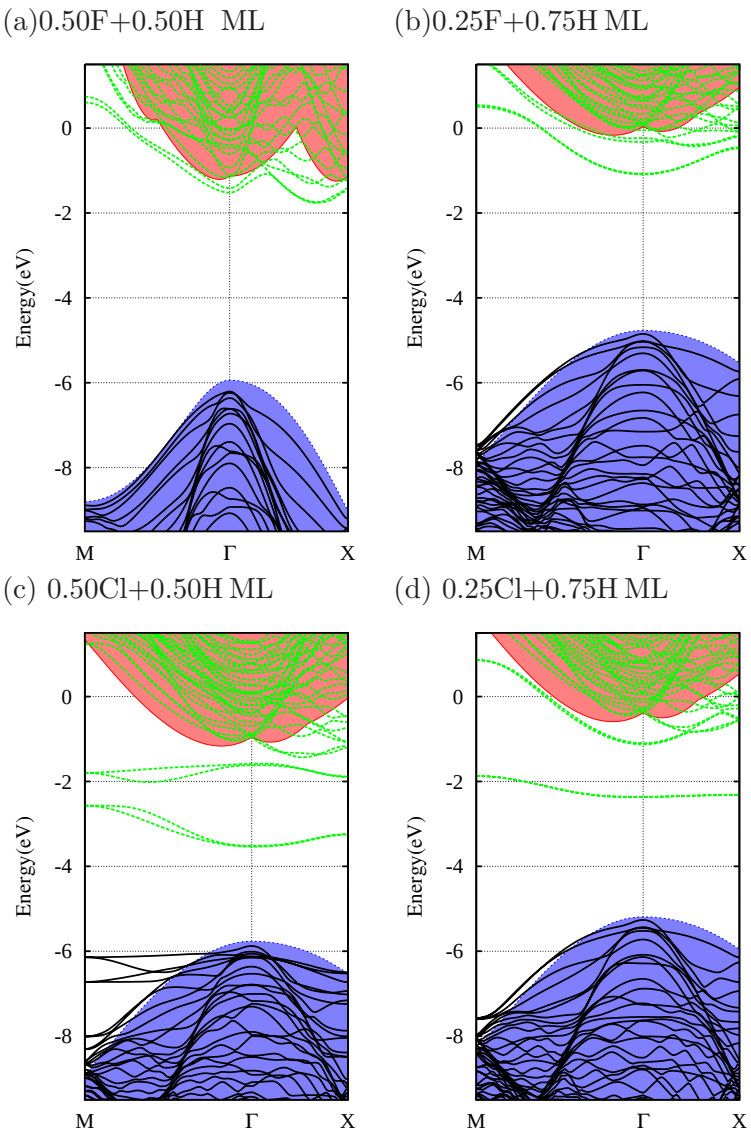

Figure 6.14: Electronic band structures corresponding to partial surface coverages of F and Cl on a H–terminated (110)–(1 × 1) diamond surface. Occupied (solid, black) and unoccupied (dotted, green) states of terminated surfaces are superimposed upon the electronic band structure of bulk (shaded regions). The zero of the energy scale is the vacuum level.

It is worth repeating here that the computational details are similar to those used in the study of F and Cl 6.3.

6.4.1 Br on the C–terminated (001)–(2 × 1) surface

As anticipated, due to strong mutual interaction between Br atoms, high surface coverages of Br on clean surface, such as 100 and 75% are not energetically stable – in simulations at these densities the Br–atoms show a tendency to form bonds with each other in preference to the surface carbon sites. The 4×2 and 4×4 geometries are found to be the most stable configurations for 25 and 50% surface coverages of Br, respectively (Fig. 6.15). The calculated surface C–C–Br bond angles for these coverages are nearly equal to 111.5°, somewhat greater than the tetrahedral and Si–Si–Br bond angles (109°) in previous calculations [208]. For both partial coverages, the calculated C–Br bond lengths are calculated to be equal to 1.92 Å, which are within 1% of the C–Br distance of 1.94 Å in CBr_4 molecule [142].

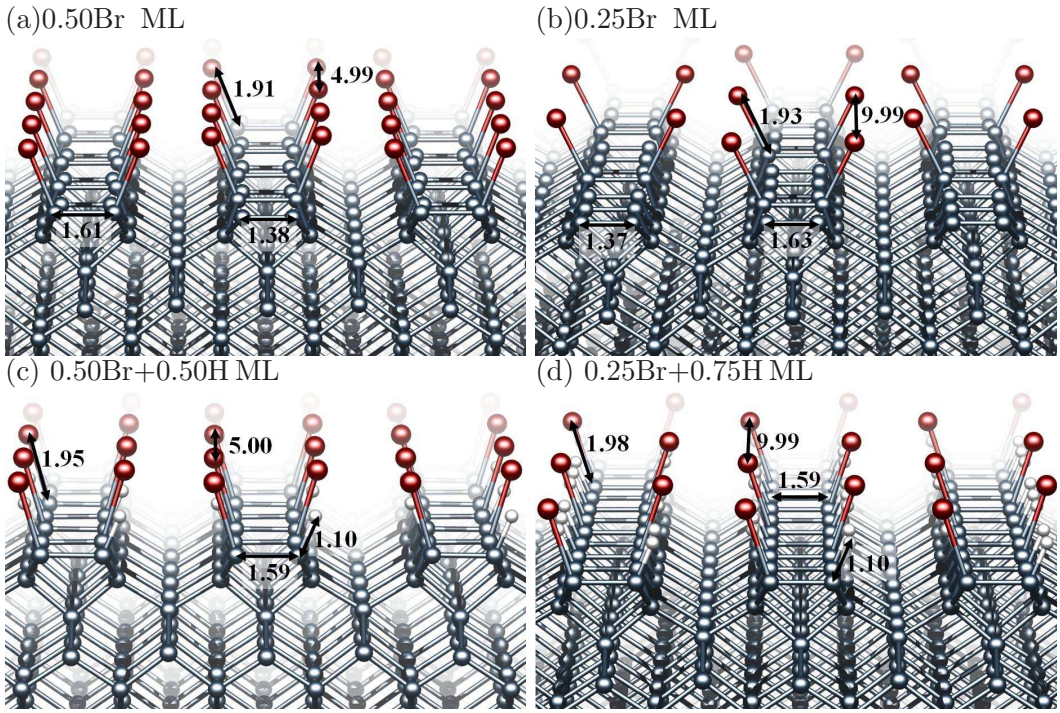

Figure 6.15: Perspective views of relaxed geometries for 50 and 25% Br termination of reconstructed C– and H–terminated (001)–(2 × 1) diamond surfaces. Distances indicated are in Å. Small, medium and large spheres represent H, C and Br, respectively.

As previously suggested [172, 180], the effect of steric interaction is clearly evident on adsorption energy, which decreases rapidly with increasing surface coverage (Table 6.4).

The adsorption energy of Br at a 25% coverage is found to be close to that of H at 100%, indicating that Br surface coverage of around 25% is likely to be achieved in practice. The EA of energetically stable structures of pure Br–terminated diamond surfaces is nearly independent of surface coverage, exhibiting a PEA of around 0.45 eV for both 25 and 50% coverage. This is smaller than the EA of clean or fluorinated diamond [93].

The trend in previous studies indicates that that NEA diamond, such as hydrogenated diamond, is chemically more suitable for bio–functionalisation than a PEA diamond [194, 197–201]. Nevertheless, for the remote monitoring of chemical process, which is based on colour changes from photoluminescent (PL) nitrogen–vacancy (NV) centres, the PEA of fluorinated diamond, is also important [197]. The small but positive EA of brominated diamond may be of some interest in terms of suitability for bio–functionalisation without the detrimental impact upon the NV centres that arise from a NEA.

The band structures corresponding to 50 and 25% of Br chemisorbed on a C–terminated surface are shown in Figs. 6.16(a) and (b). The band structures of terminated surfaces are superimposed upon the band structure of bulk diamond. For both pure and mixed partial termination, the underlying bulk bands are derived from an equivalent surface cross–section of bulk diamond.

Since in comparison to C–H surface dipoles, the effect of C–Br surface dipoles is very small, for both 25 and 50% surface coverages of Br, the shift in the band structure with respect to a clean surface is negligible (compare Figs. 6.16(a) and (b) with Fig.5.7(a)). The relatively small impact of Br can be understood from the small, positive electronegativity difference between Br (2.69 Pauling scale) and C (2.55 Pauling scale). This contrasts with the case of hydrogenation, where H (2.33 Pauling scale) is much less electronegative than C, leading to a large offset between the locations of the valence band tops, as shown in comparison to Fig. 5.7(b).

Inspection of wave functions corresponding to partial surface coverages of Br on C–terminated surface suggests that the empty electronic states in the energy range from -4 to -3 eV (Fig. 6.16(a) and (b)) are strongly localised on surface C atoms. They are mainly constituted from π^*–like orbitals (Fig. 6.17(a)). An additional unoccupied band located in the vicinity of the bulk conduction band minima near -2 eV (Fig. 6.16(a) and (b)) originate from an anti–bonding combination of Br p–orbitals with the host π surface states,

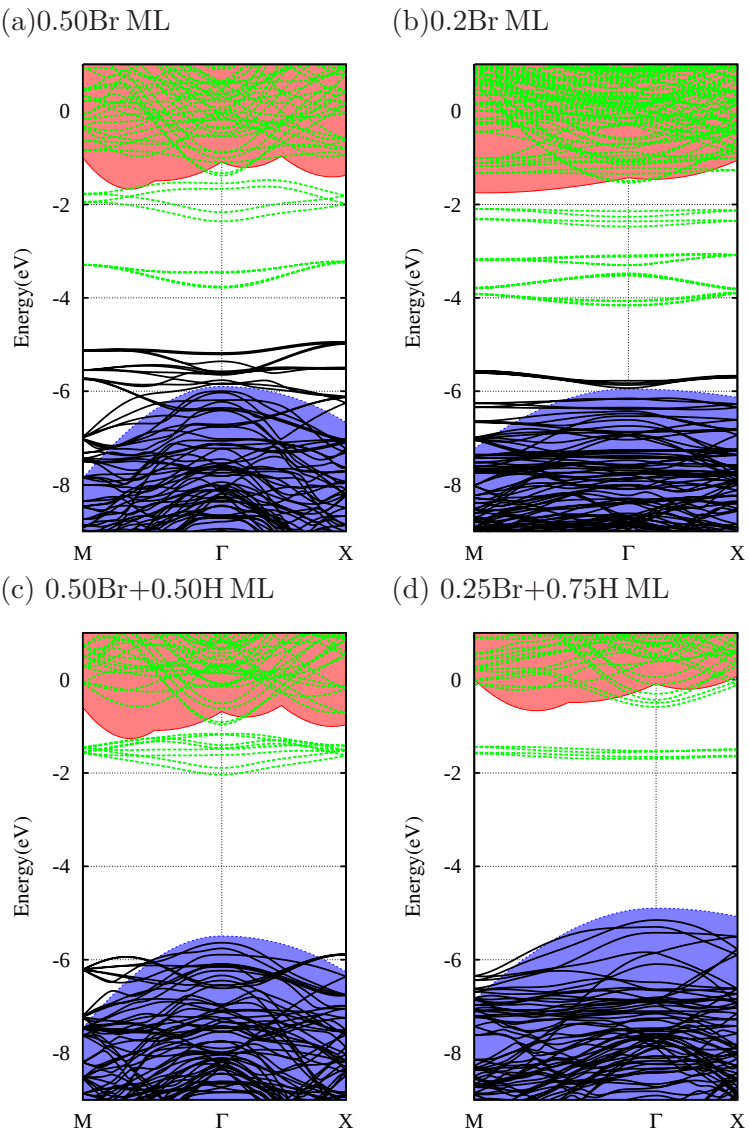

Figure 6.16: Electronic band structures for different surface coverages of Br on the reconstructed (001)–(2 × 1) diamond surface. Occupied (solid, black) and unoccupied (dotted, green) states of terminated surfaces are superimposed upon the band structure of bulk diamond (shaded regions). The zero of the energy is the vacuum level.

(Fig. 6.17(b)).

Table 6.4: Calculated adsorption energy per Br atom (E_{ads}) (eV), electron affinity (eV) and bond lengths (Å) for different coverages of the (001)–(2×1)C and (001)–(2×1)H surfaces of diamond by Br. For H–terminated surfaces, the coverage refers to the fraction of H–sites substituted by Br. C–C bond lengths in parentheses are for dimers not connected to Br.

%	E_{ads}	EA	$d_{(\text{C}-\text{C})}$	$d_{(\text{C}-\text{Br})}$	$d_{(\text{C}-\text{H})}$
			C–termination		
50	1.82	0.45	1.61 (1.38)	1.91	–
25	2.11	0.52	1.63 (1.37)	1.94	–
0	–	0.61	– (1.35)	–	–
			H–termination		
50	1.91	0.01	1.59	1.95	1.10
25	2.07	−0.57	1.59 (1.60)	1.98	1.10
0	–	−1.96	– (1.61)	–	1.10

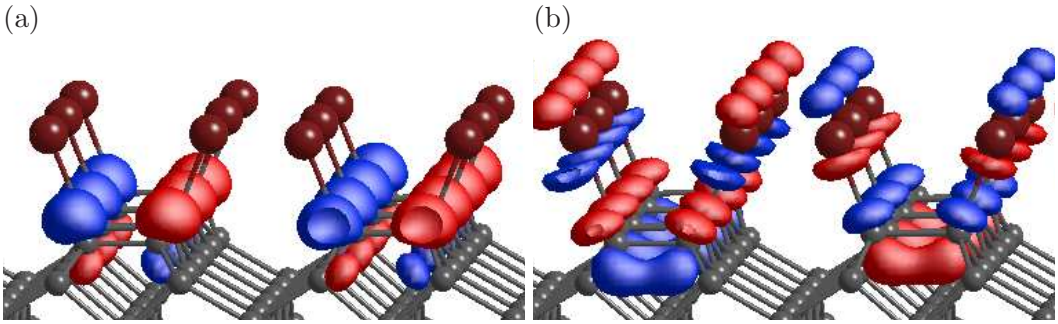

Figure 6.17: Plot of the wave function iso–surfaces for 50% coverage of Br on C–terminated 2×1 diamond (100) surface. (a) and (b) correspond to the zone–centre states around −3.5 and −2.0 eV in Fig. 6.16(a), respectively.

6.4.2 Br on the H–terminated (001)–(2×1) surface

Many chemical treatments, used for the surface processing, may result in a mixed termination, such as bromination via the use of hydrogen bromide. There is little data available for

mixed H/Br termination on diamond, however, the presence of H surface bonds, in addition to Br surface bonds, has been often observed in the cases of Si and Ge [209].

Mixed H and Br termination reduces the EA relative to the H–free case and a negative value of $-0.57\,\text{eV}$ is calculated for 25% Br coverage. This can be attributed to the increasing number of of C–H surface dipoles, which generally reduces the EA of clean surface. It is found that the 2×2 and 2×4 geometries are the most stable configurations for the adsorption of 50 and 25% of Br on an otherwise hydrogenated diamond surface (Fig. 6.16). The 25% coverage of Br on a 2×2 geometry also exhibits similar adsorption energy to that calculated for equivalent coverage of Br on a 2×4 geometry.

The calculated C–Br (1.98 Å) and C–H (1.10 Å) bond lengths for 25% Br coveage are similar to those of 50%. The calculated surface C–C–Br bond angles for 50 and 25% are 107.3 and 108.4°, respectively, slightly smaller than the bond angles calculated for pure Br termination. Reduction in surface C–C–Br bond angles probably indicates the extent of steric interaction between H atoms.

Figs. 6.16(c) and (d) show the band structures corresponding to (50% Br + 50% H) and (25% Br + 75% H) combinations. For both mixed surface coverages of Br, the unoccupied electronic states near $-1.70\,\text{eV}$ (Fig. 6.16(c) and (d)), are delocalised and made of an anti–bonding combinations of Br p–orbitals with states arising from the reconstructions. The calculated upward shifts (relative to a clean surface) in the band structures of mixed 50 and 25% Br terminated surfaces are found to be 0.30 and 1.00 eV, respectively, consistent with the relative values of the EAs.

6.5 Chapter summary

The chemical modification of diamond surfaces is motivated by a number of possible applications. For example, halogen termination is currently a area of investigation in the modification of nano–diamond particles containing the NV optical centre [192, 210]. Here it is crucial that the optical centre is in the negative charge state, so the PEA of halogen termination protects against the generation of a p–type surface layer driven by a NEA.

In addition to the impact upon the electron affinity, the thermal stability of the surface termination is also of great significance in some applications. For example, hydrogen and

oxygen termination of diamond surfaces may be unstable in high–temperature thermo–tunnel energy generation applications.

The simulation of halogen termination of low index diamond surfaces, with a wide range of surface structures (i.e. adsorbate periodicities), has therefore been performed to shed light upon both the adsorption energy of these species, and their impact upon the EA, from which some conclusions have been derived.

Where the aim is to achieve as high a coverage as possible, the best choice of halogen termination is fluorine, with 100% coverage being energetically stable for all surface orientations examined. The adsorption energy for fluorine is calculated in the 2.7–4.4 eV/atom range, so that if 100% coverage were attained and desorption proceeded by loss in pairs, one would expect stability to high temperatures. Indeed, this is supported by the limited available experimental evidence [186]. These energies compare favourably with the comparable energies for H–termination which lie in the 1.0–2.8 eV/atom range.

Due to weak energetic stability, Cl and Br are both less likely to saturate a diamond surface in high coverages, and are therefore less favourable in terms of both thermal stability and EA control. For example, for Cl on (001)–2×1, the difference in the adsorption energies at 100 and 50% is such that the *average* adsorption energy for the second 50% of the 100% coverage is very close to zero. This means that when the coverage is high and approaching 100%, it must *cost* energy to take more Cl atoms from the Cl_2 gas phase and attach them to the surface. This would imply a maximum coverage of less than 100%, although the specific maximum coverage likely to be achieved cannot be obtained from the currently available data. This is in sharp contrast to the case of F termination, since the average adsorption energy per F atom in the 50–100% range is 3.75 eV, close to the adsorption energy at low coverage.

Another issue is whether one considers the halogen or the surface to be the limiting factor in the termination chemistry. Whilst 100% Cl on the (001) surface yields the same energy output as 50% on the surface and 50% in gas, a higher amount of energy is released from the same quantity of Cl gas by doubling the area of diamond involved. If the supply of Cl is limited, then our calculations show that the coverage will be spread out. Indeed, since the adsorption energy for F–termination also tends to increase with decreasing coverage, the F–termination would also tend to be spread out if the supply of F is limited. Indeed,

the surface coverage will depend on details of the gas phase; however, chemical kinetics are less important in current context.

For the equilibrium structures of both F– and Cl–terminations, there is a modest impact upon the EA with orientation. The calculated adsorption energies are more strongly dependent on the surface orientation, suggesting that among the low index planes, the (001)–2×1 surface may represent the most stable. Based upon F and Cl results, inspection of remaining Br–terminated diamond (110) and (111) surface orientation is therefore less important.

Combination of hydrogen and halogens is also of some interest, and has already been seen in the fluorinated nano–diamonds [192]. The ability to chemically modify a surface to obtain both negative and positive EAs is indeed very important. Since the EA of a mixed halogen and hydrogen terminated surface can be reasonably well represented by a weighted average of the fully–terminated constituent surfaces, based upon the 100% fluorinated surfaces yielding PEAs in the range 2.1–2.5 eV and 100% H–termination yielding NEAs in the range 1.96–2.41 eV, theoretically mixed termination can offer various values of EA, suitable for the specific applications in which the diamond surface is to be employed. In case of heavy molecules, such as for pure Br–termination, the electron affinity is nearly independent of surface coverage. However, in line with mixed F– and Cl–termination, addition of hydrogen on unterminated sites reduces the EA.

A very high surface concentration ($\approx 100\%$) of H is known to be possible, and by exposing carbon–terminated surfaces to a halogen source under suitable temperature conditions, high levels of halogen termination are expected to be viable. However, achieving the full range of mixed contributions of halogens and hydrogen is likely to represent a challenge in terms of sample preparation.

Although, high coverage (100%) of Br is completely unstable, low coverages (25%) of Br are energetically comparable with respect to a fully hydrogenated diamond surface and therefore can be achieved by exposing a clean surface to a suitable bromine source under controlled environments. This could be of particular interest for direct attachment of high coverages of some commonly used bromine–functionalised–biomolecules, such as 4–bromostyrene, quinolinium and isoquinolinium bromides, on a clean diamond surface [211].

Chapter 7

Ultra thin films of transition metals and their oxides on diamond

> If I have ever made any valuable discoveries, it has been owing more to patient attention, than to any other talent.
>
> Isaac Newton (1642–1727)

7.1 Introduction

Diamond with an NEA is of particular interest for photocathode and thermionic applications because of the underlying electrical and thermal properties intrinsic to diamond [22, 23, 87, 166–169, 212–214]. A large NEA, where the vacuum level lies below the conduction–band minimum, enables conduction–band electrons to be emitted into vacuum with little or no barrier.

A widely–adopted and perhaps the simplest approach, to produce an NEA with diamond, uses hydrogen surface treatments [22,23,166,212,213]. The C–H surface bonds form a dipole layer and the resultant electric field causes the bands to bend upward, thus lowering the work function significantly from that of carbon terminated diamond at 5 eV, to around 3 eV. However, the reduced work function is still too high for low–temperature thermionics, and operation at elevated temperatures (above 500 °C) results in the desorption of hydrogen, and a substantial increase in work function [24].

In recent years, a wide range of alternative surface terminations including halogens,

oxygen [93], alkali–halides [94, 95] and alkali–oxides [21], have been explored, which provide some control over χ. However, most either increase the work function or are unstable at high temperatures (above $\sim 400\,^{\circ}\mathrm{C}$) and hence, are not suitable for thermionics. For example, F– and O–termination, which are relatively thermally stable in comparison to H, result in the positive χ and increase the work function [22,93], whereas CsO, which yields a low value of work function, is found to be unstable above $\sim 377\,^{\circ}\mathrm{C}$ [96, 214–216]. Similar issues have been encountered with alkali halides [94,95]. Perhaps the best candidate currently proposed to address both NEA and thermal stability is monolayers of lithium–oxide [21]. However, Li–based coatings are not robust enough under typical semiconductor device fabrication processes. Hence, for an efficient electron emitter, a low work function and thermally stable diamond surface remains to be identified.

Owing to the superlative electrical properties in conjunction with the excellent adhesion [217,218], transition–metals (TMs), are obvious candidates for solid–state devices operating under extreme conditions [86, 219–222]. Research conducted on pure TM–coated diamond surfaces suggests that a significant reduction in χ is also achievable [24, 133, 223–226], facilitating the use of diamond for cold cathode electron emission applications [99, 227], including the realisation of thermo–tunnel devices [84].

Experimental evidence suggests that the coatings of TMs, such as Cu, Ni, Co, Zr, Au, and Ti, yield a thermally stable NEA, even at around mono–layer (ML) coverage [24, 133, 225, 226]. For example, sub–monolayer (0.50Å thick) deposition of titanium on diamond (111) surfaces yields an NEA and a reduced Schottky barrier height of $1 \pm 0.20\,\mathrm{eV}$ [226]. Some of these experimental and theoretical studies [24, 133, 202, 225, 228, 229] indicate that the oxide of TMs (TMOs) may also have great potential for thermionics, as in addition to improved adhesion and thermal stability, there is a possibility of significant reduction in χ resulting from large metal–oxygen dipoles akin to those predicted for lithium oxide termination [21].

Estimation of χ is important not only for thermionics but is also a key parameter to understand the TM–diamond interfacial characteristics relevant to electronic devices. An accurate extraction of the barrier–height, ϕ_B, from χ has been demonstrated in a number of models for TM–semiconductor interfaces of Si and Ge, as well as some group III–V compounds [230–232]. According to the most commonly used Schottky–Mott model for an

ideal interface between a metal and a p–type semiconductor used [24,133] for metal–diamond interfaces, the barrier height can be described as a function of χ as

$$\phi_{\mathrm{B}} = E_{\mathrm{g}} - (\phi_{\mathrm{M}} - \chi), \tag{7.1}$$

where ϕ_{M} is the metal work function and E_{g} is the band–gap of diamond.

Quantum–chemical simulations are well placed to predict the characteristics of TM/TMO–diamond interfaces. Previously, investigation of metal/metal oxide–semiconductor interfaces has largely been of wide–gap, ionic semiconductors and covalent narrow–gap semiconductors [223, 230, 233–235]. Diamond, as a wide–gap, covalently–bonded material, has received relatively little theoretical attention to–date.

Quantum chemical calculations [202, 229, 236] for selected TM–diamond interfaces have demonstrated that, in addition to the chemical nature of TMs, surface coverage has a discernible effect upon adhesion and electronic properties. For example, Ti adatom and 25% surface coverages exhibit significantly different adsorption energies per adsorbate atom of 7.19 and 6.62 eV, respectively [202]. Although results of a recent study on Cu– and Ti–diamond (111)–oriented interfaces are not directly comparable to the present study, the calculated work of separation, which is the measure of interfacial adhesion, decreases with the carbide formation enthalpy ΔH_{f} (Ti<Cu) [229], *i.e.* more energy is required to remove a carbide forming metal from the diamond surface.

Schottky barrier heights of TM–diamond interfaces have been examined both in computational and experimental studies [24, 133, 225, 226, 236], but the impact of ultra thin TM/TMO layers on the stability and electrical/electronic properties is largely unexplored at an atomistic level. To understand the complex interactions between adsorbates and the diamond surface, quantum–mechanically based computational studies are of great interest. In this chapter, the results of density functional simulations into the energetics and χ_{s} of diamond (001) surfaces covered by either TMOs or up to a mono–layer of selected TMs, such as Cu, Ni, Ti, V and Zn, have been presented. The choice of metals and their oxides guided in part by the metals used in experiment, and in part to include metal species which have qualitatively different carbon chemistries.

7.2 Theoretical Technique

For the study of TMs, the basis sets consist of independent sets of s–, p–, and d–type Cartesian Gaussian functions of four widths, amounting to forty functions per atom. A slightly smaller vacuum of 13 Å is used in current simulations and as described in Chap. 3 and 6, a gird of ghost atoms is added into the vacuum to overcome the evanescent nature of the surface states. The slab thickness and other computational details, such as the cutoff and Brillouin zone sampling are described in Chaps. 6 and 3.

To check the validity of the LDA functional in the current context, different tests have been performed. For example, the calculated lattice constants for ground–state configurations of Cu (3.54Å), Ni (3.42Å), Ti (a=2.87, c=4.55Å) V (2.91Å) and Zn (a=2.59, c=4.63Å)are calculated to be within 5% of experimental values and previous comparable tight–binding calculations [237, 238]. Additionally, the heat of formation for TiC and VC are reproduced to within 1% of experiments [239, 240].

Work functions (eV) for different bulk metals, such as Cu(4.76), Ni (5.23), Ti(4.36) and V(4.34) are calculated to be within 0.1 eV of literature values [142]. Based upon these comparators, it can be concluded that the treatment of the TMs is within the norms of LDA calculations, and suitable for the current study.

Similar to halogen termination, for surfaces with sub–monolayer coverages, a wide variety of symmetrically non–equivalent structures were explored to establish the most probable candidate for the lowest energy arrangement. For example, with 25% coverage, surface cells with (2×2) and (4×1) arrangement, along with the permutations of arrangements with (4×2) and (4×4) periodicities were included. It is worth noting here that the metal–carbon bond–lengths vary significantly. In this study, only those relaxed structures have been included, which are strongly chemically bonded to the surface. The relaxed structures for which the bond–lengths are bigger than 15% of the reported metal–carbon bond-lengths in the corresponding organo–metallic compounds [142] are not included.

To calculate the adsorption energy per adsorbate atom (E_{ads}) corresponding to each equilibrium structure, this chapter utilises a slightly different form of adsorption energy equation, as described in previous Chap. 6

$$E_{\mathrm{ads}} = \frac{1}{n}\left(E_{\mathrm{tot}} - E_{\mathrm{surface}} - n\mu_{\mathrm{X}}\right), \tag{7.2}$$

where μ_X is the chemical potential of a free metal atom and E_{tot} is the total energy of either a clean or an oxygenated diamond $a \times b$ slab terminated by n metal atoms. In the case of pure TM termination, $E_{surface}$ represents the total energy of a clean reconstructed $a \times b$ diamond slab, while for TMOs, $E_{surface}$ will be the total energy of an oxygenated (ether configuration) $a \times b$ diamond slab.

Due to multiplet, functional, and basis–set effects it is difficult to calculate accurate energies of free transition metal atoms using standard density functional techniques. To mitigate such errors, first, the energy per atom for each metal species in the corresponding bulk metal are calculated and then the experimental cohesive energies [241] [Cu (3.49 eV), Ni(4.44 eV), Ti (4.85 eV), V (5.31 eV) and Zn (1.35 eV)] are added to obtain an estimate of the free atom energy.

For thermodynamically stable metal adsorption onto the diamond surface, the adsorption energies must then be negative, assuming that the loss of metals from the surface during annealing is via evaporation into the atomic state. It is important to put the absolute adsorption energies into context. For example, one might also consider the theoretical cohesive energies of Cu (4.29 eV), Ni (5.98 eV), Ti (6.29 eV), V (6.49 eV) and Zn (1.91 eV) as a reference [241]. Such an approach would lead to considerably higher adsorption energies, but has no effect upon the relative energies of different sites or surface coverages.

7.3 Results

In this section, adsorption of TMs (Cu, Ni, Ti, V and Zn) and their oxides onto a clean reconstructed 2×1 diamond (100) surface has been summarised. Since identification of high–symmetry sites is understood to be a prerequisite for metal atom adsorption, a brief discussion on potential TM high–symmetry sites has also been included.

7.3.1 Methodology validation and identification of high symmetry sites for TM atom adsorption

As mentioned in the previous Chap. 6, the current approach has been validated against literature values for clean, hydrogenated, and ether–terminated diamond. The electron affinities, structures, and adsorption energies are in good agreement with both theory and

experiments [18–25]. In addition, allowing for the impact of functional, basis set and surface periodicities on calculations, it is also noted that the calculated properties of Ti terminated surfaces are in reasonable agreement with recent theoretical studies [202]. More detailed comparisons are presented in Sec. 7.3.4.

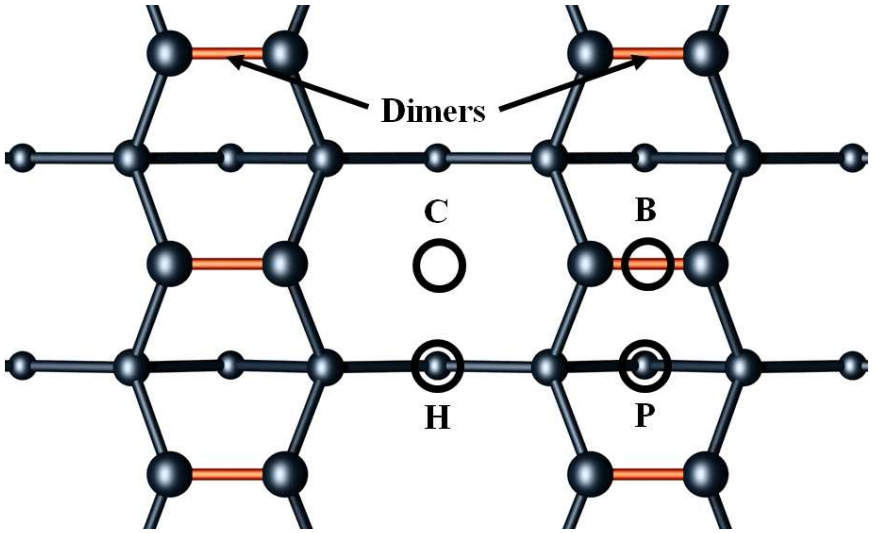

Figure 7.1: Plan view of high symmetry adsorption sites on reconstructed C–terminated (001)–(2 × 1) diamond surface. Symbols and rings indicate the sites defined in the text. The grey circles indicate the carbon atoms in the top three layers of the diamond surface, with increasing depth indicated by decreasing size.

In order to put the different potential equilibrium structures into context, it is convenient to label the high–symmetry sites occupied by metal atoms at different surface coverages. This is done with reference to the assumption, as made in previous studies, that prior to metal atom adsorption, the 2×1 reconstruction is retained [171]. Then four high–symmetry sites can be labelled [202, 242, 243] the pedestal (P), bridge (B), hollow (H), and cave (C) sites, as shown schematically in Fig. 7.1.

To further assess the surface site stability, two other atomic arrangements have also been examined. Perspective views of atomic arrangements corresponding to the 1 ML coverage are shown in Fig. 7.2. The first configuration [Fig. 7.2(a)] is similar to a mono–hydrogenated diamond (100) surface, while the second configuration (Fig. 7.2(b)) can be obtained by placing adsorbates midway between P and H sites. These structures are found to be relatively high

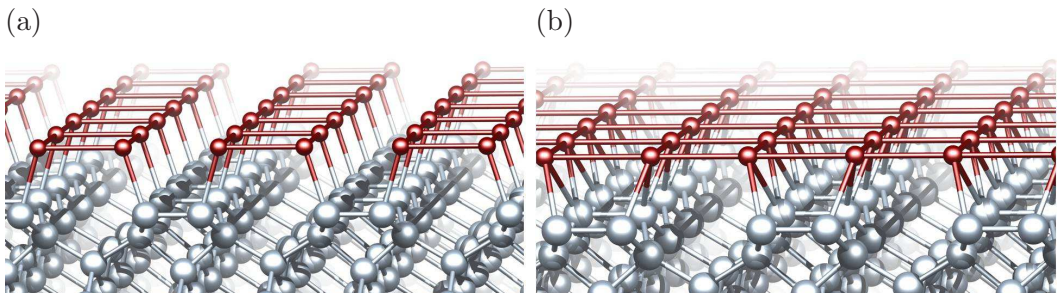

Figure 7.2: Perspective views of 1 ML of TMs on low–symmetry sites of reconstructed (001)–(2 × 1) diamond surface.

in energy for each surface coverage for all metals examined and therefore are not discussed here.

For the candidate metal species, the main objective is to identify the equilibrium structures for adatoms, 0.25, 0.50, and 1 ML of Cu, Ni, Ti, V and Zn on diamond (001) oriented surfaces. Particularly for low surface coverages, it is important to note that there are many ways to achieve the same average surface atom density. For example, one adatom per four surface carbon sites corresponding to 25% might be described using reconstructed 2 × 2, 4 × 1, 4 × 2 or any number of other surface cells. These three geometries have been included in the evaluation of the equilibrium properties of 0.25 ML coverages. For the calculations of adatom adsorption energy, a 4 × 4 supercell, made up from four primitive 2 × 1 surface unit cells, is used to model the clean substrate. For the most stable relaxed structures for different surface coverages of the selected TMs, thermodynamic stability and electronic properties are discussed in following sections.

7.3.2 Cu termination

Copper is an attractive TM for both the CVD process and metal contact fabrication [24, 244–246]. Additionally, applications such as heat sinks, where the material properties of both copper and diamond are essential [245] mean that diamond–copper interfaces are of particular interest. Since copper does not readily form a carbide, it might be expected to form a relatively abrupt and chemically inert junction with diamond.

Based upon the poor co–ordination strength of Cu with carbon in organo–metallic compounds, at low coverages of Cu the B and C sites might be expected to be favoured as

they have the lowest metal–carbon co–ordination of the four sites. In adatom calculations, copper prefers the C site, with other sites representing meta–stable locations. The adatom adsorption energies are listed in Table 7.1.

Table 7.1: Calculated adatom adsorption energy per adsorbate atom (E_{ads}) for Cu, Ni, Ti V and Zn (eV). In each case, the most stable site is indicated by the underlining.

	Site			
Metal	B	C	H	P
Ti	-	−2.85	−3.54	<u>−5.36</u>
V	-	−5.41	−5.60	<u>−6.00</u>
Ni	−2.40	−1.92	−1.84	<u>−2.73</u>
Cu	−1.18	<u>−1.58</u>	−0.95	−1.23
Zn	0.38	<u>−0.22</u>	-	0.94

For 0.25, 0.50, and 1 ML of Cu on the diamond surface, the equilibrium structures obtained in this study are shown in Fig. 7.3, and the adsorption energies are summarised in Table 7.2. Similar to adatom adsorption, the C site on 4×1 (0.25 ML) and 2×1 (0.5 ML) geometries are found to be the most stable, while the H site for all surface geometries is unstable. It is also notable that among the structures examined for 0.25 ML, the minimum in energy occurs where Cu atoms lie on adjacent C sites, indicating that inter–adsorbate interactions stabilise the adsorption of copper.

For 1 ML of Cu, a combination of B and C sites gives the most stable configuration, as shown in Fig. 7.3(a). Configurations including other pairings, such as P+C, P+H and B+H, are found to be either metastable or unstable (Table 7.2). It is important to note here that Cu terminated diamond surfaces exhibit negative adsorption energies, which are increasingly stabilised with reducing Cu coverage. This indicates that Cu–Cu interaction is helping to stabilise the surface.

Depending upon the surface coverage and adsorbate sites, Cu–C bond lengths vary between 1.9 and 2.2 Å, consistent with the Cu–C bond lengths in organo–metallic com-

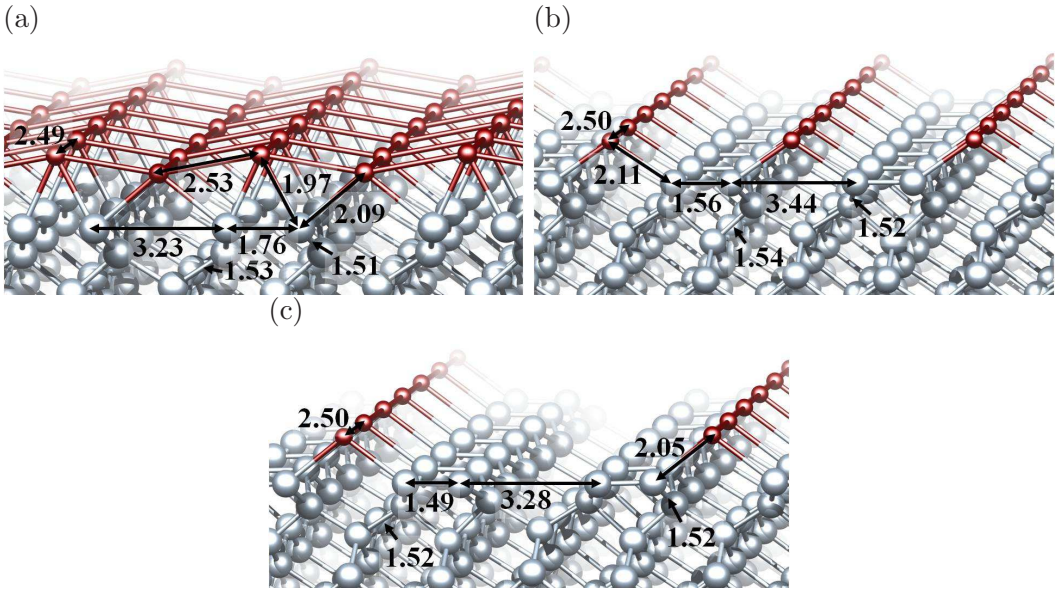

Figure 7.3: Perspective views of relaxed geometries for (a) 1.00, (b) 0.50, and (c) 0.25 ML of Cu on the (001)–(2 × 1) diamond surface. Bond–lengths are indicated in Å.

pounds [142]. Relaxed structures (Fig. 7.3) retain the underlying C–C 2 × 1 reconstruction at 0.25 and 0.50 ML, but this is unstable for 1 ML. The interaction between Cu atoms has also a significant effect upon χ; the values vary between a PEA of 0.10 eV and a NEA of −0.55 eV with coverage and geometry (Table 7.2).

To further illustrate the electronic properties as a function of coverage, the band–structures corresponding to the most stable configurations of 0.25, 0.50, and 1 ML are examined. The band–structures of C–terminated surfaces, plotted in full in Fig. 5.7, are superimposed upon those of the Cu–terminated surfaces in Fig. 7.4. States resembling those from the carbon dimers on unterminated (001) surfaces of π and π^* character lie around the top of the bulk valence–band. Fig. 7.4(a) shows that for 1 ML of Cu, several occupied and unoccupied states are present above the diamond valence–band. Inspection of wave functions of the filled and empty levels suggests the partially occupied states around −4.10 eV and the empty band around −1.00 eV correspond to d–orbitals localised in the Cu layer, whereas the empty states around −1.80 eV are due to hybridised orbitals related to both C and Cu atoms.

Table 7.2: Calculated adsorption energy per Cu atom, E_{ads}, χ, Schottky barrier, ϕ_{B}, dimer bond–length $d_{(\mathrm{C-C})}$ and carbon–copper bond–length $d_{(\mathrm{C-Cu})}$, for varying coverages of Cu on a diamond (001) surface. Energies are in eV, lengths in Å. The B+H and P+H configurations for 1 ML, and the H site for 0.25 and 0.50 ML, are unstable.

Coverage (ML)	Site	Geometry	E_{ads}	χ	ϕ_{B}	$d_{(\mathrm{C-C})}$	$d_{(\mathrm{C-Cu})}$
1.00	B+C	2×1	−2.93	−0.55	0.44	1.76	1.97–2.09
1.00	P+C	2×1	−2.83	0.05	1.04	1.73	2.08–2.23
0.50	B	2×1	−1.51	−0.24	0.75	1.60	1.96
0.50	C	2×1	−2.51	−0.66	0.34	1.56	2.11
0.50	P	2×1	−1.57	−0.57	0.42	1.57	2.13
0.25	B	4×1	−1.53	−0.31	0.68	1.37–1.58	1.95
0.25	C	4×1	−2.16	0.10	0.89	1.49	2.05
0.25	P	4×1	−1.59	−0.13	0.86	1.37–1.57	2.12

There are fewer bands in the diamond gap for partial surface coverages, and they are less dispersive. In the case of 0.50 ML, partially occupied states near −5.90 eV originate from a strong anti–bonding combination of surface Cu d–orbitals with the host π^*–like states, while the fully unoccupied states around −2.30 eV are the results of bonding combination of surface π– and Cu d–orbitals. For 0.25 ML, pairs of electronic states near −4.50 and −2.00 eV are similar to those observed for 0.50 ML, and formed from bonding and anti–bonding of Cu d–orbitals with the host surface reconstructions. The nature of the wave function iso–surfaces for 100 and 25% surface coverages of Cu is depicted in Fig. 7.5.

7.3.3 Ni termination

Previous studies of the Ni–diamond interface [225,236] indicate that Ni adsorption may lead to a NEA. Photoemission spectra confirm a sharp NEA peak [225], however the magnitude of the NEA is not known. Despite the low thermodynamic stability of nickel–carbide, Ni shows a strong adhesion with the diamond surface and the reactions of Ni atoms with

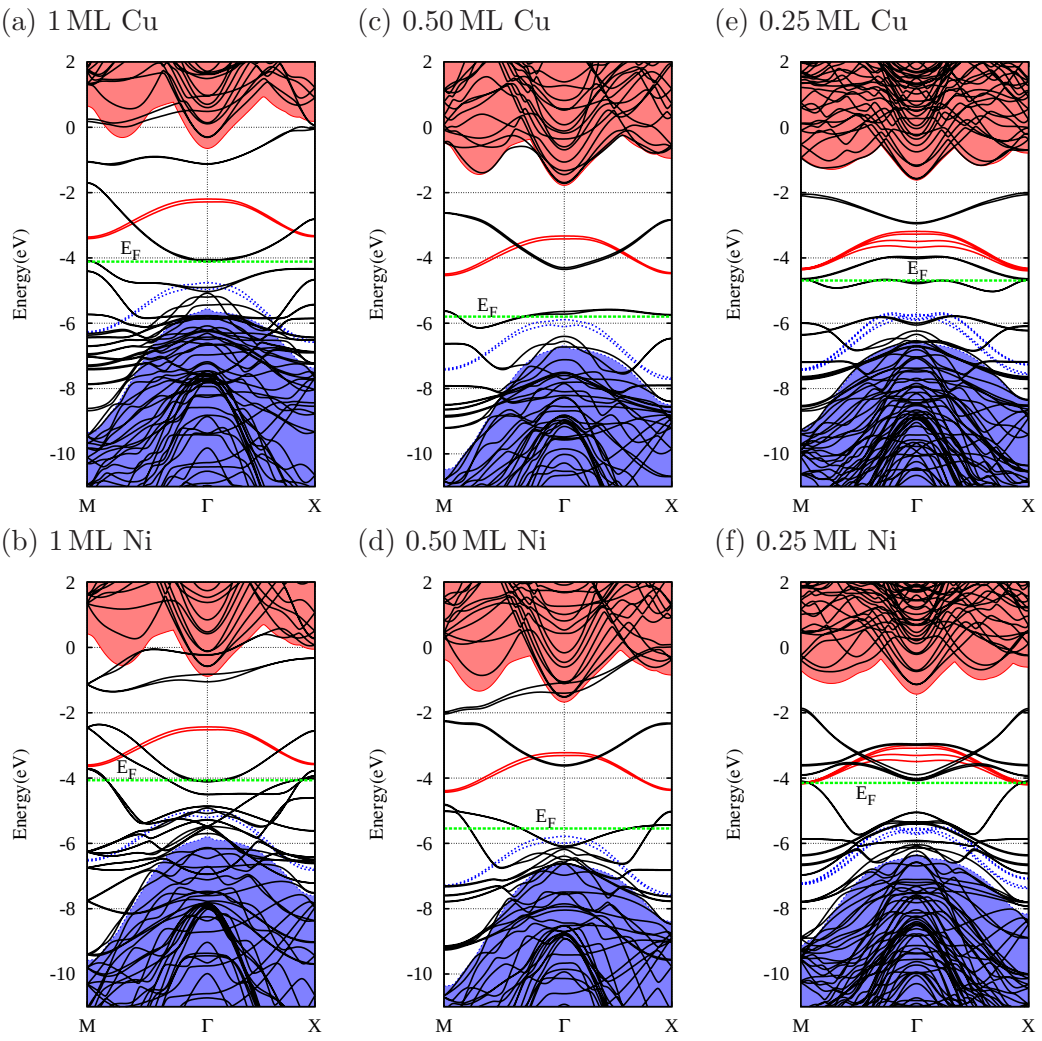

Figure 7.4: Band structures in the vicinity of the band–gap along high–symmetry directions in the Brillouin–zone for various coverages of Cu and Ni on (001) diamond surfaces. Black lines represent the states of the metal terminated surfaces with the occupancy indicated by the location of the Fermi–level. Blue and red lines correspond to occupied and empty states of the C–terminated surface (Fig. 5.7(a)). The zero of the energy scale is the vacuum level, and the C–terminated surface band structure is aligned such that the average potential in the bulk of the slab is co–incident with the same region in the metal–terminated cases.

diamond surface are highly exothermic (Table 7.3). In contrast to Cu, adatom adsorption of Ni favours the P site (Table 7.1), being 0.33 eV more stable than the B site.

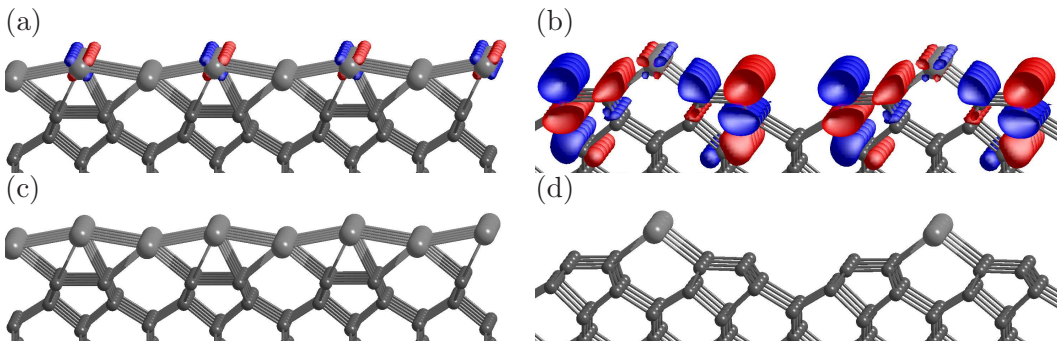

Figure 7.5: Plot of the wave function iso–surfaces for 100 and 25% coverage of Cu on diamond (100) surface. (a) and (b) correspond to the zone–centre states around −4.00 and −4.70 eV in Fig. 7.4 (a) and (e), respectively. The big and small gray spheres represent Cu and C atoms, respectively.

The stability of the P site is reduced with increasing coverage, where B and C sites are favoured (Table 7.3). In common with Cu, the B+C configuration is found to be the most energetically favourable arrangement for 1 ML of Ni. Furthermore, at 0.25 ML coverage, for every high symmetry site, adsorption of Ni on 4×1 geometry (where surface adsorption sites are adjacent) is more stable than that on 2×2 and 4×2 geometries, again indicating the energetic favourability of structures with metals on adjoining sites.

It is found that an underlying 2×1 reconstruction in the upper most carbon layer is unstable for 1 ML of Ni. However, as with Cu, for Ni this 2×1 reconstruction is preserved at lower surface coverages. The C–Ni bond–lengths lie in the 1.82–2.12 Å range, close to the C–Ni bond–lengths [142] in organo–metallic compounds (∼1.90 Å). The adsorption energies, listed in Table 7.3, show that the formation of a metal layer from Ni is more energetically favourable than the corresponding reaction with Cu. Experimentally, it is known [24] that thin Cu layers have a tendency to form islands on diamond surfaces. The stronger interaction between Ni and diamond observed here may suggest that island formation will be less prevalent in this case.

Akin to Cu adsorption on 2×1 and 4×1 geometries, Ni–Ni interactions appear to have an impact upon χ. At 0.25 ML a small PEA is calculated, whereas 0.50 and 1 ML coverages yield NEAs of −0.78 and −0.29 eV, respectively. The higher stability and very small barrier height of nickel on diamond, relative to Cu, makes it more favourable for the formation of

Table 7.3: Calculated adsorption energy per Ni atom, E_{ads}, χ, Schottky barrier, ϕ_{B}, dimer bond–length $d_{(\text{C}-\text{C})}$ and carbon–nickel bond–length $d_{(\text{C}-\text{Ni})}$, for varying coverages of Ni on a diamond (001) surface. Energies are in eV, lengths in Å. The P+C configuration for 1 ML is unstable.

Coverage (ML)	Site	Geometry	E_{ads}	χ	ϕ_{B}	$d_{(\text{C}-\text{C})}$	$d_{(\text{C}-\text{Ni})}$
1.00	B+C	2×1	-4.25	-0.29	0.15	2.50	1.85
1.00	B+H	2×1	-4.10	0.20	0.63	2.54	1.82–2.07
1.00	P+H	2×1	-3.60	0.67	1.1	2.50	2.06
0.50	B	2×1	-3.12	-0.56	-0.13	1.51	1.87
0.50	C	2×1	-3.34	-0.78	-0.33	1.96	1.92
0.50	H	2×1	-2.91	0.70	1.13	1.70	2.12
0.50	P	2×1	-2.98	0.13	0.56	1.50	2.07
0.25	B	4×1	-3.18	-0.26	0.17	1.37–1.50	1.88
0.25	C	4×1	-3.06	0.28	0.71	1.49	1.99
0.25	H	4×1	-2.38	0.50	0.93	1.53	2.01
0.25	P	4×1	-2.99	0.30	0.73	1.37–1.50	2.07

ohmic contacts, which are actually highly desirable in the development of low resistance metal–diamond interfaces for diamond electronics.

The band structures corresponding to different coverages of Ni are shown alongside those of Cu–termination. Similar to Cu–termination, as shown in Fig. 7.4, several bands are present in the band–gap of the underlying clean diamond. In all cases, states in the band-gap of the underlying diamond are linear combinations of Ni 3*d*–orbitals, and in the cases of partial coverage, π and π^* states from the underlying surface reconstructions.

7.3.4 Ti termination

Consistent with its carbide forming nature, Ti experimentally exhibits strong adhesion with the diamond surface, able to withstand the high temperatures, and is compatible with conventional diamond growth and device processing techniques [217, 247]. Additionally, the

growth rate on carbide forming substrates is higher than on substrates that do not form a carbide [247]. Strong adhesion at the metal–diamond interface may reasonably be expected to affect the electronic and structural properties significantly. In our simulations, adsorption energies for all surface coverages of Ti are more favourable than those found for Cu and Ni (Table 7.4).

Table 7.4: Calculated adsorption energy per Ti atom, E_{ads}, χ, Schottky barrier, ϕ_{B}, dimer bond–length $d_{(\mathrm{C-C})}$ and carbon–titanium bond–length $d_{(\mathrm{C-Ti})}$, for varying coverages of Ti on a diamond (001) surface. Energies are in eV, lengths in Å. The P+C configuration for 1 ML is unstable.

Coverage (ML)	Site	Geometry	E_{ads}	χ	ϕ_{B}	$d_{(\mathrm{C-C})}$	$d_{(\mathrm{C-Ti})}$
1.00	B+C	2×1	-4.60	-0.29	0.85	1.61	2.22
1.00	B+H	2×1	-5.08	0.35	1.51	1.65	2.19–2.32
1.00	P+H	2×1	-4.72	1.56	2.70	2.49	2.25
0.50	B	2×1	-3.66	-2.00	-0.86	1.79	1.98
0.50	C	2×1	-3.91	-2.05	-0.91	1.66	2.12
0.50	H	2×1	-5.02	0.21	1.35	1.65	1.97–2.26
0.50	P	2×1	-3.77	0.52	1.66	1.73	2.14
0.25	B	4×1	-3.86	-1.52	-0.38	1.38–1.74	1.99
0.25	C	4×1	-3.33	-0.72	0.42	1.51	2.17
0.25	H	4×2	-4.71	-0.90	0.25	1.62	2.04–2.19
0.25	P	2×2	-4.69	-3.64	-2.50	1.64	2.03

For Ti adatom adsorption, the P site exhibits a highly exothermic adsorption of 5.36 eV per Ti atom (Table 7.1). On increasing the surface coverage to 0.25 ML, the P site becomes less stable, and Ti atoms marginally prefer H sites. This result shows a small quantitative deviation with previous calculations [202] of Ti terminated diamond surfaces which suggested a P site for this coverage. This difference may arise from the periodicity of the surface cell, as the most stable, 4×2 surface geometry for a 0.25 ML coverage was not reported previously. It is found that for 0.25 ML of Ti, the H site on 4×2 geometry is just 0.10 eV/atom higher

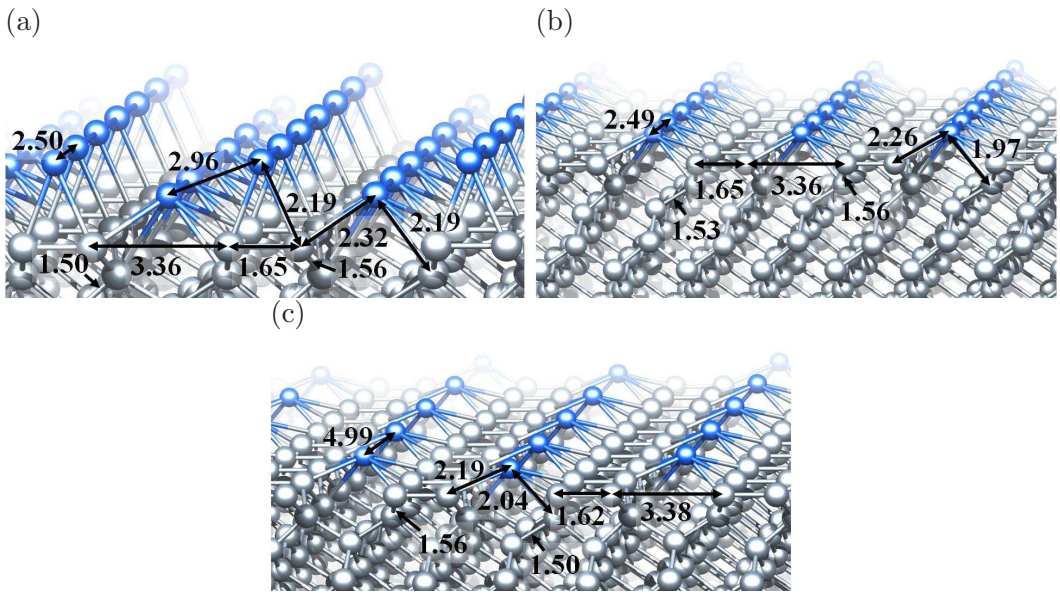

Figure 7.6: Perspective views of relaxed geometries for (a) 1.00, (b) 0.50, and (c) 0.25 ML of Ti on the (001)–(2×1) diamond surface. Bond–lengths are indicated in Å.

in energy than the P site on 2×2 geometry. The calculated adsorption energies for the P site on 4×2 geometry and the H site on 2×2 are found to be virtually indistinguishable at -4.69 and -4.65 eV/atom, respectively.

Calculations for 0.50 ML coverage are qualitatively in agreement with previous calculations [202], which also found the H site as the most energetically favourable location. By considering the difference between experimental and theoretical cohesive energies (1.44 eV) and the effect of functional and basis sets, one can compare the calculated adsorption energies with those reported previously [202]. Using LDA cohesive energies for the most stable configurations, adatom, 25%, and 50% coverages are calculated here to be 6.80, 6.13, and 6.46 eV, respectively, which agree well with the previously calculated adsorption energies [202] of 7.19, 6.62 and 6.85 eV, respectively.

For 1 ML of Ti, a combination of B+H sites is the most stable, with the equilibrium geometry shown schematically in Fig. 7.6 (a). The P+C combination is unstable, spontaneously reconstructing to B+H. It is worth noting that the H site shown in Fig. 7.6 (c) is favoured quite generally for Ti termination. Based upon inter–nuclear distances, relaxed

structures indicate the formation of four strong Ti–C covalent bonds at this site.

The calculated single and dimer C–C bond lengths for 2×1–(100) clean and H–terminated diamond surfaces are found to be 1.61 and 1.37 Å, respectively [93]. Here these bond lengths are used as the criterion to compare the surface C–C bond lengths of metal–terminated surfaces. For the most stable surface sites, even at high Ti coverages (Fig. 7.6), the 2×1 C–C reconstruction is retained. The C–C bond–length of 1.65 Å is around 20% greater than the dimer bond–length of the clean surface, but just 2.5% greater than the H-terminated surface, indicating that the reconstruction is a single C–C bond, allowing for covalent bonding between the surface C sites and the Ti adsorbates. Calculated surface C–Ti bond–lengths (∼2.15 Å) are consistent with C–Ti bond–lengths (2.17 Å) in organo–metallic compounds [142].

Ti adsorption strongly impacts the electrical properties. The calculated χ increases with increasing Ti coverage. For 0.25 ML, an NEA of -0.90 eV is calculated. For the low–energy P site, the NEA is very large at -3.64 eV, a consequence of this structure giving rise to simultaneously large charge transfer between the adsorbate and the surface, and a large geometric separation of the charges. The tendency towards a PEA with increasing coverage reflects the impact of the direct interaction between neighbouring Ti atoms on the surface.

The band–structure of the most stable configurations are shown in Fig. 7.7. It is observed that in comparison to 1 ML of Cu or Ni, a large number of highly dispersed states are present. The electronic states in the energy range from -2.00 to -5.00 eV are mainly d–orbitals, localised within the surface Ti layer.

For both 0.50 and 0.25 ML of Ti [Fig. 7.7 (c) and (e)], the band structures show surface bands which are found to have significant $3d$ character. The electronic states in the middle of the bulk band gap are due to either essentially Ti–related d–orbitals, or to an antibonding combination of these orbitals with surface π^*–like states. As an interesting feature, the electronic band structure corresponding to 0.25 ML [Fig. 7.7(e)] shows a small band gap of around 0.7 eV along the M–Γ–X branches.

7.3.5 V termination

The vanadium/diamond interfacial structures have received very little attention to–date. However, vanadium–carbon bond functionalities on the diamond surface, and particularly

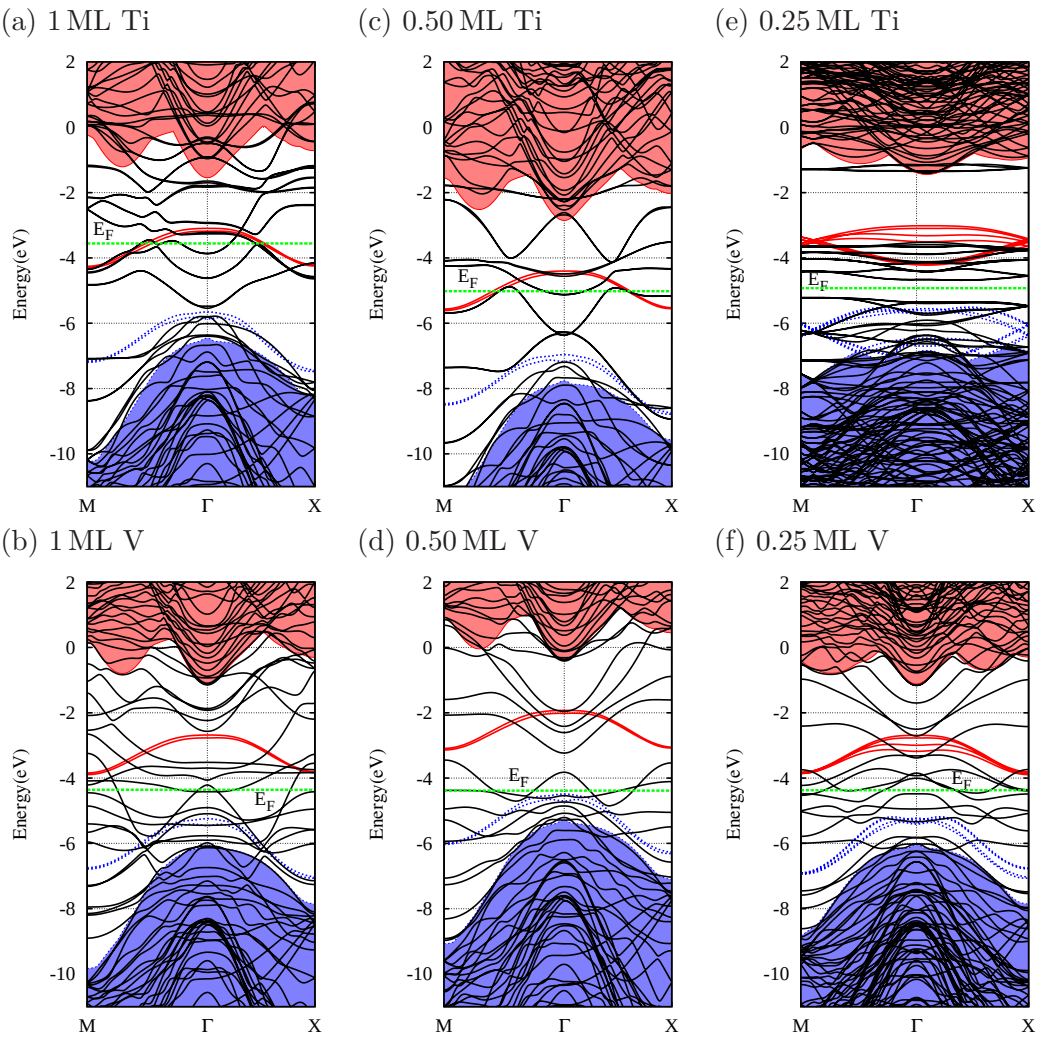

Figure 7.7: Band structures in the vicinity of the band–gap along high–symmetry directions in the Brillouin–zone for various coverages of Ti and V on (001) diamond surfaces. Lines, shading and alignment is as in Fig. 7.4.

on nano–diamond, have the potential for use in metal–induced stoichiometric and catalytic transformations [248, 249]. Vanadium readily forms a carbide and is therefore expected to behave in a fashion closer to Ti than to Cu or Ni.

In line with Ti adatom adsorption, the P site is the most energetically favourable for a V adatom (Table 7.1), followed by the H site. Both P and H sites exhibit exothermic reactions relative to a clean diamond surface and vanadium metal in addition to being highly exothermic with respect to free V atoms.

Table 7.5: Calculated adsorption energy per V atom, E_{ads}, χ, Schottky barrier, ϕ_{B}, dimer bond–length $d_{(\mathrm{C-C})}$ and carbon–vanadium bond–length $d_{(\mathrm{C-V})}$, for varying coverages of V on a diamond (001) surface. Energies are in eV, lengths in Å. The P+C configuration for 1 ML and the P site for 0.50 ML are unstable.

Coverage (ML)	Site	Geometry	E_{ads}	χ	ϕ_{B}	$d_{(\mathrm{C-C})}$	$d_{(\mathrm{C-V})}$
1.00	B+C	2×1	-5.99	-0.38	0.79	2.50	2.16
1.00	B+H	2×1	-6.45	-0.03	1.14	1.69	2.22–2.45
1.00	P+H	2×1	-6.22	0.86	2.04	1.71	2.38–2.45
0.50	B	2×1	-5.25	-1.66	-0.49	1.68	2.04
0.50	C	2×1	-6.06	-1.55	-0.38	1.60	2.17
0.50	H	2×1	-6.60	-0.76	0.41	1.68	2.30
0.25	B	4×1	-5.33	-1.15	0.02	1.37–1.66	2.04
0.25	C	2×2	-5.80	-0.95	0.22	1.58	2.14
0.25	H	4×1	-6.10	0.02	1.20	1.52	2.34
0.25	P	4×1	-5.87	-0.43	0.74	1.37–1.64	2.17

For partial surface coverage of V, the H site on 4×1 and 2×1 is found to be the most energetically favourable, consistent with the view that inter–adsorbate interactions are energetically favoured. Similar to Ti, the combination of sites B and H gives the most stable arrangement for 1 ML adsorption. It is important to note here that for 0.50 ML, the P site is completely unstable: in the absence of an artificial symmetry constraint, in our simulations all V atoms initially located at P sites move spontaneously to H sites.

Unlike Ti termination, the C–C reconstruction is lost for 1 ML, while it is retained at partial surface coverages. The measured C–V bond–lengths are in the 2.04–2.45 Å range, close to the value of 2.11 Å found in organometallic systems [142]. The adsorption energy increases from around -6.0 eV for an individual adatom, to around -6.5 eV/atom for the complete monolayer, consistent with the formation of chemically stable C–V covalent interactions.

As already described for Cu, Ni, and Ti, the interaction between vanadium atoms has also

a significant impact upon χ. Due to the complex interplay between vanadium–carbon and vanadium–vanadium interactions, both in terms of charge exchange and geometry, surfaces with 1 ML of V exhibit a small NEA, whereas at 0.50 ML V coverage, a large NEAs of -0.76 eV is determined.

The band–structures (Fig. 7.7) corresponding to the most stable structures are found to be qualitatively similar those of Ti.

7.3.6 Zn–termination

In addition to Cu, Ni, Ti and V, the kinetics and the electronic properties of Zn have also been investigated. The key properties, such as adsorption energies per Zn atom, bond lengths and χ_s, are listed in Table 7.6. The relaxed structures of Zn–terminated diamond surfaces are analogous to that of Cu–terminated diamond, as in line with Cu–termination, the site C for adatom, 0.25 and 0.50 ML, and the configuration B+C for 1 ML are found to be the most stable.

Table 7.6: Calculated adsorption energy per Zn atom, E_{ads}, χ, Schottky barrier, ϕ_{B}, dimer bond–length $d_{(\text{C}-\text{C})}$ and carbon–zinc bond–length $d_{(\text{C}-\text{Zn})}$, for varying coverages of Zn on a diamond (001) surface. Energies are in eV, lengths in Å. (In addition to the site H for 0.25 and 0.50 ML, the B+H, P+C and P+H configurations for 1 ML are also unstable.)

Coverage (ML)	Site	Geometry	E_{ads}	χ	ϕ_{B}	$d_{(\text{C}-\text{C})}$	$d_{(\text{C}-\text{Zn})}$
1.00	B+C	2×1	-1.22	0.19	2.03	1.58	2.30–2.36
0.50	B	2×1	0.21	-0.60	1.24	1.85	1.99
0.50	C	2×1	-1.42	-1.40	0.44	1.61	2.03
0.50	P	2×1	0.31	-0.84	1.00	1.77	2.20
0.25	B	4×1	0.20	-0.20	1.64	1.37–1.83	1.99
0.25	C	2×2	-1.35	-0.92	0.92	1.62	1.98
0.25	P	4×1	0.29	-0.35	1.49	1.37–1.76	2.20

Zinc, which has the lowest melting temperature (419.53 K) in comparison to Cu (1084.62

K), Ni (1455 K), Ti (1668 K) and V (1890 K) [142], exhibits a small cohesive energy of 1.35 eV [241]. It is therefore unsurprising that due to small cohesive energy, reactions of Zn metal atoms with the clean diamond surface are less exothermic relative to those of Cu, Ni, Ti and V. There is an initial increase in the adsorption energy for the 2×1 diamond surface with 0.50 ML of adsorbed Zn (from -1.35 to -1.42 eV), followed by a decrease (to -1.22 eV) as the Zn coverage increased to 1 ML. A $III^r d$ order polynomial fitting of adsorption energy vs surface coverage plot suggests that around 0.40 ML of Zn on diamond surface will be the most energetically favourable surface coverage. The trend in χ is similar to the adsorption energy calculations, where the 0.50 ML coverage of Zn exhibits a large NEA of -1.40 eV.

For 1 ML of Zn, which is the least stable coverage among the examined surface coverages, there is a large elongation in C–Zn bond length, indicating a weak chemical bonding between Zn–layer and the diamond surface. The C–Zn bond lengths at low coverages are in reasonable agreement with the average C–Zn bond length of 1.98Å in Zn–based organometallic compounds [250]. Additionally, for the most stable geometries of surface coverages investigated, the surface C–C reconstruction is retained.

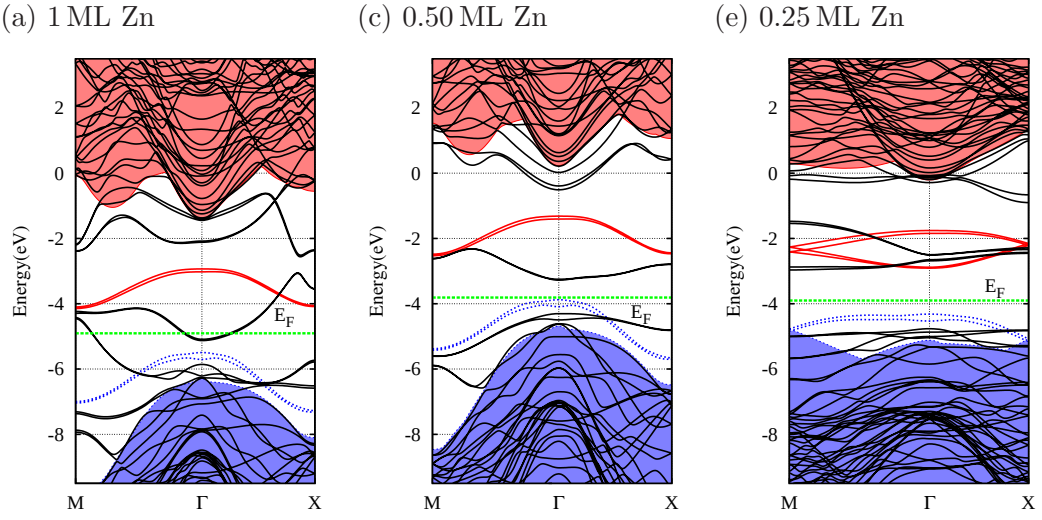

Figure 7.8: Band structures in the vicinity of the band–gap along high–symmetry directions in the Brillouin–zone for 100, 50 and 25 ML coverages Zn on (001) diamond surfaces. Lines, shading and alignment are as in Fig. 7.4.

The band structures for different surface coverages of Zn on a diamond (100) surface

are shown in Fig. 7.8. The impact of a large elongation in C–Zn bond lengths on the band structure of 1 ML of Zn is evident in wave function analysis. It is noted that for all surface coverages of Zn, the fully and partially unoccupied electronic states below the conduction band minima originate from a linear combination of Zn $3d$ orbitals with π and π^* states of the underlying surface reconstructions.

In brief, it can be said that in addition to the chemical nature of TMs, surface coverage strongly influences the electronic and structural properties of diamond. Partial surface coverages of TMs, particularly Ti and Zn, have great scientific and technological relevance because of their good thermodynamic stability and affinity. However, such coverages may suffer chemical instability in ambient conditions, as exposure to atmospheric gases are prone to surface modifications.

Given the fact that most TMs have a strong tendency to form thermodynamically and chemically stable oxides, investigation on the interaction of oxygen with TM–terminated diamond surfaces is of particular relevance in the current context. In the next section of this chapter, diamond surface with adsorbed oxides of Cu, Ni, Ti and Zn are discussed. Vanadium, which can exhibits 4 different stable forms of oxide, is not comprised in this study due to computational challenges.

7.3.7 Transition Metal oxides

As described in Chap. 5, it is understood that on the (001)–diamond surface, oxygen binds in an ether form, whereas hydrogen termination takes the form of a structure where second–neighbour carbon sites reconstruct, and the remaining surface sites are saturated by hydrogen. In both cases the surface is completely chemically bonded.

Where TMs are bonded to the oxygen terminated surface, the connectivity must be altered to allow for bond formation. This is found to occur by the formation of a (2×1) reconstruction akin to that seen in H–termination. In this case, oxygen in the negative oxidation state are monovalent, rather than divalent. Combining the -1 oxidation state of the surface oxygen with the native oxidation state of each TM, it is possible to reduce the otherwise large number of possible surface arrangements for the various monolayers of TMOs: this results in 25%, 50% and 100% of the surface site coverage for MOs that normally adopt M_2O, MO and MO_2 stoichiometries, respectively. For example, as shown

schematically in Fig. 7.9, each Ti^{4+} and Zn^{2+} ion in the stoichiometric films is balanced by four and two oxygen atoms, respectively.

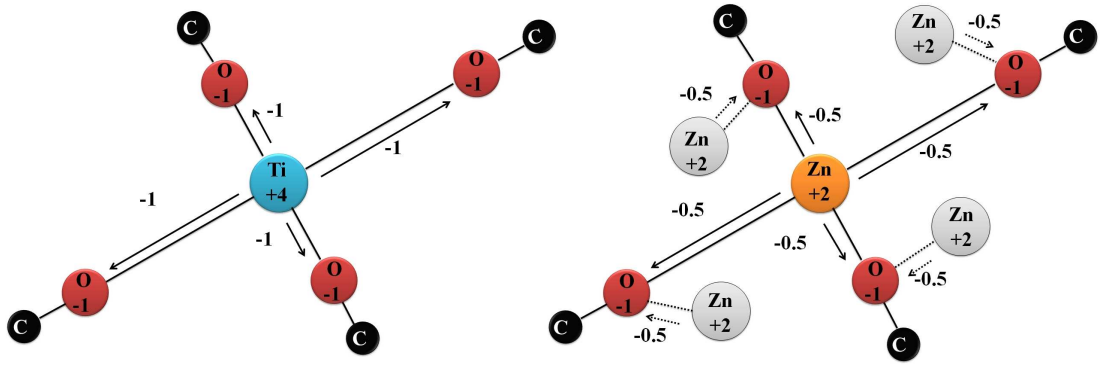

Figure 7.9: The oxidation states corresponding to a diamond surface with adsorbed oxides of (a) Ti and (b) Zn.

Similar to the halogens and pure TM terminations, a wide range of possible surface geometries for each stoichiometry were examined, including those where the TMs are bonded directly to the diamond, leading to a C–TM–O surface termination. In all cases examined, structures where the oxygen atoms act as linkers between the diamond and the TM were energetically favoured, and it is only such arrangements that are discussed in the remainder of this section.

The impact of adopting the appropriate stoichiometries can be seen in the adsorption energy listed in Table 7.7; it is found that the most stable configurations of Ti, Ni, and Zn occur for ratios of 1:4, 1:2, and 1:2, respectively. The equilibrium configurations corresponding to oxides of zinc and titanium are shown schematically in Fig. 7.10. In the case of Cu it is noted that the adsorption energy for the ratio 1:1 is slightly lower than that of the ratio 1:2. These correspond to the cupric and cuprous oxides. The enthalpy of formation of cuprous oxide (Cu_2O, $-169\,\mathrm{kJ/mol}$) is slightly greater than that of cupric oxide (CuO, $-157\,\mathrm{kJ/mol}$), with the differences in formation enthalpy showing good agreement with the corresponding structures on diamond, ($\Delta H \approx 0.1\,\mathrm{eV}$ per Cu atom, and $\Delta E_{\mathrm{ads}} \approx 0.06\,\mathrm{eV}$).

The adsorption energies listed in Table 7.7 are broadly comparable with those found for the same TM species on the oxygen–free (001)–diamond surface (Sec. 7.3.2, 7.3.3 7.3.4 and 7.3.6), confirming that TMs are strongly attached to an oxygen–terminated diamond surface.

Table 7.7: Calculated E_{ads} (eV), χ (eV) and bond lengths (Å) for different TMO stoichiometries (M:O) adsorbed onto (001)–diamond. $d_{(\text{C}-\text{C})}$ is the C–C reconstructed–bond length, with $d_{(\text{C}-\text{O})}$ and $d_{(\text{O}-\text{M})}$ being average C–O and O–metal distances, respectively. The periodicity of the surface reconstruction is indicated as $2 \times N$, as shown for ZnO in Fig. 7.11. d_z (Å) is the rumpling, *i.e.* the difference in the z–positions of TM atoms relative to the layer of oxygen (Fig. 7.10).

					d			
TM	M:O	$2 \times N$	E_{ads}	χ	C-C	C-O	O-M	d_z
	1:1	1	−5.35	1.74	1.63	1.39	2.22	1, 38, 1.20
Ti	1:2	1	−6.15	1.57	1.63	1.38	1.96	0.92, 0.70
	1:4	2	−7.60	−3.10	1.66	1.36	1.82	0.59
	1:1	2	−2.67	1.41	1.69	1.35	1.82	1.31
Ni	1:2	1	−3.80	−0.16	1.63	1.39	1.84	0.57, 0.29
	1:4	2	−2.69	1.67	1.75	1.32	1.76	0.29
	1:1	1	−2.05	0.05	1.63	1.37	2.12	1.20, 1.02
Cu	1:2	1	−2.35	−1.28	1.63	1.38	1.92	0.80, 0.23
	1:4	2	0.03	1.13	1.74	1.33	1.85	0.41
	1:1	1	−1.00	0.30	1.65	1.38	2.15	1.28, 1.21
Zn	1:2	1	−1.13	−3.05	1.64	1.37	1.90	0.79, 0.46
	1:4	1	0.97	−0.40	1.66	1.31	1.96	0.79

Since in most of cases, adsorption of TMs onto an oxygenated diamond surface is exothermic, one may expect better thermal stability from metal oxides at elevated temperatures in comparison to commonly used surface terminations, such as H, and other alkali halides and oxides. As an example, in the case of the most energetically favourable stoichiometry, 1:4, of titanium oxide, to extract a Ti atom from an oxygenated diamond surface and brings it in the gaseous form, one will have to provide thermal energy equivalent to 7.60 eV. Alternatively, one might envisage the desorption of an oxide species, leaving behind a clean diamond surface. For the titanium–oxide case, release of a TiO_2 unit from the surface would require

(a) Titanium oxide (b) Zinc oxide

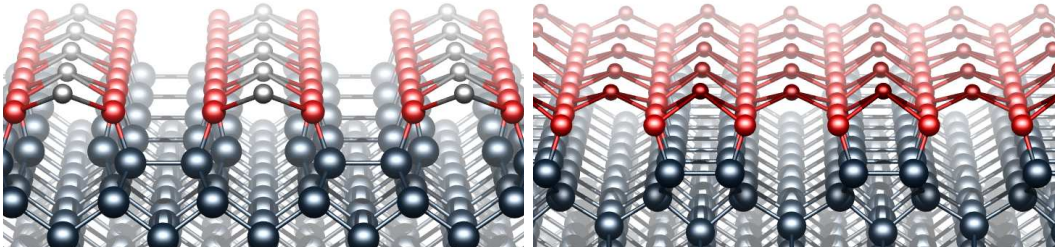

Figure 7.10: Perspective views of the diamond surface with adsorbed oxides of (a) Ti and (b) Zn. Black, big red, gray and small red spheres represent C, O, Ti and Zn atoms, respectively.

around 7 eV, again suggestive of a high thermal stability, although a detailed kinetic model would be required to fully explore this question. The relatively weak binding corresponding to 1:4 of Cu, Ni, and Zn suggest that at very low coverages, island formation may occur and mixed termination with both TMO islands and pure C–O surfaces are likely to be achieved in practice.

The periodicity of the underlying diamond reconstruction is found to have a relatively weak impact upon either adsorption energy or χ. As an example, for stoichiometric ZnO, two isomers are shown in Fig. 7.11. The ground state periodicity is indicated in Table 7.7.

The most stable stoichiometries of TMOs, particularly, oxides of Ti and Zn, exhibit large NEAs of around 3.1 eV, significantly higher than H–termination (2 eV), but slightly smaller than 3.89 eV predicted for LiO [21].

As mentioned in Table 7.7, the most stable stoichiometries of Ti and Zn exhibit large NEAs relative to those of Cu and Ni. In order to explain the difference in χ of TMOs, the electronegativities of TMs are therefore taken into account. The electronegativities (Pauling scale), which are 1.54, 1.65, 1.90, and 1.91 for Ti, Zn, Cu, and Zn, respectively, indicates that for a given stoichiometry, the bond–polarity, which strongly impacts the χ, of for Ti and Zn should be greater than for Cu and Ni.

In addition, examination of rumpling [251] is also helpful in semi–quantitatively interpretation of χ. The electronegativities of Cu and Ni are very close, but the rumpling of CuO exceeds that of NiO, consistent with the more negative χ (Table 7.7) for CuO termination. Although Zn is less electropositive than Ti, the greater rumpling of ZnO termination leads

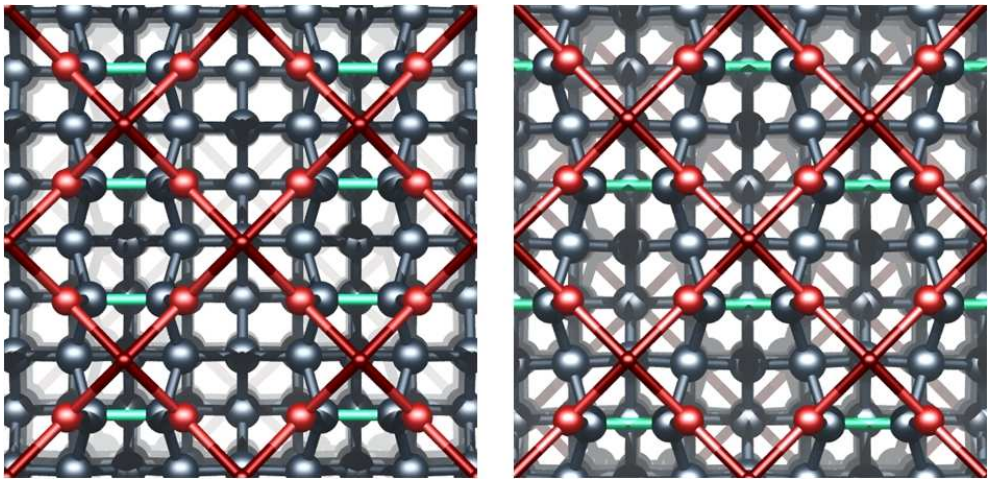

Figure 7.11: Top views of 2×1 (left) and 2×2 (right) geometries of a ZnO terminated diamond surface. The surface dimers are shown in green.

to Zn and Ti terminations having very similar NEAs. The difference between the Ni and Cu cases highlights the necessity to not only take the nuclear arrangement into account when considering the origin and magnitude of NEAs, but also an accurate simulation of the electronic spatial arrangement.

Akin to a H–terminated diamond, the resultant electric field from the metal to oxygen layer of these surface dipoles causes the energy bands to bend in an upward direction and thus reduces χ. This picture is indeed supported by Mulliken population analysis [136]. Mulliken charge distribution plots for the most stable stoichiometries of the investigated TMOs are shown in Figs. 7.12 and 7.13. It is important to mention here that the absolute magnitudes of the atomic charges yielded by Mulliken population analysis have little physical meaning, since they display a high degree of sensitivity to the atomic basis set with which they were calculated. However, in the present context, consideration of their relative values reveals useful information. Both TM and oxygen atoms possess a large amount of partial charge, where Ti–O and Zn–O surface bonds are more polar than Cu–O and Ni–O surface bonds.

An excess of metal on the oxygenated diamond surface decreases the magnitude of charge transfer, rendering χ less negative. Calculations that are performed for a monolayer (Table 7.7) and somewhat thicker metal layers, such as metal bi–layers, also indicate that

(a) Copper oxide

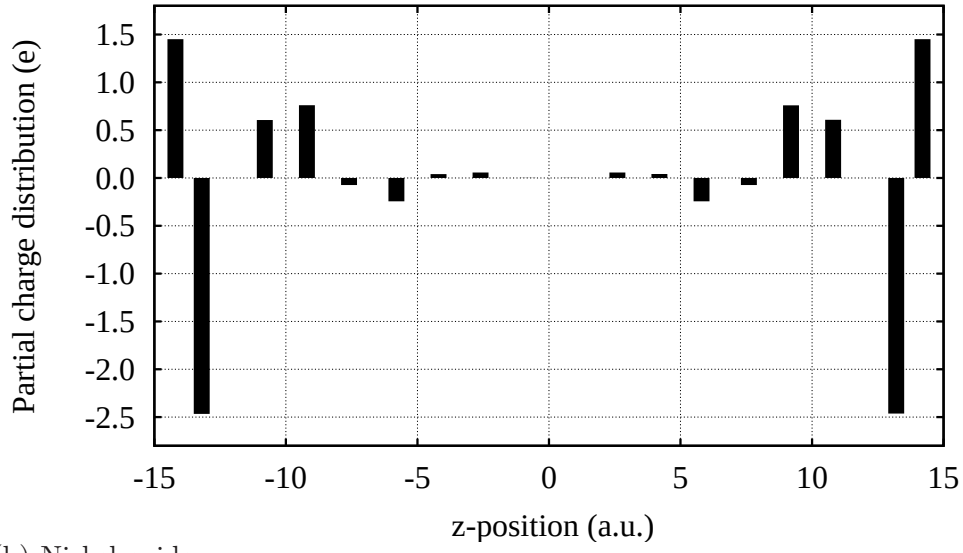

(b) Nickel oxide

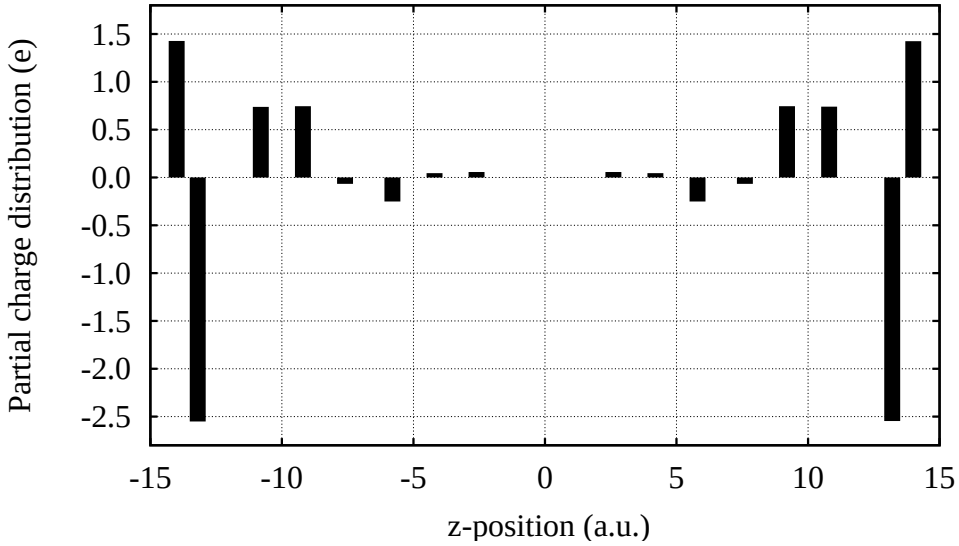

Figure 7.12: Mulliken population analysis for the most stable stoichiometries of Cu and Ni oxides. For each plot the zero of the x–axis is the middle of the diamond slab.

thicker metal layers of all four TMs studied result in a positive χ. This is entirely consistent with the experimental studies, where relatively thick coatings of Cu, Ni, Zr and Co all yield [24, 133, 215, 225, 226] positive values for χ.

The electronic band structures of the most stable stoichiometries of TMOs are shown

(a) Titanium oxide

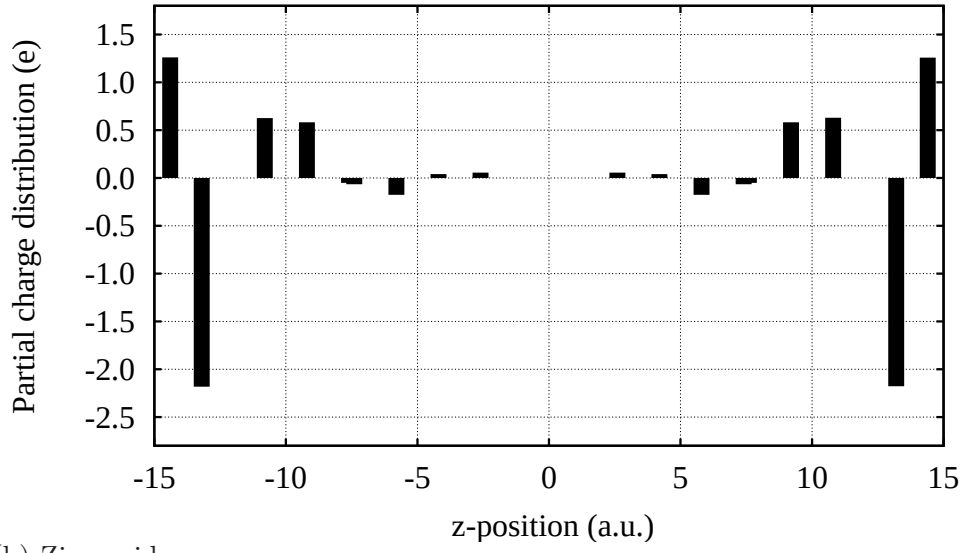

(b) Zinc oxide

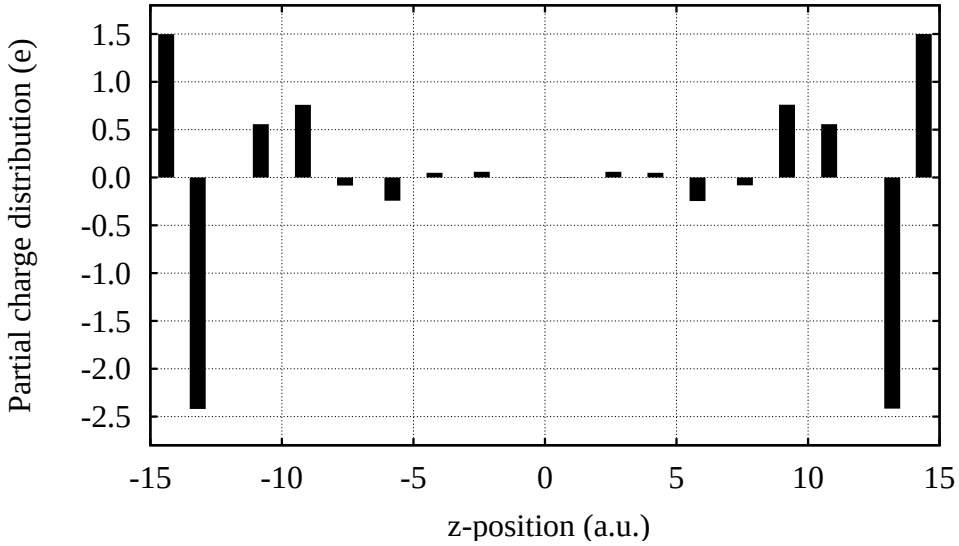

Figure 7.13: Mulliken population analysis for the most stable stoichiometries of Ti and Zn oxides. For each plot the zero of the x–axis is the middle of the diamond slab.

in Fig. 7.14. Consistent with a hetero–structure of two insulators, the band structures are found to be non-metallic in nature. However, depending upon the chemical nature of system, the band gap, as shown in Fig. 7.14 (b) (c) and (d), is widened or reduced. Wave function analysis indicates that for all four systems, the occupied electronic states below the bulk

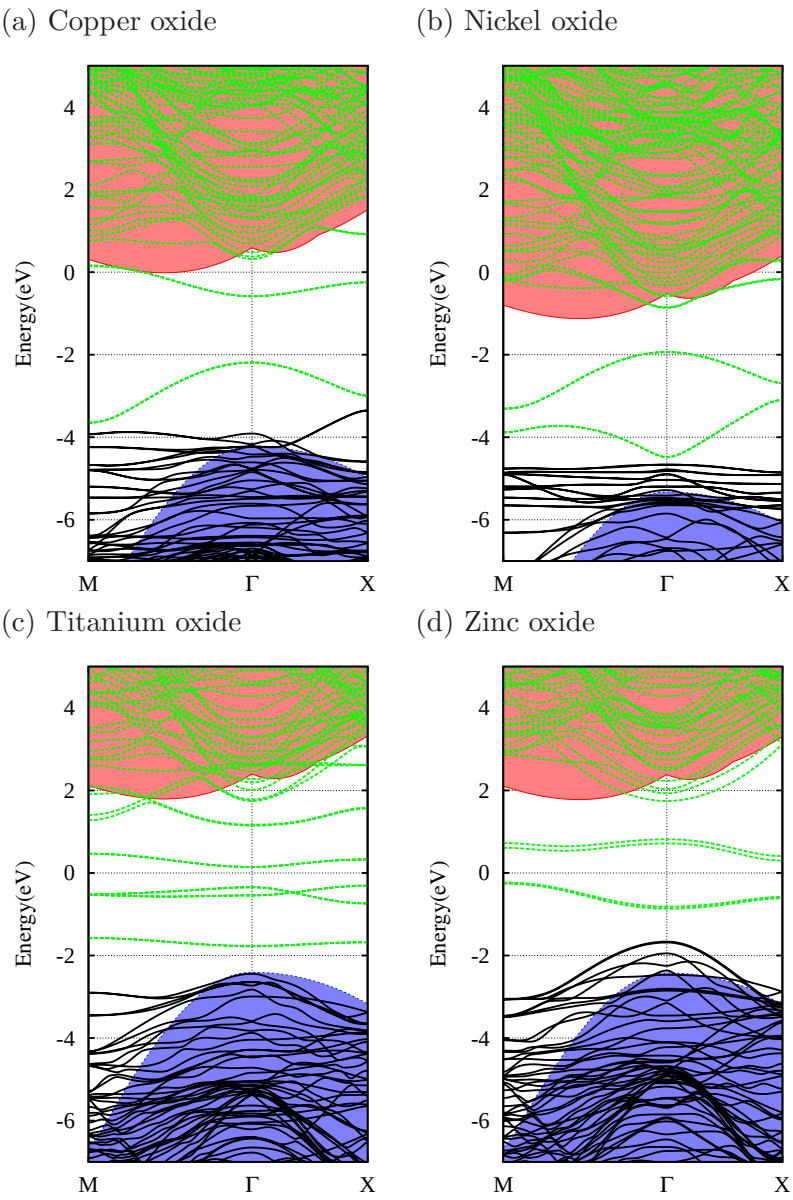

Figure 7.14: The electronic band structures corresponding to the most stable stoichiometries of TMOs. Occupied (black) and unoccupied (green) states of terminated surfaces are superimposed upon the electronic band structure of the bulk diamond (shaded regions). The zero of the energy scale is the vacuum potential for each system.

conduction band minima in the band gap are oxide related states, originating from a linear combination of p and d–like orbitals of oxygen and metal atoms, respectively(Fig. 7.15).

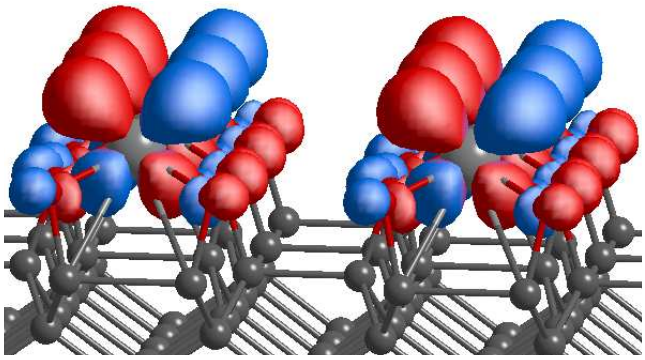

Figure 7.15: Plot of the wave function iso–surfaces for the unoccupied electronic states, which lie below the conduction band minima between 0.00 and −4.00 1 in Fig. 7.14 (a) and (b), between 1.00 and −2.00 eV in Fig. 7.14 (c) and (d), respectively.

It is instructive to assess the bonding in the monolayer surface coverage by comparing the calculated surface bond–lengths (Table 7.7) with suitable reference materials. In the monolayer systems, TM–O bond lengths are within 6% of the average TM–O bond lengths in the corresponding bulk metal–oxides [252,253], but close to the values at a pure metal-oxide surface [254]. The average C–O bond length is around 9% shorter than the calculated value for ether–terminated diamond (001)–surface [135], but within 1% of the values typical for C–O^- bonds [255]. The bond–lengths are therefore entirely consistent with expectations for the context. Although the surface C–C reconstruction increases relative to that of a comparable fully hydrogenated surface, it is observed that the underlying 2×1 and 2×2–reconstruction are retained for all stoichiometries, for all TMOs studied. The surface C–C bond lengths on 2×2 geometry are relatively larger than those on 2×1 geometry.

These findings show that a careful control is necessary while depositing ultra–thin TMO layers on diamond, as uncontrolled deposition may well result in stoichiometries that reduce the desired impact upon the χ. Selective deposition of such ultra thin TMOs films is likely to be technologically challenging. However, the use of atomic layer deposition and scanning probe based lithography for atomic scale patterning of TMs on diamond surface may offer a laboratory solution to test the impact of the ultra–thin TMO layers.

7.4 Chapter summary

In summary, density-functional simulations were performed for pure TMs and TMOs terminated diamond (100) surfaces. Both TM and TMO terminations, which hold great potential

for surface coatings of diamond-based electron emitters, are being discussed simultaneously.

In the case of pure TMs termination, based upon the metal–diamond chemical interactions, there is a clear divide with regard to whether the metals form carbides or not. For Ti and V, which form carbides, the metal atoms interact strongly with the surface carbon atoms, while Cu, Ni and Zn, which do not readily form carbides, exhibit weaker interactions. As a consequence of the C–metal interactions, the surface reconstructions are strongly affected by the adsorbates and at a high surface coverage (1 ML) of Cu, Ni and Zn, the underlying C–C reconstructed bonds are unstable, whereas for all surface coverage of Ti and V, the C–C reconstruction is retained. Relaxed geometries also indicate that metal atoms interact strongly with each other. In the case of non-carbide forming TMs, metal-metal interactions appear more significant than the carbide forming metals.

Additionally, the chemical nature of the metal and surface coverages have a qualitative impact upon both the energies of adsorption and χ. From the calculated adsorption energies of Cu, Ni, Zn, Ti and V, it can be concluded that diamond surface treatment with carbide forming metals, as evidenced by Ti and V, would yield a more thermodynamically stable termination in comparison to non-carbide forming metals.

The *absolute* magnitude of the adsorption energy deserves further discussion. The main source of variance arising between differing calculations and experiment is likely to be the way in which the energy of the metal atoms are taken into account. In this study, in line with common practice in this field, the energy of a free metal atom is taken into account as the reference state. As noted in the introduction, there is some difficulty in obtaining accurate values for the energies of free atoms due to a number of computational and quantum-mechanically based issues. As an example, in the case of the carbide forming species, it is found that the cohesive energies of V and Ti differ by 0.20 eV according to theory, and 0.46 eV in experiment. More significantly, the difference between the theoretical and experimental cohesive energies of V, Ti, Ni, Zn, and Cu are 1.18, 1.44, 1.54, 0.56 and 0.80 eV/atom. Using the theoretical of the energies per atom will therefore, on average, lead to an overestimate in the adsorption energy of more than 1 eV, and when comparing absolute energies between models, the uncertainty in the value of the reference state of the adsorbate must be considered with great care.

Nevertheless, the very large adsorption energies obtained relative to free atoms whether

referenced to calculated or experimental data reflect a process whereby individual metal atoms leave the surface only at high temperatures. As a consequence of the large adsorption energies one can conclude that, at least in the cases of the metal species analysed in this paper, the adsorbates would persist on the diamond surface to relatively high temperatures prior to the desorption of individual atoms into a vapour.

However, this conclusion must be treated with care. It is possible, if not likely, that some metal species would be prone to migration over the surface at a temperature below that required for desorption. If this can happen, either during deposition or subsequent annealing, then the metal atoms may migrate to form islands on the surface rather than desorb. The likelihood of this can be considered in a thermodynamic sense by examining the adsorption energies relative to the native elemental state of each TM adsorbate species. In the cases of both Cu and Ni, at all coverages the adsorption energy is *positive* relative to the metals in the bulk metal state, so that for these species, at low coverage, island formation tends to be energetically favoured. In contrast, for Ti and V, for the most stable structure at each coverage the adsorption energy remains less than or equal to zero, even when referenced to the bulk metals, so that the aggregation into islands is less energetically favoured.

Of the species examined, Zn, Ti and V exhibit large and NEAs at low coverages, while Cu and Ni tend to yield an NEA at high surface coverages. In addition to the chemical nature and surface coverage, χ is also sensitive to the adsorption site. For example, the H and P sites at 0.50 ML surface coverage of Ti give PEAs that differ by 0.4 eV. Even more significant is that at 0.25 ML of Ti, the B and P sites give large NEAs which differ by more than 2 eV due to a combination of charge transfer and geometric factors.

Overall, these calculations suggest that it is possible to produce surface treatments that yield a large NEA on diamond by depositing a sub-monolayer coverage of TMs. However, selective deposition of sub-monolayer coverages of TMs is likely to be technologically challenging. The use of atomic layer deposition and scanning probe based lithography for atomic scale patterning of TMs on diamond surface [256, 257], may offer a potential solution in the laboratory.

In the band structures of TMs, at higher surface coverages, most of the electronic states in the band gap are associated with either localised 3*d*-orbitals centred on metal atoms or

with a set of states reflecting the bonding interactions between C and metal atoms made up from with sp^n hybrids and d-orbitals. An underlying carbon-dimer character is generally visible in terms of π-related deep bands only at partial surface coverages, where there are wave-functions with π^* character.

The calculated Schottky barrier heights calculated for ultra-thin, 1 ML of Cu, Ni, and Ti are and 0.44, 0.63, and 1.51 eV, respectively, may be compared with the experimental Schottky barrier heights for few layer thick TMs, which are respectively 0.70, 0.70, and 1.20 eV [24, 133, 225, 226]. The agreement between theory and experiment is viewed as very reasonable, and the small differences can be attributed to combinations of the true metal thickness, photovoltaic effects in measurements and the presence of interfacial impurities, such hydrogen and particularly oxygen. The calculated Schottky barrier height for Ni in this study shows a quantitative difference with the Schottky barrier height of 0 eV, calculated previously [236], but in the previous study their results are based on ideal, unrelaxed structures.

In comparison to pure TMs and other surface terminations, particularly LiO and CsO, TMO coatings seem advantageous because of their impact upon the electronic properties and compatibility with device fabrication processes. Examination of the energetics and χ of TMO terminated diamond surfaces suggests that for a correct stoichiometry, ultra thin coatings of TMOs, particularly the oxides of Ti and Zn, cause a large downward shift of around 3 eV in the work function, resulting in a predicted small value of around 1.4 eV. Since the reactions of TMs with oxygenated diamond are highly exothermic, in addition to excellent chemical stability, a better thermal stability at elevated temperatures in comparison to H and CsO can be obtained. It is notable in particular that Ti has the advantage over Cs- and Li-based χ modification in that it is already commonly used in semiconductor processing. However, based upon the relationship between TM electronegativities and the resultant χ, combined with knowledge of the thermal stability of other TMOs, allows for further predictions. For example, Sc and V are also of particular interest, as these have favourable electronegativities and readily form thermally stable oxides.

Part III

Conclusions

Chapter 8

Overview: Diamond as the electron emitter for thermo–tunnel devices

A man is but the product of his thoughts what he thinks, he becomes.

M. K. Gandhi (1869 – 1948)

This project has centred on overcoming the issues involved in developing a high–power diamond–based thermo–tunnel device for energy harvesting applications. First, a thorough investigation was performed to test the feasibility of the thermo–tunnel device for an efficient thermal energy conversion. Thereafter, density functional simulations were performed for different diamond/adsorbate interfaces to reduce the work function of the clean diamond from 4.5–5.0 eV to 1–2 eV so that it could be used in the fabrication of the thermo–tunnel devices. Although a general summary is given at the end of each chapter, the major conclusions that have been drawn from the thesis work are summarised here.

Calculations performed for a simple thermo–tunnel device structure show that the choice of physical parameters, such as interelectrode separation, electrode work function and temperature, is critical in terms of impact upon the output power density and heat conversion efficiency. Under optimal conditions, an output power–density of around 10^6 W.m^{-2}, and a thermal efficiency in the range 8–12% can be achieved via a thermo–tunnel device. It is important to point out here that these values are calculated for electrode temperatures between 500–700 K, where some issues, such as surface flatness and thermal stability of terminated diamond surface, can be of critical importance. These problems may prevent

thermo–tunnel devices from achieving the high efficiency by damaging the ultra–thin vacuum gap and increasing the work function of diamond–based electrodes. Although thermal losses are significant for high electrode temperatures (between 500–700 K), these do not affect the order of magnitude of the power–output density, which is generally very high for small values of interelectrode separation and electrode work function due to the tunnelling effect.

Density functional simulations, as implemented in the AIMPRO code, were performed for different diamond/adsorbate interfacial structures, including the previously reported H–terminated and O–terminated diamond surfaces. The work function values calculated for H and O terminations are found to be in good agreement with previous studies and suggest that H–termination reduces the work function of the diamond by inducing an NEA, while O increases it by inducing a PEA. In recent studies, H–termination has been noted to be of significant interest for a number of applications, such as photocathode and surface conductive devices. However, due to the high work function and weak thermal stability, H–terminated diamond is not suitable in the context of thermo–tunnelling devices.

Calculations performed for different halogen/diamond surfaces suggest that, due to the highly electronegative nature of halogens, most induce a large PEA and therefore are not suitable for thermo–tunnelling device application. For example, the F–termination yields a PEA of around 2.7 eV, followed by rather smaller PEAs for Cl and Br. Smaller values for χ of Cl and Br in comparison to that of F are consistent with the trend in the electronegativity and C–halogen bond lengths.

Nevertheless, F is calculated to exhibit a remarkably good thermodynamic stability with respect to H and therefore, is of significant interest for the modification of nanodiamond particles containing the negatively charged nitrogen–vacancy (NV^-) optical centres, where the positive EA of fluorinated diamond protects against the generation of a p–type surface layer driven by the negative EA. In the case of the halogen atoms, such as Cl and Br, strong steric effects lead to a weak thermodynamic stability, preventing diamond surface from achieving high surface coverages ($\approx$100%). Partial surface coverages of Cl and Br are found to be rather thermodynamically stable and therefore hold significant potential for biomedical applications, which generally require specific types of surface functionalities in order to immobilise heavy protein or drug molecules on the diamond surface. Depending

upon the concentrations of hydrogen and halogens, mixed termination of diamond can yield χ in the range from -2.5 to 2.5 eV, without significantly affecting the thermodynamic stability.

In the further stages of the project, transition metals (TMs) that are compatible with device fabrication processes, were investigated. Calculations show that TMs, such as Cu, Ni, Zn, Ti and V, are highly thermally stable in comparison to pure halogens, hydrogen and mixed surface terminations, which in turn also offer a greater degree of control over χ. The energetics of metal/diamond interfaces allow us to identify the chemical nature of both carbide and non–carbide forming TMs. Carbide forming TMs, such as Ti and V, exhibit more negative adsorption energies and show strong adhesion to diamond surface, whereas non–carbide forming TMs, such as Cu, Ni and Zn, exhibit rather less negative adsorption energies and weak interaction. Investigated partial surface coverages of TMs show that, carbide forming TMs, such as Ti and V, exhibit negative EAs in the range from -1.7 to -3 eV. A large NEA of TM coated diamond could be of particular interest for thermionics, as the reactions of TMs with diamond surface are highly exothermic with respect to that of commonly used H and CsO terminations and may improve the thermal stability.

Given the fact that most TMs have a strong tendency to form thermodynamically and chemically stable oxides, ultra thin layers of TMO adsorbed on to a diamond surfaces were also examined in this work. Similar to CsO and LiO, the oxides of specific TMs, such as Zn and Ti, induce a large NEA of around -3 eV, which can reduce the work function of a clean diamond from 4.5–5.0 eV to 1–2 eV. The average resulting work function of around 1.5 eV is much lower than the reported values of the best available option (H–termination) and hence, generating a great deal of possibilities for diamond–based thermionics. In conjunction with a high melting point, strong adhesion of metal oxides with diamond surface is highly advantageous, allowing thermo–tunnel devices to work at even higher temperatures (> 700 K). A further reduction in the average work function (≈ 1.5 eV) is likely to be achieved through doping (n–type) and high temperature operation since both parameters significantly impact the position of the Fermi level. Under such circumstances, when the effective work function of diamond-based electrode is close to 1 eV, calculations suggest that the thermo–tunnel device will yield high output power density and efficiency of around 10^6 W.m^{-2} and 12%, respectively.

8.1 Future developments

The success in an accurate modelling of the thermo–tunnel device structure and in the prediction of a suitable surface termination for low work function diamond electrode has led to a step forward in the direction of fabricating an efficient diamond–based thermo–tunnel device, which will be capable of delivering a very high output power density in hostile environments. However, prior to starting fabrication work for such devices, there are still two key areas that remain to be explored and require significant attention.

The first area comprises the experimental validation of the predicted values of χ for different TMO/diamond terminations, which further poses a number of technical challenges. These include the controlled deposition of an uniform ultra thin oxide film onto a diamond surface and a careful control over the stoichiometric ratio of TM and O. Failure in achieving the uniformity and the correct stoichiometry of TMOs may significantly reduce the desired impact of χ upon the work function of diamond. In tandem with such theoretical predictions, an experimental analysis is also ongoing within the group to evaluate the localised work function of terminated diamond surfaces using Kelvin probe force microscopy, thermionic emission and ultraviolet photoemission spectroscopy. After this has been achieved, the experimental determination of the impact of such treatments upon electron emission will be explored.

The second area involves the engineering of a nanoscale vacuum gap between two diamond electrodes. Although a nano–scale vacuum gap between two microsized tips has already been demonstrated previously, for a mm sized electrode area this has not been reported. It is a very important issue because a large surface area of the electrode is highly desirable for high power output. Fabrication of a nanoscale vacuum gap that could also survive high temperature operation is an extremely difficult task. In many cases, it is noticed that the heat flux within the surface causes a differential thermal expansion from one side relative to other, leading to thermal expansion–caused deformation into a dome like shape that may cause the device failure by destroying the nanoscale vacuum gap. In addition to the above mentioned research areas, future work should also include the device packaging and testing in high radiation environments to obtain an insight into how extreme conditions impact the device characteristics.

Bibliography

[1] C. R. Saha, T. O'Donnell, H. Loder, S. Beeby, and J. Tudor, IEEE Transactions on Magnetics **42**, 3509 (2006).

[2] C. B. Williams, C. Shearwood, M. A. Harradine, P. H. Mellor, T. S. Birch, and R. B. Yates, IEE Proceedings - Circuits, Devices and Systems **148**, 337 (2001).

[3] S. P. Beeby, M. J. Tudor, and N. M. White, Measurement Science and Technology **17**, R175 (2006).

[4] *Sustainable Energy Harvesting Technologies – Past, Present and Future*, edited by Y. K. Tan (InTech, Janeza Trdine 9, 51000 Rijeka, Croatia, 2011).

[5] A.C.M. de Queiroz, 53rd IEEE International Midwest Symposium on Circuits and Systems (MWSCAS) 404 (2010).

[6] S. Kim, J. Park, H. Ahn, D. Liu, and D. Kim, Microelectronics Journal **42**, 988 (2011).

[7] J.F. Li, W.S. Liu, L.D. Zhao, and M. Zhou, NPG Asia Materials **2**, 152 (2010).

[8] G. Zeng, J. E. Bowers, J. M. O. Zide, A. C. Gossard, W. Kim, S. Singer, A. Majumdar, R. Singh, Z. Bian, Y. Zhang, and A. Shakouri, Appl. Phys. Lett. **88**, 113502 (2006).

[9] C. J. Vineis, A. Shakouri, A. Majumdar, and M. G. Kanatzidis, Advanced Materials **22**, 3970 (2010).

[10] C. B. Vining, Nat. Mater. **8**, 83 (2009).

[11] Committee on Thermionic Research, Aeronautics Technology, and National Research Council Space Engineering Board, *Thermionics Quo Vadis? An Assessment of the DTRA's Advanced Thermionics Research and Development Program* (The National Academies Press, Washington, D.C., 2001).

[12] M. S. El-Genk and Y. Momozaki, Energy Conversion and Management **43**, 911 (2002).

[13] Y. Hishinuma, T. H. Geballe, B. Y. Moyzhes, and T. W. Kenny, J. Appl. Phys. **94**, 4690 (2003).

[14] G. Despesse and T. Jager, J. Appl. Phys. **96**, 5026 (2004).

[15] N. Tatsumi, A. Ueda, Y. Seki, Y. Nishibayashi, and T. Imai, SEI TECHNICAL REVIEW 15 (2007).

[16] F. Zocchi, J. Appl. Phys. **56**, 2972 (1984).

[17] S. J. Sque, R. Jones, and P. R. Briddon, Phys. Status Solidi A **202**, 2091 (2005).

[18] Z. Zhang, M. Wensell, and J. Bernholc, Phys. Rev. B **51**, 5291 (1995).

[19] M. J. Rutter and J. Robertson, Phys. Rev. B **57**, 9241 (1998).

[20] G. Kern and J. Hafner, Phys. Rev. B **56**, 4203 (1997).

[21] K. M. O'Donnell, T. L. Martin, N. A. Fox, and D. Cherns, Phys. Rev. B **82**, 115303 (2010).

[22] F. Maier, J. Ristein, and L. Ley, Phys. Rev. B **64**, 165411 (2001).

[23] J. B. Cui, J. Ristein, and L. Ley, Phys. Rev. Lett. **81**, 429 (1998).

[24] P. K. Baumann and R. J. Nemanich, Phys. Rev. B **58**, 1643 (1998).

[25] L. Diederich, P. Aebi, O. M. Küttel, and L. Schlapbach, Surface Sci. **424**, L314 (1999).

[26] *World Energy Outlook 2012* (International Energy Agency, Paris, 2012).

[27] G. Anastasi, M. Conti, M. D. Francesco, and A. Passarella, Ad Hoc Networks **7**, 537 (2009).

[28] F.C. Krebs, Solar Energy Materials and Solar Cells **93**, 394 (2009).

[29] K. Neuhoff, Oxford Review of Economic Policy **21**, 88 (2005).

[30] in *Space Nuclear Power*, edited by J. A. Angelo and D. Buden (Orbit Book Company, Malabar, Florida, 1985).

[31] S. P. Beeby, R. N. Torah, M. J. Tudor, P. Glynne-Jones, T. O'Donnell, C. R. Saha, and S. Roy, J. Micromech. Microeng. **17**, 1257 (2007).

[32] P. Glynne-Jones, M. J. Tudor, S. P. Beeby, and N. M. White, Sensors and Actuators A **110**, 344 (2004).

[33] S. P. Beeby, M.J. Tudor, R.N. Torah, S. Roberts, T. O'Donnell, and S. Roy, Microsystem Technologies **13**, 1647 (2007).

[34] Sardini E. and M. Serpelloni, Sensors and Actuators A: Physical **172**, 475 (2011).

[35] N. N. H. Ching, H. Y. Wong, W. J. Li, P. H. W. Leong, and Z. Wen, Sensors and Actuators A: Physical **97–98**, 685 (2002).

[36] E. Koukharenko, S. P. Beeby, M. J. Tudor, N. M. White, T. O'Donnell, C. Saha, S. Kulkarni, and S. Roy, Microsyst. Technol. **12**, 1071 (2006).

[37] R. Torah, P. Glynne-Jones, M. Tudor, T. O'Donnell, S. Roy, and S. Beeby, Measurement Science and Technology **19**, 125202 (2008).

[38] P. Wang, X. Dai, X. Zhao, and G. Ding, Proceedings Power MEMS 2009 296 (2009).

[39] N. S. Hudak and G. G. Amatucci, J. Appl. Phys. **103**, 101301 (2008).

[40] Y. Arakawa, Y. Suzuki, and N. Kasagi, Proc. PowerMEMS .

[41] P. D. Mitcheson, B. H. Stark, P. Miao, E. M. Yeatman, A. S. Holmes, and T. C. Green, Proc. Eurosensors **3**, 492 (2003).

[42] G. Despesse, T. Jager, J. J. Chaillout, J. M. Leger, A. Vassilev, S. Basrour, and B. Charlot, Symposium on Design, Test, Integration and Packaging of MEMS/MOEMS (DTIP 2005) 386 (2005).

[43] H. Lo and Y.C. Tai, Journal of Micromechanics and Microengineering **18**, 104006 (2008).

[44] D. Hoffmann, B. Folkmer, and Y. Manoli, Journal of Micromechanics and Microengineering **19**, 094001 (2009).

[45] K. A. Cook-Chennault, N. Thambi, M. A. Bitetto, and E. B. Hameyie, Bulletin of Science, Technology & Society **28**, 496 (2008).

[46] S. Roundy and P. K. Wright, Smart Materials and Structures **13**, 1131 (2004).

[47] Y. B. Jeon, R. Sood, J. H. Jeong, and S. G. Kim, Sensors and Actuators A: Physical **122**, 16 (2005).

[48] H. B. Fang, J. Q. Liu, Z. Y. Xu, L. Dong, L. Wang, D. Chen, B. C. Cai, and Y. Liu, Microelectronics Journal **37**, 1280 (2006).

[49] M. Renaud, K. Karakaya, T. Sterken, P. Fiorini, C. V. Hoof, and R. Puers, Sensors and Actuators A: Physical **145–146**, 380 (2008).

[50] D. Shen, J. H. Park, J. Ajitsaria, S. Y. Choe, H. C. Wikle III, and D. J. Kim, Journal of Micromechanics and Microengineering **18**, 055017 (2008).

[51] M. Marzencki, Y. Ammar, and S. Basrour, Sensors and Actuators A: Physical **145–146**, 363 (2008).

[52] Y. Liao and H. A. Sodano, Smart Materials and Structures **17**, 065026 (2008).

[53] R. Elfrink, T. M. Kamel, M. Goedbloed, S. Matova, D. Hohlfeld, Y. Andel, and R. Schaijk, Journal of Micromechanics and Microengineering **19**, 094005 (2009).

[54] S. L. Kok, N. M. White, and N. R. Harris, Measurement Science and Technology **20**, 124010 (2009).

[55] T.J. Kaźmierski and S. Beeby, *Energy harvesting systems: principles, modeling and applications* (Springer, New York, 2010).

[56] R. Duggirala, R.G. Polcawich, M. Dubey, and A. Lal, Journal of Microelectromechanical Systems **17**, 837 (2008).

[57] R. W. Miles, G. Zoppi, and I. Forbes, Materials Today **10**, 20 (2007).

[58] R. W. Miles, K. M. Hynes, and I. Forbes, Progress in Crystal Growth and Characterization of Materials **51**, 1 (2005).

[59] G. J. Snyder and E. S. Toberer, Nat. Mater. **7**, 105 (2008).

[60] R. Venkatasubramanian, E. Siivola, T. Colpitts, and B. O'Quinn, Nature **413**, 597 (2001).

[61] T. C. Harman, M. P. Walsh, B. E. laforge, and G. W. Turner, Journal of Electronic Materials **34**, L19 (2005).

[62] S.K. Chou, W.M. Yang, K.J. Chua, J. Li, and K.L. Zhang, Applied Energy **88**, 1 (2011).

[63] *Mid-infrared Semiconductor Optoelectronics*, Vol. 118 of *Springer Series in Optical Sciences*, edited by A. Krier (Springer, London, 2006).

[64] M. Bosia, C. Ferraria, F. Melinoa, P. R. Pinellib, M. Spinab, and M. Venturinib, Proceedings of ECOS 2012 - The 25th international conference on efficiency, cost, optimization, simulation, and environmental impact of energy systems 88 (2012).

[65] F. A. M. Koeck and R. J. Nemanich, J. Appl. Phys. **112**, 113707 (2012).

[66] J. W. Schwede, I. Bargatin, D. C. Riley, B. E. Hardin, S. J. Rosenthal, Y. Sun, F. Schmitt, P. Pianetta, R. T. Howe, Z. Shen, and N. A. Melosh, Nat. Mater. **9**, 762 (2010).

[67] A. D. Smith, M. Tinkham, and W. J. Skocpol, Phys. Rev. B **22**, 4346 (1980).

[68] A. D. Smith, W. J. Skocpol, and M. Tinkham, Phys. Rev. B **21**, 3879 (1980).

[69] J. Marschall and A. Majumdar, J. Appl. Phys. **74**, 4000 (1993).

[70] A. N. Korotkov and K. K. Likharev, Appl. Phys. Lett. **75**, 2491 (1999).

[71] L. D. Hicks and M. S. Dresselhaus, Phys. Rev. B **47**, 12727 (1993).

[72] G. D. Mahan, J. Appl. Phys. **76**, 4362 (1994).

[73] G. D. Mahan and L. M. Woods, Phys. Rev. Lett. **80**, 4016 (1998).

[74] G. D. Mahan, J. Appl. Phys. **83**, 4683 (1998).

[75] Y. Hishinuma, T. H. Geballe, B. Y. Moyzhes, and T. W. Kenny, Appl. Phys. Lett. **78**, 2572 (2001).

[76] Y. Hishinuma, B. Y. Moyzhes, T. H. Geballe, and T. W. Kenny, Appl. Phys. Lett. **81**, 4242 (2002).

[77] G. Gerstenmaier, Y. C.; Wachutka, Therminic 2005: International Workshop on Thermal Investigation of ICs and Systems 270 (2005).

[78] E. T. Enikov and T. Makansi, Nanotechnology **19**, 075703 (2008).

[79] M. F. O'Dwyer, T. E. Humphrey, R. A Lewis, and C. Zhang, Journal of Physics D: Applied Physics **42**, 035417 (2009).

[80] T. E. Humphrey, M. F. O'Dwyer, and H. Linke, Journal of Physics D: Applied Physics **38**, 2051 (2005).

[81] T. L. Westover and T. S. Fisher, Phys. Rev. B **77**, 115426 (2008).

[82] A. N. Tavkhelidze, J. Appl. Phys. **108**, 044313 (2010).

[83] A. N. Tavkhelidze, V. Svanidze, and L. Tsakadze, Journal of Vacuum Science & Technology A: Vacuum, Surfaces, and Films **26**, 5 (2008).

[84] F. A. M. Koeck and R. J. Nemanich, Diamond Relat. Mater. **15**, 217 (2006).

[85] F. A. M. Koeck and R. J. Nemanich, Diamond Relat. Mater. **18**, 232 (2009).

[86] P. W. May, Phil. Trans. R. Soc. A **358**, 473 (2000).

[87] R. S. Balmer, J. R. Brandon, S. L. Clewes, H. K. Dhillon, J. M. Dodson, I. Friel, P. N. Inglis, T. D. Madgwick, M. L. Markham, T. P. Mollart, N. Perkins, G. A. Scarsbrook, D. J. Twitchen, A. J. Whitehead, J. J. Wilman, and S. M. Woollard, J. Phys. Cond. Matter **21**, 364221 (2009).

[88] A. K. Tiwari, J. P. Goss, P. R. Briddon, N. G. Wright, A. B. Horsfall, R. Jones, and M. J. Rayson, Phys. Rev. Lett. under review (2012).

[89] A. K. Tiwari, J. P. Goss, P. R. Briddon, N. G. Wright, A. B. Horsfall, R. Jones, H. Pinto, and M. J. Rayson, Phys. Status Solidi A **209**, 1709 (2012).

[90] A. K. Tiwari, J. P. Goss, P. R. Briddon, N. G. Wright, A. B. Horsfall, and M. J. Rayson, Phys. Status Solidi A **209**, 1697 (2012).

[91] A. K. Tiwari, J. P. Goss, P. R. Briddon, N. G. Wright, A. B. Horsfall, and M. J. Rayson, Phys. Status Solidi A **209**, 1703 (2012).

[92] A. K. Tiwari, J. P. Goss, P. R. Briddon, N. G. Wright, A. B. Horsfall, and M. J. Rayson, Phys. Rev. B **86**, 155301 (2012).

[93] A. K. Tiwari, J. P. Goss, P. R. Briddon, N. G. Wright, A. B. Horsfall, R. Jones, H. Pinto, and M. J. Rayson, Phys. Rev. B **84**, 245305 (2011).

[94] K. W. Wong, Y. M. Wang, S. T. Lee, and R. W. M. Kwok, Diamond Relat. Mater. **8**, 1885 (1999).

[95] K. H. Wong, Y. M. Wang, S. T. Lee, and R. W. M. Kwok, Appl. Surf. Sci. **140**, 144 (1999).

[96] L. Diederich, O. M. Küttel, P. Aebi, E. Maillard-Schaller, R. Fasel, and L. Schlapbach, Diamond Relat. Mater. **7**, 660 (1998).

[97] F. Maier, F. Riedel, B. Mantel, J. Ristein, and L. Ley, Phys. Rev. Lett. **85**, 3472 (2000).

[98] F. A. M. Koeck and R. J. Nemanich, Diamond Relat. Mater. **14**, 2051 (2005).

[99] M. Suzuki, T. Ono, N. Sakuma, and T. Sakai, Diamond Relat. Mater. **18**, 1274 (2009).

[100] W. F. Paxton, M. Howell, W. P. Kang, and J. L. Davidson, Journal of Vacuum Science & Technology B: Microelectronics and Nanometer Structures **30**, 021202 (2012).

[101] F. A. M. Koeck, R. J. Nemanich, A. Lazea, and K. Haenen, Diamond Relat. Mater. **18**, 789 (2009).

[102] K. Uppireddi, T. L. Westover, T. M. Fisher, B. R. Weiner, and G. Morell, J. Appl. Phys. **106**, 043716 (2009).

[103] W. Zhu, C. Bower, G. P. Kochanski, and S. Jin, Solid-State Electronics **45**, 921 (2001).

[104] T. Ito, T. Watanabe, M. Irie, J. Nakamura, and T. Teraji, Diamond Relat. Mater. **12**, 434 (2003).

[105] N. Tatsumi, A. Ueda, K. Tanizaki, Y. Nishibayashi, and T. Imai, SEI TECHNICAL REVIEW **66**, 36 (2008).

[106] M. Born and J. R. Oppenheimer, Ann. Phys. **84**, 457 (1927).

[107] *Electronic Density Functional Theory: Recent Progress & New Directions*, edited by J. F. Dobson, M. P. Das, and G. Vignale (Kluwer Academic Publishers, New York, 1998).

[108] R. M. Dreizler and E. K. U. Gross, *Density Functional Theory* (Springer, Berlin, 1990).

[109] J. C. Slater, Phys. Rev. **35**, 210 (1930).

[110] P. Hohenberg and W. Kohn, Phys. Rev. **136**, B864 (1964).

[111] W. Kohn and L. J. Sham, Phys. Rev. **140**, A1133 (1965).

[112] U. von Barth and L. Hedin, J. Phys. C **5**, 1629 (1972).

[113] J. P. Perdew and Y. Wang, Phys. Rev. B **45**, 13244 (1992).

[114] J. P. Perdew, K. Burke, and M. Ernzerhof, Phys. Rev. Lett. **77**, 3865 (1996).

[115] J. P. Perdew and A. Zunger, Phys. Rev. B **23**, 5048 (1981).

[116] S. Goedecker, M. Teter, and J. Hutter, Phys. Rev. B **54**, 1703 (1996).

[117] D. Ceperley, Phys. Rev. B **18**, 3126 (1978).

[118] D. M. Ceperley and B. J. Alder, Phys. Rev. Lett. **45**, 566 (1980).

[119] M. J. Rayson and P. R. Briddon, Phys. Rev. B **80**, 205104 (2009).

[120] M. J. Rayson and P. R. Briddon, Computer Phys. Comm. **178**, 128 (2008).

[121] M. J. Rayson and P. R. Briddon, Phys. Rev. B **77**, 035119 (2008).

[122] M. J. Rayson, Phys. Rev. E **76**, 026704 (2007).

[123] M. J. Rayson, Phys. Rev. B **75**, 153203 (2007).

[124] P. R. Briddon and R. Jones, Phys. Status Solidi B **217**, 131 (2000).

[125] R. Jones and P. R. Briddon, in *Identification of Defects in Semiconductors*, Vol. 51A of *Semiconductors and Semimetals*, edited by M. Stavola (Academic Press, Boston, 1998), Chap. 6.

[126] R. Jones, in *New methods for modelling processes within solids and at their surfaces*, edited by C. R. A. Catlow, A. M. Stoneham, and Sir John Meurig Thomas (Oxford Science Publications, New York, 1993), Chap. *Ab initio* cluster calculations of defects in solids, pp. 157–163.

[127] R. Jones, B. J. Coomer, J. P. Goss, B. Hourahine, and A. Resende, in *Special defects in semiconducting materials*, Vol. 71 of *Solid State Phenomena*, edited by R. P. Agarwala (Scitech Publications Ltd., Zuerich-Uetikon, Switzerland, 2000), Chap. The interaction of hydrogen with deep level defects in silicon, pp. 173–248.

[128] G. B. Bachelet, D. R. Hamann, and M. Schlüter, Phys. Rev. B **26**, 4199 (1982).

[129] N. Troullier and J. L. Martins, Phys. Rev. B **43**, 1993 (1991).

[130] C. Hartwigsen, S. Goedecker, and J. Hutter, Phys. Rev. B **58**, 3641 (1998).

[131] H. J. Monkhorst and J. D. Pack, Phys. Rev. B **13**, 5188 (1976).

[132] D. A. Liberman, Phys. Rev. B **62**, 6851 (2000).

[133] P. K. Baumann and R. J. Nemanich, J. Appl. Phys. **83**, 2072 (1998).

[134] C. J. Fall, N. Bingeli, and A. Baldereschi, J. Phys. Cond. Matter **11**, 2689 (1999).

[135] S. J. Sque, R. Jones, and P. R. Briddon, Phys. Rev. B **73**, 085313 (2006).

[136] R. S. Mulliken, J. Chem. Phys. **23**, 1833 (1955).

[137] J. A. Pople and D. L. Beveridge, in *Approximate Molecular Orbital Theory* (McGraw-Hill, New York, London, 1970).

[138] http://aimpro.ncl.ac.uk/ .

[139] E.C. Teague, J. Res. Nat. Bur. Stand. **91**, 171 (1986).

[140] M. Arik, J. Bray, and S. Weaver, Nanosci. Nanotechnol. Lett. **2**, 189 (2002).

[141] Roland Kjellander and Stjepan MarcÃĎlja, Chemical Physics Letters **112**, 49 (1984).

[142] *CRC handbook of chemistry and physics*, 87 ed., edited by D. R. Lide (CRC Press, Boca Raton, Florida, USA, 2006).

[143] Y. Tang, Ph.D. thesis, North Carolina State University., 2007.

[144] S. J. Sque, Ph.D. thesis, School of Physics, University of Exeter, 2005.

[145] M. Werner, P. Gluche, M. Adamschik, E. Kohn, and H. J. Fecht, International Symposium on Industrial Electronics, Proceedings ISIE'98. **1**, 147 (1998).

[146] M. Thumm, Diamond Relat. Mater. **10**, 1692 (2001).

[147] J. R. Brandon, S. E. Coe, R. S. Sussmann, K. Sakamoto, R. Spörl, R. Heidinger, and S. Hanks, Fusion Eng. and Design **53**, 553 (2001).

[148] in *Stone: Properties, Durability in Man's Environment, Applied Mineralogy*, edited by E. M. Winkler (Springer-Verlag, New York, 1975), Vol. 2.

[149] J. Ristein, Surface Science **600**, 3677 (2006).

[150] J. E. Graebner, Diamond Relat. Mater. **5**, 1366 (1996).

[151] J. Singh, *Physics of semiconductors and their heterostructures* (McGraw-Hill, New York, 1993).

[152] T. Vogel, J. Meijer, and A. Zaitsev, Diamond Relat. Mater. **13**, 1822 (2004).

[153] G. Braunstein and R. Kalish, J. Appl. Phys. **54**, 2106 (1983).

[154] L. G. Wang and A. Zunger, Phys. Rev. B **66**, 161202 (2002).

[155] M. Nesládek, Semicond. Sci. Technol. **20**, R19 (2005).

[156] J. P. Goss, P. R. Briddon, S. J. Sque, and R. Jones, Diamond Relat. Mater. **13**, 684 (2004).

[157] S. J. Sque, R. Jones, J. P. Goss, and P. R. Briddon, Phys. Rev. Lett. **92**, 017402 (2004).

[158] R. Kalish, C. Uzan-Saguy, B. Philosoph, V. Richter, J. P. Lagrange, E. Gheeraert, A. Deneuville, and A. T. Collins, Diamond Relat. Mater. **6**, 516 (1997).

[159] S. Koizumi, T. Teraji, and H. Kanda, Diamond Relat. Mater. **9**, 935 (2000).

[160] A. Kraft, Int. J. Electrochem. Sci **2**, 355 (2007).

[161] X. Ling, P. Zhang, R. Li, D. Fan, and X. Yao, Surface and Interface Analysis (2012).

[162] S. Prawer, C. Uzan-Saguy, G. Braunstein, and R. Kalish, Appl. Phys. Lett. **63**, 2502 (1993).

[163] E. B. Lombardi, A. Mainwood, and K. Osuch, Phys. Rev. B **76**, 155203 (2007).

[164] J. P. Goss, R. J. Eyre, and P. R. Briddon, Physica Status Solidi (B) **245**, 1679 (2008).

[165] P. Strobel, M. Riedel, J. Ristein, and L. Ley, Nat. Mater. **430**, 439 (2004).

[166] C. Bandis and B. B. Pate, Phys. Rev. Lett. **74**, 777 (1995).

[167] W. L. Yang, J. D. Fabbri, T. M. Willey, J. R. I. Lee, J. E. Dahl, R. M. K. Carlson, P. R. Schreiner, A. A. Fokin, B. A. Tkachenko, N. A. Fokina, W. Meevasana, N. Mannella, K. Tanaka, X. J. Zhou, T. van Buuren, M. A. Kelly, Z. Hussain, N. A. Melosh, and Z.-X. Shen, Science **316**, 1460 (2007).

[168] J. D. Rameau, J. Smedley, E. M. Muller, T. E. Kidd, and P. D. Johnson, Phys. Rev. Lett. **106**, 137602 (2011).

[169] X. Chang, Q. Wu, I. Ben-Zvi, A. Burrill, J. Kewisch, T. Rao, J. Smedley, E. Wang, E. M. Muller, R. Busby, and D. Dimitrov, Phys. Rev. Lett. **105**, 164801 (2010).

[170] C. Kress, M. Fiedler, W. G. Schmidt, and F. Bechstedt, Phys. Rev. B **50**, 17697 (1994).

[171] P. Krüger and J. Pollmann, Phys. Rev. Lett. **74**, 1155 (1995).

[172] T. I. Hukka, T. A. Pakkanen, and M. P. D'Evelyn, J. Phys. Chem. **99**, 4710 (1995).

[173] A. Scholze, W. G. Schmidt, and F. Bechstedt, Phys. Rev. B **53**, 13725 (1996).

[174] K. C. Pandey, Phys. Rev. B **25**, 4338 (1982).

[175] C. Stampfl, T. E. Derry, and N. W. Makau, J. Phys. Cond. Matter **22**, 475005 (2010).

[176] T. E. Derry, N. W. Makau, and C. Stampfl, Journal of Physics: Condensed Matter **22**, 265007 (2010).

[177] P. G. Lurie and J. M. Wilson, Surface Science **65**, 453 (1977).

[178] A. A. Stekolnikov, J. Furthmüller, and F. Bechstedt, Phys. Rev. B **65**, 115318 (2002).

[179] M. Asmann, J. Heberlein, and E. Pfender, Diamond Relat. Mater. **8**, 1 (2001).

[180] K. Larsson and S. Lunell, J. Phys. Chem. A **101**, 76 (1997).

[181] I. Schmidt and C. Benndorf, Diamond Relat. Mater. **7**, 266 (1998).

[182] I. Schmidt and C. Benndorf, Diamond Relat. Mater. **8**, 231 (1999).

[183] I. Schmidt and C. Benndorf, Diamond Relat. Mater. **10**, 347 (2001).

[184] J. A. Chaney and C. S. Feigerle, Surface Sci. **425**, 245 (1999).

[185] T. Kondo, H. Ito, K. Kusakabe, K. Ohkawa, Y. Einaga, A. Fujishima, and T. Kawai, Electrochemica Acta **52**, 3841 (2007).

[186] S. Hadenfeldt and C. Benndorf, Surface Sci. **402–404**, 227 (1998).

[187] M. A. Ray, T. Tyler, B. Hook, A. Martin, G. Cunningham, O. Shenderova, J. L. Davidson, M. Howell, W. P. Kang, and G. McGuire, Diamond Relat. Mater. **16**, 2087 (2007).

[188] A. Freedman and C. D. Stinespring, Appl. Phys. Lett. **57**, 1194 (1990).

[189] A. Freedman, J. Appl. Phys. **75**, 3112 (1994).

[190] V. S. Smentkowski and J. T. Yates Jr., Science **271**, 193 (1996).

[191] K. J. Rietwyk, M. Wanke, H. M. Vulling, M. T. Edmonds, P. L. Sharp, Y. Smets, Q.-H. Wu, A. Tadich, S. Rubanov, P. J. Moriarty, L. Ley, and C. I. Pakes, Phys. Rev. B **84**, 035404 (2011).

[192] V. Petráková, A. Taylor, Fendrych F. Kratochvílová, I., Kučka J. Vacík, J., J. Štursa, P. Cí gler, M. Ledvina, A. Fišerová, P. Kneppo, and M. Nesládek, Adv. Funct. Mater. **22**, 812 (2012).

[193] C. E. Nebel, B. Rezek, D. Shin, H. Uetsuka, and N. Yang, J. Phys. D **40**, 6443 (2007).

[194] A. Hartl, E. Schmich, J. A. Garrido, J. Hernando, S. C. R. Catharino, S. Walter, P. Feulner, A. Kromka, D. Steinmuller, and M. Stutzmann, Nature Mater. **3**, 736 (2004).

[195] J. Ristein, Appl. Phys. A **82**, 377 (2006).

[196] G. Dearnaley and J. H. Arps, Surf. Coat. Tech. **200**, 2518 (2005).

[197] V. Petráková, A. Taylor, I. Kratochvílová, F. Fendrych, J. Vacík, J. Kučka, J. Štursa, P. Cígler, M. Ledvina, A. Fišerová, P. Kneppo, and M. Nesládek, Adv. Func. Mat. **22**, 812 (2011).

[198] J. B. Miller and D. W. Brown, Langmuir **12**, 5809 (1996).

[199] M. R. Lockett and L. M. Smith, Langmuir **25**, 3340 (2009).

[200] W. Kulisch, C. Popov, D. Gilliland, Ceccone. G., J. P. Reithmaier, and F. Rossi, Surf. Coat. Tech. **206**, 667 (2011).

[201] C. Popov, H. Vasilchina, W. Kulisch, F. Danneil, M. Stüber, S. Ulrich, A. Welle, and J. P. Reithmaier, Diamond Relat. Mater. **18**, 895 (2009).

[202] Y. Jia, W. Zhu, E. G. Wang, Y. Huo, and Z. Zhang, Phys. Rev. Lett. **94**, 086101 (2005).

[203] D. Petrini and K. Larsson, The Journal of Physical Chemistry C **111**, 795 (2007).

[204] J. Y. Lee and M.-H. Kang, Phys. Rev. B **69**, 113307 (2004).

[205] M. Bedzyk and G. Materlik, Surface Sci. **152**, 10 (1985).

[206] M. P. D'Evelyn, Y. L. Yang, and S. M. Cohen, J. Chem. Phys. **101**, 2463 (1994).

[207] R. Martín, P. C. Heydorn, M. Alvaro, and H. Garcia, Chemistry of Materials **21**, 4505 (2009).

[208] P.-L. Cao and R.-H. Zhou, J. Phys. Cond. Matter **5**, 2897 (1993).

[209] H.-Y. Hou, H.-H. Wu, J.-Y. Chung, and D.-S. Lin, J. Phys. Chem. C **115**, 13262 (2011).

[210] I. Kratochvílová, A. Kovalenko, A. Taylor, F. Fendrych, V. Řezáčová, J. Vlček, S. Záliš, J. Šebera, P. Cígler, M. Ledvina, and M. Nesládek, Phys. Status Solidi A **207**, 2045 (2010).

[211] A. Krueger and G. Lang, D. Jarre, SBDD XVII 150 (2012).

[212] I. L. Krainsky and V. M. Asnin, Appl. Phys. Lett. **72**, 2574 (1998).

[213] D. Takeuchi, H. Kato, G. S. Ri, T. Yamada, P. R. Vinod, D. Hwang, C. E. Nebel, H. Okushi, and S. Yamasaki, Appl. Phys. Lett. **86**, 152103 (2005).

[214] W. E. Pickett, Phys. Rev. Lett. **73**, 1664 (1994).

[215] M. W. Geis, J. C. Twichell, J. Macaulay, and K. Okano, Appl. Phys. Lett. **67**, 1328 (1995).

[216] K. P. Loh, J. S. Foord, R. G. Egdell, and R. B. Jackman, Diamond Relat. Mater. **6**, 874 (1997).

[217] T. Tachibana, B. E. Williams, and J. T. Glass, Phys. Rev. B **45**, 11968 (1992).

[218] T. Teraji, S. Koizumi, and Y. Koide, J. Appl. Phys. **104**, 016104 (2008).

[219] K. Das, V. Venkatesan, K. Miyata, D. L Dreifus, and J. T. Glass, Thin Solid Films **212**, 19 (1992).

[220] J. W. Glesener, A. A. Morrish, and K. A. Snail, J. Appl. Phys. **70**, 5144 (1991).

[221] A. T. Collins, Semicond. Sci. Technol. **4**, 605 (1989).

[222] in *Diamond Films and Coatings: Development, Properties and Applications*, edited by Robert F. Davis (William Andrew Publishing, New York, 1994), Chap. Properties of Solids.

[223] R. L. Bell, in *Negative Electron Affinity Device* (Clarendon Press, Oxford, 1973).

[224] M. W. Geis, J. C. Twichell, and T. M. Lyszczarz, J. Vac. Sci. and Technol. B **14**, 2060 (1996).

[225] J. van der Weide and R. J. Nemanich, Phys. Rev. B **49**, 13629 (1994).

[226] J. van der Weide and R. J. Nemanich, J. Vac. Sci. and Technol. B **10**, 1940 (1992).

[227] M. W. Geis, N. N. Efremow, J. D. Woodhouse, M. D. McAleese, M. Ma rchywka, D. G. Socker, and J.F. Hochedez, IEEE Electron Device Letters **12**, 456 (1991).

[228] I. Motochi, N. W. Makau, and G. O. Amolo, Diamond Relat. Mater. **23**, 10 (2012).

[229] H. Guo, Y. Qi, and X. Li, J. Appl. Phys. **107**, 033722 (2010).

[230] L. J. Brillson, Surface Sci. Reports **2**, 123 (1982).

[231] S. M. Sze and K. K. Ng, *Physics of Semiconductor Devices*, 3 ed. (John Wiley & Sons, Hoboken, New Jersy, 2006), Chap. Metal-Semiconductor Contacts.

[232] E. H. Rhoderick and R. H. Williams, in *Metal-Semiconductor Contacts* (Clarendon Press, Oxford, 1988).

[233] S. B. Zhang, M. L. Cohen, and S. G. Louie, Phys. Rev. B **32**, 3955 (1985).

[234] S. Kurtin, T. C. McGill, and C. A. Mead, Phys. Rev. Lett. **22**, 1433 (1969).

[235] J. Tersoff, Phys. Rev. B **30**, 4874 (1984).

[236] W. E. Pickett and S. C. Erwin, Phys. Rev. B **41**, 9756 (1990).

[237] M. J. Mehl and D. A. Papaconstantopoulos, Phys. Rev. B **54**, 4519 (1996).

[238] A. Aguayo, G. Murrieta, and R. de Coss, Phys. Rev. B **65**, 092106 (2002).

[239] M. Binnewies and E. Milke, *Thermochemical data of elements and compounds* (Wiley, New York, 1999).

[240] R. G. Coltters, Mater. Sci. Eng. **76**, 1 (1985).

[241] P. H. T. Philipsen and E. J. Baerends, Phys. Rev. B **54**, 5326 (1996).

[242] Y. Morikawa, K. Kobayashi, and K. Terakura, Surface Sci. **283**, 377 (1993).

[243] T. Abukawa and S. Kono, Phys. Rev. B **37**, 9097 (1988).

[244] M. Sommer, R. Haubner, and B. Lux, Diamond Relat. Mater. **9**, 351 (2000).

[245] Z.-B. Ma, Q.-C. Wu, X.-S. Shu, J.-H. Wang, C.-X. Wang, and X.-F. Li, Plasma Sci. and Tech. **2**, 207 (2000).

[246] X. Wang and J. R. Smith, Phys. Rev. Lett. **87**, 186103 (2001).

[247] B. V. Spitsyn, L. L. Bouilov, and B. V. Derjaguin, J. Cryst. Growth **52**, 219 (1981).

[248] J. M. Rosset, C. Floriani, M. Mazzanti, A. Chiesi-Villa, and C. Guastini, Inorg. Chem. **29**, 3991 (1990).

[249] G. P. Bogatyreva, M. A. Marinich, E. V. Ishchenko, V. L. Gvyazdovskaya, G. A. Bazalii, and N. A. Oleinik, Phys. of the Solid State **46**, 738 (2004).

[250] S. E. Denmark, J. P. Edwards, and S. R. Wilson, Journal of the American Chemical Society **114**, 2592 (1992).

[251] J. Goniakowski and C. Noguera, Phys. Rev. B **79**, 155433 (2009).

[252] J. Sun, H. T. Wang, J. He, and Y. Tian, Phys. Rev. B **71**, 125132 (2005).

[253] S.-D. Mo and W. Y. Ching, Phys. Rev. B **51**, 13023 (1995).

[254] S. J. Thompson and S. P. Lewis, Phys. Rev. B **73**, 073403 (2006).

[255] Z. Zhou, X. Cheng, X. Zhou, and H. Fu, Chemical Physics Letters **353**, 281 (2002).

[256] J. R. Tucker, C. Wang, and T.-C. Shen, Nanotechnol. **7**, 275 (1996).

[257] T.-C. Shen, C. Wang, J. W. Lyding, and J. R. Tucker, Appl. Phys. Lett. **66**, 976 (1995).